UNIVERSITY OF Southampton

Faculty of Engineering and Physical Sciences

School of Engineering


# Improving Bone Healing Using Polymeric Nanoparticle Mediated Delivery of Wnt Agonists

by

**Alethia Ruth Hailes**

ORCID ID https://orcid.org/0000-0001-6819-6781

Thesis for the degree of Doctor of Philosophy

April 2022

**University of Southampton**

# Abstract

Faculty of Engineering and Physical Sciences

Engineering

Thesis for the degree of Doctor of Philosophy

**Improving bone healing using polymeric nanoparticle mediated delivery of Wnt agonists.**

Alethia Ruth Hailes

Bone fractures and their complications are prevalent medical issues with high financial costs and loss in quality of life. Pharmaceutical treatments to aid bone fracture repair are not yet available in clinic, despite their potential for improving fracture outcomes. Therapeutic candidates such as Wnt agonists may improve the quality and rate of healing by boosting key signalling involved in fracture repair. However, these therapies are limited by off-target effects and poor bioavailability at the injury site. Polymeric nanoparticles (polymersomes; PMs) may provide a solution by enabling controlled spatio-temporal drug delivery. This research aimed to develop a PM drug delivery therapeutic for the controlled and localised delivery of a Wnt agonist to a bone injury site, in order to promote bone repair and ultimately improve fracture healing outcomes. In this study, the efficiency of PMs for encapsulating Wnt agonists BIO and CHIR and achieving *in vitro* induction of a Wnt signalling response was assessed using techniques of UV-Vis spectroscopy and a luciferase reporter cell line. Here PMs were successfully produced with a sufficient dose of BIO and CHIR to induce Wnt signalling. In contrast to free compounds, PM-encapsulated BIO and CHIR prevented cytotoxicity when incubated with primary bone cells. This study also assessed the *in vivo* localisation of PMs using an IVIS imaging method which semi-quantified a fluorescent PM payload distribution within a mouse bone injury model. It was found that following injury, either immediate or a 7-day delayed IV administration of PMs resulted in passive accumulation at a target bone injury site. Additionally, a preliminary study using a clodronate liposome pre-treatment to deplete the macrophage population of MPS organs found no significant change in PM accumulation to a target bone injury site. Finally, this study tests the hypothesis that PM-encapsulated BIO can induce Wnt signalling activity and osteogenic differentiation *in vivo.* RT-qPCR analysis of tissues of high PM accumulation extracted 24 or 48 hours following IV treatment of PM-BIO revealed disparate *in vivo* gene expression of Wnt signalling inhibitors (*Axin2 and Dkk1*) depending on the presence of a bone injury, as well as the induction of early osteogenic gene expression (*Runx2*) at a target injured bone. Overall the findings presented in this thesis demonstrate that PM delivery of a Wnt agonist provides a viable bone-promoting therapeutic which could improve fracture healing outcomes.

# TABLE OF CONTENTS

# TABLE OF FIGURES

Table of Figures

Table of Figures

# TABLE OF TABLES

# RESEARCH THESIS: DECLARATION OF AUTHORSHIP

Print name: ALETHIA HAILES

Title of thesis: Improving bone healing using polymeric nanoparticle mediated delivery of Wnt agonists.

I declare that this thesis and the work presented in it are my own and has been generated by me as the result of my own original research.

I confirm that:

1. This work was done wholly or mainly while in candidature for a research degree at this University;
2. Where any part of this thesis has previously been submitted for a degree or any other qualification at this University or any other institution, this has been clearly stated;
3. Where I have consulted the published work of others, this is always clearly attributed;
4. Where I have quoted from the work of others, the source is always given. With the exception of such quotations, this thesis is entirely my own work;
5. I have acknowledged all main sources of help;
6. Where the thesis is based on work done by myself jointly with others, I have made clear exactly what was done by others and what I have contributed myself;
7. Parts of this work have been published as:

**Publications:**

Scarpa, E., Janeczek, A.A., **Hailes, A.,** de Andrés, M.C., De Grazia, A., Oreffo, R.O.C., Newman, T.A. and Evans, N.D. (2018) 'Polymersome nanoparticles for delivery of Wnt-activating small molecules', Nanomedicine: Nanotechnology, Biology and Medicine, 14(4), pp. 1267–1277. doi:10.1016/j.nano.2018.02.014

**Abstracts:**

"A method for assessing the quality of bone repair using a modified polarised microscope (Polscope)" *10th UK Mesenchymal Stem Cell Meeting, 5th December 2016,* York, UK.

Research Thesis: Declaration of Authorship

"Optimising nanoparticle mediated drug delivery for improved fracture outcome" *Southampton Medical and Health Research Conference, 14-15th June 2017,* University Hospital Southampton, Southampton, UK.

"Optimising nanoparticle mediated drug delivery for improved fracture outcome" *17th Annual Conference of the Tissue and Cell Engineering Society (TCES), 5-7th July 2017,* Manchester, UK. TCES abstracts are published in eCells & Materials.

"Optimising nanoparticle mediated drug delivery for improved fracture outcome" *Future investigators of regenerative medicine* (*FIRM) symposium, 25-th-28th September 2017*, Hotel Cap Roig, Girona, Spain.

"Improving fracture outcome using nanoparticle-mediated drug delivery" PGR Conference for Engineering Sciences, 16th January 2018, Grand Harbour Hotel, Southampton, UK.

"Improving fracture outcome using nanoparticle-mediated drug delivery" *PGR Conference for Engineering Sciences*, 15th January 2019, Grand Harbour Hotel, Southampton, UK.

"Improving fracture outcome using polymeric nanoparticle mediated delivery of Wnt agonists to promote repair" *Tissue Engineering and Regenerative Medicine International Society (TERMIS) EU, 27th-31st May 2019*, Rhodes, Greece.

"Fracture localisation of osteogenic polymersomes and modulation of their accumulation by Kupffer cell depletion" *Southampton Medical and Health Research Conference, 11-12th June 2019,* University Hospital Southampton, Southampton, UK.

Signature: ..... Date: 22nd May 2021

*In a world where you can be anything…*

*be kind.*

# ACKNOWLEDGEMENTS

In 2010 whilst attending Medlink I first learnt of an exciting new (to me!) medical field: *nanomedicine*. After publishing a Gedankenexperiment with my friend Richard Buckley, I was hooked on nano being the future of medicine. I endeavoured to find research opportunities as I started studying biomedical science at the University of Southampton in 2013. I have my tutor Dr Claire Clarkin to thank for encouraging me to pursue this and putting me in touch with Dr Tracey Newman, which has led me here: 12 years on from first learning of nanomedicine, finishing a PhD thesis about it! It has been an incredible journey, supported by many truly wonderful and inspirational people who deserve to be acknowledged here.

My first acknowledgment must go to Dr Tracey Newman, one half of my awesome supervisory team. Tracey has been a true mentor, who has believed in me and guided me through learning what it means to be a great scientist and a supportive leader. It is the opportunities Tracey gave me during my undergraduate degree that enabled me to undertake this PhD, and it is thanks to Tracey's walks and pep talks, empathetic ear, and advice that I made it through to completion.

I would not be here today if it were not for my main supervisor, Dr Nick Evans, who gave me the opportunity of this PhD and has been a shoulder to lean on especially towards the end. Nick has been such a great mentor, challenged me when needed, and has also been so understanding and supportive. I am grateful for all I have learnt from him and will carry his advice into my future career.

I must also credit this PhD opportunity to Edo, who taught and supported my first steps as a scientist. Edo, I am forever grateful for your friendship and hope (as your minion!) I have done you proud whilst building on the foundation you laid. Huge thanks must also be given to Ed, my early additional supervisor (I learnt from the best for imaging!); to Jon May, for being a brilliant assistant with the animal work and confidant; and to Shmma, an inspirational lady and valued support. I owe Shmma a great deal for showing me I can come back and I can do this!

I consider myself very lucky to have been a part of two amazing research groups: TAN lab with its extended B85 family, and the Bone & Joint group. A huge thanks must be given to all those I have had the pleasure of working alongside, for being so supportive and fun - the tea breaks, lunches and socials have been the best!

This thesis would not have been possible without the technical support teams of the BRF and the Bone & Joint research group. From the BRF: Vikki, Lisa, Andrew, Russell, and Neil; and from Bone & Joint: Kate, May, Julia, Stuart, and a special thanks to Janos. Thank you also to the support team at DSTL.

There are two colleagues who I must give a special thanks to, without whom I would not have completed this PhD. Anna, for being such a caring friend and a wonderful example of kindness and perseverance, and Eleanor, for being a constant source of encouragement, laughter, and a shoulder to cry on. I could not have asked for a better lab partner to share this PhD journey with; I will miss our rants together and cherish your friendship.

I must also thank my amazing family for all of their love, prayers, and support, especially my parents for their multiple helpful suggestions of how to “fix the noo-noos”. Thank you also to my close friends for always cheering me on.

My final and most important acknowledgment must go to my husband, Peter, who is my rock and I thank God every day that I have him by my side. Thank you for taking care of me, being so loving and patient (especially in proof-reading this whole thesis!) – I could not have done this without you.

# DEFINITIONS AND ABBREVIATIONS

**α-MEM** – alpha modification of Eagle's Minimum Essential Media
**ALP** – Alkaline Phosphatase
**ALD** – Alendronate
**ATP** – Adenosine Triphosphate
**Axin2** – Axin-like protein (aka axin inhibition protein or conductin)
**BIO** – 6'bromoindirubin-3'-oxime; a hemi-synthetic derivative of indirubins originally found in mollusks and plants
**BMP-(x)** e.g. **BMP-2** – Bone Morphogenetic Protein 2; protein of the TGF-β superfamily
**rhBMP** – recombinant human Bone Morphogenic Protein
**BMSC** – Bone Marrow Stromal/Skeletal Cells
**CHIR** – CHIR-99021 (aka. 6-[[2-[[4-(2,4-Dichlorophenyl)-5-(5-methyl-1H-imidazol-2-yl)-2-pyrimidinyl]amino]ethyl]amino]-3-pyridinecarbonitrile); an aminopyrimidine derivative
**CI** – Confidence Interval
**C.Lat** or **CL** – Contralateral
**Col(x)a1** e.g. **ColXa1** – Collagen type 10
**CXCR(x)** e.g. **CXCR4** – Chemokine receptor 4
**Dkk1** – Dickkopf WNT signalling pathway inhibitor
**DLS** – Dynamic Light Scattering
**DMF** – N, N-Dimethylformamide
**DMEM** – Dulbecco's Modified Eagle Medium
**ECM** – Extracellular Matrix
**EDTA** - Ethylenediaminetetraacetic Acid
**Eif3f** – Eukaryotic translation initiation factor 3 subunit F
**ELISA** – Enzyme-Linked Immunosorbent Assay
**F** – Fractured/injured femur
**FACS** – Fluorescence-Activated Cell Sorting
**FGF** – Fibroblast Growth Factor
**Gapdh** – Glyceraldehyde 3-phosphage dehydrogenase; enzyme
**GDF-(x)** e.g. **GDF-5** – Growth Differentiation Factor 5; protein in the TGF-β superfamily
**GSK-3β** – Glycogen Synthase Kinase 3 beta
**GT** – Goldner's Trichrome
**hBMSC** – human Bone Marrow Stomal Cells
**H&E** – Hematoxylin and Eosin
**Hif-1α** – Hypoxia-inducible factor 1 alpha; transcription factor subunit
**HO-1** – Heme Oxygenase 1; enzyme
**HPLC** – High Performance Liquid Chromatography
**IHC** – Immunohistochemistry
**iNOS** – inducible Nitric Oxide Synthase; enzyme
**ISH** – In Situ Hybridisation
**IL-(x)** e.g. **IL-1α** – Interleukin 1 alpha (aka hematopoietin 1); cytokine of the Interleukin 1 family

**IP** – Intraperitoneal
**IV** – Intravenous
**IVIS** – *In Vivo* Imaging System
**KO** – Knockout; transgenic model
**MADLS** – Multi-Angle Dynamic Light Scattering
**mBMSC** – mouse Bone Marrow Stromal Cells
**MCSF** – Macrophage Colony-Stimulating Factor; cytokine
**mESC** – mouse Embryonic Stem Cells
**µCT** – micro Computed Tomography
**Mmp(x)** e.g. **Mmp2** – Matrix metalloproteinase 2 enzyme (aka. type IV collagenase, gelatinase A)
**MPS** – Mononuclear Phagocytic System (aka reticuloendothelial system RES)
**MSC** – Mesenchymal Stem Cells, specifically bone marrow stromal cells
**NP** – Nanoparticle
**NTA** – Nanoparticle Tracking Analysis
**Oc** – Osteocalcin (aka bone gamma-carboxyglutamic acid-containing protein)
**Osx** – Osterix (aka Sp7)
**Opn** – Osteopontin
**OPG** – Osteoprotegerin
**PBS** – Phosphate Buffered Saline
**PCL** – Polycaprolactone
**PDGF** – Platelet Derived Growth Factor
**PEG** – Polyethylene Glycol (aka polyethylene oxide PEO or polyoxyethylene POE – dependent upon molecular weight)
**PLA** – Polylactic Acid (aka polylactide)
**PLGA** – Polylactic-co-Glycolic Acid
**PM** – Polymersome
**PM-BIO/CHIR** – Polymersome-encapsulated BIO or CHIR
**PM-Empty** – Polymersomes loaded with PBS
**PTH** – Parathyroid Hormone
**RANKL** – Receptor Activator of Nuclear factor Kappa-B Ligand (aka. TNFSF11, OPGL)
**RLU** – Relative Light Units
**RT-qPCR** – Reverse Transcription quantitative real time Polymerase Chain Reaction
**Runx2** – Runt-related transcription factor 2
**SDF-1** – Stromal cell Derived Factor 1
**Sox(X)** e.g. **Sox9** – SRY-box transcription factor 9
**SSC** – Skeletal Stem Cell
**TE** – Tris/EDTA
**TEM** – Transmission Electron Microscopy
**TGF-β(x)** e.g. **TGF-β1** – Transforming Growth Factor beta 1; cytokine of the TGF-β superfamily
**TNF-α** – Tumour Necrosis Factor alpha; cytokine of the TNF superfamily
**TRAP** – Tartrate-Resistant Acid Phosphate; bone surface protein
**UV-Vis** – Ultraviolet-Visible light absorbance spectroscopy
**Vegf** – Vascular endothelial growth factor
**WT** – Wild Type

# CHAPTER 1

## INTRODUCTION

### 1.1 FRACTURE TREATMENT NEEDS TO BE IMPROVED

Reduction, bandaging, and splinting are the remedies described in ancient Egyptian and Greek texts for the treatment of bone fractures. It is somewhat remarkable that in the year 2021 these strategies continue to form the basis of clinical guidance in fracture treatment. With technological and medical advances, why is this the case? The body's regenerative capability is wonderfully demonstrated in the healing of bone, and yet there is more to understand as fracture incidence continues to be one of the long-term challenges in health care.

Estimates are that a fracture occurs once every three seconds worldwide. This is based on an estimated prevalence of 9.0 million fractures per year (Johnell and Kanis, 2006); however, this statistic only measures osteoporotic fractures, and therefore the total number of fracture incidents may be even greater still. Indeed, the majority of epidemiology studies on fracture incidence focus on osteoporotic and fragility related fractures, with little consideration of the number of trauma-related incidents. 3.5 million fragility fracture incidents were reported in Europe in 2010, with hip fractures reported as the most prevalent followed by vertebral fractures and forearm fractures (Hernlund *et al.*. 2013). There are preventative treatments widely used in an attempt to reduce osteoporotic related fractures, the most common of which being bisphosphonates particularly alendronate due to its proven efficiency and lower cost. However as Hernlund et al highlights, compliance and persistence with such preventative treatment is poor and only a minority of high fracture risk patients are identified to then access preventative treatments. The majority of fractures are recorded as occurring in the older population, and with our aging population, fractures present a growing health care challenge which will require efficient preventative and post-fracture treatment, as well as a growing economic burden (*World Population Prospects - Population Division - United Nations*, no date); the cost in Europe alone in 2010 was estimated at €37 billion (Hernlund *et al.* 2013),. However, it is important to note that many of the fracture incident statistics and financial data referenced in this publication are produced from a collection of studies, many of which are now over 15 years old and therefore are unlikely to accurately reflect the current situation. A more recent UK cohort study from 2003-2013 revealed an annual hospital cost associated with hip fractures to be

£1.1 billion (£2139 - £14,163 per patient) (Leal *et al.*, 2016). As well as direct cost to care services, often underreported are the indirect costs to the patient with loss of earnings over a long recovery time and any additional social care costs for associated morbidity.

It is clear that bone injuries are a prevalent medical issue with financial and time costs to both patients and health care services, despite the considerable improvements to treatment options made over recent decades. It is recognised that successful fracture healing is likely to be best achieved through replicating and supporting the natural healing process, which requires optimal biological and mechanical conditions. Current treatments, which depend on individual case severity and medical history, arguably heavily focus on mechanical interventions with/without surgery, and focus less on creating ideal biological conditions (Claes, Recknagel and Ignatius, 2012).

## 1.2 COMPLICATIONS

Even with mechanical interventions, many fractures (in particular hip and vertebral fractures) have complications particularity amongst the elderly, and are subsequently associated with long-lasting health effects and increased mortality risk (Hernlund *et al.*, 2013). In a 2016 study on patients aged 50+ years in England, the 1-year mortality risk was 3.2-fold higher following a fracture as compared to the general population. The major causes of death post fracture are reported as neoplasms, respiratory diseases and circulatory diseases (Klop *et al.*, 2016).

As well as increasing with age Klop et al study reveals a higher mortality risk in men compared to women as well as marked increases in BAME (Black, Asian and minority ethnic) ethnicities. The reason for these differences are arguable poorly understood, challenged by unpicking a number of influencing lifestyle, genetic and socioeconomic factors and a lack of dedicated studies. For ethnicity, studies have highlighted that black patients are less likely to receive the same level of rehabilitation and physical therapy than white patients, (Klop *et al.*, 2016; Johnson *et al.*, 2019).

Complications depend on a variety of factors as will be discussed in **section 1.5**; they can be divided into types including: delayed unions, non-unions, contractures, algodystrophy, myositis ossificans, osteomyelitis, and septicaemia (*Complications from Fractures. Information and treatment | Patient*, no date). Of particular note are non-unions, in which no bridging of the fracture gap occurs, which are often reported to occur in 5-10% of treated fracture cases (Kostenuik and Mirza, 2017). However, there are little data available to support this frequently-referenced statistic. In the UK, a study conducted from 2005-2010 on a Scottish cohort found 18.9 per 100,000 population per year are treated for a non-union (Mills and Simpson, 2012). A later study compared this to the total number

of fracture incidents (6800) in the same period, and found 1.9% of adult fracture cases resulted in a non-union: 1.5% in women and 2.3% in men, with the highest rate of over 5% in the 35-44 years age group (Mills, Aitken and Simpson, 2017). This study also found non-union to most commonly occur in the forearm Radius and ulna, however at 75 years and over the highest non-union incidence were of the femur and pelvis (Mills, Aitken and Simpson, 2017). Both age and sex are recognised from large scale systematic reviews to be risk factors of non-union. As well as the aforementioned study by Mills and Simpson, (2012), Zura *et al.* (2016) also found a slightly higher rate of non-union for men at 5.4% compared to women at 4.6%. It is notably hard to separate other confounding factors which may result in this trend, such as if men undertake higher risk energetic activities resulting in these observed differences. At a biological structural level, sex differences in periosteal and endocortical diameters, and in how cortical thickness changes with age, have been linked to females having a higher risk of fractures with age (Duan *et al.*, 2003). However, less studied and understood are sex differences in ability to heal fractures, which is needed to fully ascertain biological explanations for possible age and sexual dimorphisms observed in fracture non-union rates, which could subsequently impact the design of potential therapies.

Standard care for non-union is surgical insertion of a bone graft or substitute, with or without fixation. This exposes patients to the risks of invasive surgery for a second time and results in additional costs to health care services, for treatment (reported as an average of £30,000 per patient - relevant for the years 1992-2003) (Patil and Montgomery, 2006), bed space, and further cost to the patient with a prolonged recovery time (especially if an allograft is taken, producing two wounds). There are no approved alternative therapies available for the treatment or prevention of non-unions. Future preventative pharmaceutical treatments, aimed at improving fracture outcomes by inducing optimal biological conditions for bone healing, could not only address non-union conditions but also have the potential to improve recovery times for all patients with a bone injury, thereby reducing pressure on health care services. There is therefore a great need to research pharmaceutical treatments, which can act as alternatives or work adjunct to surgery, to improve fracture outcome.

This literature review aims to identify possibilities for such treatments. The normal fracture repair process in a healthy individual is described in **section 1.3**. **Section 1.4** details the published evidence on cell signalling in bone injury and repair, and **section 1.5** summarises the current understanding of the causes of poor fracture outcomes.

## 1.3 BONE FRACTURE HEALING: MODEL STAGES AND BIOLOGICAL PROCESSES

Healthy bone is a complex environment comprised of particular tissue structures and specialised cells; the anatomical features of a typical healthy long bone are depicted in **Figure 1.1**. Bone constantly breaks down and rebuilds itself (remodelling) to adjust size and shape during development, homeostasis, and in response to stress and injury. When a bone fractures, the tissue structure and vasculature of both the bone and surrounding soft tissue are disrupted. This damage elicits a sequence of events the first of which address potentially life-threating issues, i.e., potential haemorrhaging and infection, and secondly to repair the tissue, restoring its original function and homeostasis.

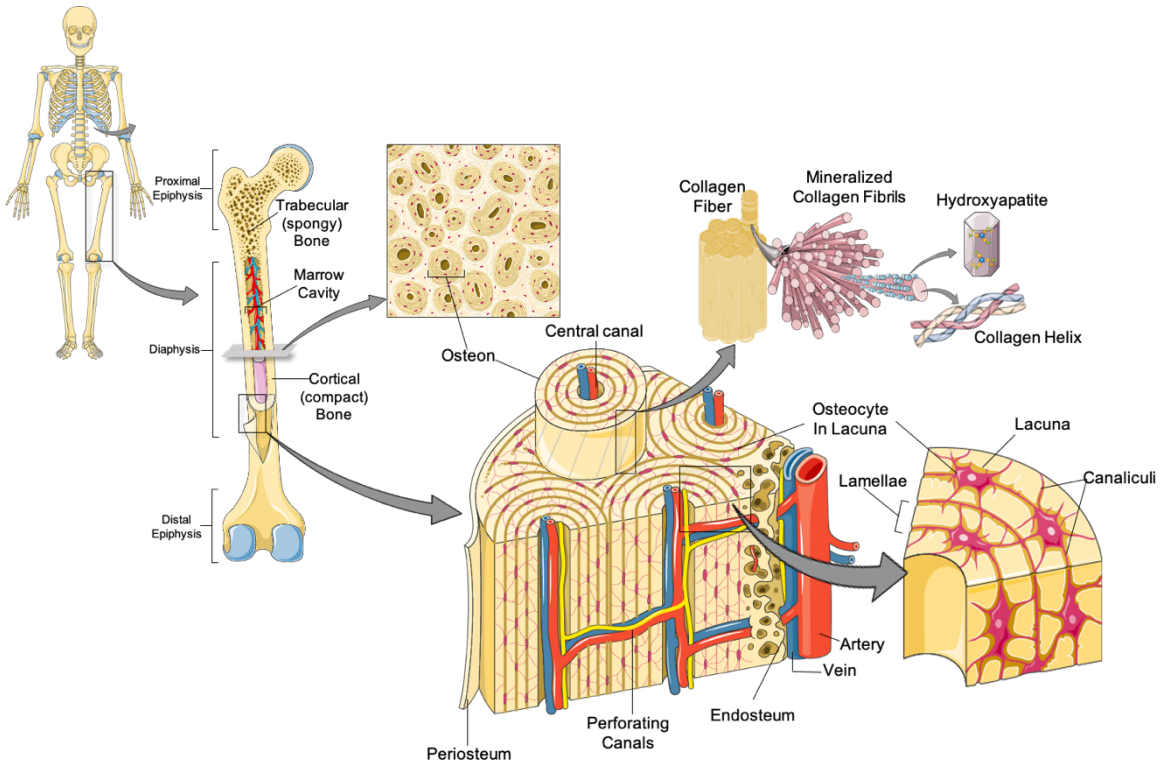


***Figure 1.1: Bone – its structure, tissue, and cells***

*Long bones (e.g., femurs) have a central marrow cavity within the diaphysis region which contains bone marrow (including cellular and fatty tissue) and blood vessels. Surrounding this cavity is a layer of spongy trabecular bone structure, which is also present predominantly at the end epiphysis regions; its honeycomb like structure contains bone marrow filled cavities. Encasing this is a layer of compact/cortical bone tissue structure, which then connects to the periosteum membrane covering the bone's surface. Cortical bone is structurally composed of rod-shaped units called osteons, which have a central (haversian) canal encasing blood vessels and nerves, surrounded by concentric layers (lamellae) of bone tissue. This bone tissue is comprised of mineral and organic material and water. The organic material or matrix (osteoid) is made up of collagen fibres, proteins including structural proteins (e.g., Fibronectin, Osteocalcin, Osteonectin, Osteopontin), enzymes (e.g., Alkaline Phosphatase (ALP)), and growth factors. The mineral material consists of hydroxyapatite (a calcium, phosphorus, and oxygen hexagonal crystal), amongst other apatites. Within bone tissue are gaps called lacuna which contain osteocyte cells. The bone marrow contains haematopoietic cells which give rise to platelets and multiple blood and immune cell types, including osteoclasts, as well as skeletal stem cells which give rise to osteoblasts amongst other cell types. Osteoblasts produce osteoid, which becomes calcified bone matrix, and eventually become an encased osteocyte. Osteoblasts work in tandem with osteoclasts which break down bone matrix to regenerate and remodel bone tissue giving it its structure. Directing this process are numerous interacting subcellular molecules/proteins in signalling pathways. (Parts of this figure's graphics are credited to smart.servier.com)*

Bone regeneration is a complex and highly orchestrated process that involves the coordination of cells, molecular signalling factors, and an extracellular matrix. Histological observations of fractures from humans and animal models have provided a conventional three-stage model of the biological events, in particular the tissue and cellular changes which occur during fracture healing: inflammation, repair, and remodelling, depicted in **Figure 1.2** (Schindeler *et al.*, 2008; Einhorn and Gerstenfeld, 2014). It is important to note that although the general mechanisms of repair seem to be similar between small animals, large animals and humans, the speed of healing is greater in small animals. Furthermore *in vivo* these discrete stages overlap temporally, and the cell types involved exist spatially in close association, thereby influenced by paracrine signalling. However, the three-stage model with rodent repair timings will be used to review our current understanding of the process of fracture healing in the following sections.

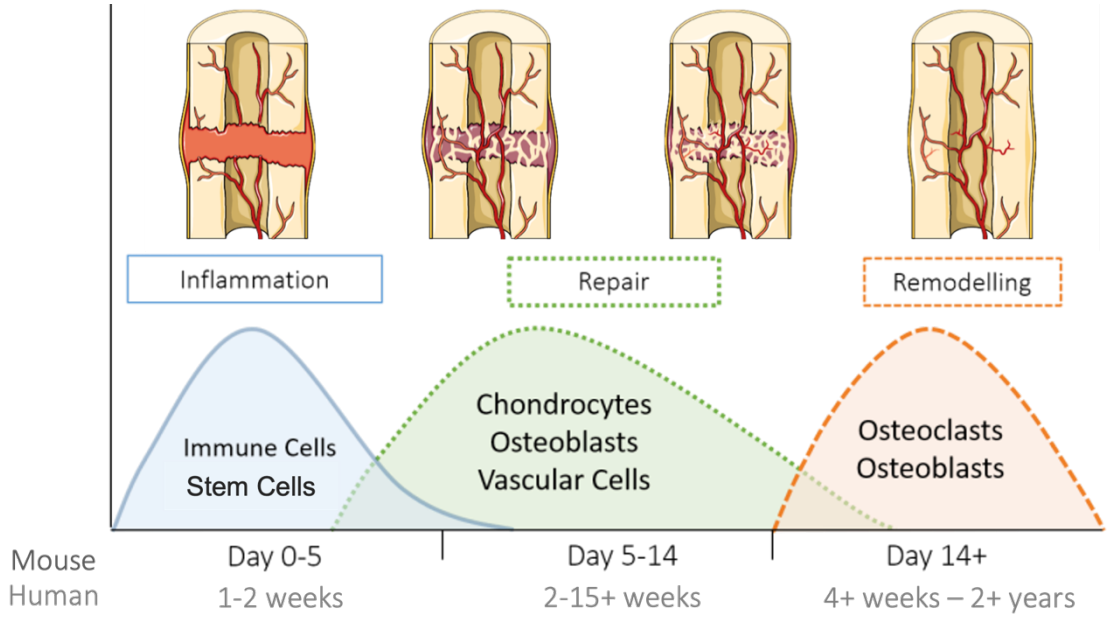


***Figure 1.2: The three-stage model of fracture repair***

*A schematic showing the three histologically identified stages of fracture repair: inflammation, repair, and remodelling, and the key cell types which are involved in each stage. Timings are shown for mice* (Morgan, Giacomo and Gerstenfeld, 2014) *and humans* (Frost, 1989; Prosser *et al.*, 2012). *The inflammation stage shows a hematoma filling the fracture gap and increased activity of immune cells and stem cells required to combat infection and produce bone and cartilage progenitor cells. This overlaps into the repair stage with callus formation to fill the fracture gap. Hypoxic conditions drive blood vessel formation and increase subsequent osteoblast activity to produce a mineralized bone matrix and bone resorption by osteoclasts. This overlaps with a remodelling stage where osteoblasts and osteoclasts produce and resorb bone matrix to reform an ordered bone structure ultimately healing the fracture gap to achieve its original functions, such as mechanical load bearing* (Einhorn and Gerstenfeld, 2014; Morgan, Giacomo and Gerstenfeld, 2014). *(Parts of this figure's graphics are credited to smart.servier.com)*

### 1.3.1 Inflammation

As with any injury to the body, the start of the healing process is an inflammatory response, characterised by swelling and pain caused by cells releasing chemicals, increased movement of fluid from blood vessels to tissue, and compression on nerves. All of these responses aid in the immobilisation of the injury site, preventing further use and damage.

With bone vasculature receiving roughly 10-15% of the resting cardiac output, blood loss from a fracture can readily exceed 1L; this is a risk for shock (Tomlinson and Silva, 2013). Depending on the circumstances of injury, a bone fracture can be closed (in which the broken bone is contained in the surrounding tissue) or open (in which the bone breaks through the skin). In both cases, though especially open fracture, the surrounding tissue which forms a protective barrier is disrupted, resulting in susceptibility to potentially serious infection. The body mitigates these risks with the formation of a haematoma, which histologically has long been characterised: platelets bound to subendothelial collagen form a platelet plug which transitions to a fibrin clot, to a loose matrix and then to a denser granulation tissue (Weigel 1986).

Within the haematoma a complex milieu of signalling factors, including: chemotactic factors released through platelet degranulation, complement factors, proinflammatory cytokines released from necrotic tissue, and integrin expressed on fibrin; these act together to attract resident and circulating inflammatory cells/lymphocytes (E.g. neutrophils, eosinophils, macrophages, dendritic cells, T-cells, B-cells and mast cells) (Park and Barbul, 2004; Yuasa *et al.*, 2015; Loi *et al.*, 2016). Recruited cells secrete additional signalling factors, which work together with the signalling in the haematoma to induce specific cellular responses, facilitating the removal of damaged tissue, protecting against infection, promoting angiogenesis, and recruiting stem cells. Stem cells and progenitor cells mobilise and migrate to the site of injury along the network of newly-produced fibrous tissue and differentiate into specific cell types required for healing (Park and Barbul, 2004; Stroncek and Reichert, 2007).

This process of haematoma formation has been observed in fracture sites (Sfeir *et al.*, 2005; Schindeler *et al.*, 2008; Einhorn and Gerstenfeld, 2014), though the precise signals depend on the cellular and tissue environment. The stem cells recruited and involved in bone healing are multipotent mesenchymal stem cells, better referred to as skeletal stem cells (SSCs) due to their ability to develop distinct skeletal cell lineages, unlike the mesenchymal stem cells found in other tissues (Bianco and Robey, 2004). These cells were originally identified from extracted bone marrow samples and were found to be capable of differentiating into chondrocytes (cartilage-producing cells), osteoblasts (which produce and mineralise bone tissue), and adipocytes (Bielby, Jones and

McGonagle, 2007). The resultant cell type depends on the signalling environment, which will be described in **section 1.4.5**.

### 1.3.2 Repair

In the repair phase of bone healing, the body's response can be considered as the tasks required to restore normal tissue function. The first task is to reduce instability; this is achieved through the removal of damaged tissue and the production of a provisional matrix to fill any gap in tissue structure, reducing strain. The second task is to alleviate hypoxia with blood vessel formation (angiogenesis); this coincides with matrix removal to make room for the new vasculature. Blood vessels allow for the distribution of nutrients and recruited immune or progenitor cells. Finally, of particular importance for bone's function is restoring the ability to bear load. This involves ossification, the laying down of bone to unify the break, which is then remodelled to the site's original mechanical loading architecture of cortical and trabecular bone structures.

Where there is some mechanical instability, a combination of intramembranous ossification (also known as primary/direct bone formation), where SSCs transition directly into bone producing osteoblasts, and endochondral ossification, where bone formation follows the formation of a cartilage matrix, occurs. Primary bone formation is seen to occur in areas of high stability, such as at the callus exterior. At the centre of the callus, where there is low oxygen tension, chondrogenesis occurs, whereby chondrocytes derived from skeletal stem cell progenitors produce a 'soft' cartilaginous scaffold, replacing granulation tissue. As chondrocytes differentiate further the cartilage extracellular matrix is mineralised and finally the hypertrophic chondrocytes undergo apoptosis. Gradually the cartilaginous matrix is resorbed and replaced by osteoid, a mineralised irregular woven bone produced by osteoblasts, resulting in a 'hard' callus (Einhorn, 1998; Schindeler *et al.*, 2008; Einhorn and Gerstenfeld, 2014). It has been suggested that this repair stage is when mechano-responsiveness via osteoprogenitor cells returns, as application of load bearing immediately following a fracture (i.e. during the inflammation stage) inhibited healing, however application of low level load during early fracture callus resulted in improved fracture healing (Gardner *et al.*, 2006).

At the same time, differentiated vascular endothelial cells form new blood vessels within the callus in the process of angiogenesis. The increased oxygen tension enables differentiation of recruited osteoprogenitors into bone-producing osteoblasts (Schindeler *et al.*, 2008), and a change of pH from acidic to slightly alkaline; this creates the optimal environment for the osteoblast alkaline phosphatase activity required for mineralisation (Sfeir *et al.*, 2005).

Of note hypoxic conditions also promote bone resorption by osteoclasts, enabling space for vessel formation and the final repair stage of bone remodelling (Section 1.3.3). The majority of literature also suggest that low O2 levels promote osteoclast differentiation; however there are also studies which contradict this, complicated by differing experimental techniques and a lack of standardized Oxygen levels defining hypoxia. For a more detailed discussion see the systemic review by Tan, Mohamad Hazir and Alias (2021).

### 1.3.3 Remodelling

Following ossification, a period of remodelling occurs. Here, osteoclasts resorb the hard callus of woven bone, while osteoblasts produce bone in an organised lamellar structure, which better supports mechanical load. Cycles of osteoblast and osteoclast activity result in the remodelling of the original bone structure.

## 1.4 FRACTURE REPAIR SIGNALLING

The sequence of processes in fracture healing is well characterised, and within each of the repair stages specific cell signalling events occur. Here, the term 'signalling' encompasses the intracellular production & release of molecules for paracrine and endocrine cell communication, including: signalling the responses of cell movement, proliferation, differentiation (involving production of cell phenotype markers), and production of extracellular structural proteins; all of which are required in the processes of fracture repair. Understanding the contributions these signalling factors make to fracture repair will enable identification of suitable targets for therapy to influence repair and either treat or prevent poor fracture outcomes. In particular, it is desirable for a substance to have a direct action on bone production, without there being substantial negative feedback upon other essential pathways if its action is increased. Accordingly, these factors will now be reviewed in more detail for their production timings and theorised actions. For some of these factors further evidence for their therapeutic benefit to promote bone production is reviewed in more detail in **section 1.6**.

### 1.4.1 The importance of the haematoma in initiating repair signalling

The haematoma is understood to be of critical importance in supporting cell migration and initiating the signalling events for optimal fracture healing. This has been shown using animal models where the removal of a fracture haematoma results in delayed or non-union (Grundnes and Reikerås, 1993; Park *et al.*, 2002). Mizuno *et al.* (1990) demonstrated the osteogenic potential of a haematoma by transplanting a four day fracture haematoma to a sub periosteal and intramuscular site within a rat model, and observing bone growth. Oe *et al.* (2007) demonstrated that extracted human haematomas contain mesenchymal stem cells capable of differentiating into both chondrogenic and osteogenic phenotypes. Extraction and investigation of fracture supernatant has further demonstrated that secreted factors have an osteoinductive role (Tsunoda, Mizuno and Matsubara, 1993) as well as potential to form new blood vessels (Street *et al.*, 2000). Despite this knowledge, as Schell *et al.* (2017) argue, clinical routine fracture treatment still fails to fully recognise the healing potential of the haematoma, with certain irrigation, reduction, and fixation techniques.

Our understanding of how a haematoma is formed and which cells and signalling pathways are involved has largely come from studies of wound repair (Park and Barbul, 2004; Kolar *et al.*, 2010). However contrary to wound healing, after repair and remodelling, bone presents no scar tissue and therefore the cellular activity may not recapitulate wound healing. Indeed Schmidt-Bleek *et al.* (2009) demonstrated this using a sheep model to compare the cellular composition and expression of a

bone haematoma with a muscle soft tissue haematoma, and found an increased number of regulatory T-helper cells which coincided with high IL-10 expression unique to the bone haematoma.

The identification of the active cellular composition within the context of a bone healing environment, and its contribution to the production and release of signalling molecules, has notably been lacking within literature. However, with a combination of experimental techniques the cell signalling events unique to this complex regenerative tissue are beginning to be identified, as described in the following subsections.

### 1.4.2 Identifying signalling molecules involved in fracture repair: temporal analysis

With the use of animal models and gene expression analysis we have some temporal understanding of the signalling molecules involved in repair, a selection of which are depicted in **Figure 1.3.** Rodent and sheep fracture model studies have tracked the peak expression of these signalling factors and inferred roles during the related stages of repair. For example, expression of TNF-α and IL-1 peaks within 24 hours post-injury, declines after 3 days and is then upregulated again during the late stages of healing, suggesting TNF-α and IL-1 have roles in the initiation of repair as well as supporting bone remodelling (Kon *et al.*, 2001; Cho, Gerstenfeld and Einhorn, 2002; Schmidt-Bleek *et al.*, 2014). During days 14-21 post injury, BMP-3, BMP-4, BMP-7, and BMP-8 are expressed, times at which histological analysis shows cartilage resorption, osteoblast influx, and increased bone formation, suggesting these bone morphogenic proteins (BMPs) have roles in these processes. Across days 2 to 21, BMP-5 and BMP-6 are expressed; this prolonged expression suggests a regulatory role (Cho, Gerstenfeld and Einhorn, 2002). As well as histological observation aided by tissue-specific stains, the temporal expressions of specific matrix proteins have also been examined to distinguish repair stages and cross-referenced for associated signalling factor expression. For example Cho *et al.* (2002) found in mice at 7 days post-fracture, expression of collagen II, a cartilaginous matrix protein, coincides with TGF-β2&3 peak expression.

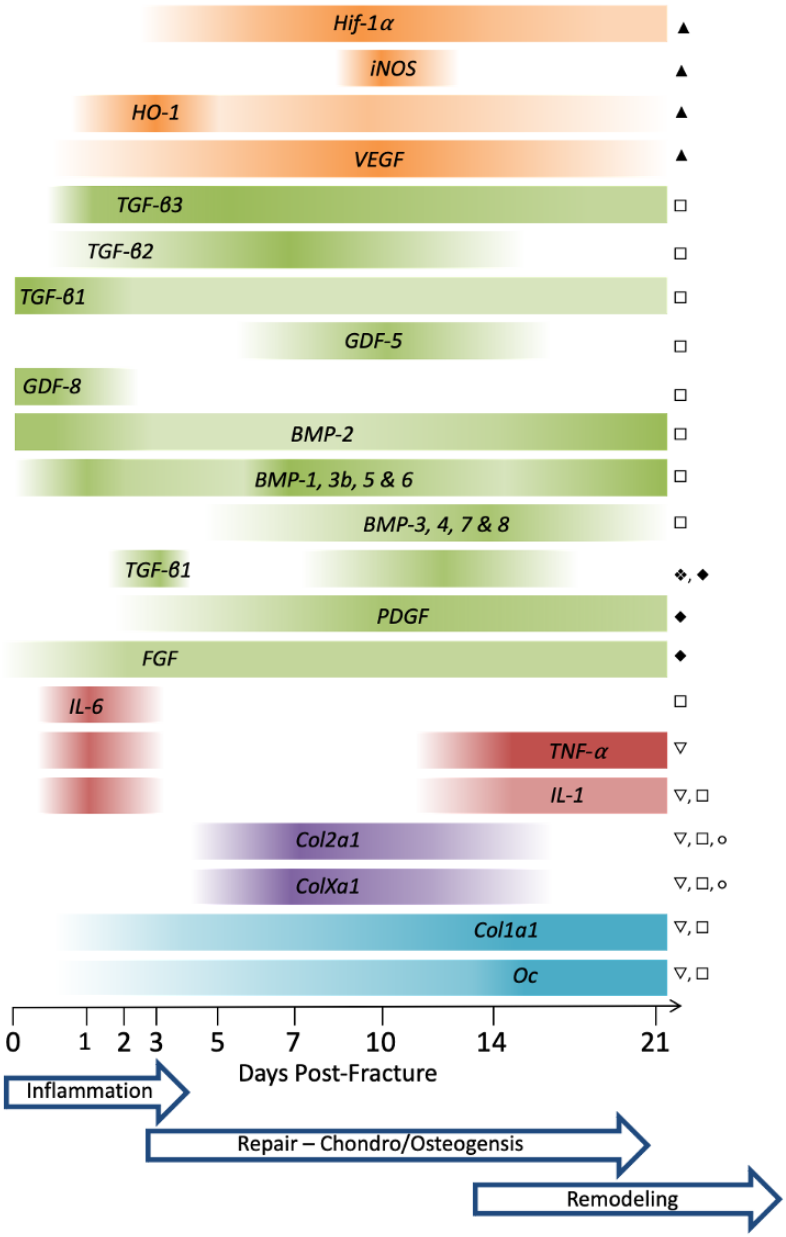


***Figure 1.3: The temporal expression of genes of interest in fracture repair***

*Collated fracture gene expression data from research using rodent fracture models and early quantification methods (Northern Blotting and RPA PCR). Colours group related genes: Orange = Hypoxia and angiogenesis factors; Green = Growth factors; Red = Pro-inflammatory cytokines; Purple = Chondrogenic factors; Blue = Osteogenic factors. Data extracted from ❖ Joyce et al. (1990), ◆ Bolander, (1992), ▽ Kon et al. (2001), □ Cho, Gerstenfeld and Einhorn, (2002), ○ Gerstenfeld et al. (2003) and ▲ Komatsu and Hadjiargyrou, (2004).*

Development of transcriptomic and proteomics mass array profiling has uncovered hundreds of active genes during fracture healing stages, this extends work from earlier studies that focussed on ECM, growth factors and cytokines. For example, microarray gene expression analysis on a rodent fracture model by Li *et al.* (2005) revealed unique expression of functional genes related to ion transporter activity, which dominated day 1 post fracture. At days 1 and 2, genes for cytoskeleton organisation, biogenesis, and inflammatory response dominated; at day 4, unique genes were those involved in morphogenesis, organogenesis, calcium binding, cell adhesion, and bone structural proteins. Similarly, Rundle *et al.* (2006) found at day 3 post fracture genes involved in protein metabolism actin cytoskeleton, and organogenesis showed change in expression. At day 11 genes *Col10a1* and *Col2a1* (related to collagen production) and *Chm01* (related to cell growth) dominated. Lehmann *et al.* (2005) also identified genes and gene families prominently expressed during the chondrogenic phase of repair (days 5-10), namely matrix metalloproteinases (*Mmp 2, 9, 13 and 14*) and angiogenic factors (*Ang2, Pedf, Vegf*).

These studies, plus others, have expanded the knowledge of the gene families functioning during repair, and through quantifying relative expression have inferred important signalling pathways. Such a high number of active genes reveals the complexity of the signalling in fracture repair. However, an understanding of what signalling specifically drives repair events forward, and as such has a weighted importance for successful healing, is arguably more useful for therapy design. Here techniques to uncover the role of various cells and signalling molecules are required.

### 1.4.3 Identifying cells and signalling molecules involved in fracture repair: visual and spatial analysis

The basis of our understanding of the role these signalling factors have in the healing process comes in part from aforementioned research which related elevated expression to histological observations of the repair stage i.e., inflammation, chondrogenesis, osteogenesis. However, as these events can occur simultaneously in different microenvironments within a healing callus, arguably gross gene expression dominated by highly expressed factors only shows part of the complex signalling interaction that occurs for successful healing. Studies have investigated further where these signalling factors are expressed spatially within a fracture site, using Immunohistochemistry (IHC) and In Situ Hybridisation (ISH) techniques; furthermore, studies have histologically identified associated cell types which may produce or respond to the expressed molecules. An overview is presented in **Figure 1.4**.

Historically, cell gross morphological features and associated histological stains bound to particular matrix components have aided cell identification and been cross examined with immunolocalised (IHC/ISH) signalling factors. For example Kon *et al.* (2001) identified TNF-α expression associated with macrophages and other unspecified inflammatory cells during early inflammation/repair and later in repair with mesenchymal cell and hypertoric chondrocytes, osteoblast cells, and macrophages. These observations lead to the theory that TNF-α may carry out multiple functions at different times during fracture healing due to the diversity of cells that express this cytokine (Kon *et al.*, 2001). In another example, Komatsu and Hadjiargyrou (2004) identified HIF-1α and VEGF high expression associated with proliferating chondrocytes (near boundaries of cartilage and newly formed bone) and osteoblasts in regions of new bone at 10 days post fracture, whereas hypertrophic chondrocytes (at the centre of cartilaginous soft callus) had little to no staining. These observations supported the theory that in response to hypoxia HIF-1α signaling induces VEGF angiogenic response to allow new blood vessel formation in the fracture callus (Komatsu and Hadjiargyrou, 2004).

Whilst cell phenotypic markers have been characterized, fluorescence-activated cell sorting (FACS) analysis has been used alongside IHC and ISH to assess specific cell population numbers and locations to further deduce roles during repair. For example Raggatt *et al.* (2014) identified within a mouse fracture model macrophages (f4/80+Mac-2+) localised within the fracture granulation tissue, and adjacent to areas of chondrogenesis (+ve toluidine blue stain) and vascular structures 7 days post-injury. Schmidt-Bleek *et al.* (2009) identified within a sheep fracture haematoma 1-4 hours post-injury the percentage of monocyte/macrophage population decreased, and lymphocyte percentage increased with greater numbers of T-helper cells (CD4+) compared to cytotoxic T-cells (CD8+). Between 4 and 12 hours the percentage of macrophages (CD14+) increased, and T-helper cells decreased. These data were then cross-examined with peak expression of pro-inflammatory cytokines IL-1β (4 hr), TNF- α(4 and 24 hr), MCSF (4 and 24 hr), and IL-6(12 hr), as well as anti-inflammatory cytokines IL-10 (24 hr) and TGF-β (4 and 36 hrs) (Schmidt-Bleek *et al.*, 2014).

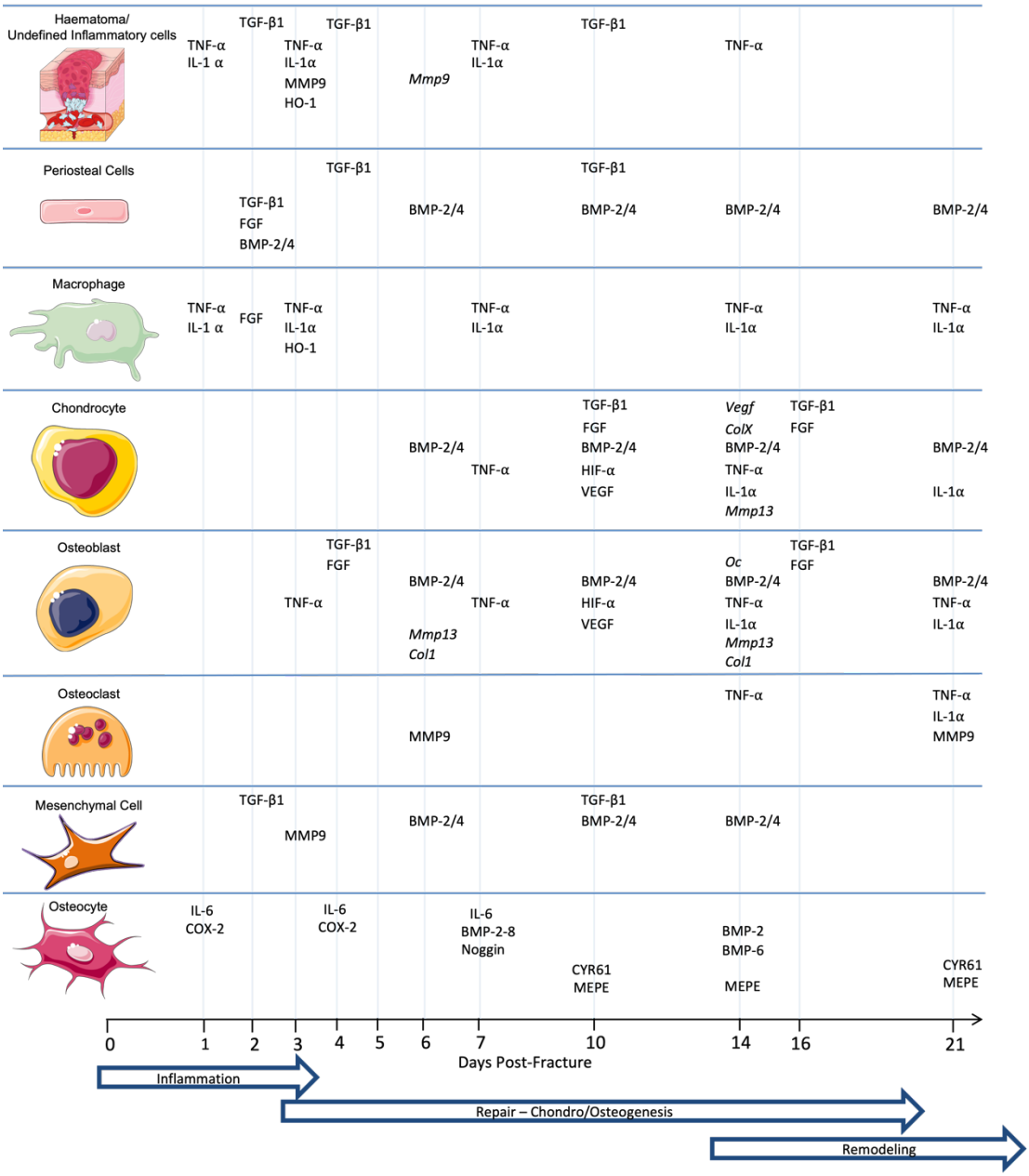


***Figure 1.4: Spatial expression of signalling molecules and associated cells***

*Schematic of histologically identified key cell types involved in fracture repair. Expressed signaling factors spatially found to associate with each cell type, as identified by IHC and ISH studies, are listed aligned at the investigated timepoint post fracture across the three stages of repair. These signalling factors are either produced by or cause a response for each cell type. The information shown is extracted from the following studies:* Joyce *et al.*, 1990; Bolander, 1992; Bostrom *et al.*, 1995; Hadjiargyrou, Ahrens and Rubin, 2000; Kon *et al.*, 2001; Colnot *et al.*, 2003; Komatsu and Hadjiargyrou, 2004; Lu *et al.*, 2004; Behonick *et al.*, 2007; Yu *et al.*, 2010; Wu *et al.*, 2014; Choy *et al.*, 2020*. (Parts of this figure's graphics are credited to smart.servier.com)*

### 1.4.4 Effects of dysregulating signalling factor production on bone repair

To unpick the relative importance of certain signalling pathways on successful repair, transgenic models which knockout (KO) elements of signalling pathways, and models which force/elevate expression and go on to show an effect upon the healing process, have been useful strategies.

In a study by Kon *et al.* (2001), TNF-α signalling was suggested to be required at multiple stages of repair. Indeed Gerstenfeld *et al.* (2003) used a transgenic mouse model with TNF-α receptor KO (p55-/-&p75-/-) and through histological and gene expression assessment observed a delay in chondrogenic differentiation, endochondral tissue resorption, and delayed osteoclast accumulation and activity. This suggests that TNF-α has a role in MSC recruitment or differentiation, chondrocyte apoptosis, and promoting endochondral remodelling by osteoclasts (Gerstenfeld, Cullinane, *et al.*, 2003). Repair is only delayed rather than inhibited in the absence of TNF-α, this suggests TNF-α is not a critical factor for the repair process but rather part of an additive, or synergistic, signalling effect. A balance of signalling factors is essential for efficient repair as Hashimoto *et al.* (1989) demonstrated by exposing rats to prolonged and high concentrations of TNF-α which resulted in inhibition of fracture healing.

In another example, Lange *et al.* (2010) demonstrated, as we have seen in previous gene expression data, that IL-1β expression elevated within 2 days post-injury in both non-stable and stabilised mice fracture models. However in a mouse KO for IL-1β receptor or wild type (WT) mice injected with an excess of IL-1β at the fracture site, the resultant effects upon repair were no different or negligible compared to controls (Lange *et al.*, 2010). This demonstrates that the action of certain signalling molecules upon cells can alter healing to different extents. Uncovering signalling factors which result in successful repair or act on cells which are particularly necessary for certain repair stages is therefore important for future therapies.

Certain molecules have become a dominant focus in research for therapeutic potential; one example is BMPs, where in BMP-2 deficient mice there is a lack of initiation of fracture healing (Tsuji *et al.*, 2006). Evidence of the osteoinductive action of BMPs when applied as a therapeutic for fracture repair is reviewed in **section 1.6.2.**

As well as exploring the roles of individual signalling factors, methods to prevent whole cell populations from performing signalling functions have been investigated for their effects upon fracture healing. Immunohistochemistry has been used to identify that in an early fracture site haematoma 3 days post injury, a greater population of neutrophils (MCA771G antibodies) resided in

the callus than macrophages (F4/80 antibody) (Xing *et al.*, 2010); the same relationship has been observed from cytometric analysis at days 2 and 5 post-injury in both non-stabilised and stabilised fractures (Wang *et al.*, 2013). However, despite being the greater population, neutrophils appear to have a less important role in initiating repair compared to macrophages. Notably in Chung *et al.* (2006), neutrophil reduction (via neutralising anti-serum) did not affect the presence of other inflammatory cells (monocytes and lymphocytes) or the expression of signalling factors (TNF-a, IL-1β, PDGF-β, TGF-β1), although at day 10 cartilaginous tissue was reduced. In Raggatt *et al.* (2014), a macrophage Fas-inducing apoptosis mouse fracture model was used to induce macrophage depletion at time of injury, which resulted in the absence of callus formation; macrophage depletion at 5 days following injury resulted in a reduced callus formation (Raggatt *et al.*, 2014). This demonstrates macrophages are necessary for initiating fracture repair and have an additive role during repair progression.

The pivotal role of macrophages is seen in the identification of resident macrophages ($F4/80^{+}$) upon the endosteal and periosteal surfaces of unfractured bone; Ozaki *et al.* (2000) demonstrated in a rat fracture model that removal of the periosteum prior to injury resulted in reduced chondrogenesis. Xing *et al.* (2010) studied a mouse model in which C-C Chemokine Receptor type 2 (CCR2) required for macrophage recruitment was knocked out, a reduced number of macrophages were seen in the fracture site 3 days post injury. Impaired vascularisation and delayed callus formation 7 days post injury, and delayed remodelling at day 21 was also seen in the $CCR2^{-/-}$ (Xing *et al.*, 2010).

In addition to tissue resident macrophages, recruited inflammatory macrophages rapidly infiltrate tissues compromised by injury. Depending on the environmental cues present within an injured tissue, inflammatory macrophages are polarised towards an appropriate activation pathway within a broad spectrum. At one end of this spectrum are pro-inflammatory M1 macrophages which are critical in destroying foreign organisms and in fighting infections; at the other end are anti-inflammatory M2 phenotype macrophages, involved in wound healing, tissue repair, debris scavenging, and angiogenesis (Wu *et al.*, 2013). In bone repair specifically, a study by Schlundt *et al.* (2018) identified pro-inflammatory M1 macrophages (positive immuno-stain for CD68 and CD80) present at the injury site predominantly 24 hours post fracture (the inflammation stage). Three days post fracture (early repair stage), M2 macrophages (CD68 and CD206) are also present at the injury site, and by 7 days post fracture are the dominant type present, suggesting a role of M2 macrophages in callus maturation. At 21 days post fracture (remodelling stage) neither CD80 nor CD206 positive macrophages were present, suggesting another phenotype of macrophage has influencing activity at this point. Schlundt *et al.* (2018) also used IL-4 and IL-13 to induce specifically

the M2 phenotype via a collagen scaffold inserted into the fracture gap. It was found that this treatment significantly enhanced bone formation, further supporting that M2 macrophages have an important role in bone repair (endochondral ossification). These data suggest that further to their role in inflammation a fine balance of M1 and M2 macrophage activity is required for successful fracture healing (Schlundt *et al.*, 2018).

### 1.4.5 *In vitro* evidence for the functions of expressed signalling factors

More understanding of cell-specific signalling factor production and responses has been derived from *in vitro* studies. Primary human cells isolated from the bone marrow (variously described as mesenchymal stem cells (MSCs) or bone marrow stromal cells (BMSCs), and most recently skeletal stem cells (SSCs)) which are able to differentiate into functional skeletal tissues have been characterised. The effects of signalling molecules on the cell proliferation and differentiation of MSCs have been studied, a diagram summarising the principle findings is shown in **Figure 1.5**.

Edgar *et al.* (2007) demonstrated the role of BMP-2 in directing the expression of other BMPs (-3,-4,-5, and-8) and MSC osteogenic differentiation, where MSC differentiation into osteoblasts is reduced when BMP-2 activity is blocked by an antibody. As differentiation is reduced rather than inhibited, this study shows that the action BMP-2 has upon differentiation is additive. PDGF is thought to have a role in repair and remodelling, PDGF-BB secreted by cell line osteoclasts inhibits osteoblast differentiation (Kubota *et al.*, 2002), and PDGF-AA has been found to promote MSC differentiation to osteoblasts (Li *et al.*, 2014).

As well as direct signalling effects, an understanding of the cross-talk between signalling molecules and signalling pathways has been derived from *in vitro* studies. Human MSCs treated with TNF-α, and cells with constituent active NF-κB inducing kinase IKK2 treated with TNF-α, resulted in enhanced expression of BMP-2 and ALP, an increase in calcium deposition, and matrix mineralisation; this suggests the TNF-α and NF-κB pathways enhance osteoblast activity (Hess *et al.*, 2009). Inhibiting the NK-κB pathway did not prevent BMP-2 expression but blocked enhancement of BMP-2 expression following TNF-α treatment, suggesting TNF-α via the NF-κB pathway supports BMP-2 production and possibly osteoblast differentiation, but is not essential for it (Hess *et al.*, 2009). For a recent review of signalling molecule cross-talk see (Grafe *et al.*, 2018).

Healing requires cell recruitment of SSCs and progenitor cells. There is evidence from *in vitro* studies that the chemotactic potential of certain signalling molecules results in recruitment of SSCs.

SSCs migrate along a chemotactic gradient towards TNF-α in a dose-dependent manner (Fu *et al.*, 2009). TNF-α drives migration of muscle-derived stromal cells and osteogenic differentiation but notably at low concentrations; high concentration exposure leads to inhibition of this effect (Glass *et al.,* 2011). This study also demonstrates the presence of osteo-lineage cells in muscle neighbouring a fracture, as cells extracted from muscle 3 days post fracture differentiated *in vitro* to osteoblasts and produced bone nodules, suggesting a possible recruitment location (Glass *et al.*, 2011). It is important to note that although these studies use primary cell sources, these cells may respond differently in a complex injury environment having multiple signals, physiological dosage, and varying proximity to cells which produce TNF-α.

PDGF is thought to have a role in the migration and proliferation of SSCs. Ozaki *et al.* (2007) demonstrated this *in vitro* by assessing the chemoattractant ability of several growth factors and cytokines for human SSCs. It was found that PDGF-BB has the strongest chemoattractant capacity when measured in isolation. Additionally, it was found that factors including epidermal growth factor (EGF), TGF-α, and FGF-2 have an additive effect when SSC cell surface receptors are not shared, although for the case of FGF-2 and PDGF a combined exposure resulted in suppression of SSC migration (Ozaki *et al.*, 2007). However, these *in vitro* results were collected using non-physiological concentrations of the involved signalling factors (Thurairajah, Broadhead and Balogh, 2017), and more information is required regarding their expression pattern to ascertain whether these combinations would occur *in vivo*.

In addition to TGF-α and PDGF, there are many other factors reported as influencing SSC migration to the site of injury. The chemokine stromal cell-derived factor 1 (SDF-1) and C-X-C chemokine receptor 4 (CXCR4) axis explains the mobilisation of SSCs originating from the bone marrow. In a non-injured state, the physiological levels of SDF-1 are highest within the bone marrow that retains SSCs. At the site of injury, high concentrations of SDF-1 released from platelets and hypoxic endothelia (Massberg *et al.*, 2006) produce a chemoattractive gradient that draws SSCs from the bone marrow to the fracture callus (Ceradini *et al.*, 2004). Hoggatt and Pelus, (2011) have reviewed the experimental evidence supporting this paradigm.

*In vitro* studies have also informed of important signalling events which regulate tissue resorption by osteoclasts and bone production by osteoblasts, a key coupling mechanism involved in bone remodelling. The coupling of osteoclast and osteoblast activity is regulated by secreted signalling factors: receptor activator of nuclear factor κB ligand (RANKL), osteoprotegerin (OPG), and macrophage colony-stimulating factor (MCSF). SSCs and osteoblasts produce the cytokine RANKL, which is required for osteoclast differentiation from progenitor cells. RANKL is inhibited from

interacting with its receptor when bound to OPG, produced by osteoblasts. This protein thereby inhibits subsequent osteoclast formation (Takahashi, Udagawa and Suda, 1999; Hofbauer *et al.*, 2000). SSCs and osteoblasts also produce MCSF, which is required for the differentiation of haematopoietic stem cells into osteoclasts and their proliferation, as well as osteoclast survival and cytoskeletal rearrangement during bone resorption (De Vries *et al.*, 2015).

It is important to note these signalling mechanisms established *in vitro* have to be interpreted as such, i.e., their function *in vivo* may differ due to the complex multitude of signalling stimuli present. Accordingly, when assessing a therapeutic candidate, a combination of methods is typically beneficial.

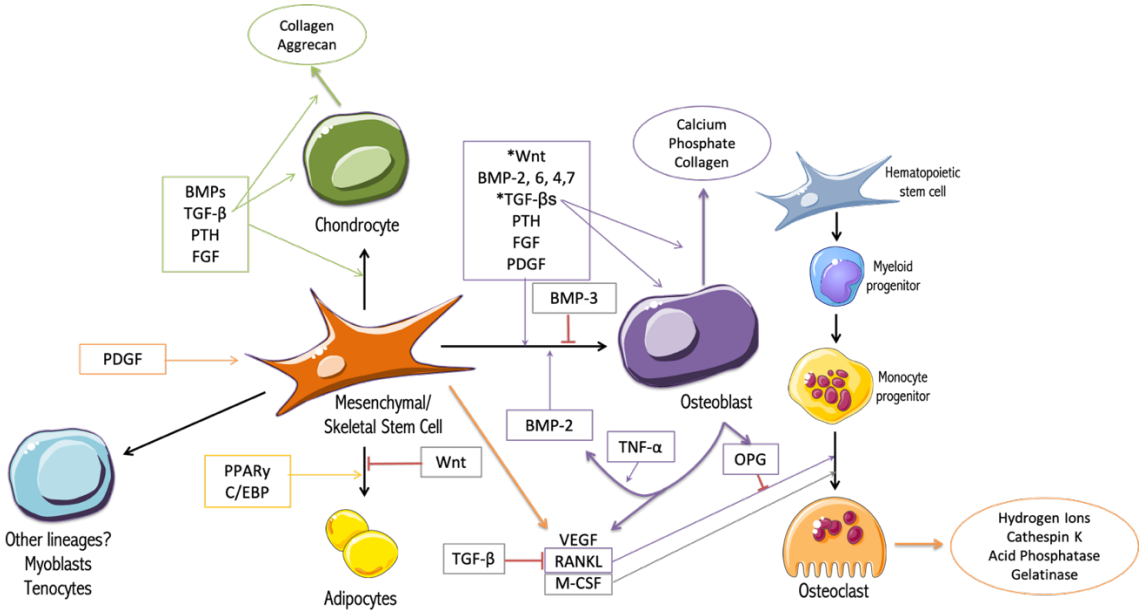


***Figure 1.5: A schematic of a selection of signalling factors involved in the differentiation of Mesenchymal/Skeletal Stem Cells (MSCs), identified from in vitro studies***

*Boxes surround factors involved in the differentiation (thin arrow to black arrow), proliferation (thin arrow to cell), and release of molecule/matrix affecting proteins (thin arrow to thick arrow) of each cell type separated by colour: Chondrocyte (green), Adipocyte (Blue), and Osteoblast (Purple). Thick coloured arrows depict factors secreted form specific cell types. Black arrows represent differentiation. Red lines indicate inhibition. * = Signalling factor can either promote or inhibit depending on dose and timing and cell differential state. Note that the signalling relationships depicted are only a brief selection of published studies to date and cross signalling interactions have not been included. For further information read source references: (Dimitriou, Tsiridis and Giannoudis, 2005; Edgar et al., 2007; Hess et al., 2009; Tang and Daniel Lane, 2012; Li et al., 2014; Hankenson, Gagne and Shaughnessy, 2015; Grafe et al., 2018). (Parts of this figure's graphics are credited to smart.servier.com)*

### 1.4.6 Understanding the origins of cells active in fracture healing

Histology and IHC have identified key cells present at various stages of fracture repair, and signalling studies *in vitro* and *in vivo* have built knowledge of their functions. Studies have also focused on better understanding the origins of cell populations, particularly through the use of contemporary genetic lineage tracing methods utilising Cre/lox transgenic mice models. An example cell lineage for osteoblasts and their associated transcriptional markers is shown in **Figure 1.6**.

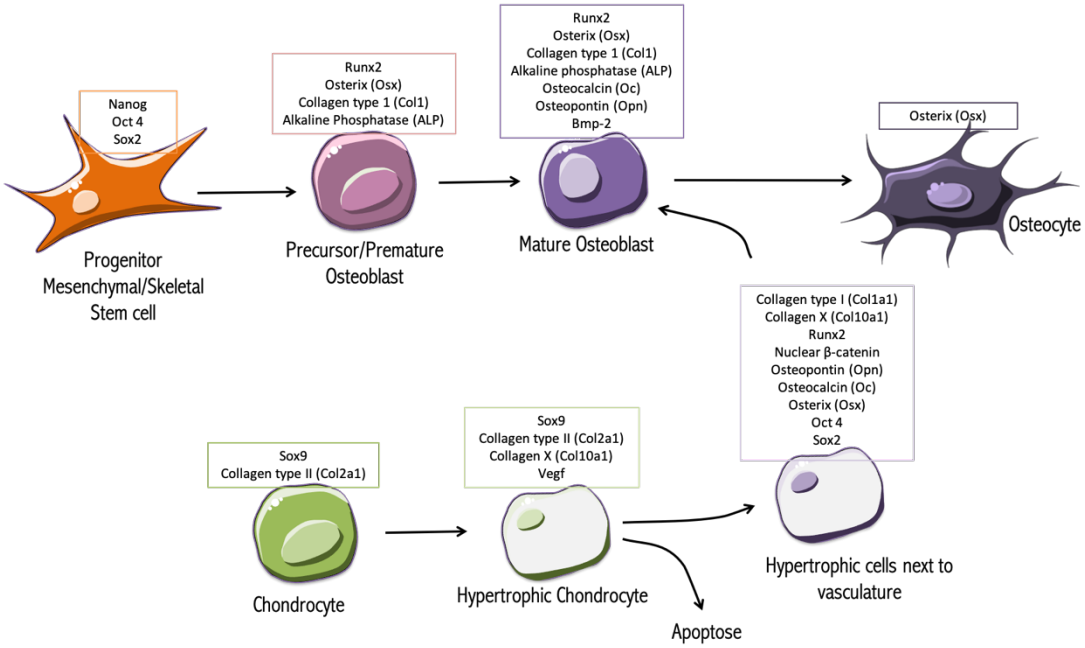


***Figure 1.6: Proposed cell lineage and transcriptional phenotype markers***

*The identifying markers of SSC lineage cells are listed in the box above each cell type. Of note these lists are not exhaustive. Arrows represent differentiation. Information extracted from Hu et al., 2017.*

For example, Hu *et al.* (2017) utilised Cre/lox transgenic mice models and ISH to present compelling evidence against a previously established dogma that hypertrophic chondrocytes undergo apoptosis and osteoprogenitor cells enter the fracture callus to replace cartilage with bone. Instead, it is suggested that hypertrophic chondrocytes transdifferentiate into osteoblasts. Hypertrophic cells adjacent to vasculature and at transition junctions displayed markers of proliferation and had overlapping expression of hypertrophic chondrocyte and osteoblast markers. The only cells that presented markers of apoptosis were those in close proximity to osteoclasts. Of note, identified 'hypertrophic osteoblasts' expressed *Runx2* and nuclear localisation of β-catenin, which indicated activation of canonical Wnt signalling and suggests this signalling pathway activation is required for this transition (Hu *et al.*, 2017). Osteoblasts may express a variety of gene combinations, even within the same population. It is thought that this could explain the variations in bone microarchitecture

across different sites, and the variation in their responses to disease and treatments across geographically distinct bone regions (Clarke, 2008). A full understanding of the signalling events that influence osteoblast development could be used to increase this cell's population and actions during bone healing.

More recent research by Kegelman *et al.* (2021) under Boerckel's lab, using onset-inducible knockout mice (Osx-Cre$^{tetOff}$), has highlighted the importance of the transcriptional regulators Yes-associated protein (YAP) and transcriptional co-activator with PDZ-binding motif (TAZ) as critical mediators of osteoblast progenitor proliferation and differentiation, not only during bone development but specifically during fracture repair. YAP/TAZ deletion during development was found to impair callus formation and mineralisation of a fracture; it is suggested that this is due to developmental deficiencies in the progenitor cell pool. Deletion of YAP/TAZ just before fracture however had no effect on cartilaginous callus formation, but impaired the proliferation and differentiation of osteoblast precursors located in the periphery of the fracture callus, resulting in delayed mineralisation (Kegelman *et al.*, 2021). In a study by Pan *et al.* (2018), selective deletion of YAP from osteoblast lineage cells (osteoblast progenitors, matrix producing osteoblasts, and matrix embedded osteocytes) in the context of bone homeostasis (as opposed to fracture repair) also caused a reduction in cell proliferation and differentiation and increased adipocyte formation, resulting in bone loss. Interestingly osteoblast lineage YAP was found to maintain β-catenin accumulation in the cytoplasm and nucleus, suggesting YAP has a role in facilitating Wnt signalling induced osteogenesis (Pan *et al.*, 2018). Future studies of this sort which seek to understand cell-specific signalling mechanisms with onset inducible knock out mice and how they may be unique to the context of specifically fracture repair will help to inform targeted treatments to increase bone formation.

### 1.4.7 Human information

It is important to note the majority of studies that have shaped our cellular and molecular understanding of fracture repair have come from animal studies. We have less information on the specific timing and signalling for humans due to inherent issues with human based control studies such as sample acquisition, variability in fractures and co-morbidities.

Gene expression profile studies have revealed a plethora of cytokines elevated during fracture repair. Kolar *et al.* (2011) analysed the haematoma of patients extracted 6-72 days post-fracture and reported increased expression of genes related to hypoxia (*LDHA*), angiogenesis (*VEGF*), inflammation (*IL-6, IL-8*), cell migration (*CXCR4*), and osteogenic differentiation (*SPP1, RUNX2*). Hauser *et al.* (1997) investigated the concentration of cytokines (by ELISA technique) in the fracture

soft tissue haematomas and plasma samples extracted within or after 48 hours post fracture. Of note, pro-inflammatory molecule IL-6 previously mentioned to be elevated in animal studies **(Figure 1.3)** was also elevated in this study within 48 hours. Interestingly, contrary to animal studies Hauser did not find significant levels of TNF-α and IL-1β within the haematoma or plasma samples, possibly due to different sample extraction sites or species variation. Instead flow cytometry analysis revealed increased expression of membrane associated TNF, particularly in the monocyte population within the haematoma as opposed to circulating cells (Hauser *et al.*, 1997). This suggest that at least for humans, early fracture response involves TNF activity but in a membrane/juxtracrine signalling mechanism. Of note, Hauser's study uses a method in which the extracted haematoma is treated with urokinase, which may enable cytokines not active *in vivo* to be released – therefore interpretation must be considered appropriately. However a more recent study by Pountos *et al.* (2019) which does not use this method also identified elevated concentrations of the signalling molecules studied by Hauser, plus an extensive profile of other cytokines. However, note that these elevations were measured relative to patient plasma concentrations rather than samples from uninjured control volunteers. Arguably plasma cytokine concentrations will be impacted by the presence of an injury, and hence specific upregulation as a result of the injury cannot be determined without baseline measurements.

## 1.5 FACTORS THAT AFFECT BONE HEALING

As previously mentioned, certain fracture cases result in delayed healing or the development of a non-union. There are two classes of non-union: hypertrophic, indicated by the formation of cartilage in the fracture gap and often caused by inadequate stability rather than biological limitations, and atrophic, in which scar tissue is found in the fracture gap (Kostenuik and Mirza, 2017). In order to effectively treat a condition, first a clear understanding of the causes is needed. However, for impaired fracture healing the precise causes are both patient-specific and the result of a complex interplay of factors, which are then difficult to dissect. Both animal fracture models and human cohort studies have provided an understanding of the general risk factors associated with developing a non-union and the possible mechanisms behind them. These factors include those relating to the patient, such as genetic conditions, disease state, age, diabetes, smoking, nutritional deficiencies, and the use of anti-inflammatory agents; also local environmental factors, namely the type and location of the fracture, local infection, the extent of soft tissue injury, compartment syndrome, and mechanical stability (Schindeler *et al.*, 2008; Kostenuik and Mirza, 2017). Evidence for some of these factors will be discussed in the following subsections, in order to establish which underlying mechanisms could be influenced for treatment.

### 1.5.1 Local environmental factors

The specific events and mechanisms that occur during fracture repair are greatly influenced by the location of the fracture, and whether it disrupts cortical and/or trabecular bone. Indeed, in a controlled comparative study it was shown that cortical repair within the diaphysis region occurs at a faster rate than cortical repair within the epiphysis (Monfoulet *et al.*, 2010). Mechanical stability is another factor, which has a direct effect upon the degrees of endochondral and intramembranous ossification (Einhorn and Gerstenfeld, 2014). Interventions such as surgical fixation and intermittent load bearing are known to influence the mechanical strains sensed by osteocytes, which signal responses accordingly (Schindeler *et al.*, 2008). Reduced stability and intermittent compression promote cartilage formation and favour endochondral ossification. Other intermittent forces, namely tension and shear stress, also promote fibrous tissue formation. Conversely, regions of low stress and increased stability favour intramembranous ossification (Shapiro, 2008). In addition, rigid fixation and no loadbearing cause impaired healing (Schindeler *et al.*, 2008). A mechanical stimulus is also known to have an effect upon stem cell differentiation. It has been shown that tensile and compressive stress results in osteogenic differentiation (Thurairajah, Broadhead and Balogh, 2017).

Fracture stability as well as the extent of the injury can directly affect the location from which osteoprogenitor cells are recruited, such as the periosteum, endosteum, marrow, blood vessels, and the surrounding soft tissue, as shown by experiments using transgenic lineage tracking (Schindeler *et al.*, 2008; Shapiro, 2008). For closed fractures, stem cells present within the fracture callus originate mainly from the periosteum (Einhorn & Gerstenfeld 2014), whereas for an open fracture or in studies where the periosteum is stripped, stem cells originate predominantly from the surrounding muscle (Liu *et al.* 2011; Monfoulet *et al.* 2010).

### 1.5.2 Age

Fracture healing efficiency is reduced in the elderly, and there is a greater number of non-unions reported amongst this demographic (Taormina *et al.*, 2014). A comparison study of fracture repair in adult and elderly mice has shown elderly mice have delayed formation of cartilage and bone and overall decreased bone formation (Lopas *et al.*, 2014). It is thought that changes to the number or responsiveness of stem cells is a key factor. Marrow allografts from elderly patients show reduced osteogenic potential and often display fatty degeneration (Leucht *et al.*, 2013). Leucht *et al.* (2013) extracted bone marrow grafts from aged and young mice and found those from aged mice had a reduced expression of osteogenic genes and an increased expression of adipogenic genes. These changes were attributed to a reduced expression of Wnt ligands and Wnt target genes, and reduced Wnt responsiveness (Leucht *et al.*, 2013). In another mouse study, Lu *et al.* (2005) demonstrated a delay in cell differentiation and periosteal reaction leads to prolonged endochondral ossification.

It is clear from these studies that bone healing is inefficient in the elderly due to a delay or reduction in mechanisms, however these studies also show that endochondral and intramembranous ossification is still possible. Leucht *et al.* (2013) demonstrated that the osteogenic potential of bone grafts from aged mice could be restored when exposed to exogenous Wnt3a protein. This suggests that influencing the Wnt pathway may provide a possible treatment to prevent delayed healing or non-union development in the elderly. This is discussed further alongside other treatment approaches for poor fracture outcome in **section 1.6.**

With the knowledge that cells are still capable of their molecular and signalling actions, a reason for their reduced activity is still unknown. One line of thought is that changes arise from systemic changes caused by age-related health conditions, including osteoarthritis, cardiovascular disease (Farhat and Cauley, 2008), and dementia. Connected to this is research into age-related changes on inflammatory regulators, namely macrophages. Clark *et al.* (2020) demonstrated how in a young vs. old mouse fracture model; infiltrating macrophage numbers were comparable; however,

transcriptomic evaluation of the macrophages present in the elderly subjects presented an up-regulation of pro-inflammatory genes. Furthermore, preventing recruitment of macrophages in old mice improved healing outcomes (Clark *et al.*, 2020). Further investigation is required into the systemic changes that occur with age-related conditions that could influence the cellular mechanisms involved in fracture healing.

### 1.5.3 Infection and fracture severity

A cohort study of 736 cases of open long bone fractures found that deep infection and high-severity fractures have a statistically significant association with non-unions and delayed healing (Westgeest *et al.*, 2016). Since atrophic non-unions are associated with a deficiency of MSCs at the fracture site (Thurairajah, Broadhead and Balogh, 2017), this can be explained by the reduction in stem cell function and numbers (due to terminal differentiation) that can result from an inflammatory response.

### 1.5.4 Vascularisation

Sufficient vascularisation and blood supply to a site of injury is another factor that can affect bone healing, as the vascularisation facilitates stem cell migration from distant sites and their survival (Thurairajah, Broadhead and Balogh, 2017). In animal models, devascularisation is used as a method to induce non-unions (Ogilvie *et al.*, 2004). Direct inhibition of angiogenesis has been shown to suppress callus and woven bone formation (Hausman, Schaffler and Majeska, 2001). In a study of human open tibia fractures it was found that those with arterial occlusion, causing an inadequate blood supply, had significantly greater incidence of delayed healing or non-union (Dickson *et al.*, 1994).

It is important to note, however, that in some animal studies in which atrophic non-union conditions are induced, an adequate blood supply still remained within the injury site. It is therefore suggested that for some non-union cases this factor has less impact on the development of a non-union than originally thought (Brownlow, Reed and Simpson, 2002; Ogilvie *et al.*, 2004). Nevertheless, studies have shown that fracture repair is enhanced and non-union models are induced to heal by exogenous vascular endothelial growth factor (VEGF) (Eckardt *et al.*, 2005; Kumar *et al.*, 2010; Clarkin and Gerstenfeld, 2013); this may be attributed to the increased cell recruitment that can result from new blood vessel formation. Accordingly, VEGF can be of therapeutic benefit alongside other treatments, especially for non-union cases where there is extensive vascular damage.

### 1.5.5 Summary

All of the discussed factors collectively influence the repair environment and therefore determine the sufficiency and rate of bone healing. It is clear from the literature that there are three primary areas that if addressed could improve healing outcomes: controlling infection, ensuring adequate blood supply, and influencing cellular bone regenerative capabilities. Here pharmacological fracture treatments could be of use, especially exogenously applied signalling factors to influence cellular regenerative behaviours - a treatment strategy not currently present in clinical care other than for osteoporosis treatment (Hoang-Kim *et al.*, 2009). An overview of researched pharmacological fracture treatments that could be employed as alternative or adjunct to surgical treatment are discussed in the next **section 1.6**. In addition, recent medical advances have introduced the possibility of employing genetic or serum-based detection of biomarkers that may identify individual risk factors for non-union occurrence. This holds future promise for tailoring treatments to patient- and fracture-specific characteristics (Kostenuik and Mirza, 2017).

## 1.6 THERAPEUTICS TO IMPROVE FRACTURE OUTCOME

Therapies that are an alternative or adjunct to surgery are being researched in the hope of improving bone fracture healing outcomes and reducing recovery time. Approaches include the use of scaffolds (made of various biomaterials) either alone or in conjunction with growth factors, stem cell therapy, or the delivery of drugs (namely growth factors or molecules that influence repair mechanisms) to the site of injury. Each of these treatment approaches has a vast amount of current research and development. This thesis focuses on a drug delivery approach, which arguably has the advantage of being a minimally invasive treatment option that would not depend on surgery for delivery. Details of the current approaches within biomaterial and stem cell therapies are outside the scope of this work; however, more information can be found in the relevant literature (Dawson and Oreffo, 2008; O'Brien, 2011; Gong *et al.*, 2015).

Understanding of the cellular signalling that occurs in conventional (as described in **section 1.4**) and impaired (as described in **section 1.5**) fracture healing has identified key signalling factors and pathways that are involved in the repair process. This section reviews the use of some of these growth factors, and the molecules that act upon these pathways, as potential treatments that could be delivered to a fracture site to promote healing.

### 1.6.1 Parathyroid hormone

Parathyroid hormone (PTH) is known to have a stimulatory effect upon bone formation (Selye, 1932). Although it is not directly expressed within bone tissue, the presence of its receptor enables a signalling effect (Kostenuik and Mirza, 2017). PTH-related drugs are currently available for the treatment of osteoporosis and have shown promise for fracture treatment in several animal studies and a clinical trial. Peichl *et al.* (2011) reported accelerated healing in women with osteoporotic pelvic fractures treated with PTH injection compared to a saline injection. In a mouse fracture model, PTH treatment was shown to increase mineralised callus volume in micro computed tomography (µCT) analysis, indicating enhanced repair (Kakar *et al.*, 2007). Related PTHrP, expressed by osteoblasts, is also thought to have a stimulatory effect on bone formation by promoting the differentiation, survival, and activity of MSCs and chondrocytes, and by preventing premature cartilage mineralisation. Anabolic effects have been observed in both human and animal studies following exogenous PTHrP administration (Kostenuik and Mirza, 2017). The precise signalling mechanisms underlying the effects of PTH and PTHrP on bone formation are yet to be fully understood, although Kakar *et al.* (2007) suggested PTH treatment induces canonical Wnt signalling. There is also evidence that PTH-induced bone formation is affected by timing of delivery, as continuous delivery of PTH causes a catabolic response, signalling to maintain calcium levels in serum by sequestering it from bone; conversely, intermittent administration causes an anabolic response increasing bone formation (Michalski and McCauley, 2017).

Overall, clinical studies in humans to investigate the benefits of PTH or PTHrP in the treatment of delayed healing or non-unions are currently lacking. Therefore it is not yet clear if PTH treatment is a viable option for fracture treatment. In addition, evidence suggests a need for temporal control over the delivery of PTH. This thesis addresses this need by exploring the potential of nanoparticle drug delivery, discussed later in **section 1.8**. However, it may also be argued that PTH may not be the best molecule to use in a treatment, as it only has an indirect influence upon the signalling mechanisms involved in fracture repair. This is in contrast to, for example, BMP and Wnt signalling, which have been shown to have a direct role in fracture repair. Therefore, it may be more beneficial to target these pathways directly, as discussed in **sections 1.6.2 and 1.7.**

### 1.6.2 Bone morphogenetic protein

Bone morphogenetic protein (BMP) was first identified as an osteoinductive compound from experiments involving transplanting bone extracts and observing ectopic bone formation (Urist and Strates, 1971; Reddi and Huggins, 1972; Urist *et al.*, 1984). As explained in **section 1.4**, BMPs have

shown *in vitro* to be important in promoting MSC differentiation, and *in vivo* for the overall promotion of fracture healing.

Recombinant BMPs (rBMPs) have so far been the most successful agent, reaching clinical trials and gaining FDA approval. rBMP-2 treatment has been shown to induce cartilage formation and thereby promote endochondral ossification (Minear, *et al.*, 2010). rBMP-2 was approved in 2004 for open tibial fracture treatment following results from one clinical trial. In this study, 450 patients were treated with either standard care (intramedullary nail fixation) alone, or along with BMP-2 in an absorbable collagen sponge. 12 months post treatment, a 44% reduction in secondary intervention is reported for the BMP-2 treated group compared to standard care alone, as well as faster healing (58% compared to 38% in standard treatment) (Govender *et al.*, 2002).

However, despite both BMP-2 and BMP-7 reaching clinical trials and having promising effects in animal studies, the results from their wider use in humans have been less profound. For example, a BMP-7 clinical trial involving 124 patients with non-unions at least 9 months old received standard care alongside either autologous bone grafts or BMP-7 in collagen carrier. No significant improvement to healing between two treatment groups was found (Friedlaender *et al.*, 2001), although BMP-7 was approved as an alternative to autograft treatment (Kostenuik and Mirza, 2017). One explanation for this reduced effect in humans may be related to observations of BMP's action to inhibit Wnt signalling (Minear, Leucht, Miller, *et al.*, 2010). Wnt signalling is known to be required for osteogenesis, as detailed in **section 1.7**. Accordingly, in conditions where intramembranous ossification is favoured, BMP may prevent healing; conversely, in situations where endochondral ossification involving chondrogenesis is favoured, BMP treatment may be more beneficial (Minear, Leucht, Miller, *et al.*, 2010). Notably in long bone fracture repair, a mixture of intramembranous and endochondral ossification occurs and is influenced by injury severity and mechanical support. For a full break (with both cortical walls and periosteum disrupted), intramembranous ossification repair occurs with firm fixation, whereas less fixation results in endochondral ossification (Einhorn, 1998; Le *et al.*, 2001; Gerstenfeld, Cullinane, *et al.*, 2003). For more minor breaks (e.g. drill hole defect models), intramembranous ossification repair occurs (Monfoulet *et al.*, 2010). Hence for minor breaks or firm fixation, BMP treatment may hinder healing progression.

Since its adoption for clinical use, further studies have raised concerns over the safety risks associated with the use of rBMPs, including heterotopic ossification and the risk of cancer (Einhorn and Gerstenfeld, 2014). This has led to questions over current recommended dosing, which is far larger than would occur physiologically. There is growing evidence to suggest a lower dose is just as effective. Schmidt-Bleek *et al.* (2016) used a rat model and compared 50 µg (the clinical equivalent

dose-to weight ratio) to 5 µg BMP-2 dosage to treat a 5 mm critical-sized femoral defect. The results showed that a bridging was achieved by 2 weeks for both treatment doses (Schmidt-Bleek *et al.*, 2016). Gibbs *et al.* (2016) used a laponite nanoparticle gel to apply a localised, physiological dose of BMP-2 and demonstrated successful osteogenic enhancement *in vitro* and ectopic bone induction *in vivo*.

Overall, BMP has shown promise for a single-molecule fracture treatment, though research suggests that its use is primarily beneficial for particular fracture cases, such as where endochondral ossification is favoured, and stimulation can be achieved from low doses. Accordingly, other signalling molecules or combinatory treatments could prove more effective at improving fracture outcome.

### 1.6.3 Combination therapies

In a physiological context, multiple signalling pathways are activated simultaneously to aid repair. Therefore, there is a potential benefit to therapies that present a combination of signalling factors. Lin *et al.* (2014) used a rabbit segmental defect model to investigate the healing potential of adipose derived stem cells modified to persistently express BMP-2 and VEGF. Under this treatment, bone union and remodelling was observed after 8 months, whereas a control group treated with stem cells alone displayed non-union (Lin *et al.*, 2014). Similarly, Kumar *et al.* (2010) investigated treatment of a mouse segmental defect using MSCs transduced with a virus expressing BMP-2 and VEGF, and found enhanced bone formation, vascularity, and osteoblastogenesis, compared to treatment with MSCs alone.

## 1.7 TARGETING THE WNT SIGNALLING PATHWAY TO IMPROVE FRACTURE OUTCOME

As mentioned in **section 1.5**, delayed healing and non-unions result from a patient-specific amalgamation of possible contributing factors. Drug therapies to prevent or treat these conditions therefore need a general target for boosting bone formation which in turn could be used to treat all fracture cases, ideally improving recovery time as well as outcome. As mentioned in **section 1.6**, targeting pathways known to have important roles in bone formation during repair may provide this boosting therapy. Research into BMP treatment has so far been the most successful (reaching clinical trial), however fracture outcome results have not been substantial enough to meet the clinical need and serious adverse effects of heterotopic bone formation has raised safety concerns (Arzeno, Wang and Huddleston, 2018). Furthermore, since BMP treatment primarily leads to endochondral ossification (cartilage) based repair, alternative or supportive treatment options are required

(Marcellini, Henriquez and Bertin, 2012). Another signalling pathway that has been found to have an essential role in bone formation and repair is the Wnt signalling pathway, and hence this has become an attractive therapeutic target. Before discussing current research into potential treatments, this section reviews in detail our current understanding of the role Wnt signalling has during bone formation, homeostasis, and in particular bone repair. Additionally, evidence is presented for why targeting this pathway may provide a successful therapeutic target, and potential issues are highlighted.

### 1.7.1 The Wnt signalling pathway

There are a few known Wnt signalling pathways, namely the canonical or β-catenin dependent signalling pathway, the non-canonical planar cell polarity pathway (PCP), and the non-canonical Wnt/$Ca^{2+}$ pathway. Activated by specific Wnt proteins, each of these have been found to have roles in bone formation, homeostasis, and repair.

In canonical Wnt signalling, a Wnt protein binds to its cell surface receptor frizzled (FZD), which in turn associates with lipoprotein receptor related protein (LRP) receptors. This association activates dishevelled (DVL) and recruitment of the axin protein complex. This complex consists of four proteins, namely adenomatosis polyposis coli (APC), AXIN, casein kinase-1 (CK1), and glycogen synthase kinase 3 (GSK-3). When Wnt is not present, GSK-3β is responsible for phosphorylating and targeting β-catenin for degradation via the proteasome. When the Wnt pathway is activated, GSK-3β activity is inhibited, enabling the cytosolic β-catenin concentration to increase. β-catenin then translocates to the nucleus and associates with the T-cell factor/lymphoid enhancer-binding factor (TCF/LEF) family of transcription factors, inducing the expression of Wnt target genes. Wnt target genes include *AXIN2*, fibronectin, *OSF-2*, *RARG*, *CONNEXIN43*, *TCF4*, and *LEF1* (Zhong, Gersch and Hadjiargyrou, 2006; Leucht *et al.*, 2013; Janeczek *et al.*, 2015); their expression is dependent on cell and tissue type (Ramakrishnan and Cadigan, 2017).

Activation of the non-canonical PCP pathway results in actin cytoskeleton rearrangement for cell polarisation and migration. A Wnt protein ligand binds to its FZD receptor and activates recruited DVL. DVL associates with dishevelled associated activator of morphogenesis 1 (DAAM1) to form a complex that leads to downstream activation of the RHO GTPase; this subsequently activates RHO-associated kinase (ROCK) and myosin, which leads to actin cytoskeleton rearrangement. DVL also forms a complex with RAC GTPase, which then activates Jun kinase (JNK). Downstream events from JNK are yet to be resolved, along with any resultant gene expression from either branch of this pathway (Baron and Kneissel, 2013; Komiya and Habas, 2014). The non-canonical Wnt-$Ca^{2+}$ pathway

in development is known to be activated by Wnt-5a and Wnt-11 (Komiya and Habas, 2014). Here, Wnt binding to FZD and receptor-tyrosine-kinase-like orphan receptor (ROR) leads to downstream release of intracellular calcium. This is achieved by Wnt-activated G protein signalling which stimulates phospholipase C (PLC) and leads to a subsequent downstream increase in dystroglycan 1 (DAG) and inositol 1,4,5-trisphosphate type 3 (IP3); IP3 then stimulates $Ca^{2+}$ release. Intracellular $Ca^{2+}$ activates several proteins including protein kinase C (PKC) and Calcium dependent kinase II (CAMKII) which subsequently activates transcription factor NFAT (Komiya & Habas 2014; Baron & Kneissel 2013; Monroe *et al.* 2012). Each of these pathways are depicted in **Figure 1.7**.

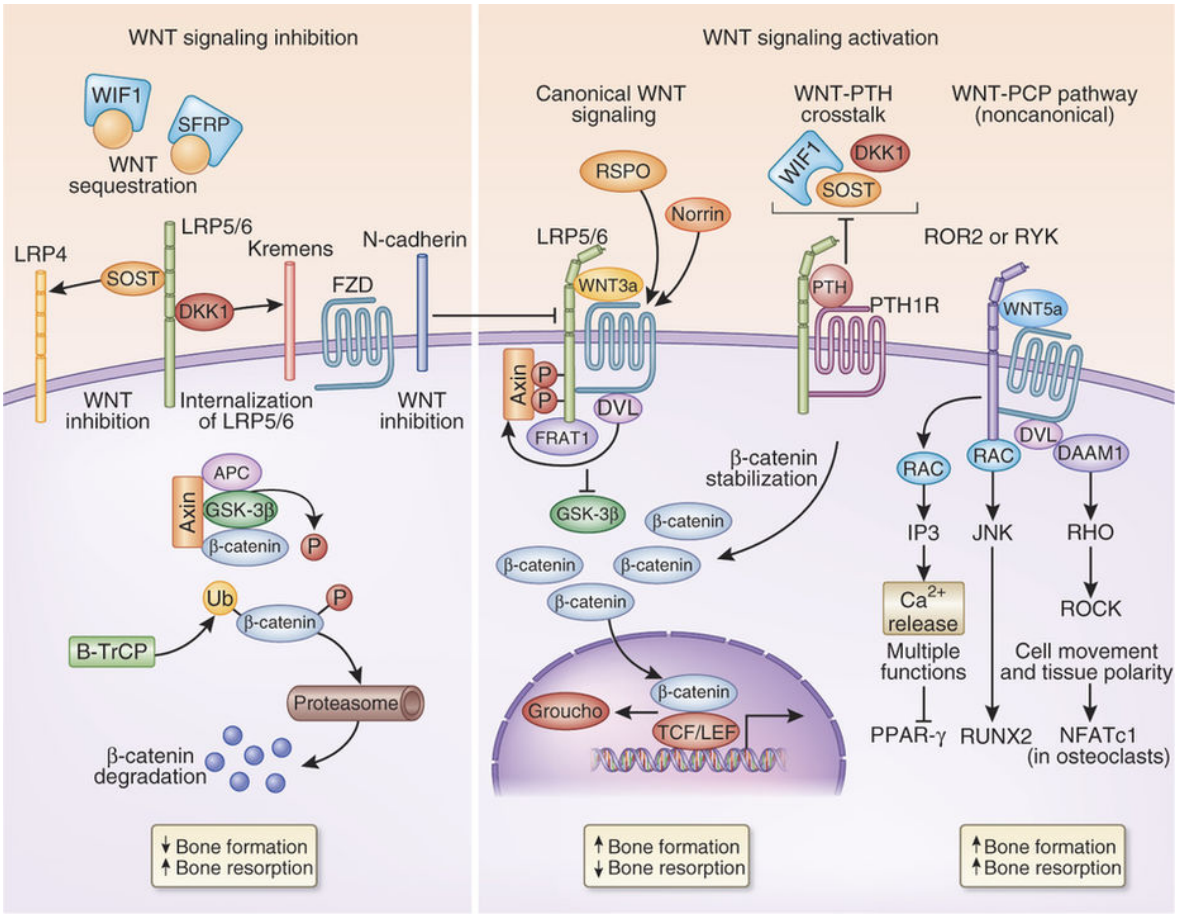


***Figure 1.7: Schematic of canonical and non-canonical Wnt signalling pathways***

*Reproduced from (Baron and Kneissel, 2013).*

### 1.7.2 Wnt signalling in bone formation and homeostasis

The Wnt signalling pathway is known to have an important role in bone formation and homeostasis. This has been highlighted in humans with genetic conditions which affect bone mass. PCR gene sequencing has identified loss of function mutations in the Wnt co-receptor LRP5 as the cause of low bone mass in the genetic condition osteoporosis-pseudoglioma syndrome. Van Buchem disease and

sclerosteosis, both high bone mass conditions, have been found to be caused by mutations in the SOST gene, preventing the expression of sclerostin, a protein secreted by osteoclasts which binds to Wnt co-receptors and inhibits signalling (Brunkow *et al.*, 2001; Loots *et al.*, 2005). The LRP5 gene was also found in a genome wide association study (GWAS) to be associated with decreased bone mineral density (BMD), osteoporosis, and increased osteoporotic fracture risk independent of BMD (Richards *et al.*, 2008). Likewise in animal studies, KO of LRP5 resulted in low bone mass, whilst increased expression of WNT10b resulted in increased bone mass (Bennett *et al.*, 2005). One mechanistic explanation for this effect is that Wnt signalling in osteoblasts and osteocytes is thought to indirectly inhibit osteoclast differentiation via OPG secretion (a decoy receptor for RANKL), evidenced from osteocyte specific β-catenin KO mice which are observed to have progressive bone loss (Kramer *et al.*, 2010).

In animals, developmental studies in which components of the Wnt signalling pathway are knocked out and in of mice embryos have established the fundamental role of Wnt signalling for successful skeletogenesis, but they have also identified mechanisms for its effects (Day *et al.*, 2005; Hill *et al.*, 2005; Kaback *et al.*, 2008). Day *et al.* (2005) and Hill *et al.* (2005) used Wnt signalling reporter mice and β-catenin KO mice to examine their effects in mesenchyme progenitor cell differentiation during different developmental stages of endochondral and intramembranous ossification. These experiments established that specifically canonical Wnt signalling is essential for mesenchymal progenitor cell differentiation into osteoblasts and repression of differentiation into chondrocytes, identified by histological staining and osteogenic (*Runx2, Osx, ColI, Oc*) vs. chondrogenic (*Sox9, ColII*) specific gene expression. This mechanism has been supported through *in vitro* cell line experiments. Exposing progenitor cell lines to Wnt signalling agonists or inducing ectopic expression of signalling components resulted in inhibition of adipogenesis and induction of osteoblastogenesis. This was determined by gene/protein expression analysis as well as cell staining for mineralisation or lipid formation, thus identifying fully differentiated mature cell states (Bennett *et al.*, 2002, 2005; Kennell and MacDougald, 2005).

Arguably, determining the mechanistic role of Wnt signalling in the whole process of osteogenesis (which includes progenitor differentiation to premature/precursor osteoblasts, and further differentiation into mature osteoblasts with bone matrix production activity) within a cell line does not necessarily reflect the Wnt responsive behaviour of primary cells *in vivo*. A later *in vivo* developmental experiment by Rodda (2006) identified stable β-catenin-Wnt signalling as essential to specifically progenitor cell differentiation to osteoblast precursors (Runx2$^{+}$ and Osterix, Osx$^{+}$), and for the osteoblast precursor to stay in this phenotype, as β-catenin KO in progenitors and precursors

gave rise to chondrocytes. In addition, β-catenin-Wnt signalling in osteoblast precursors is required for differentiation into mature bone matrix producing cells, as β-catenin KO in precursor cells resulted in an absence of histochemical signals for matrix ossification. However, continual β-catenin signalling in these osteoblast precursors increases proliferation and causes premature ossification from matrix producing cells but with no osteocalcin ($Oc^+$) expression, characterising terminally differentiated osteoblasts (Rodda, 2006). This data highlighted a stop in Wnt signalling may occur during later osteoblast differentiation stages *in vivo* to enable normal bone formation.

The importance of the temporal control of Wnt signalling has further been supported *in vitro* from studies using adult primary SSCs. In three separate studies, constant exposure of human isolated bone marrow stromal cells (hBMSCs) containing unselected SSCs to Wnt-3a proteins for time periods ranging from 4 to 27 days was found to inhibit osteogenic differentiation. This was assessed by a decrease in ALP gene expression/activity and the absence of mineralisation, thereby identifying the lack of transition to a mature osteoblast state (Boer *et al.*, 2004; Boland *et al.*, 2004; Janeczek *et al.*, 2015). 4 day exposure (Boer *et al.*, 2004) and 12 day exposure (Boland *et al.*, 2004) did however promote hBMSC proliferation. In contrast, Janeczek *et al.* (2015) found that transient exposure to Wnt-3a for 24 hours increased ALP activity and produced mineralisation, indicating a promoting effect upon osteogenesis. Boland *et al.* (2004) also investigated a transient exposure of Wnt-3a over a longer period of 12 days; after another 12 days post-exposure, no change was observed in mineralisation compared to controls and ALP activity decreased, suggesting that transient Wnt signalling activation also has a time dependent effect upon osteogenesis. However, it is important to note that many factors affect these *in vitro* experiments, which often differ between studies. These factors include the inherent patient to patient variability of cell sources, the use of different cell passage numbers, and varying osteogenic culture conditions, all of which can influence analysed gene expression, protein activity, and overall successful osteogenic differentiation. Mechanistic findings must therefore be considered in light of this and need to be validated *in vivo*.

Overall, these studies highlight that Wnt signalling has important functions in both bone formation and bone homeostasis, which gives a strong indication that Wnt signalling has a significant role in bone repair. The mechanism of effect of Wnt signalling, as revealed from developmental studies and *in vitro* primary cell cultures, gives insight into possible mechanisms, including temporal complexities, which may occur for bone formation during repair. Likewise mechanisms of Wnt signalling in homeostasis, including cross talk with osteoclasts and the bone environment (which, although not extensively discussed here, are reviewed in Baron and Kneissel, (2013)), may give insight into mechanisms that occur for bone remodelling during repair. However, it is important to distinguish

these studies from those which assess Wnt signalling during repair of a bone injury. This is due to evidence which suggests that Wnt signalling effects differ in this repair situation, as will now be discussed.

### 1.7.3 Wnt signalling during repair

Chen *et al.* (2007) measured β-catenin protein expression in both mouse and human fracture samples at different timepoints during repair and established that canonical Wnt signalling is activated throughout fracture repair. To ascertain a more precise role, a TCF-Wnt signalling reporter mouse was used to investigate specific cell Wnt activation across stages of fracture repair, identified by histological stains. It was found that canonical Wnt signalling is activated in early stages of chondrogenesis and in osteogenesis but downregulated in late chondrogenesis and osteoblast maturation into osteocytes. Furthermore, when β-catenin was specifically inactivated in mice, no bridging of a fracture gap was observed and no osteoblasts were detected compared to controls; in addition, transcription factors associated with chondrogenic differentiation (*Sox9*) and osteogenic differentiation (*Runx2*) were downregulated (Chen *et al.*, 2007). Together this evidence suggests that Wnt signalling is essential for osteogenesis but, contrary to bone development studies, Wnt signalling activation is also necessary for cartilage formation involving chondrogenesis.

The requirement of Wnt signalling for successful bone healing was also demonstrated by Kim *et al.* (2007) where inhibiting Wnt signalling in mice by inducing sustained expression of *Dkk1* resulted in reduced bone formation as determined by histological staining. In addition, staining for *Runx2* and ALP expression revealed that Wnt signalling inhibition results in no progenitor cell differentiation and no mature osteoblast mineralisation activity. Interestingly Kim *et al.* (2007) also assessed fracture healing in mice using a gain of function mutation in the LRP5 gene to induce constant Wnt activation, and also observed a delay in bone healing, suggesting temporal Wnt signalling also has importance in bone repair (Kim *et al.*, 2007). This too was observed by Chen *et al.* (2007): when β-catenin was constantly expressed, *Sox 9* and *Runx2* expression decreased and no bridging of the fracture occurred. Furthermore Chen *et al.* induced both β-catenin inactivation and continual expression specifically in cells of the osteoblast lineage and found that healing was inhibited in β-catenin inactivation and instead enhanced with stabilised β-catenin expression. This suggests that contrary to *in vitro* findings continual Wnt signalling, specifically in osteoblasts involved in bone repair, promotes osteoblast maturation and subsequent bone formation. Therefore, targeting osteoblasts specifically could be of therapeutic benefit, however greater understanding is still needed of the optimal point within the repair process to start such treatment.

In addition to activity in the osteogenic and chondrogenic phases of repair, canonical Wnt signalling has also been found to have a role in the remodelling phase. Bao *et al.* (2017) selectively inhibited β-catenin in the late stage of fracture healing (3-8 weeks post fracture) in a mouse model and observed a decrease in bone formation and an increase in bone resorption. In addition by using $Catnb^{lox(ex3)}$ mice which respond to an injectable activator for stable β-catenin protein expression, Bao *et al.* (2017) enabled control of the level of β-catenin activation and observed that constitutive activation increased bone mass but delayed remodelling, whereas slight activation of β-catenin increased bone formation and to a lesser extent hindered bone resorption. This study suggests that a reduced level of Wnt signalling is required in the later stages of healing for successful repair, which could have implications for Wnt signalling targeted therapies; more specifically, it suggests targeted administration at the early stages of healing, so as not to delay remodelling.

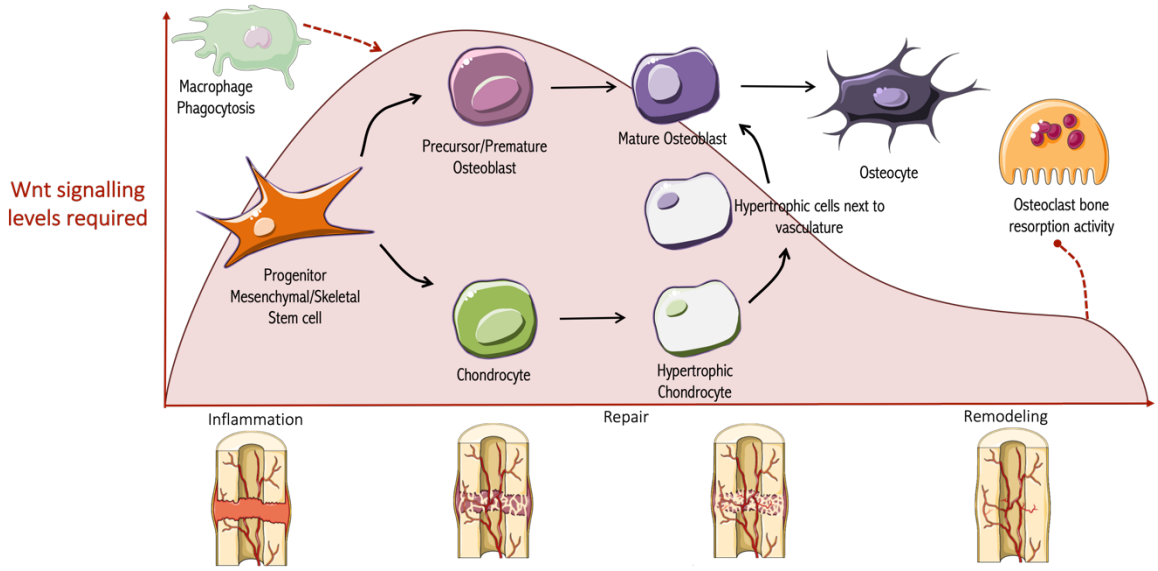


***Figure 1.8: Wnt signalling and the cells involved in fracture repair.***

*Schematic of the stages of bone repair and the cells involved in repair which are influenced by levels of Wnt signalling. Wnt signalling activity is represented by the red curve. Red dotted arrow represents theory that macrophage signalling activity increases Wnt activity during early phases of fracture repair* (Cho *et al.*, 2014). *Red dotted line with stop represents Wnt signalling inhibiting osteoclast bone activity - as Wnt signalling levels decrease in the later remodelling stage of bone healing osteoclast activity/bone resorption increases*(Bao *et al.*, 2017).*Information extracted from* Chen *et al.*, 2007; Kim *et al.*, 2007; Bao *et al.*, 2017; Hu *et al.*, 2017. *(Parts of this figure's graphics are credited to smart.servier.com)*

Immunoblotting and PCR techniques have enabled insight into the gene and protein expression of Wnt pathway members, including proteins, Wnt signalling targets, and osteogenic and chondrogenic cell markers at different timepoints during repair, identified by histological stains (Hadjiargyrou *et al.*, 2002; Zhong, Gersch and Hadjiargyrou, 2006; Chen *et al.*, 2007; Kakar *et al.*, 2007; Kim *et al.*, 2007; Kaback *et al.*, 2008). **Figure 1.9** presents a visual representation of the findings of studies which have

specifically investigated the temporal expression of Wnt related genes and proteins in rodent bone injury models. It is important to note that the earliest timepoint measured within these studies is three days post-injury. Therefore, details of gene expression during this earliest stage of repair currently presents a gap in the literature which needs to be addressed. Although these studies have given great insight into the temporal effects of Wnt signalling, these techniques also lack spatial or cell-specific expression information.

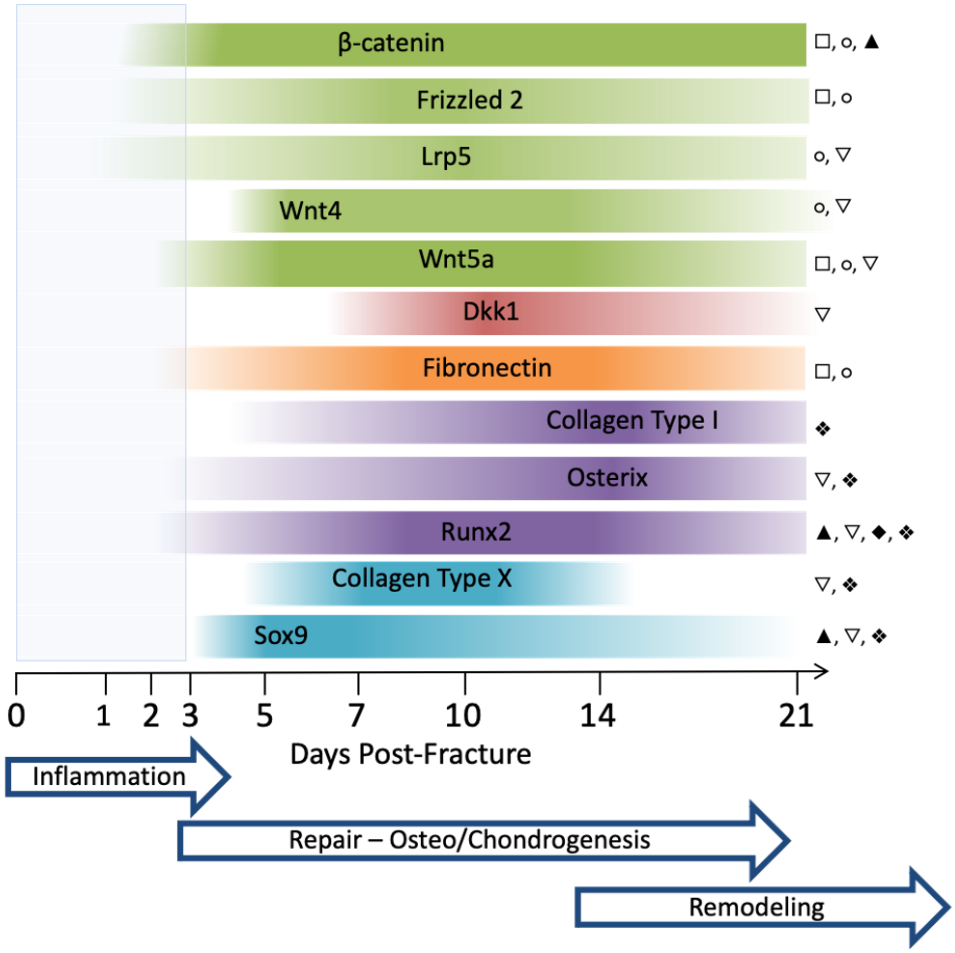


***Figure 1.9: Timing of Wnt-related gene expression following a bone injury in a murine model***

*A visual representation of the findings from studies which have specifically investigated the temporal expression of Wnt related genes and proteins in rodent bone injury models. Colours group related gene markers: green = members of the Wnt signalling pathway; red = inhibitor of Wnt signalling pathway; orange = Wnt signalling target; purple = osteogenic marker; light blue = chondrogenic marker. Increasing colour intensity signifies an increase in expression shown in relation to the three-stage model of bone healing (Blue arrows). Data extracted from □ Hadjiargyrou et al. (2002); ○ Zhong, Gersch and Hadjiargyrou (2006); ▲ Chen et al. (2007); ▽ Kakar et al. (2007); ◆ Kim et al. (2007); ❖ Kaback et al. (2008).*

Techniques using Wnt responsive reporter mice and in situ hybridisation combined with histological staining are facilitating an initial understanding of the spatial and temporal activation of Wnt signalling during repair, and furthermore details of specific Wnt protein receptor and target gene expression as well as osteogenic and chondrogenic marker gene expression. Using mice with a mono-cortical defect, Kim *et al.* (2007) determined that Wnt signalling is activated and localised within an injury callus 24 hrs, 48 hrs and 3 days following injury. This is during the inflammatory period; however, activity is not detected within cells of inflammatory origin. In the later repair stage (up to 28 days post injury), Wnt activity is localised to both within and around the injury callus; however, expression of particular Wnt ligands, receptors, and inhibitors varied in location, highlighting spatial differences in specific Wnt signalling effects (Kim *et al.*, 2007). Indeed, central and outer callus regions are known to progress through overlapping healing stages at different rates (Schindeler *et al.*, 2008). Of particular interest, Wnt protein Wnt-5a expression was localised in all investigated regions and is known to activate the non-canonical Wnt signalling pathway (Baron and Kneissel, 2013). This highlights that both canonical and non-canonical pathways have a role in fracture healing and may have differing effects which need to be further understood in a repair situation, as this could affect the choice of Wnt signalling target for therapy. It would be of further use to understand what specific cell types produce Wnt proteins and inhibitors temporally during fracture repair.

These results all provide evidence that Wnt has a strong osteoinductive action during repair and therefore presents an attractive target for fracture treatments. Research into the potential therapeutic benefit of Wnt is reviewed in **section 1.7.4**. It is, however, important to note that *in vivo,* osteogenesis is determined by a complex interplay of various signalling events, of which Wnt signalling is one part, as listed in **section 1.4**. For example, Wnt signalling and BMP signalling are known to have a negative signalling feedback mechanism. Minear *et al.* (2010) demonstrated rBMP-2's ability to repress Wnt signalling within cells of the osteoblast lineage, preventing subsequent differentiation. Interestingly the effects of rBMP differed depending on the location of the responsive cells. In the injured periosteum, rBMP stimulation relieved Wnt-dependent *Sox 9* inhibition, causing upregulation and increasing subsequent differentiation of cells into chondrocytes. In the endosteum, inhibition of Wnt signalling by rBMP caused downregulation of *Runx2* and Collagen type I, preventing osteoblast differentiation. In the muscle surrounding the injury, Wnt signalling inhibition resulted in Smad-1, -5, and -8 phosphorylation and subsequent cell proliferation and differentiation to chondrocyte lineage (Minear, Leucht, Miller, *et al.*, 2010). This study therefore highlights an additional spatial variation in cell responses to signalling events. However, the concentration of BMP exposure (1 mg/mL) is not representative of endogenous conditions (Schmidt-Bleek *et al.*, 2016); accordingly, this may not reflect the extent of Wnt inhibition in different locations within a fracture

site *in vivo*. This evidence demonstrates the complexity of the interaction between the factors that affect bone formation, and particularly sometimes their apparently contradictory nature, often derived from limits in experimental design (e.g. under-/over-represented physiological conditions). However, what is clear is that there are feedback mechanisms and regulation that serves to control excessive bone formation during repair that needs to be considered and understood further both spatially and temporally to produce effective treatments to influence these mechanisms.

### 1.7.4 Therapeutic approaches to target the Wnt signalling pathway

Knowledge of Wnt activity during fracture healing (as explained in **section 1.7.3**) has highlighted this signalling pathway as an attractive target for a therapeutic to stimulate bone formation. Several treatment approaches for activating the Wnt signalling pathway have been investigated and will be discussed here.

One such approach is to use a Wnt protein to cause extracellular activation. In a study employing a mouse fracture model, liposomal encapsulated Wnt-3a was administered 3 days following injury. It was subsequently found that mineralisation and osteoid deposition, as well as remodelling, had occurred sooner in the treatment group compared to control groups (3 days and 28 days post injection, respectively). Furthermore, osteogenic genes *Runx2*, collagen type II, and osteocalcin, were expressed sooner in the treatment group (24 hours post injection), and there was an increase in proliferating cells. It was therefore concluded that the bone promotion effect of Wnt-3a treatment was achieved by increased proliferation of skeletal progenitors, which then rapidly differentiated to osteoblasts (Minear, Leucht, Jiang, *et al.*, 2010).

One disadvantage to approaches using a single Wnt ligand is that particular Wnt proteins have different signalling effects, necessitating a greater understanding of which Wnt ligand receptors are present during bone repair. Additionally, further understanding is required of whether a chosen Wnt ligand will generate the desired bone formation effect. Most of the reviewed evidence for *in vivo* Wnt signalling during repair suggests that canonical Wnt signalling is important for osteogenesis, although the non-canonical signalling role still needs to be understood. Previously, different Wnt proteins have been classified as either canonical stimulating (e.g. Wnt-1, -3a, -8, -10b) or non-canonical stimulating (e.g. Wnt-4, -5a, -11) (Hoeppner, Secreto and Westendorf, 2009). However, there is now evidence to suggest that the activation of a pathway may not be directed by a specific ligand-receptor combination. Instead, cell-specific expression of particular receptors and co-receptors, but also the intracellular location of receptor binding partners (e.g. DVL), will dictate which signalling pathways are activated upon the same ligand binding. Therefore choosing a particular Wnt

ligand for treatment may not precisely direct the intended canonical signalling pathway outcome for the cells it interacts with, adding additional complexity (Komiya and Habas, 2014). In addition the use of Wnt proteins has the challenges associated with administering an insoluble and highly hydrophobic protein (Minear, Leucht, Jiang, *et al.*, 2010).

Another potential approach is to inhibit the activity of a natural Wnt inhibitor, thereby indirectly creating an increase in naturally-occurring Wnt signalling. Natural inhibitors of Wnt signalling include Dickkopf (Dkk1), sclerostin, Wnt modulator in surface ectoderm (Wise), secreted Fizzled related proteins (Sfrps), and Wnt inhibitory factor (Wif-1) (Baron and Kneissel, 2013). Ominsky *et al.* (2011) used a sclerostin targeted antibody treatment in a rat femoral fracture model and cynomolgus monkey osteotomy model; following treatment, significant improvements were observed in bone formation, mass, and strength, resulting in a smaller fracture gap, observed at an earlier timepoint, compared to controls (Ominsky *et al.*, 2011). This treatment has gone on to gain clinical approval in the treatment of osteoporosis under the name Romosozumab (Evenity). Although Romosozumab has shown to decrease the risk of fragility related fractures, questions over its potential for use in promoting general fracture repair (Saag *et al.*, 2017) remain open, as a recent trial found use of Romosozumab in hip fracture treatment did not improve outcomes compared to placebo (Schemitsch *et al.*, 2020). It is important to note healthy bone tissue will also be exposed to any fracture treatment which targets the Wnt signalling pathway, therefore Wnt signalling mechanisms in bone homeostasis will be affected and need to be considered in therapeutic design. In bone homeostasis, the mechano-stimulated osteocyte secretion of sclerostin inhibits the Wnt signalling effect on osteoblast bone formation. Accordingly, inhibition of sclerostin has the effect of increasing bone mass in healthy tissue (Baron and Kneissel, 2013). This further highlights the importance for a treatment to exhibit temporal control over Wnt signalling.

### 1.7.5 GSK-3β Inhibitors

As well as administering exogenous ligands to boost repair, there are small molecules that can modulate intracellular components of the signalling pathways involved in fracture healing. In the Wnt pathway, inhibitors that act on GSK-3β are able to activate downstream canonical signalling, notably mitigating the need for specific extracellular ligands and receptor expression. This could therefore activate canonical Wnt signalling in a wider variety of cell types, and hence presents an appealing therapeutic option.

There are a number of pharmacological inhibitors of GSK-3 which are being investigated for use in treating conditions such as neurodegenerative diseases and diabetes. Amongst them 6-

bromoindirubin-3'-oxime (BIO) and CHIR-99021 have been selected for study in this thesis owing to reports of greater selectivity (Meijer, Flajolet and Greengard, 2004).

6-bromoindirubin-3'-oxime (BIO) is a synthetic derivative of the indirubin 6-bromoindirubin, which is naturally found in the Tyrian purple dye from gastropod molluscs. BIO was found to inhibit GSK-3 kinase through interactions with the ATP binding site. CHIR-99021, henceforth referred to as CHIR, is a synthetically-derived aminopyrimidine also found to selectively inhibit GSK-3 by hydrogen bond interactions with the ATP-binding domain of the enzyme (Ring *et al.*, 2003; Wagner *et al.*, 2016). By competitively inhibiting GSK-3β kinase phosphorylation of β-catenin for subsequent degradation, BIO and CHIR enable β-catenin to accumulate in the cytosol, translocate to the nucleus, and initiate downstream expression of Wnt target genes. *In vivo*, BIO has been found to mimic Wnt signalling effects during development, for example inducing Wnt genes and dorsal-axis formation in developing Xenopus embryos (Meijer *et al.*, 2003). *In vitro*, BIO has been found to maintain an undifferentiated state of human and mouse embryonic stem cells (Sato *et al.*, 2004). Meanwhile, CHIR has been investigated for controlling blood glucose for treatment of type II diabetes (Ring *et al.*, 2003). This evidence shows that BIO and CHIR are able to activate Wnt signalling in a variety of biological systems and have the potential to do so during fracture repair; studies that demonstrate their osteoinductive effect are hence described below.

*In vitro*, CHIR induces osteoblastogenesis and increases mineralisation in a ST2 cell line (Bennett *et al.*, 2005). CHIR has also been found to inhibit the differentiation of the preadipocyte 3T3-L1 cell line, preventing adipogenesis (Bennett *et al.*, 2002). More specifically, this study found CHIR's activation of canonical Wnt signalling blocks induction of master adipogenic transcription factors C/EBPα and PPARγ, ultimately preventing adipogenesis. However, this effect is only observed within 3 days of exposure, suggesting this cell type has a window of sensitivity to Wnt signalling (Bennett *et al.*, 2002). The ability of CHIR to activate the Wnt pathway in these cell lines suggests that these small molecules could activate Wnt signalling involved in BMSC differentiation.

A review of the evidence for the effects that exposure to BIO/CHIR has upon human BMSCs reveals a complex and contradictory set of results. This is mainly due to the fact that studies vary widely in several key areas: choice of BIO/CHIR concentration, choice of BIO/CHIR exposure time (ranging from 1 hour to 5 weeks), whether exposure is continuous or temporal, and when experimental tests are performed (ranging from 24 hours to 6 weeks post-exposure).

Previously within our own lab, work performed and published by Scarpa *et al.* (2018) showed that hBMSCs incubated with BIO over a 24 hour period resulted in a significant increase in the expression

of *AXIN2*, confirming activation of the Wnt signalling pathway, as well as *RUNX2* and Osterix (*OSX/SP7*), which are key transcription factors required for osteoblast differentiation. However, no evidence of mature osteoblast differentiation was found. Likewise Clough *et al.* (2018) used a 1 hour BIO exposure and found an upregulation of *RUNX2*, but also an increase in ALP activity, which is important for bone mineralisation and a marker of early and late osteoblast differentiation, 8 days post exposure. Hoffman, Takahata and Benoit (2011) found 24-hour BIO exposure resulted in increased hBMSC cell proliferation and an upregulation of *RUNX2* 6 weeks later, but subsequent osteoblast maturation was inhibited. Similarly, Frith *et al.* (2013) reported that hBMSCs incubated with CHIR show inhibited osteogenesis, as assessed by a lack of *ALP* gene expression and activity as well as no positive mineralisation stain. Interestingly, reverse transcription quantitative real-time polymerase chain reaction (RT-qPCR) analysis revealed an upregulation of *AXIN2* – confirming activation of the Wnt pathway – but also pro-osteogenic factors such as *RUNX2*, *DLX5,* and *MSX2*, as well as a downregulation of *ALP* expression. One explanation for this observed effect could be the length of time the cultured BMSCs were incubated with CHIR, which in this case was continuously for 7 and 21 days (Frith *et al.*, 2013). Continual exposure to BIO for 8 days however was shown to increase ALP activity, but only up to a concentration of 400 nM (Krause *et al.*, 2010), and a further 17 days of exposure conversely resulted in a positive mineralisation stain. One result that did remain consistent across studies for short- or long-term exposure of BIO/CHIR, even up to 5 weeks (Huang *et al.* 2018), was an upregulation of *RUNX2*. This implies that early osteogenic differentiation has been initiated within BMSCs. The experimental methods and findings of each of the publications reviewed here are summarised in **Table 1.1.**

Overall, in the same way that Wnt ligands have differing effects upon primary hBMSC culture as described and presented in **Table 1.1**, CHIR and BIO also have stimulatory or inhibitory effects upon osteogenesis *in vitro,* depending on exposure time and further complicated by varying experimental conditions.

*In vivo*, specifically focusing on studies relating to a bone environment, BIO and CHIR have also been found to have an osteoinductive effect. Clough *et al.* (2018) used BIO to enhance a spinal fusion procedure in an immune compromised rat. The treatment did not affect the volume of bone fusion but did promote denser bone formation in which osteogenesis progressed to a greater degree than controls, evidenced by histological stains showing more mature bone formation. This study shows that BIO can promote osteogenesis *in vivo*; however, arguably the effect of BIO within a fusion model in an immune compromised rat does not necessarily reflect its effects in fracture treatment. In addition, the treatment used in this study involved exposing hBMSCs to BIO for a short period *in*

*vitro*, after which the cells were implanted via a scaffold into the rat vertebrae (Clough *et al.*, 2018). For clinical application, production of BIO-exposed hBMSCs would add additional complexity and production steps, which also would depend on open surgery for treatment application; therefore, application of BIO directly arguably provides a better treatment strategy, if proven effective.

BIO and CHIR have been found to promote mineralisation and dentine secretion in a tooth repair model (Neves *et al.*, 2017). Although this study too is not reflective of a fracture situation, it is interesting to note that a greater concentration of CHIR, 5 µM, compared to BIO, 50 nM, resulted in equivalent significant mineral formation. At the time of writing and from the literature reviewed, no comparisons have been made on the effectiveness of these two Wnt agonists upon fracture repair. This is therefore one of the aims of this thesis.

A literature search revealed only three studies that have used a small molecule GSK-3β inhibitor specifically in the context of fracture repair. Administration of AZD2858, a GSK-3β inhibitor produced by AstraZeneca, to injured rats was shown to rapidly heal the fracture without pre-formation of cartilage tissue (endochondral repair) compared to controls (Sisask *et al.*, 2013). Similarly in a mouse fracture model AZD2858 was found to significantly enhance bone volume and strength evidencing healing at a faster rate than controls. However unlike the work of Sisask *et al.* (2013), this was only achieved when delivered with a targeted nanoparticle (NP) delivery system, and some cartilage formation was observed (Wang *et al.*, 2017). This discrepancy is likely due to dose discrepancies where Sisask *et al.* (2013) used daily dosing of the GSK-3β inhibitor throughout healing, whereas Wang *et al.* (2017) used a single dose 3 days post fracture. Of note Sisask *et al.* (2013) highlights how bone mineral content and densities were similarly changed in the unfractured femur of treated subjects and that a local rather than systemic administration would be advantageous to reduce off target effects in tissues which also have GSK-3β responsive cells. To resolve this issue Wang uses a targeted nanoparticle to control delivery however assessment of its effect upon the unfractured femur is lacking. Finally Low *et al.* (2017) administered free BIO to a mouse bone injury model and found no significant improvement to fracture healing compared to the control. One possible explanation for this could be that the bio-distribution of the chosen dose of BIO following intravenous (IV) administration resulted in a low concentration at the target site. As discussed later in **section 1.8**, use of a controlled delivery system can improve bioavailability of a drug. Indeed Low *et al.* (2017) also found that administration of BIO via a micelle carrier significantly increased bone mineral density and volume.

There are, however, as already alluded to, some potential issues with a GSK-3β inhibitor treatment. Firstly, this approach does not target non-canonical Wnt signalling, which could also be required in

fracture repair (Zhong, Gersch and Hadjiargyrou, 2006). Secondly, unlike targeting sclerostin, it is not selective to a bone environment; nor is it selective to specifically GSK-3β, which could lead to the activation of other cell signal processes downstream of all GSK-3 subtypes (Frame and Cohen, 2001). Thirdly, BIO in particular is known to have toxic side effects at doses that may be too low to have therapeutic effect (Naujok *et al.*, 2014). A solution to controlling the delivery of BIO/CHIR to the target injury site as well as reducing off-target effects could be to utilise a nanoparticle delivery system. This theory has formed the basis of research previously performed and published within our lab by Dr Edoardo Scarpa. Scarpa's work is the precursor to the research developed within this thesis, discussed further in **section 1.8**.

As with all the candidate therapeutics outlined above, one challenge that needs to be addressed is finding an optimal time for delivery. As discussed in **section 1.7.3**, there is evidence to suggest an optimal window of opportunity in which to influence the Wnt signalling pathway and stimulate bone formation is in early fracture healing. For a successful therapeutic, a detailed understanding of endogenous Wnt signalling is needed across the entire fracture repair process. In general, understanding of the timing of all signalling processes and feedback interactions in humans especially but even in animal models is still lacking and would benefit the development of therapeutics. Nonetheless, temporally controlled delivery of a therapeutic is an additional area in which nanoparticles could improve possible treatments.

***Table 1.1: Summary of literature determining the effects that exposure to BIO/CHIR has upon human bone marrow stromal cells***

BIO represented in red and CHIR represented in green. Colour intensity from dark to light represents high to low concentration and longest to shortest exposure time. For finding compared to control ↑ = increase, ↓ = decrease and – = same level as control/no change.

| Wnt Agonist | Concentration (nM) | Exposure Time | Continual / Temporal | Assessment and Method Details | | Assessment Time Following Exposure | Change Compared to Controls | Culture Conditions | Reference |
|---|---|---|---|---|---|---|---|---|---|
| BIO | 2000 | 24 hours | Temporal | Proliferation - cell count | | 1, 3, 6, 19, 27, 34, 37, and 41 days | ↑ | | (Hoffman and Benoit, 2015) |
| | 5000 | | | | | | ↑ | | |
| | | | | Wnt activity - gene expression (qPCR) | *SOX2* | 1 and 3 days | ↑ | | |
| | | | | | | 6, 19, 27, 34, 37, and 41 days | - | | |
| | | | | | *NANOG* | 1 and 3 days | ↑ | | |
| | | | | | | 6, 19, 27, 34, 37, and 41 days | - | | |
| | | | | | *OCT4* | 1 and 3 days | ↑ | | |
| | | | | | | 6, 19, 27, 34, 37, and 41 days | - | | |
| | | | | Cell cycle regulator - gene expression (qPCR) | *CYCLIN D1* | 1, 19 and 27 days | ↑ | | |
| | | | | | | 6, 34, 37, and 41 days | - | | |
| | | | | Osteogenesis - histology and gene expression (qPCR) | Von kossa stain (hydroxyapatite) | 43 days | - | 22 days post treatment osteogenic media for 21 days. | |
| | | | | | *RUNX2* | | ↑ | | |
| | | | | Chondrogenesis - histology and gene expression (qPCR) | Toluidine blue (glycosaminoglycans) | | - | 22 days post treatment chondrogenic media for 21 days. | |
| | | | | | *SOX9* | | ↓ | | |

| | | | | | | | | | |
|---|---|---|---|---|---|---|---|---|---|
| | | | | Adipogenesis - histology and gene expression (qPCR) | Oil red O (lipid droplets) | | - | 22 days post treatment adipogenic media for 21 days. | |
| | | | | | *PPARγ* | | ↑ | | |
| **BIO** | 200, 800 | 1 hour | Temporal | Osteogenesis - gene expression (qPCR) | *RUNX2* | 4 hours | - | Osteogenic media following BIO treatment. | (Clough *et al.*, 2018) |
| | | | | | | 1, 2 days | ↑ | | |
| | | | | | *OSX* | 4 hours, 1 and 2 days | - | | |
| | | | | Osteogenesis - protein expression (ELISA) | Osteoprotegerin | 4 days | ↑ | | |
| | | | | Osteogenesis - ALP activity assay | ALP | 8 days | ↑ | | |
| **BIO** | 2000 | 24 hours | Continual | Wnt activity - gene expression (qPCR) and immunohistochemistry | *AXIN2* | 24 hours | ↑ | Chondrogenic media | (Huang *et al.*, 2018) |
| | | | | | β-catenin nuclear localisation | | ↑ | | |
| | | 5 weeks | | Chondrogenesis - histology and gene expression (qPCR) | *SOX9* | 5 weeks | ↓ | | |
| | | | | | *COL2A1* | | ↓ | | |
| | | | | | *ACAN* | | ↓ | | |
| | | | | | Safranin O staining | | ↓ | | |
| | | | | | Alcian blue staining | | ↓ | | |
| | | | | Hypertrophic chondrocytes - gene expression | *COL10A1* | | ↑ | | |
| | | | | Osteogenesis - histology and gene expression (qPCR) | *RUNX2* | | ↑ | | |
| | | | | | *ALPL* | | ↑ | | |
| | | | | | Alizarin red (mineralisation) | | - | | |
| | | | | Dedifferentiation markers - gene expression (qPCR) | *COL1A1* | | ↑ | | |
| | | | | | *GLUT1* | | ↑ | | |

| | | | | | | | | | |
|---|---|---|---|---|---|---|---|---|---|
| | | | | Glycolysis - gene expression (qPCR) | *PGK1* | | ↑ | | |
| | | | | Wnt inhibition - protein expression (ELISA) | DKK1 | | ↑ | | |
| **BIO** | 100, 200, 400 | 8 days | Continual | Osteogenesis - ALP activity assay, protein expression (ELISA) | ALP | 8 days | ↑ | Osteogenic media without dexamethasone | (Krause *et al.*, 2010) |
| | 800 | | | | | | - | | |
| | 100, 200 | | | | OPG | | - | | |
| | 400, 800 | | | | | | ↑ | | |
| | 100, 200, 400, 800 | | | Wnt inhibition - protein expression (ELISA) | DKK1 | | ↓ | | |
| | 200, 800 | 8 Days | Temporal | Osteogenesis - histology | Alizarin red (mineralisation) | 10 and 15 days | ↑ | After 8-day treatment, 15 days in osteogenic media with dexamethasone | |
| | 200 | 17 days | Continual | Osteogenesis - histology | Alizarin Red (mineralisation) | 12 and 17 days | - | Osteogenic media with dexamethasone | |
| | 800 | | | | | | ↑ | | |
| **BIO** | 2000 | 24 hours | Continual | Osteogenesis - gene expression (qPCR) | *RUNX2* | 24 hours | ↑ | | (Scarpa *et al.* 2018; 2016) |
| | | 96 hours | | | | 96 hours | ↑ | | |
| | | 24 hours | | | *OSX* | 24 hours | ↑ | | |
| | | 96 hours | | | | 96 hours | ↑ | | |
| | | 24 hours | | Wnt signalling - gene expression (qPCR) | *AXIN2* | 24 hours | ↑ | | |
| | | 48 hours | | | | 48 hours | ↑ | | |
| | | 96 hours | | | | 96 hours | - | | |
| | | 24 hours | Temporal | Osteogenesis - ALP activity assay | ALP | 14 days | ↓ | Osteogenic media following treatment | |
| **CHIR** | 5000 | 21 days | Continual | Osteogenesis - histology and gene expression (qPCR) | Alizarin red (mineralisation) | 21 days | ↓ | Osteogenic media | (Frith *et al.*, 2013) |
| | | 7 days | | | *ALP* | 7 days | ↓ | | |

| | | | | | | | | | |
|---|---|---|---|---|---|---|---|---|---|
| | | 21 days | | | | 21 days | ↓ | | |
| | | 7 days | | | *RUNX2* | 7 days | ↑ | | |
| | | 21 days | | | | 21 days | ↑ | | |
| | | 7 days | | | *MSX2* | 7 days | ↑ | | |
| | | 7 days | | | *DLX5* | 7 days | ↑ | | |
| | | 21 days | | | *SPP1 (Osteopontin)* | 21 days | ↓ | | |
| | | 21 days | | | *COL1A1* | 21 days | ↑ | | |
| | | 21 days | | | SPARC (Osteonectin) | 21 days | - | | |
| | | 21 days | | | BGLAP (Osteocalcin) | 21 days | - | | |
| | | 7 days | | Wnt activity - gene expression (qPCR) | *AXIN2* | 7 days | ↑ | | |
| | | 21 days | | | | 21 days | ↑ | | |
| | | 7 days | | Wnt inhibition - gene expression (qPCR) | *DKK1* | 7 days | ↓ | | |
| | | 21 days | | | | 21 days | ↓ | | |
| **CHIR** | 5000 | 4 passages | Temporal | Adipogenesis - histology and gene expression (qPCR) | *FABP4* | 3 weeks | - | Adipogenic media following treatment | (Narcisi *et al.*, 2016) |
| | | | | | Oil red O (lipid droplets) | | ↑ | | |
| | | | | Osteogenesis - histology and gene expression (qPCR) | *OCN* | 18 days | ↓ | Osteogenic media following treatment | |
| | | | | | Von kossa stain (hydroxyapatite) | | - | | |
| | | | | Chondrogenesis - histology and gene expression (qPCR) | Thionin stain (glycosaminoglycans) | 5 weeks | ↑ | Chondrogenic media following treatment | |
| | | | | | Immuno-stain (Collagen type-II) | | ↑ | | |
| | | | | | *Aggrecan* | | ↑ | | |
| | | | | | *COL2a1* | | ↑ | | |

## 1.8 NANOPARTICLES - A CONTROLLED DELIVERY SYSTEM

Multiple adverse effects can result from the therapeutic use of the molecular factors described in **sections 1.6 & 1.7.4**., if not controlled for the specific location and timing of their action. This is where the use of a drug delivery technologies could provide a solution.

Delivery vehicles such as microparticles and nanoparticles have many advantages over free drug delivery. Firstly, encapsulation protects drugs from degradation before reaching a target site *in vivo* and enables the delivery of potentially toxic drugs by limiting exposure to non-target tissues. Additionally, presentation of tissue-specific targeting ligands enables targeted delivery, increasing bioavailability at the target site, and hence reducing the required dose. Furthermore, composition can be modified to be sensitive to environmental conditions such as temperature or pH, enabling control over drug release. Finally, certain formation protocols enable large reproducible batch production, which is important for any future translation to clinical treatments (Anselmo and Mitragotri, 2014).

For the purpose of delivering a therapeutic to influence cell signalling within the environment of a bone injury, nanoparticles have several advantages. The nano size scale of these vesicles enable mobility throughout the circulatory system and some evasion of certain clearance systems to potentially accumulate at a bone injury site. Additionally their size enables direct intracellular delivery of a therapeutic agent to then interact with cell signaling proteins, such as GSK-3β. Nanoparticles therefore are the chosen delivery tool of this thesis, as discussed further in this chapter.

### 1.8.1 Nanoparticles in medicine

The use of nanoparticles or nanomaterials in medicine is an ever-growing field with developments for the treatment of a number of diseases, including cancer, diabetes, asthma, and also infection. Their uses fall under three categories: diagnostics, tissue engineering, and drug delivery. The use of nanoparticles in diagnostics has enabled detection of abnormalities and disease markers at a molecular scale, for example the detection of circulating tumour cells for early cancer diagnosis (Mitragotri *et al.*, 2015). Nanomaterials used for tissue engineering are able to form scaffolds for cell attachment and movement within a fracture site (Mitragotri *et al.*, 2015). Further review of the applications and development of nanoparticles for diagnosis and tissue engineering is outside the scope of this thesis; further information can be found in several recent reviews (Farokhzad and

Langer, 2006; Mitragotri *et al.*, 2015; Shi *et al.*, 2016). This work focuses on nanoparticles used for drug delivery and their potential for fracture treatment.

Organic nanoparticles are the group primarily investigated for the delivery of small drug molecules. These include liposomes and polymeric nanoparticles. Liposomes are composed of amphiphilic lipids formed into a spherical bilayer membrane. Several are now in clinical use, such as Liposome-PEG doxorubicin (Doxil) for the treatment of HIV-related sarcoma and metastatic breast and ovarian cancer, and Liposomal Verteporfin (Visudyne) for the treatment of age-related macular degeneration (Zhang *et al.*, 2008). However, this work focuses mainly on polymersomes, as described below.

#### 1.8.1.1 Polymersomes

Polymeric nanoparticles form by self-assembly of amphiphilic block copolymers in water. Assembly is driven by the self-association of amphiphilic polymers, removing hydrophobic components from the aqueous surroundings to reduce free energy (Torchilin, 2007). The stability of the resultant structure depends upon the size of the polymer chain, its chemistry, and on physical conditions such as temperature (Discher *et al.*, 1999). Depending on the geometry of the polymer block, as dictated by the ratio of hydrophobic to hydrophilic elements of the polymer, three structures are known to form: spherical micelles, cylindrical/rod micelles, and vesicles (termed polymersomes) (Discher *et al.*, 1999; Brinkhuis, Floris and van Hest, 2011).

Polymersomes (PMs) have a hydrophobic shell region and a hydrophilic core region. This provides a distinct advantage over other types of nanoparticles by enabling the delivery of single or combination therapy, of both hydrophobic and hydrophilic drugs, in particular drugs previously disregarded due to poor solubility. In addition, compared to liposomes, the increased length, weight, and conformation possibilities of copolymer blocks provides chemical stability, creating a tougher and less permeable membrane (Discher *et al.*, 1999; Brinkhuis, Floris and van Hest, 2011).

PMs can be synthesised with a variety of polymers, which influence their surface topology and resultant cellular uptake (Brinkhuis, Floris and van Hest, 2011; Buckiová *et al.*, 2012). In addition, diverse functionality is given by conjugating moieties such as fluorescent probes, peptides, or antibodies to the polymer surface for specific recognition and improved targeting. For example, bio-conjugation of maleimides for antibody coupling enabled specific delivery of PMs to the brain in a rat model (Brinkhuis, Floris and van Hest, 2011). Stability can be increased by producing PMs to include the polymer polyethylene glycol (PEG), which partially protects from protein degradation and reduces renal clearance, thus increasing circulation time (Brinkhuis, Floris and van Hest, 2011). Rapid clearance has been the downfall for many other types of nanoparticles entering the clinic (Anselmo

and Mitragotri, 2014). It is important to note that repeated doses of PEGylated nanoparticles have been shown to cause the generation of PEG-specific antibodies, resulting in accelerated clearance (Anselmo and Mitragotri, 2014). However, even without PEGylation, the size and shape of PMs facilitates avoidance from certain clearance systems, enabling delivery of a concentrated drug payload to a target location via their eventual intracellular degradation (Mitragotri *et al.*, 2015). Polymeric nanoparticles release their drug payloads in a regulated manner through surface or bulk erosion of the particles, diffusion of the drug through the polymer matrix, or swelling followed by diffusion. Alternatively, drug release can be triggered by environmental factors such as changes in pH, temperature, ultrasound, or the presence of certain substances such as glucose (Farokhzad and Langer, 2006).

Polymersomes have been widely investigated for the treatment of cancer. Their ability to accumulate at certain tumours and inability to penetrate normal vasculature and capillaries increases tumour exposure to highly toxic chemo and radiation therapeutic drugs whilst reducing exposure to other tissue and resultant side effects. One example is GenexolPM, a Paclitaxel loaded PLA-PEG micelle NP, which has been approved in South Korea for the treatment of breast cancer, demonstrating a successful example of PM-drug loading with therapeutic efficacy (Cheng *et al.*, 2015). Swami *et al.* (2014) demonstrated the use of bone-targeting polymeric nanoparticles for the treatment of multiple myeloma in a mouse model. Mice treated with PEG-*b*-PLGA conjugated to the bone-targeting ligand alendronate and loaded with the cancer drug bortezomib showed significantly enhanced survival and decreased tumour size, when compared to control or treatment with free drug alone (Swami *et al.*, 2014). This study shows that polymeric nanoparticles have applicability to a bone environment.

For this thesis, PEG-*b*-polycaprolactone (PEG-*b*-PCL), which are both FDA-approved polymers, have been selected for experimental use. PCL has advantages over other biodegradable polymers, namely its high permeability to small drug molecules and its ability to keep a neutral pH environment upon degradation (rather than acidic, as is the case for polylactides). PCL can also be blended with other polymers or formed into a copolymer to change and improve its chemical and physical properties. Finally, PCL has slow degradation kinetics, making it a suitable vehicle for long-term drug delivery (Sinha *et al.*, 2004; Ghoroghchian *et al.*, 2006); note that should a therapeutic purpose require different degradation kinetics, alternative polymers such as polylactide (PLA), polyglycolide (PGA), and polylactic-co-glycolic acid (PLGA) could be used.

There are a number of reported methods for producing PMs, including electroformation, double emulsion, bulk and film rehydration, and solvent switch. Each of these methods have varying

limitations including low yield, small size preparation, and/or low reproducibility due to size variations. A more extensive review and comparison of methods may be found in the relevant literature (Guan, Rizzello and Battaglia, 2015). For this thesis, the solvent switch method is used, in which the block copolymer is dissolved in an organic solvent (aided by a sonication step) and then transferred to aqueous buffered solution to form polymersomes. This procedure requires later purification by dialysis or evaporation, however it benefits from high user reproducibility for consistent sized PMs (Johnston, Dalton and Newman, 2010). This is important for controlling variability when testing the effects of encapsulated drugs.

### 1.8.2 Nanoparticles in bone fracture treatment

Nanoparticles – in particular polymersomes – provide spatial and temporal control over the delivery of therapeutics. As such, they could be used for the delivery of bone inducing compounds (White *et al.*, 2013), including the Wnt agonists BIO and CHIR, which have potential to improve fracture outcome as discussed in **section 1.7.5**. Polymer based nanoparticles have previously been used specifically to deliver a treatment for bone fracture in the following studies.

Jia *et al.* (2015) used a polymer-drug conjugate micelle delivery system to deliver a statin, simvastatin, which has been shown to have bone growth promoting effects, to treat a mouse bone injury model. This treatment was found to improve fracture healing, as assessed by μCT and mineralisation staining, to a significant level above controls, whereas simvastatin treatment alone did not (Jia *et al.*, 2015). This study demonstrates how nanoparticle delivery can improve the bioavailability and effectiveness of a treatment for bone injury.

Wang *et al.* (2017) produced (PSMA-b-PS) polymeric micelle nanoparticles loaded with a GSK-3β inhibitor, AZD2858, and incorporating a peptide to target the tartrate-resistant acid phosphate (TRAP) bone surface protein. Following treatment of a mouse bone injury model, a significant improvement in fracture healing over controls and AZD2858 free treatment was observed. This result was based on μCT analysis showing increased callus formation and complete bridging before controls, alongside increased strength assessed by torsion testing, and enhanced ossification observed from histological staining (Wang *et al.*, 2017). Similarly, Low *et al.* (2017), although not using a polymer based nanoparticle, demonstrated that administration of micelles formed of GSK-3β inhibitor BIO conjugated to an aspartic acid octapeptide significantly increased bone mineral density and volume over controls and free BIO treatment. Both of these studies incorporate moieties to specifically target bone, however Wang *et al.* (2017) also presents data where targeting with TRAP did not significantly improve fracture healing over the non-targeting/passively accumulating NP

control. Arguably for clinical translation upscaling the production of a polymeric vehicle with additional chemical conjugation adds complexity. Unmodified PMs present an alternative which have already shown upscaling success in the previously mentioned cancer therapy GenexolPM.

As mentioned previously, within our lab, research on nanoparticle delivery of a Wnt agonist to treat a bone fracture has previously been performed and published by Dr Edoardo Scarpa. Scarpa *et al*. (2018) has produced such a passive targeting PM for bone injury treatment, by encapsulating BIO within PEG-*b*-PCL PMs – one of two PMs treatments also selected for use in this thesis. Scarpa has so far assessed the effects of PM-encapsulated BIO (PM-BIO) on hBMSCs, and found a significant and sustained upregulation in Wnt signalling and osteogenic gene expression (Scarpa *et al.*, 2018). In addition, (Scarpa, 2016) has characterised the intracellular uptake and payload release of these PMs. In further work, Scarpa has also begun to investigate the effects of PM-BIO treatment on a mouse bone injury model, and found from µCT measurements comparable healing effects in both treatment and control groups (Scarpa, 2016). This work hence leaves open opportunities for further research, to ascertain what features, such as loading dose, may have limited any measurable therapeutic efficacy of PM-BIO. This thesis aims to further Scarpa's research, and additionally for the first time utilise the small molecule Wnt agonist CHIR in a PM delivery system as a potential fracture treatment, following evidence to suggest that CHIR may be beneficial as a less toxic alternative to BIO (Naujok *et al.*, 2014).

## 1.9 CONCLUSION

This review has surveyed the existing literature regarding the processes involved in bone fracture repair, and the factors and process changes that can result in delayed healing or the development of non-unions. Potential therapeutics have also been discussed, in addition to the advantages of using nanoparticles as a drug delivery mechanism to provide spatio-temporally controlled delivery, thereby improving their bioavailability and reducing off-target effects. This review also highlights that there is a limited quantity of research, especially *in vivo,* utilising the potential of NPs for controlled drug delivery for the treatment of bone injuries, which this thesis aims to contribute to.

# HYPOTHESIS AND AIMS

Overall, this PhD aimed to test the hypothesis that a polymersome (PM) drug delivery therapeutic can control and localise delivery of a Wnt agonist to a bone injury site, resulting in the promotion of bone repair signalling which could ultimately improve fracture healing outcomes.

To achieve this the experimental study was broken down into four overarching hypotheses and aims, presented in each chapter of this thesis as follows.

Chapter 3 tests the hypothesis that PMs can encapsulate small molecule Wnt agonists BIO and CHIR and deliver them *in vitro* to induce a Wnt signalling response. The study aimed to:

- Develop PEG-*b*-PCL PMs loaded with two types of Wnt signalling agonists using an established solvent displacement method and analyse encapsulation efficiency.
- Determine the biological activity, namely the induction of Wnt signalling and cytocompatibility, of Wnt signalling agonists BIO and CHIR *in vitro* and compare this to activity when delivered by polymersomes.

Chapter 4 tests the hypothesis that PMs will passively accumulate at a target bone injury site when systemically administered either immediately or with a delay post injury formation. The study aimed to:

- Localise and quantify polymersome payload uptake in a characterised mouse bone injury model following immediate and delayed systemic injection.

Chapter 4 also tests the hypothesis that depletion of macrophages will change PM uptake distribution *in vivo,* reducing liver accumulation and promoting accumulation to a target bone injury site. The study aimed to:

- Determine the effect of systemically depleting macrophages upon the uptake of polymersomes in a healthy and injured mouse model.

Chapter 5 tests the hypothesis that PM-encapsulated BIO can induce Wnt signalling activity and osteogenic differentiation *in vivo.* The study aimed to:

- Determine the biological activity of BIO loaded polymersomes *in vivo* by assessing expression of Wnt signalling target genes in tissues of high PM accumulation, within 48 hours post IV administration.
- Determine the biological activity of BIO loaded polymersomes within a mouse bone injury model.

# CHAPTER 2

# METHODS AND MATERIALS

## 2.1 POLYMERSOME PRODUCTION AND CHARACTERISATION

### 2.1.1 Producing PMs loaded with hydrophobic molecules (BIO, CHIR, DiR, DiI)

To produce polymersomes (PMs) encapsulating BIO or CHIR, first 6 mL of the polymer PEG-*b*-PCL was added to 360 µL dimethylformamide (DMF). BIO/CHIR was dissolved in DMF to a concentration of 10 mM, then 40 µL of this solution was added to the 360 µL Polymer-DMF solution resulting in 0.4 mL stock solution. To dissolve the polymer the solution underwent sonication for 15-20 minutes. For DiR or DiI loading, DiR/DiI was first dissolved in DMF to a concentration of 0.1 mg/mL (98.7 µM for DiR and 107.08 µM for DiI). 400 µL of this solution was then used to dissolve the polymer, as described for BIO. The dissolved stock solution was added drop wise into 1.6 mL of phosphate buffered saline (PBS) solution under constant stirring, using Aladdin syringe pump (World Precision Instruments, Sarasota, Florida) set to 1 drop every 8 seconds. This enables PM formation with BIO/CHIR/DiR associating with the shell region. The initial 2 mL PM solution was then dialysed in 300 mL excess PBS for 48 hours, with at least 2 changes of the excess PBS before use. A schematic of this method is presented in **Figure 2.1**.

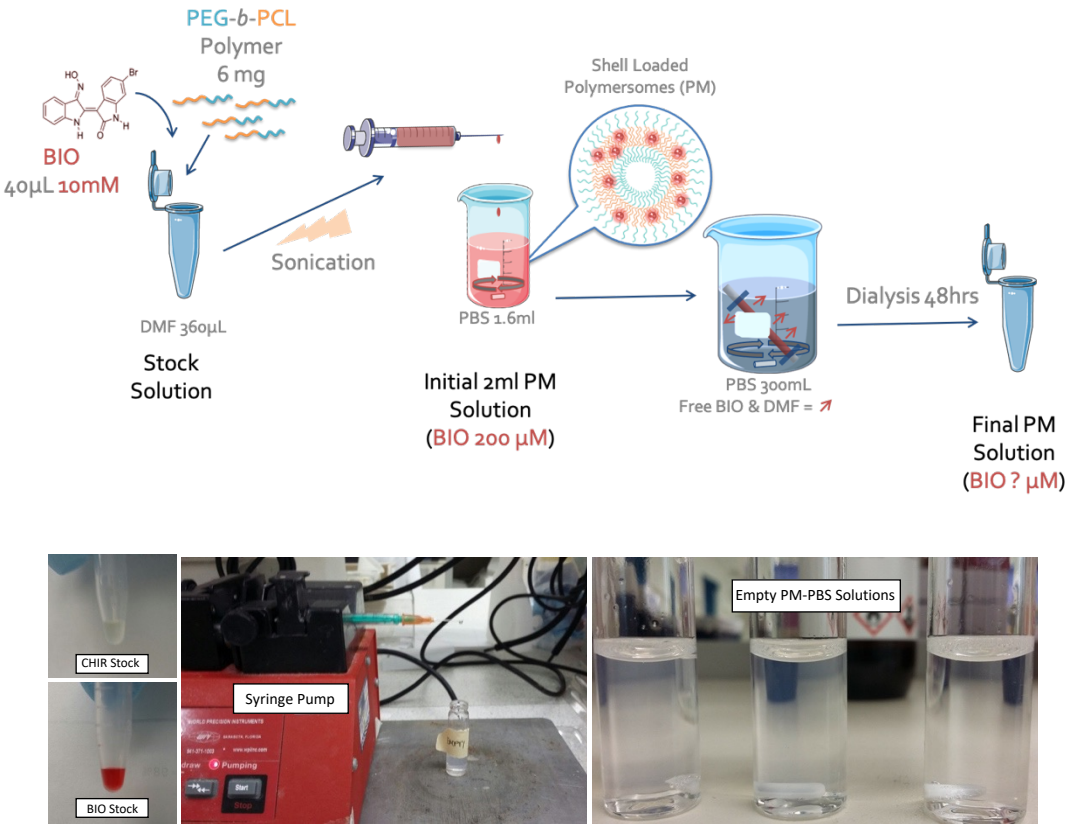


***Figure 2.1: Schematic of polyethylene glycol (5k)-polycaprolactone copolymer (18k) (PEG-b-PCL) polymersome (PM) synthesis, encapsulating example payload BIO***

*In each stage of production, BIO is represented in red. Final concentration of BIO post-dialysis determined later using absorbance spectroscopy. (Parts of this figure's graphics are credited to smart.servier.com)*

### 2.1.2 Measuring encapsulation efficiency

To quantify the amount of BIO/CHIR encapsulated in the produced PM solution, the absorbance of the solution was measured across 190-800 nm wavelengths using an ultraviolet visible light (UV-Vis) spectrophotometer (Nanodrop 200c; Thermo Fisher Scientific, UK). Standard curves were created for both BIO and CHIR from known concentration measurements produced by serial dilution in either PBS (for CHIR) or DMF (for BIO). 300 µL of solutions were measured three times in black-walled glass cuvettes following baseline correction with $dH_20$. PM solutions were diluted with PBS or DMF when necessary, to avoid saturation, and BIO/CHIR final concentrations were calculated using standard curve measurements and accounting for the dilution factor. Dilutant controls of PBS and DMF alone were also measured. The encapsulation efficiency (EE%) was calculated as indicated below:

$$EE\ (\%) = \frac{Concentration\ of\ reagent\ in\ PMs\ post\ dialysis.}{Total\ concentration\ of\ reagent\ added\ to\ PM\ prep.} \times 100\%$$

### 2.1.3 Size characterisation of PMs

To determine the size of produced PMs, PM solutions (post 48 hr dialysis) were diluted 1 in 10 in PBS and filtered through Millipore filter (0.22 µm) before measuring the hydrodynamic diameter and polydispersity by DLS (Zetasizer Nano ZS ZEN3600, or Zetasizer Ultra, Malvern, UK). 12 mm disposable plastic cuvettes were used and temperature set to 25.0°C. For measurements taken on the Zetasizer Nano, a detection angle of 173° was used and an automatic attenuator and cuvette measurement position was selected. Average measurements were taken from 3 technical repeats (repeat measurement of the same sample), each measurement consisted of 12 data collection runs with a 10 second acquisition time per run. For measurements taken on the Zetasizer Ultra, multi-angle dynamic light scattering (MADLS) with measurement angles at 173°, 13°, and 90° was selected, whilst the attenuator, cuvette position, and number of sub runs and duration was determined automatically by the machine algorithm. Average measurements were calculated from 3 sample repeats taken from a single batch of PMs. Measurements taken on same day as experimental use of PM batch or as close to this time as possible.

### 2.1.4 PM batch particle concentration assessment

To determine the concentration of particles in a produced batch of PMs, Nanoparticle tracking analysis (NTA), and multi-angle dynamic light scattering (MADLS) (Zetasizer Ultra, Malvern, UK) measurements were taken. For NTA analysis PM samples were diluted 1 in 10 in PBS and filtered through 0.22 µm Millipore filter before being sent to Malvern for analysis. Raw data was returned and analysed with dilution factors taken into account.

For measurements taken on Zetasizer Ultra, PM samples were diluted 1 in 10, filtered (0.22 µm), and MADLS with particle concentration analysis was selected. The run setting was determined automatically by the machine algorithm. Average measurements were calculated from 3 sample repeats taken from a single batch of PMs and dilution factor considered.

## 2.2 *IN VITRO* BIOLOGICAL ACTIVITY AND VIABILITY OF PM-ENCAPSULATED BIO/CHIR

### 2.2.1 *In vitro* Wnt activity luciferase assay

3T3 murine fibroblast Wnt reporter cell line cells were cultured in Dulbecco's modified eagle medium (DMEM) supplemented with 10% (v/v) fetal bovine serum (FBS) and 1% (v/v) penicillin-streptomycin (P/S) and stored in a humidified chamber set at 37°C and 5% $CO_2$. Cells were passaged every 2-3 days at 70-80% confluence, using 1% (v/v) trypsin in Dulbecco's phosphate-buffered saline (DPBS) solution. 48 hours prior to the assay reading, cells were seeded onto a white walled and clear base well plate at 15,000 cells/well (1.05 x $10^5$ cell/$cm^2$) in 50 µL DMEM supplemented with 5% (v/v) FBS, 0.5% (v/v) P/S and 25 mM HEPES (pH 7.3). 17 hours before the assay reading, 50 µL of the following prepared reagents were added to the wells in triplicate: free BIO and free CHIR diluted in plain DMEM (concentrations 0.5, 0.8, 1, 2, 5, 10, 20, 40 µM), and PM-BIO and PM-CHIR diluted in plain DMEM (dilutions 1/5, 1/10, 1/25, 1/50, 1/100). Plain DMEM and PMs loaded with PBS (PM-Empty) served as negative controls. Free BIO and CHIR served as positive controls. For the assay reading 100 µL of luciferase substrate and buffer (Neolite, PerkinElmer or Steady Glo, Promega) was added to the cells, and left at room temperature in the dark for 5 minutes. A luminescence reading was taken using GloMax Discover (Promega, UK) set to 1-second exposure. A schematic of this assay's mechanism is presented in **Figure 2.2**.

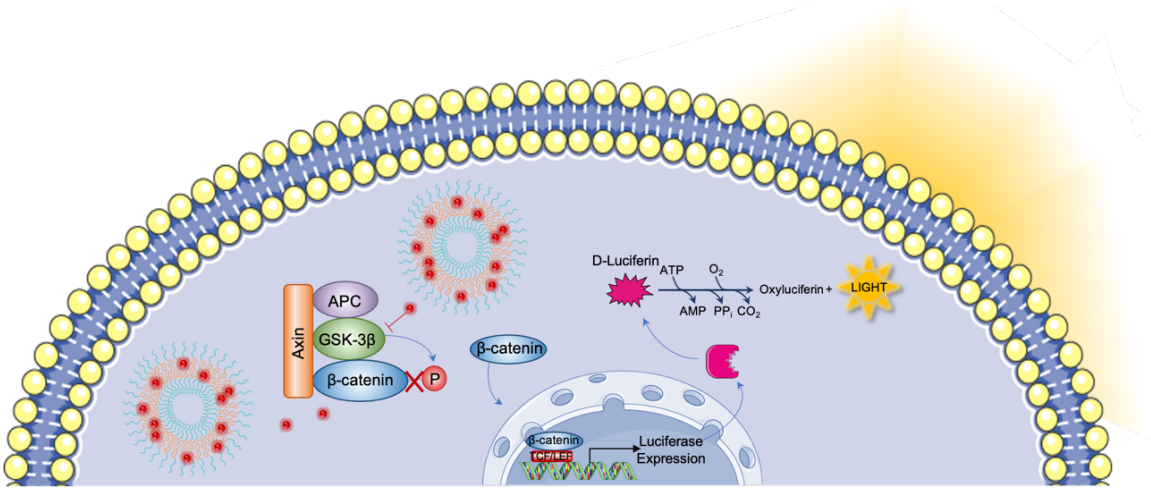


***Figure 2.2: Schematic of the intracellular activity for Wnt luciferase assay***

*PMs deliver BIO (Red dots) into a 3T3 cell. BIO indirectly activates Wnt signalling by competitively inhibiting the binding of ATP to GSK-3ß, stopping the phosphorylation (P) (signal for degradation) of ß-catenin. Subsequently ß-catenin levels increase, translocate to the nucleus, and bind to the TCF/LEF Wnt signalling promoter, enabling the transcription and translation of Wnt signalling gene targets. In 3T3 reporter cells the plasmid inserted luciferase gene (derived from the firefly) is expressed with TCF/LEF prompter activation. Upon the addition of D-luciferin substrate, the produced luciferase enzyme catalyses the oxidation of luciferin to produce light in a*

*dose-dependent manner. (Parts of this figure's graphics are credited to smart.servier.com)*

### 2.2.2 Pico green DNA quantification assay

Following the luminescence assay reading, cell lysate from each well was pipetted in triplicate into black walled 96 well plates and diluted 1 in 10 with Tris/EDTA (TE) buffer. An equal volume of 1 in 200 dilution Pico Green (Invitrogen LifeTech) was added to each well and left to incubate, at room temperature, in the dark for 5 minutes. Fluorescence measurements were taken using GloMax Discover set at 475 nm excitation and 500-550 nm emission filter. Double-stranded DNA concentration was calculated using standard curve measurements of prepared DNA concentrations diluted with TE buffer.

### 2.2.3 Isolation of human bone marrow stromal cells

Primary human bone marrow stromal cells (hBMSCs) were isolated from donated bone marrow samples collected during total hip replacement surgery of females aged 50 to 90 years, using the method established by Williams *et al.* (Williams, White and Oreffo, 2013) and illustrated in **Figure 2.3**. Tissue samples were collected from Southampton General Hospital or Spire Southampton Hospital with full patient consent and approval from Southampton and South West Hampshire Research Ethics Committee (Ref no.194/99/1 & 210/01). Using a laminar flow class 2 tissue culture hood and sterile techniques, the marrow sample, containing marrow, bone fragments and fat, was first washed by vigorous shaking with Eagle's minimum essential media alpha modification (α-MEM). Afterwards the α-MEM was aspirated off into a fresh universal tube. This wash process was repeated several times until the bone fragment appeared pale and free of blood, after which the aspirate was centrifuged at 250 × g and 4°C for 5 minutes to remove fat. The cell pellet was re-suspended in α-MEM and centrifuged two times more, before being re-suspended in 25 mL of α-MEM and this cell suspension was passed through a 70 µm cell strainer to remove bone fragments. The cell suspension was then slowly added on top of 20 mL of Lymphoprep (Stem Cell Technologies, UK) and centrifuged at 840 × g and 18°C for 40 minutes with a slow/break free de-acceleration to pellet red blood cells and granulocytes. A buffy layer above the Lymphoprep containing mononuclear cells was slowly aspirated to a fresh universal tube and washed by adding α-MEM and centrifuging at 250 × g for 5 minutes. This wash step was repeated twice before re-suspending the cell pellet in complete α-MEM (i.e. α-MEM supplemented with 10% (v/v) FBS and 1% (v/v) P/S). Finally, the cell suspension was counted using trypan-blue dye, plated into a T175cm$^2$ flask at a cell seeding density of 1 x 10$^4$ cell/cm$^2$ and incubated in a humidified chamber set at 37°C and 5% $CO_2$. The cells were left for 5 days to allow for adherence selection of bone marrow stromal cells, including unselected skeletal stem

cells, before replacing the media to wash away non-adherent cells. For passaging, the cells were lifted with 1 mL of 1x Trypsin/EDTA for 2 minutes at 37°C and re-plated at a seeding density of 2 x $10^3$ cells/$cm^2$ cultured up to passage 3 for experimental use with media changes every 2-3 days.

Previous published work within the lab has verified the cell phenotype and *in vitro* function of the bone marrow stromal cells isolated using this method (Oreffo and Triffitt, 1999; Tare *et al.*, 2012; Williams, White and Oreffo, 2013).

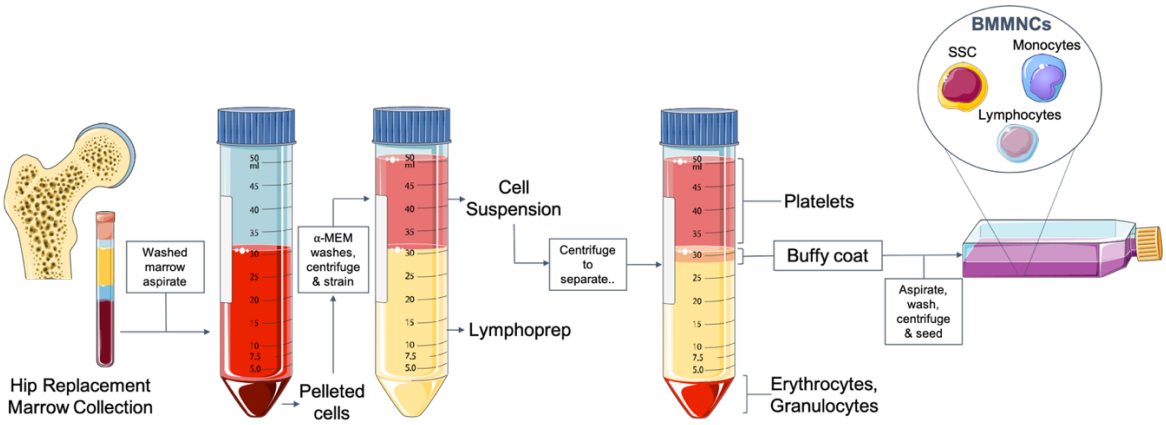


***Figure 2.3: Schematic of human bone marrow stromal cell (hBMSC, labelled BMMNCs) isolation from bone marrow sample.***

*(Parts of this figure's graphics are credited to smart.servier.com)*

### 2.2.4 Mouse bone marrow stromal cell isolation

Primary mouse bone marrow stromal cells (mBMSCs), including unselected skeletal stem cells, were isolated from 3-month-old MF1 mice culled by cervical dislocation, using the method previously established by Bakker and Klein-Nulend (2012). Under a class two laminar flow hood and using sterile conditions, mice cadavers were soaked in 70% (v/v) ethanol before their hind limbs were dissected and placed in DPBS. The femur and tibia were separated, and all connective muscle, ligaments, and tendons were cut away. The bones were then cleaned in fresh DPBS and any remaining soft tissue was gently scraped clear. Using micro dissecting scissors, the ends of the bones were cut off leaving the central diaphysis region. Using a 5 mL syringe and 25-gauge needle, the marrow cavity was reamed out and flushed with 1 mL of α-MEM, collected into an Eppendorf tube. This washing was repeated several times until the bone appeared pale. The cell suspension was then passed through a 70 µm cell strainer to remove any residual tissue or bone fragments, before centrifuging at 219 × g for 4 minutes. The cell pellet was then re-suspended in complete α-MEM (α-MEM + 10% (v/v) FBS + 1% (v/v) P/S) and seeded into a T25$cm^2$ flask and incubated in a humidified chamber set at 37°C and 5% $CO_2$ for 5 days to allow cell adherence. The cells were then passaged by washing twice with DPBS,

then digested with 1 mL of 1x Trypsin/EDTA for 2 minutes at 37°C, after which 5 mL complete α-MEM was added and the cell suspension was centrifuged at 310 × g for 4 minutes. After removing the supernatant, the cell pellet was re-suspended in complete α-MEM and seeded into a T75cm$^2$ flask. The cells were passaged every 3-4 days. After 3 passages a more select population of mBMSCs remained, suitable for experimental use.

### 2.2.5 Mouse osteoblast isolation

In the interest of reducing the number of mice used for study under NC3R guidance, the surplus long bone shafts flushed of bone marrow in the method above (**section 2.2.4**) were used to isolated mouse osteoblast cells, another cell type from a bone environment, for *in vitro* experimental use. The bone shafts were retained and placed in PBS for osteoblast processing. The bone diaphysis was cut into small pieces 1-2 mm in length and placed in a 15 mL falcon tube with 2 mL of PBS and washed by inversion and pipette trituration. PBS was collected carefully as to avoid collecting any bone fragments and discarded. This wash process was repeated 3 times. A 2 mg/mL collagenase II solution was made with complete α-MEM (α-MEM + 10% (v/v) FBS + 1% (v/v) P/S) as the dilutant and 3.5 mL was added to each tube with washed bone fragments. This digestion solution and bone fragments were then incubated in a humidified chamber set at 37°C and 5% $CO_2$, whilst on a shaker set to 200 rpm, for 2 hours. At 30-minute intervals samples were shaken by hand to ensure agitation. The digestion solution was then removed, and the bone fragments washed with PBS 3 times, before being placed in a T25cm$^2$ flask with 5 mL of complete α-MEM and incubated. After 14 days, with media changes every 2-3 days, substantial cell growth around bone fragments was observed. The cells were then passaged by washing twice with DPBS and incubating with 1 mL of 1x trypsin for 5 minutes at 37°C, after which 5 mL complete α-MEM was added and the cell suspension was centrifuged at 800 × g for 4 minutes. After removing the supernatant, the cell pellet was re-suspended in complete α-MEM and seeded into a T25cm$^2$ or T75cm$^2$ flask. Media was changed every 2-3 days and once cells reached sub confluency were passaged a maximum of 3 times before being used in testing or alamarBlue proliferation experiment.

### 2.2.6 alamarBlue cell viability assay

alamarBlue is an oxidation-reduction (REDOX) indicator, which both fluoresces and changes colour when resazurin is reduced to resorufin. Therefore, fluorescence intensity can be used as a readout of cell metabolic activity, where increasing fluorescence indicates reducing alamarBlue. alamarBlue fluorescence measurements are affected by both the number of cells and the length of the

incubation time, therefore optimised values of these two conditions for a cell type of interest, BMSCs, were identified by the following method. Isolated human and mouse BMSCs were seeded at a range of densities between 500 and 80,000 cells/well on a 96 well plate and incubated for 48 hours, after which alamarBlue was added and incubated at 37°C. Fluorescence measurements were then taken every hour for 8 hours.

Following optimization, hBMSCs or mBMSCs were seeded onto a black walled clear base 96 well plate at a seeding density of 20,000 cells/well for human and 5000 cells/well for mice, in 100 µL of complete α-MEM. Cells were incubated for 48 hours in a humidified chamber set at 37°C and 5% $CO_2$. After 48 hours the media was replaced with 100 µL of the following reagents, with 5 wells per condition: free BIO and free CHIR, each at increasing concentrations of 0.5, 0.8, 1, 2, 5, 10, 20, and 40 µM in plain α-MEM, and PM-BIO, PM-CHIR, and PM-Empty, at dilutions of 1/2, 1/5, 1/10, 1/25, 1/50, and 1/100 in plain α-MEM. Control wells received fresh media with no reagents added and a DMF control was also assessed at concentrations equivalent to those present in free BIO/CHIR dilutions from stock. Cells were incubated with reagents for 24 hours before replacing media with 110 µL of 1x alamarBlue reagent (Invitrogen, Thermo Fisher), made up in plain α-MEM. Cells were incubated in darkness for 4 hours. Reduced alamarBlue fluorescent signal was measured using GloMax Discover (Promega, UK), set to 520 nm excitation and 580-640 nm emission for 0.3 s integration time.

### 2.2.7 alamarBlue cell proliferation assay

Isolated mouse osteoblast cells (Section 2.2.5), a cell type likely to be exposed to the polymersome delivered Wnt agonist used in this thesis study, were seeded onto a black walled clear base 96 well plate, with 8 sets of 4 wells for each of the following seeding densities (in 100 mL of complete α-MEM): 100, 156, 312, 625, 1250, and 2500 cells/well. Cells were incubated for 24 hours in a humidified chamber set at 37°C and 5% $CO_2$, after which the media for each set of cell seeding densities was replaced with 100 µL of the following reagents: 2 µM free BIO, 10 µM free CHIR, PM-BIO (200 µM), PM-CHIR (1 mM), and PM-Empty (1 in 10 dilution). Control wells received fresh media with no reagents added and a DMF control was also assessed at concentrations equivalent to those present in free CHIR dilution from stock. In addition to a reagent or control media each solution had a 1 in10 dilution of alamarBlue added and were mixed before applying to cells. Cells were incubated in the dark and removed for alamarBlue fluorescence measurements at the following set time intervals: 1, 2, 3, 6, 7, and 8 days. alamarBlue fluorescence was measured using GloMax Discover (Promega, UK), set to 520 nm excitation and 580-640 nm emission for 0.3 s integration time.

### 2.2.8 Statistics

Statistical analysis was performed using GraphPad Prism software (GraphPad, USA, version 8.2). Where two groups are compared, a parametric unpaired t test was performed. Where three or more groups are compared a one-way ANOVA with a Dunnett multiple comparisons to the control test was performed. For all tests a Gaussian distribution is assumed, and statistical significance is defined as $\alpha = 0.05$. Numerical values are presented as the mean ± standard deviation unless otherwise stated.

## 2.3 LOCALISATION OF POLYMERSOMES *IN VIVO*

All surgical procedures, pre and post procedure care, and animal handling were performed in line with NC3R guidance and standards. MF1 mice (44 ± 8 g) were acclimatised to facilities for at least 1 week before experimental use. Mice received free access to irradiated RM1 (SDS) food and water and were housed in rooms with 12 hours light/dark cycle under controlled humidity of 45-65% and a temperature of 20-24°C.

For the *in vivo* experiments in this work, male or female mice were selected for each study as follows:

| Study | Number of mice used | Sex |
|---|---|---|
| Bone injury characterisation and liver toxicity assessment (Section 2.3.1) | N = 9 | Male |
| PM distribution in mice with and without a bone injury (Section 2.3.2) | N = 17 | Female |
| Assessing macrophage depletion (clodronate pre-treatment) upon PM distribution in mice with and without a bone injury (Section 2.3.3) | N = 10 | Male |
| Assessing *in vivo* Wnt signalling activity in mice with and without a bone injury (Section 2.4.2) | N = 22 | Female |

The selection of male vs female mice for each study was based in part due to breed availability at the scheduled start of the experiments, and consideration was made to limit the possible different hormonal cycles between subjects that could influence bone repair. However it is recognised that future study needs to include both sexes to evaluate any differences relating to sex. N numbers for each of these pilot studies were chosen according to available laboratory time and resource constraints (and with consideration of the NC3R principle of reducing experimental numbers). For this project a decision was made to gather some data for each experimental question. The data from these studies could in future be used in power calculations to ensure appropriate numbers of replicates are included for determining statistically significant results.

### 2.3.1 Mouse surgery for bone injury characterisation and liver toxicity assessment

Male MF1 mice aged 3 months underwent surgery to produce a femoral defect. Surgeries for this collaborative study were performed by Dr Edoardo Scarpa (Personal licence number I1211ECA0, under project licence 30/2880 and procedure 2).

To start mice were weighed and then administered 0.1 mL/10 mg (10 µL/g) of Hypnorm and Hypnovel (1:1 ratio) by intraperitoneal (IP) injection for general anaesthesia and pain relief. Once an anaesthetised state was confirmed the mice had their left leg and hip area shaved and sterilised before commencing surgery. Here, a 2 cm incision was made along the skin of the left lateral thigh, before blunt dissection was used to separate the muscle tissue and expose the diaphysis of the femur. Using a Dremel with a 1 mm drill bit, a bore-hole was created at the distal diaphysis region of the femur through the cortical wall, exposing the marrow beneath. The muscle was then realigned and the skin sutured.

Within 1 hour post-surgery, mice were treated with an IV injection of 100 µL PM-DiR and 100 µL PM-DiI (n=6) or received no injection (control, n=3) (IV injections were performed by technician Vikki English). N numbers for this initial pilot study were chosen according to available laboratory time and resource constraints. Following treatment, the mice were then separated into 3 groups, one for each study timepoint of 0, 7, and 10 days post-surgery, on which the mice were killed (via schedule 1 neck dislocation) for tissue collection. The tissue was then processed for histological assessment of bone injury repair over time, liver toxicity to PM treatment, and further study of PM accumulation in liver tissue and femurs (see **section 2.3.7**).

A schematic depicting this experimental plan is provided in **Figure 2.4**. Note this study was a joint investigation alongside Dr Edoardo Scarpa.

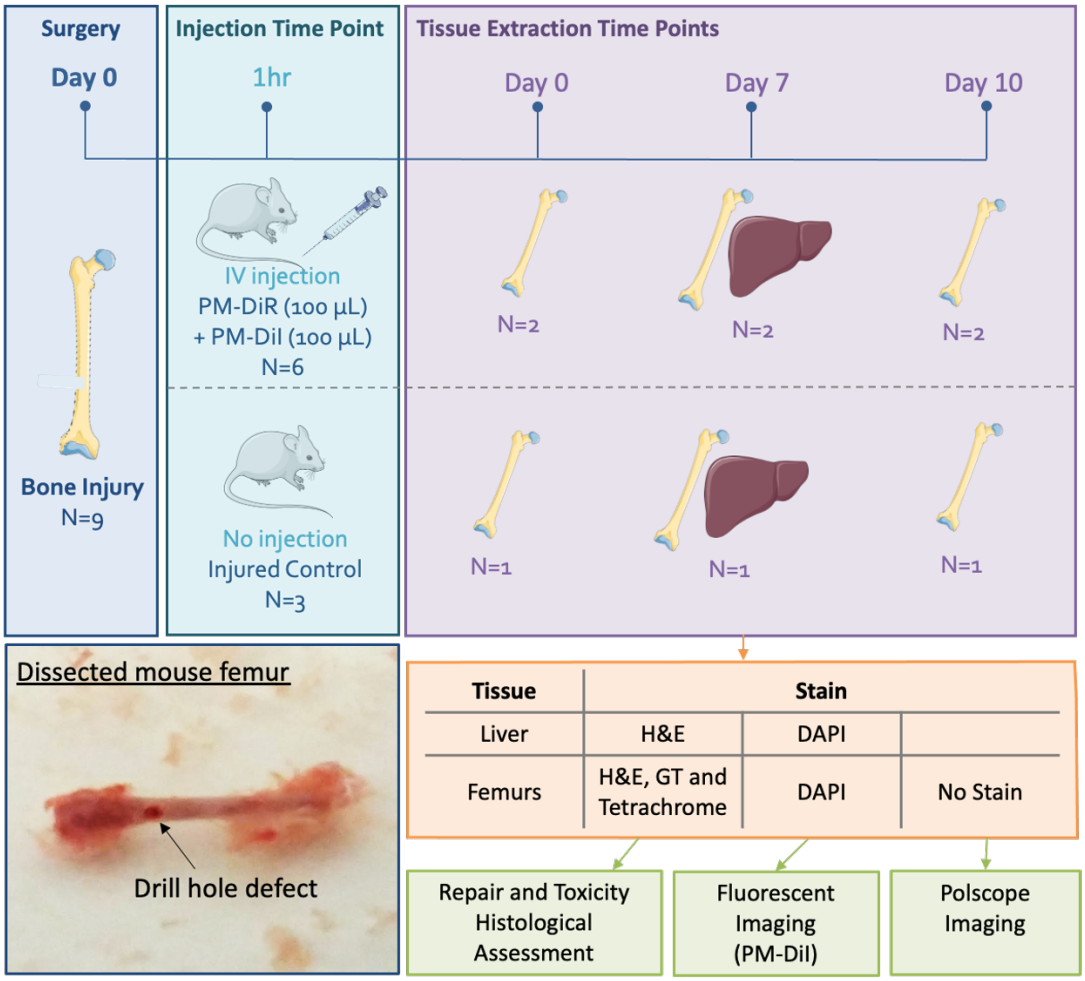


***Figure 2.4: Experimental plan for characterising bone injury repair and assessing PM-DiI accumulation within male MF1 mice injured femurs as well as liver accumulation and toxicity.***

*(Parts of this figure's graphics are credited to smart.servier.com)*

### 2.3.2 Mouse surgery for assessment of delayed PM treatment on PM localisation

For the study of PM distribution *in vivo* female MF1 mice aged 3-4 months were assigned by simple randomisation into two groups: (1) injured mice, which underwent surgery to produce a drill defect to the left femur as described in **section 0**, and (2) non-injured mice. For the mice that underwent surgery, two forms of anaesthesia were used between iterations of this study due to a review and change in the project licence protocol.

For the first round of study mice were administered 10 µL/g of Hypnorm and Hypnovel (1:1 ratio) by IP injection for general anaesthesia and pain relief (25G needle). Surgeries were performed by Dr Edoardo Scarpa (Personal licence number I1211ECA0, under project licence 30/2880 and procedure 2). In the second round of study mice were administered a pre- and post-surgery subcutaneous dose of analgesia Buprenorphine 0.015 mg/mL, totalling 3.4 µL/g and anaesthetised with isoflurane gas. A

follow up dose of 100 µl of Buprenorphine was given 24 hrs following surgery and administered as needed according to any pain indictors from the mice. Surgeries were performed by Alethia Hailes (Personal licence number (PIL) I86BD4DDE, under project licence P96B16FBD, protocol 2). Following surgery, injured mice were randomly allocated to two treatment groups. Group A was administered with a 200 µL IV injection of PM-DiR and PM-DiI (50:50 mix) 1-hour post-surgery (n=4). Group B was administered the same treatment only 7 days post-surgery (n=6). Controls in both groups received IV injection of PMs loaded with PBS (PM-Empty) 200 µL (n=2) (IV injections were performed by Vikki English and Alethia Hailes, using a 29G needle). 48 hours post-injection the mice were killed by neck dislocation, after which whole body, extracted tissue and organs were imaged using IVIS (see **section 2.3.5**) and the tissue processed for sectioning (see **section 2.3.7**).

The mice which did not undergo surgery were allocated to different control treatments (IV injections performed by Alethia Hailes):

- Non-injured control: mice received 200 µL IV injection of PM-DiR/DiI (n=2)
- Free/non-PM-loaded fluorescent dye control: mice received 100 µL IV injection of DiR-Lipid suspension (n=2) (see **section 2.3.3** for the DiR-Lipid production method).
- Naive control (blank reference to provide baseline for IVIS imaging): mice received no surgery and no injections (n=1)

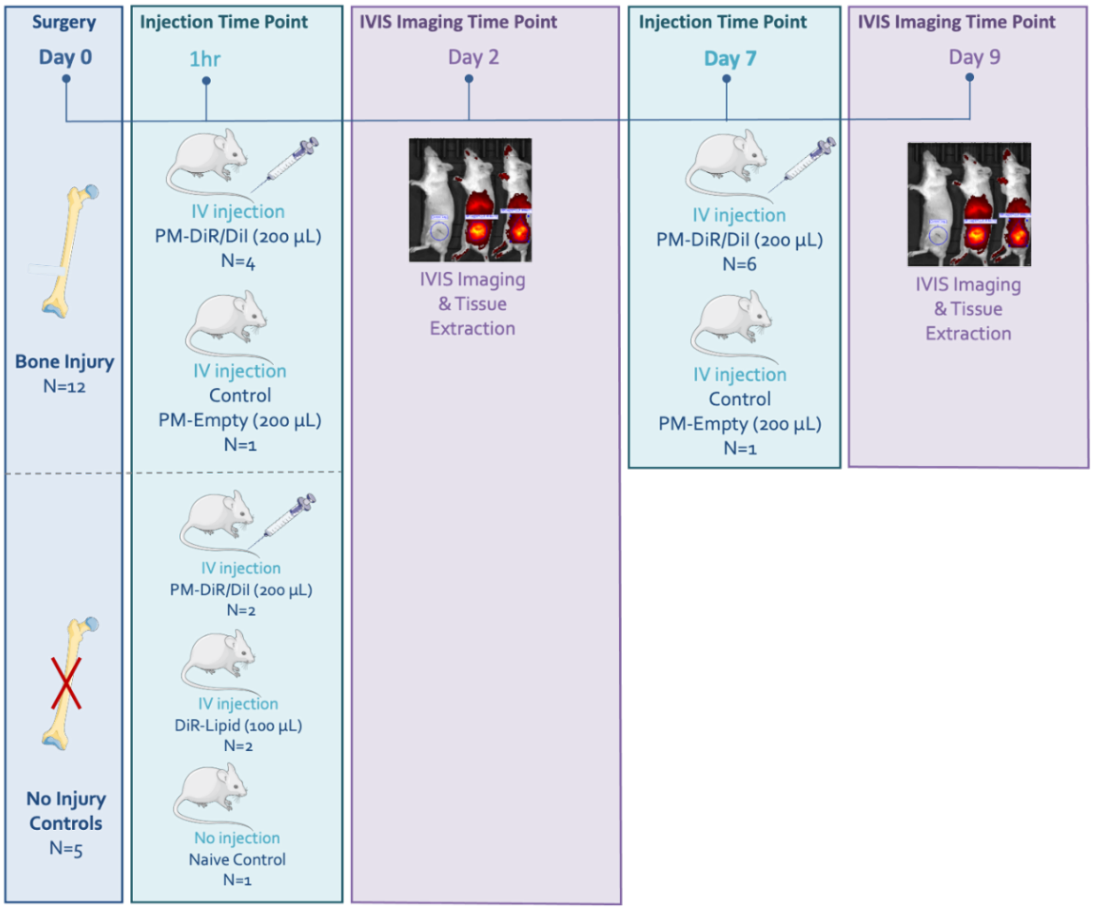


***Figure 2.5: Experimental timeline for assessment of in vivo PM localisation***

*At day 0 female MF1 mice receive bore-hole injury to left femur. PMs loaded with fluorescent dyes DiR and DiI are IV injected either 1 hour or 7 days following surgery. 48 hours following injection IVIS images are taken of whole body and extracted organs. (Parts of this figure's graphics are credited to smart.servier.com)*

### 2.3.3 DiR-Lipid production

The DiR-Lipid suspension was produced by Dr Jonathan May using the following method and kindly donated.

Stock solutions of DSPC (Avanti Polar Lipids, USA), PEG(40)stearate (Sigma/Merck) and DiR (Thermoscientific) in chloroform were mixed at a 9:1:0.05 molar ratio with a combined theoretical mass of 10 mg. Chloroform solvent was evaporated to leave a thin lipid film, which was then hydrated in PBS (2.5 mL) with stirring at 70°C for 30 min to create a lipid/dye suspension (final lipid concentration = 4 mg/mL; DiR concentration = 0.022 mg/mL). The hydrated suspension was sonicated with an immersion sonicator probe (120 W, Fisher Scientific) set to 40% amplitude for 2.5 minutes in order to dissolve any aggregates. This final solution was filtered through a 0.2 µm filter before experimental use.

### 2.3.4 Mouse surgery with macrophage depletion pre-treatment

For the study of PM distribution following pre-treatment to deplete macrophages, Male MF1 Mice aged 3 months were allocated by simple randomisation to blinded treatment and control groups. The treatment group received IV 250 µL of 5 mg/mL clodronate liposomes and control mice received a 250 µL IV injection of PBS liposomes. The treatment administration and data analysis was blinded by use of an independently-assigned code and ear clipping for mouse identification.

Due to unforeseen complications in surgery, four of the mice involved in this study could not undergo surgery to create a femoral defect. In the interest of NC3R principles as the mice had already received clodronate or PBS liposomes pre-treatment, a non-injured group was assigned. Additionally, of the mice with a bone injury, two subjects had to be discounted from analysis due to an error in PM dosing where one mouse received another's dose resulting in a double and absent signal at imaging. This resulted in the following n number set up.

48 hours following injection, mice within each treatment block were allocated randomly into two groups: non-injured (n=4) and injured (n=6). Injured mice underwent surgery to produce a drill defect to their left femur as described in **section 0**. Within 1 hour post-surgery mice were then treated with 200 µL of PM-DiR. Non-injured mice were treated with 200 µL of PM-DiR/DiI (PMs produced with 10x less DiR than those described in **section 2.1.1**). 48 hours following PM injection mice were killed by neck dislocation, after which whole body, extracted tissue and organs were imaged using IVIS (see **section 2.3.5**) Extracted livers and femurs were then processed for sectioning and Immunohistochemistry (IHC) assessment (see **section 2.3.9**). This experimental plan is depicted in **Figure 2.6**.

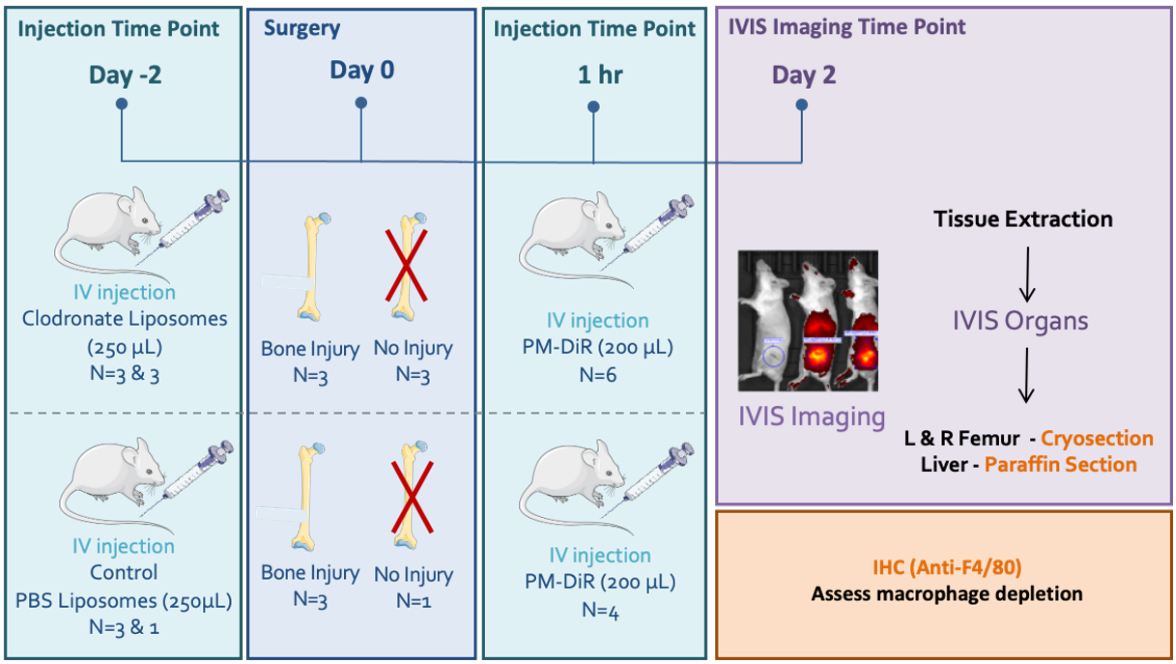


***Figure 2.6: Experimental plan for assessing the effect of macrophage depletion upon PM distribution in vivo for mice with and without a bone injury***

*(Parts of this figure's graphics are credited to smart.servier.com)*

### 2.3.5 IVIS imaging

For *in vivo* and *ex vivo* imaging of DiR loaded PMs, an IVIS Lumina Series III (Perkin Elmer, USA) was used. Whole body fluorescent images of mice, placed in dorsal, ventral, and lateral orientations, were taken 48 hours following PM IV injection. The mice then underwent dissection to isolate organs which were then imaged *ex vivo*. Images were acquired with scan parameter set to measure DiR epifluorescence with the following settings: Excitation filter = 740 nm, Emission filter = 790 nm, 1-2 second exposure time, field of view D, Binning factor 4-8, F/stop 2. Images with sufficient raw photon counts (close to or above 600) were then selected for analysis using Living Image Software (version 4.5, PerkinElmer, USA). Acquired images were corrected with adaptive fluorescent background subtraction. Measurement regions of interest (ROI) were selected by two methods: for whole body images and extracted bones a circle or square was drawn to enclose hot spots of fluorescent signal and duplicated for each subject to keep size consistent; for extracted tissues the threshold tool was used and set to outline the entire tissue. Fluorescence intensity was quantified by extracting ROI total radiant efficiency ([p/s] / [µW/cm$^2$]) and average radiant efficiency ([p/s/cm$^2$/sr] / [µW/cm$^2$]) measurements and subtracting the control subject's background signal (normalised to area for total radiant efficiency ROI). An example of this is pictured in **Figure 2.7**.

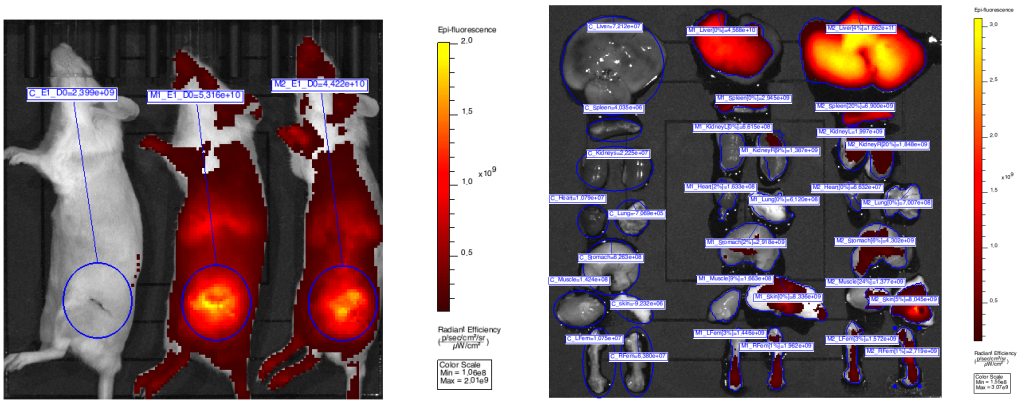

***Figure 2.7: Example region of interest (ROI) selection***

*Example IVIS images of mice whole body and extracted tissue, showing placement of ROI circle shapes for the extraction of total and average radiant efficiency measurements in whole body images (left) and threshold ROI outline method for extracted tissues (right). Coloured heat scale represents intensity of fluorescence from IV injected DiR loaded polymersomes. Yellow = high and Red = low fluorescent intensity measured as radiant efficiency ([p/s/cm²/sr] / [µW/cm²]).*

### 2.3.6 Statistics

Statistical analysis was performed using GraphPad Prism software (GraphPad, USA, version 8.2). Where two groups are compared, a parametric unpaired t test was performed, and where the comparison was within the same subject, a paired t-test was performed. Where three or more groups are compared a one-way ANOVA matched (for organs within one mouse subject) with a Tukey's multiple comparisons test was performed. Where two factors are compared – e.g. bone treatment and contralateral comparison – a matched two-way ANOVA with a Sidak's multiple comparisons test was performed. For all tests, a Gaussian distribution is assumed, and statistical significance is defined as $\alpha = 0.05$. Numerical values are presented as the mean ± standard deviation unless otherwise stated.

### 2.3.7 Tissue processing

Extracted tissue samples were washed in PBS and fixed by immersion in 0.4% (v/v) paraformaldehyde (PFA), after which, bone samples only were decalcified by immersion in 5% (w/v) EDTA-Tris and kept on a tube roller for 10-14 days (with 1 change of solution), and then processed for embedding in either paraffin wax or optimal cutting temperature compound (OCT) to be frozen.

Tissue set to be paraffin embedded was dehydrated through a series of Ethanol solutions (EtOH) in $dH_2O$ (% v/v): 50%, 90%, 100%, and 100%, followed by 50:50 mix of 100% EtOH and Histo-Clear, and then 100% Histo-Clear twice, each for 1 hour, kept on tube roller at room temperature (RT). Samples were then incubated in molten paraffin wax for 1 hour before finally embedding into blocks for

sectioning. Paraffin embedded samples were sectioned using a HM355-S microtome (Microm International GmbH, Germany) to a 7 µm thickness, placed onto pre-warmed charged glass slides and then left to dry in a warming chamber set to 37°C for 4 hours before storing at room temperature/4°C.

Tissues set to be cryo-embedded, following fixation were further processed by cryoprotecting in 30% (w/v) sucrose in $dH_2O$ solution, left at 4°C until the tissue sunk, before then cryo-embedding. Tissue samples were washed in PBS and covered in OCT before being placed into a cryomold and completely covered in OCT. The cryomold was then placed onto a cooling bath of Propan-2-ol and dry ice. Once frozen the blocks were stored at -80°C for later sectioning.

Cryo-embedded tissues were sectioned using a Microm H500 cryostat (Thermo Fisher, UK). The temperature was set between -27°C and -24°C, subject to room conditions and the tissue type. 7 µm sections were collected onto charged glass slides and left to air-dry for 15 minutes before storing at -40°C.

When sectioning, femur samples were cut along the coronal plane, whilst liver samples were cut along the sagittal plane (**Figure 2.8**).

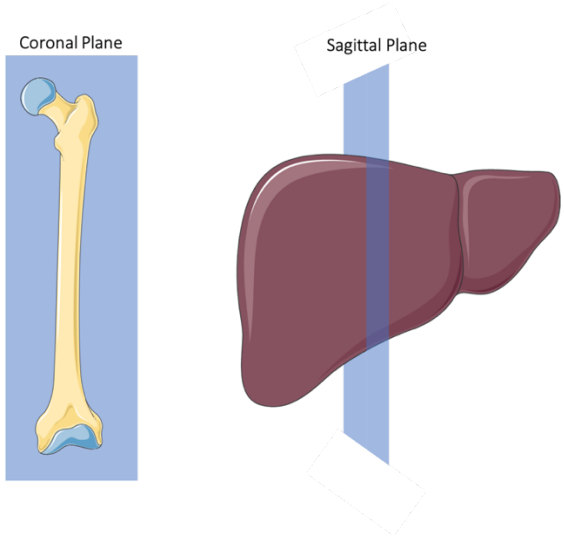


***Figure 2.8: Sectioning orientation of tissue samples***

*Left image of femur shows sectioning orientation in blue at coronal plane. Right image of liver shows sectioning orientation in blue at sagittal plane. (Parts of this figure's graphics are credited to smart.servier.com)*

### 2.3.8 Histology

#### 2.3.8.1 DAPI staining and fluorescent imaging

Cryosectioned bone and liver samples selected for fluorescent imaging were first washed in phosphate-buffered saline (PBS) for ten minutes. After which, for nuclear staining, sections were coated with a 1:100 diluted DAPI solution and incubated at room temperature in the dark for five minutes. Slides were then mounted using Hydro-mount and coverslipped before imaging. Images were taken using a Nikon fluorescence microscope set to detect DAPI (λex 340 nm, λem 488 nm) and DiI (λex 549 nm, λem 565 nm).

#### 2.3.8.2 Hematoxylin & Eosin (H&E)

Selected bone and liver paraffin sections were first de-waxed and rehydrated through a series of Histo-Clear and ethanol washes, before staining with Wiegert's hematoxylin solution, differentiating in 1% (v/v) acid alcohol, and then staining with eosin solution. Sections were then dehydrated through a series of EtOH and Histo-clear before mounting in DPX and applying a glass coverslip ready for imaging. For full protocol details and recipes see **section S.1.3.**

#### 2.3.8.3 Goldner's Trichrome (GT)

Selected bone sections were first de-waxed and rehydrated through a series of Histo-Clear and ethanol washes, after which sections were stained with hematoxylin and differentiated in 1% (v/v) acid alcohol. The sections were then immersed in a series of stains with washes in 1% (v/v) acetic acid between each of the following stains: Ponceau-fuchsin-azophloxin solution, Phosphomolybdic acid/orange G solution, and light green solution. After final washes in 1% (v/v) acetic acid, sections were rinsed in distilled water, mounted in DPX, and coverslipped ready for imaging. For full protocol details and recipes see **section S.1.3.**

#### 2.3.8.4 Tetrachrome

Selected bone sections were stained using the modified Tetrachrome method (Ralis and Watkins, 1992). In brief, sections were de-waxed and rehydrated through a series of Histo-Clear and ethanol washes, then stained with hematoxylin and differentiated in 1% (v/v) acid alcohol. The sections were then immersed in 90% (v/v) EtOH before staining with the following: 1% (w/v) Phosphotungstic acid solution, 0.1% (v/v) aniline blue solution, Picro-orange, and Ponceau mixture. Between each stain, sections were washed in distilled water. Finally, sections were dehydrated through a series of EtOH

and Histo-Clear before mounting in DPX and applying a glass coverslip ready for imaging. For full protocol details and recipes see **section S.1.3.**

### 2.3.9 Immunohistochemistry

To identify macrophage cell populations within liver and bone sections, immunohistochemistry was performed using rat anti-mouse F4/80 monoclonal antibody (Invitrogen). Unless otherwise stated all steps were performed at room temperature. Briefly, selected paraffin sections were dewaxed and rehydrated through a series of Xylene and ethanols. Sections were coated with 1% (v/v) $H_2O_2$ in Methanol for 15 minutes to quench endogenous peroxidase activity. Antigen retrieval was performed by submerging section slides in 10 mM sodium citrate buffer, heating in the microwave for 2 minutes and then leaving to cool for 5 minutes before submerging in tap water for 5 minutes to finish cooling. After washing slides in PBS (0.05% (v/v) tween) 2 times, sections were blocked for 45 minutes with 5% (v/v) Normal Rabbit Serum to minimise non-specific binding of antibodies. The sections were then incubated overnight at 4°C with anti-F4/80 primary antibody diluted 1:50 with PBS. Negative control sections were coated in PBS only. After washing 2 times in PBS (0.05% (v/v) tween), sections were incubated for 1 hour with a biotinylated rabbit anti-rat IgG secondary antibody (Vector Laboratories) diluted 1:200 with PBS, to bind and detect the primary antibodies. After washing twice in PBS, sections were incubated for 30 minutes with avidin/biotin complex (Vectastain®, ABC Kit) solution. The immune complexes were visualised by submerging slides in diaminobenzidine (DAB) substrate. After rinsing in PBS to stop reactions, the sections were counter stained with hematoxylin, differentiated in water, and finally dehydrated through ethanols and Xylene before mounting glass coverslips with DPX ready for imaging.

### 2.3.10 Polscope imaging

Slides of paraffin processed femur sections were selected for polarised microscopy imaging from each time point, 0, 7, and 10 days post-injury. Sections were de-waxed and rehydrated using a series of Histo-Clear and graded ethanol washes (Histo-Clear x2 for 7 minutes, 100% (v/v) EtOH x2, 90% (v/v) EtOH, 50% (v/v) EtOH, all for 2 minutes). After then washing in distilled water for 5 minutes, the unstained slides were then mounted with Hydro-mount and coverslipped before imaging.

To detect collagen organisation, sections were imaged using a Nikon TiE microscope equipped with OpenPolscope hardware and software (www.openpolscope.org). Multiple Z-stack images were taken, using 10X magnification (Nikon objective MUE12100), spanning a defect area. To ensure

subsequent analysis of equivalent locations, an ROI grid system utilising a slight overlap was followed, until clear marrow was observed.

The microscope was set up by Dr Edward Rogers. The setup included a pair of liquid crystal retarders before the sample, able to produce any polarisation state of light, and a circular polariser after the sample to select left circular polarised light (CPL). The sample is illuminated with 4 different circular and elliptical polarisation (EPL) states and a greyscale image is captured in each state. The differences between these images allow calculation of the magnitude and orientation of the sample birefringence at each camera pixel. Unlike a conventional polarised microscope, this arrangement enables detection and presentation of retardance from a birefringent specimen regardless of which way it is oriented without the need for rotating the specimen by hand. The resulting images display the birefringence signal as a range of pixel intensities, which in greyscale images can be extracted as quantitative values. For an 8-bit image this range is from 0 to 255, where black pixels (with an intensity of 0) correspond to 0 nm retardance, while white pixels (with a value of 255) represent maximum retardance. Pixel intensity is affected by uniformity of illumination across the field of view therefore background correction was performed. The maximum retardance ceiling was set at 50 nm.

The polscope software also calculates the orientation of the slow axis for each pixel and displays them as a spectrum of colour. This angle corresponds to the detected structural orientation of the imaged sample. Imaged pixel values or displayed colour representing slow axis orientation is dependent upon the orientation of the sample with respect to the horizontal axis of the polscope image obtained.

## 2.4 *IN VIVO* BIOLOGICAL ACTIVITY OF PM-ENCAPSULATED BIO/CHIR

### 2.4.1 Cell culture

Frozen primary mouse embryonic fibroblasts (passage no. 1, kindly donated by Kate Parry) were defrosted and grown with complete α-MEM in a humidified incubator set at 37°C and 5% $CO_2$. Once confluent, the fibroblasts were seeded onto 2x 6 well plate at 450,000 cells/well, and after 24 hours of incubation the media was replaced with 2 mL of complete α-MEM supplemented with 5 µM of BIO. Control wells received complete α-MEM only. At 6-, 12-, and 24-hours following incubation with BIO, the media was removed from two wells; the cells were then washed twice with DPBS, lysed with 350 µL of lysis buffer RLY (Bioline, UK), and the resultant cell lysis was stored at -80°C for later RNA extraction. Control wells were lysed at the 24-hour timepoint. RNA isolation and reverse transcription was performed following the protocols described in **sections 2.4.3** and **2.4.4** with the exception that 500 ng of total RNA was used to produce cDNA for reverse transcription quantitative real-time PCR (RT-qPCR). Mouse fibroblasts were used in this study due to being a primary cell source related to the chosen *in vivo* subject of later related study available within the lab at the time.

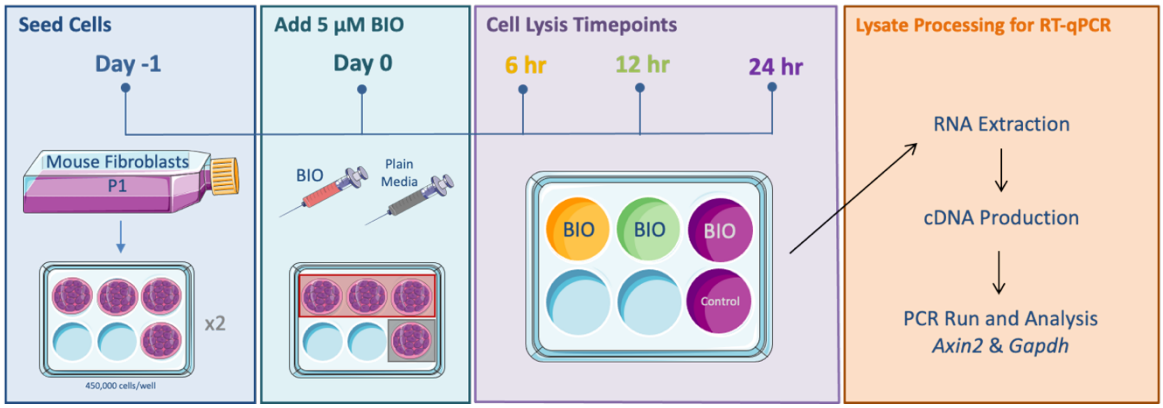


***Figure 2.9: Experiment plan for identifying BIO-induced Wnt signalling source for primer efficiency testing***

*(Parts of this figure's graphics are credited to smart.servier.com)*

This method was also applied to primary mouse bone marrow cells incubated with 5 µM of CHIR. Primary mouse bone marrow cells were extracted as described in **section 2.2.4.** Cells at passage no. 3 were seeded onto a 6 well plate at 120,000 cells/well. The same protocol was followed as above with the addition of a 48-hour time point and the exception that 48 ng of total RNA was used to produce cDNA for RT-qPCR, due to available extracted RNA yield.

### 2.4.2 Mouse surgery and tissue collection

22 female MF1 mice, aged 3 months, were separated into two groups: injured (n=6) and non-injured (n=16). Mice in the injured group underwent surgery to produce a femoral defect, as described in **section 0**. Prior to surgery, mice received ~10 µL/g of Hypnorm and Hypnovel (1:1 ratio) by IP injection for general anaesthesia and pain relief. Following surgery, the mice were administered 200 µL of PM-BIO (n=4) via IV tail vein injection. Control mice (n=2) received 200 µL of vehicle control PMs loaded with PBS (PM-Empty). 48 hours post-injection the mice were culled by neck dislocation and their liver tissue, left and right femurs were dissected. The 16 mice in the non-injured group were separated in two groups: 24-hour extraction (n=8) and 48-hour extraction (n=8). The mice within both groups received a 200 µL IV tail vein injection of either PM-BIO (n=4) or PM-Empty (n=4). At the allocated extraction time the mice were culled by neck dislocation and their liver tissue, left and right femurs were dissected. All regulated procedures were performed under the personal licence I86BD4DDE and project licence P96B16FBD protocol 1. All extracted liver tissues were immediately snap-frozen in liquid nitrogen. Extracted femurs were washed in DPBS and cleaned of residual tissue. Both ends of the femur were cut away leaving the diaphysis region, and then the bone marrow was flushed with 1 mL of DPBS and reamed out using a syringe and 23-gauge needle, until the bone appeared pale. The bone fragments were then flash-frozen in liquid nitrogen, and the flushed bone marrow was pelleted by centrifuging at 10,000 × g for 3 minutes; after removing the supernatant, the pellet was then flash-frozen in liquid nitrogen. All frozen tissue samples were stored at -80°C for later RNA isolation. This procedure is depicted in **Figure 2.10**.

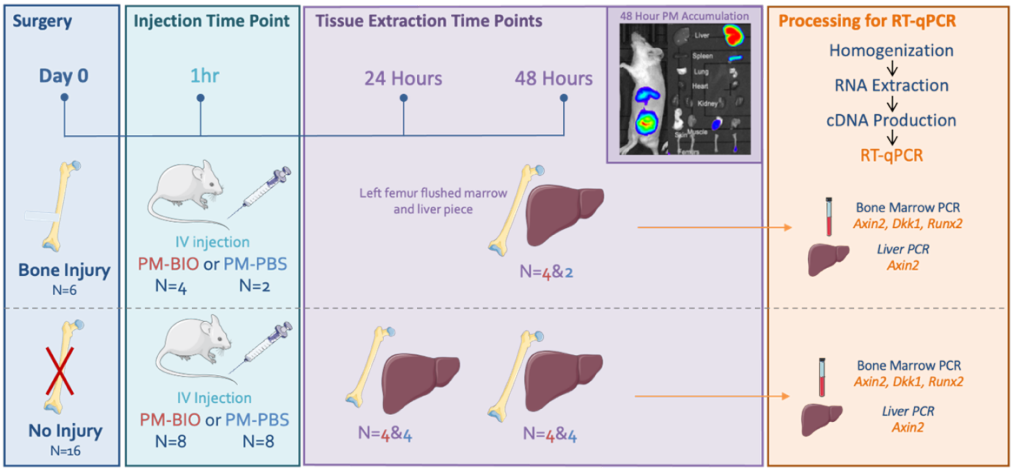


***Figure 2.10: Experimental plan for RT-qPCR analysis of polymersome-encapsulated BIO (PM-BIO) treatment 24- and 48-hours following administration to mice with and without a bone injury***

*PM-BIO subjects highlighted in red. Control PM-Empty/PBS subjects highlighted in blue. Genes selected for investigation are Wnt signalling inhibitors Axin2 and Dkk1 produced upon activation of the Wnt signalling pathway and Runx2 activated during osteogenesis. (Parts of this figure's graphics are credited to smart.servier.com)*

### 2.4.3 RNA isolation

Total RNA was isolated from 20-30 mg of liver tissue and one third of the flushed bone marrow. Snap-frozen liver samples were homogenised and lysed with a rotor-stator homogeniser in the presence of 600 µL of lysis buffer RLY (Bioline, UK). Guanidinium thiocyanate, a chaotropic salt present in the lysis buffer, enables deactivation of endogenous RNases. RNA was then isolated using ISOLATE II RNA mini kit (Bioline, UK), according to the manufacturer's instructions. The lysate was then processed through a series of spin columns as follows. Firstly, the lysate was filtered by placement on a filter membrane and spinning at 11,000 × g for 1 minute; the lysate was then diluted with an equal volume (600 µL) of 70% (v/v) ethanol, before spinning at 11,000 × g for 1 minute through a silica membrane to collect RNA. 350 µL of a membrane desalting buffer, MEM (Bioline, UK), was added and spun at 11,000 × g for 1 minute. 95 µL of a pre-prepared DNA digestion reaction mixture, i.e. DNase I and reaction buffer, was then added to the membrane and incubated at room temperature for 15 minutes. The membrane was then washed and dried in a series of spins with two wash buffers to remove any impurities (such as salts, metabolites, and cellular components). More specifically, firstly 200 µL of wash buffer RW1, followed by 600 µL of wash buffer RW2, both of which were spun at 10,000 × g for 30 seconds, then 250 µL of wash buffer RW2 was spun at 10,000 × g for 2 minutes. The purified RNA was collected in 60 µL of RNase-free water spun at 10,000 × g for 1 minute. Isolated RNA was quantified and assessed for purity using a NanoDrop spectrophotometer (Thermo Scientific). Absorbance ratio measurements at 260/280 nm and 260/230 nm of ~2.0 were considered pure for RNA and suitable for subsequent reverse transcription. NanoDrop measurement details are listed in supplementary material **section S.2**.

Snap-frozen bone marrow pellets were homogenised in the presence of 1050 µL of lysis buffer, 350 µL of which was then processed using the same protocol as previously described. Remaining lysate was stored at -80°C.

### 2.4.4 RNA reverse transcription

320 ng of total RNA from liver and bone marrow samples was used to produce cDNA, using TaqMan reverse transcription reagents (Invitrogen, Thermo Fisher Scientific). A master mix was produced comprising the following reagents: 2 µL of 10x RT buffer, 4.4 µL of 25 mM $MgCl_2$, 4.0 µL of 10 mM dNTP mix, 1.0 µL of 50 µM random hexamers, 0.4 µL of RNase inhibitor, and 0.5 µL of MultiScribe RT. The master mix was combined with the RNA sample and RNase-free water (if required) to give a total reaction volume of 20 µL. The reaction mixture was then run on a PCR thermal cycler (Veriti, Applied

Biosystems, US) using the following thermal cycle parameters: 25°C for 10 minutes, 37°C for 30 minutes, and 95°C for 5 minutes. cDNA samples were stored at -20°C for later RT-qPCR.

### 2.4.5 Primer design

Wnt target gene primers were designed using Primer3 online software (http://primer3.ut.ee). The known mRNA sequence of target genes was entered into Primer3, and the following primer criteria were specified: amplification product size of 60-150 bp, maximum Tm difference between the forward and reverse primers of 2°C, optimal Tm of 60°C, and GC% between 30% and 70%. Primer designs were selected according to the following criteria: firstly, if they specifically amplified the target gene, as verified by searching the primer sequences on the BLAST database (https://goo.gl/1PTGSR); secondly, if no secondary amplification products (e.g. primer dimers) were expected to form, as checked using Thermo Fisher Scientific's primer analyser (https://goo.gl/sU5jtg); finally, where possible, if the forward or reverse primer sequences spanned an exon junction. A list of the primers selected for use and their corresponding sequence information is shown in **Table 2.1**.

***Table 2.1: Designed primer sequence details***

| **Gene**<br>mRNA name | **ID** | **Sequence** | **Tm (°C)** | **Product Length** |
|---|---|---|---|---|
| *Axin2*<br>Mus musculus axin 2 | NM_015732.4 | F – 5'gatgtctggcagtggatgttaga3'<br>R – 3'tgggtagctctttcttatgctttg5' | 65.8<br>64.3 | 84 bp |
| *Dkk1*<br>Mus musculus dickkopf 1 | NM_010051.3 | F – 5'cacagccattttcctcg3'<br>R – 3'cggagccttcttgtcctt5' | 60.4<br>62.0 | 145 bp |
| *Runx2*<br>Mus musculus runt related transcription factor 2, transcript variant 4 | NM_001271627.1 | F – 5'agaaggcacagacagaagc3'<br>R – 3'aggacttggtgcagagttc5' | 59.8<br>59.5 | 147 bp |
| *Osterix/Sp7*<br>Transcription variant 1 | NM_130458.4 | F – 5'caaatgatagtggagaccttgc3'<br>R – 3' gacacccacagaaactctaaaaga5' | 62.4<br>62.3 | 112 bp |
| *Wnt2a*<br>Mus musculus wingless-type MMTV integration site family, member 2 | NM_023653.5 | F – 5'cttgaaacaagaatgcaagtgt3'<br>R – 3'ccattgtacttcctccagag5' | 59.4<br>58.7 | 118 bp |
| *Reference/Housekeeping Genes* | | | | |
| *Gapdh*<br>Mus musculus glyceraldehyde-3-phosphate dehydrogenase. transcript variant 2 | NM_008084.3 | F – 5'tggagtctactggtgtcttca3'<br>R – 3'gagttgtcatatttctcgtggt5' | 59.9<br>59.5 | 144 bp |
| *Tbp*<br>Mus musculus TATA box binding protein | NM_013684.3 | F – 5'cttgtacccttcaccaatgac3'<br>R – 3'acagccaagattcacggtag5' | 61.3<br>62.2 | 119 bp |
| *Eif3f*<br>Mus musculus eukaryotic translation initiation factor 3, subunit F | NM_025344.2 | F – 5'caggatgctctaagcactgtatt3'<br>R – 3'ggtctcaaagtcatcaggaacta5' | 61.7<br>61.5 | 138 bp |

| | | | | |
|---|---|---|---|---|
| *ß$_2$M*<br>Mus musculus beta-2 microglobulin | NM_009735.3 | F – 5'atggctcgctcggtgac3'<br>R – 3'cagttcagtatgttcggcttcc5' | 65.9<br>65.0 | 135 bp |
| *Polr2a*<br>Mus musculus polymerase (RNA) II polypeptide A | NM_001291068.1 | F – 5'agtgggtgaatgtgtactatgag3'<br>R – 3'aaaacctgcattgattttctc5' | 60.0<br>60.1 | 146 bp |

### 2.4.6 Primer efficiency testing

RT-qPCR was performed and analysed according to protocol details given in **section 2.4.7** with the cDNA samples from mouse embryonic fibroblasts incubated with BIO (**section 2.4.1**) – each time point along with the control sample. Primers for *Axin2* (a Wnt signalling gene target) and *Gapdh* (a reference gene) were used. The 6-hour sample presented the highest expression value above the control and was therefore selected as the positive sample for primer efficiency testing. These results are shown in **section 5.3.2**.

A 1 in 5 serial dilution of 6-hour mouse fibroblast cDNA was made with RNase-free water. Diluted cDNA samples were run on qPCR with designed primer pairs following the protocol detailed in **section 2.4.7**. Primer efficiency $E$ was calculated by creating a standard curve of the log cDNA dilutions against the cycle number ($C_T$) values at a threshold of 0.2, and then using the slope of this curve (calculated via linear regression) with the following equation (Pfaffl, 2001):

$$E(\%) = (10^{\left(\frac{-1}{slope}\right)} - 1) \times 100$$

### 2.4.7 RT-qPCR

Prepared cDNA (320 ng/µL of reverse transcribed RNA) samples were combined with a master mix of the following reagents: 5 µL RNase-free water, 2 µL forward primer with an end concentration of 1 µM, 2 µL reverse primer with an end concentration of 1 µM, and 10 µL of GoTaq polymerase (Promega, UK). This was used to produce a 20 µL reaction mixture comprised of master mix and cDNA at a ratio of 19:1. Negative control reaction mixtures were prepared with 19 µL master mix and 1µL RNase-free water. The reaction mixtures were plated in triplicate and run using the 7500 Real Time PCR detecting system (Applied Biosystems, USA). The following thermal cycle conditions were used: denature step, set at 95°C for 10 minutes, followed by amplification and quantification step, repeated for 40 cycles, set at 95°C for 15 seconds and 60°C for 1 minute. A subsequent melt curve cycle was also set at 95°C to 60°C. For analysis, $C_T$ values were selected from a fluorescence threshold value of 0.2 (which lies within the exponential phase and above background fluorescence levels). Relative gene expression $R$ was calculated using the following equation (Pfaffl, 2001):

$$R = \frac{(E_{target})^{\Delta C_{T_{target}}(control-sample)}}{(E_{reference})^{\Delta C_{T_{reference}}(control-sample)}}$$

### 2.4.8 Gel electrophoresis

RT-qPCR primer amplification products were run on a 2% (w/v) agarose gel produced from 2 mg of agarose (Sigma, USA) in 100 µL 1x TE buffer, plus 10 µL GelRed nucleic acid stain (Biotium). 10 µL of the qPCR product was mixed with 2 µL of 6x blue/orange loading dye (Promega), before 10 µL was loaded onto the gel along with 10 µL of exACTGene 50 bp mini-DNA ladder (Fisher Scientific) to verify the size of the amplification product. The gel was run at 110 V for 2 hours and then imaged with an InGenius transilluminator (Syngene, UK), with a 0.2 second exposure.

### 2.4.9 Statistics

Statistical analysis was performed using GraphPad Prism software (GraphPad, USA). Where two groups are compared, a parametric unpaired t test was performed. Where three or more groups are compared, a one-way ANOVA with a Dunnett's multiple comparison to control test was performed. Statistical significance was assessed via unpaired t-test with Welch correction compared against controls. For all tests, a Gaussian distribution is assumed, and statistical significance is defined as $\alpha = 0.05$. Numerical values are presented as the mean ± standard deviation unless otherwise stated.

# CHAPTER 3

## THE CHARACTERISATION AND BIOLOGICAL ACTIVITY OF POLYMERSOMES LOADED WITH SMALL MOLECULE WNT AGONISTS *IN VITRO*

### 3.1 INTRODUCTION

Wnt signalling is essential for successful bone formation during repair (Chen and Alman, 2009) and presents an attractive target for pharmaceutical treatments to improve outcomes after fracture. Potential issues of therapeutics targeting Wnt, detailed in **section 1.7.4,** could be resolved with a spatial and temporal controlled delivery mechanism, targeting the treatment to a fracture site. Use of a nanoparticle (NP) delivery system, specifically polymersomes (PMs), have such potential. Before assessing therapeutic effect on a bone fracture, PMs need to be developed that are stably loaded with a Wnt activating compound, and do not prevent that compound from inducing Wnt signalling, thereby producing a usable therapeutic for further investigation.

PMs have been used to package and deliver a variety of both hydrophilic and hydrophobic molecules for potential use as therapeutic or diagnostic agents, their most common application being in cancer therapy. BIND-014 – Docetaxel loaded PLA-PEG polymeric particles, currently in clinical trials for the treatment of metastatic cancers – and GenexolPM – a Paclitaxel loaded PLA-PEG micelle NP that has been approved in South Korea for the treatment of breast cancer – are two successful examples of PM-drug loading with therapeutic efficacy (Cheng *et al.*, 2015). As well as conventional pharmaceuticals, the PM loading of plasmid DNA, siRNA, and oligonucleotides have been studied for use in cancer treatment (Guan, Rizzello and Battaglia, 2015). Outside of cancer therapy, successful PM encapsulation has been demonstrated in loading siRNA against TNF-α and dexamethasone sodium phosphate for potential use in the treatment of ulcerative colitis, and the loading of glucose-binding leptin ConA for diabetes therapy (Matoori and Leroux, 2020). Loading of the antibiotics doxycycline and rifampicin into PMs has been investigated for the treatment of intracellular infections (Porges, 2021). For this thesis, the polymers polyethylene glycol and poly-ε-caprolactone have been selected to produce PEG-*b*-PCL polymersomes. A variety of drug compounds have been successfully loaded into PEG-*b*-PCL based particles; most commonly hydrophobic compounds such as

immunosuppressant Cyclosporine A, but also hydrophilic compounds such as the protein Ovalbumin (Grossen *et al.*, 2017).

Important to the therapeutic use of any of these example PM-loaded treatments is assessing the extent of successful drug/molecule loading, i.e. the encapsulation efficiency and stability. The final dose of payload exposed to an environment is a consequence of particle yield and encapsulation efficiency, both of which are influenced by production methods and polymer chemistries, plus any conjugated targeting moieties, affecting particle size and payload interactions.

PMs can be synthesised loaded with a compound by a number of methods including solvent displacement (also called nanoprecipitation), emulsification, and film rehydration, which are discussed in more detail in **section 1.8.** For this thesis a solvent displacement method is used (Johnston, Dalton and Newman, 2010).

In pharmaceutical research the quantitative and qualitative analysis of drugs uses various methods, reviewed extensively by Siddiqui, Alothman and Rahman (2017); these include amongst others titrimetric, chromatographic, and spectroscopic techniques. For polymeric nanoparticles, depending on the properties of the loaded compound, common analysis methods used are high-performance liquid chromatography (HPLC) and spectroscopy. Wang *et al.* (2017) used HPLC to quantify the concentration of the small molecule AZD2858, present in polymeric micelles. This technique has been employed not only to determine the drug payload present within PMs, but also to assess payload release over time to ascertain encapsulation stability. Zhang *et al.* (2007) used a dialysis method of collecting drug samples released from polymeric particles within the dialysate, which was subsequently quantified using HPLC. Alternatively to HPLC, Yewle *et al.* (2016) determined the encapsulation efficacy of PEO-*b*-PBD polymersomes using Ultraviolet-Visible (UV-Vis) light absorbance spectroscopy. In this technique an absorbance spectrum of manufactured PMs encapsulating a representative small molecule mBlue was measured, and the mBlue concentration was interpolated from a standard curve of free mBlue absorbance measurements at different concentrations (Yewle *et al.*, 2016). UV-Vis spectroscopy is a long-standing method for quantifying analytes and as such provides a quick and simple method widely used for calculating nanoparticle payload concentration.

As well as assessing encapsulation efficiency, techniques are also required to characterise PM properties such as size and the yield achieved through synthesis, which as previously mentioned affects the available therapeutic dose. Habel *et al.* (2015) extensively reviews the analytical tools used for the characterisation of polymer-based vesicles; this includes, amongst others, scattering,

sorting, and manipulation techniques, as well as visualisation methods. These techniques are compared using PB-PEO PMs and it was demonstrated that dynamic light scattering (DLS), one of the most routinely used sizing methods, although well-established is not suited for highly polydispersed samples due to algorithm-based bias to larger particles. Therefore, additional visual methods such as electron microscopy, in particular transmission electron microscopy (TEM), techniques are also required. Of these, cryo-TEM is the recommended method with the least artifacts and the ability to capture PMs in situ within tissue (Habel *et al.*, 2015). A study by Johnston *et al*. (2010) also used both DLS and TEM (non-cryo) to assess the morphology and size of PEG-*b*-PCL investigated in this thesis. TEM images revealed a spherical morphology with a core size 4-5 times smaller than the hydrodynamic diameter measured by DLS of 90.5 ± 9.0 d.nm (Johnston, Dalton and Newman, 2010).

This thesis overall aims to develop methods to target Wnt signalling as a means of improving fracture outcomes. There are examples in literature of nanoparticles, including polymeric nanoparticles of micelle or polymersome structures, being successfully loaded with small molecules for Wnt signalling activation. Janeczek *et al.* (2017) fabricated PEGylated liposomes associated with Wnt-3a protein. Wang *et al.* (2017) successfully produced polymeric micelles (PSMA-*b*-PS) encapsulating a small molecule GSK-3β inhibitor (AZD2858). Stable micelle formation was confirmed using dynamic light scattering (DLS), TEM imaging, and nanoparticle tracking analysis (NTA) techniques.

In this work, the small molecule Wnt agonists 6-bromo-indirubin-3'-oxime (BIO) and CHIR99021 (CHIR) were selected for investigation. These molecules negatively regulate glycogen synthase kinase 3 beta activity, thereby activating the Wnt signalling pathway (Meijer, Flajolet and Greengard, 2004). At the time of writing a select few studies have specifically investigated the loading of nanoparticles with these small molecules. Low *et al.* (2015) synthesised a BIO conjugated micelle structured nanoparticle and assessed size and release kinetics using DLS and HPLC techniques. Fan *et al.* (2020) produced PLGA PMs loaded with CHIR99021 using a single-emulsion technique and assessed size and release kinetics using SEM and UV-Vis spectroscopy techniques. The high predicted partition coefficient (logP) values for CHIR and BIO of 4.3 and 2.0 respectively suggest these small molecules are capable of interacting with the hydrophobic fraction of the PMs selected for use in this study, facilitating successful encapsulation (National Centre for Biotechnical Information 2006; 2005). This has partly been demonstrated previously by Scarpa *et al* (2018); using the same polymers and solvent displacement synthesis technique as used in this work, successful encapsulation of BIO into PEG(5k)-PCL(18k) PMs was achieved, reported at a 90% encapsulation efficiency. Here, PM size and stability was assessed using DLS, NTA, and UV-Vis spectroscopy techniques (Scarpa *et al.*, 2018).

Given the limited examples of BIO and CHIR loaded nanoparticles, this study aims to establish encapsulation efficiency and for the first time compare BIO and CHIR loading. At the time of writing no published evidence of PEG-*b*-PCL particles that encapsulate CHIR for the purpose of bone fracture treatment. Therefore, testing the efficacy of PM-CHIR production will be important before possible future experimental use.

As well as demonstrating stable production of drug loaded PMs, PM delivered compounds need to retain their pharmacological activity. This generates the need for an effective readout method of Wnt signalling activation. Many studies have investigated the Wnt signalling activity of BIO and CHIR *in vitro* (see **section 1.7.5**), however few studies have investigated this activity in the context of nanoparticle delivery. The studies by Janeczek *et al.* (2017), Wang *et al.* (2017), and Scarpa *et al.* (2018) each use nanoparticles to deliver a Wnt agonist in cell culture and all achieved signalling activation. In each of these studies, activity was determined using a luciferase reporter assay in which cells are transfected with a luciferase reporter plasmid with a TCF/LEF transcription factor binding site. Here, when β-catenin levels rise and associate with TCF, Wnt target genes are transcribed along with a luciferase enzyme which luminesces in the presence of an exogenously added substrate, enabling quantification of Wnt signalling activity. This method gives a quick and effective, though artificial, readout for Wnt signalling that can be used to compare the activity of free and PM-encapsulated BIO and CHIR.

RT-qPCR can be used for detecting Wnt signalling activity and has the advantage that primary cells and *ex vivo* tissue sources can be analysed. This provides a signalling readout which more closely reflects the response of cells within a target bone tissue environment. Scarpa, *et al.* (2018) utilised this technique to demonstrate that nanoparticle delivered Wnt agonists can activate Wnt signalling. Alternative techniques to determine Wnt signalling include antibody (IHC) or probe (ISH) detection of a known Wnt signalling factor, e.g. β-catenin. Active cells can then be visualised with fluorescence, stains, or western blot (Kim *et al.*, 2007). However, these techniques are semi-quantitative at best and are better suited to spatio-temporal investigation within tissue sources rather than quantifying Wnt signalling activity.

As well as establishing the Wnt signalling activity of PM-encapsulated BIO and CHIR, investigating an appropriate dose range that does not induce toxicity is also required before testing therapeutic efficacy. There are several commonly used *in vitro* tests which determine cytotoxicity: some relate to less favourable outcomes such as cell death, where others measure cytocompatibility, defined here as tests for changes in cell and tissue structure and function. Live/dead cell staining and imaging provides evidence of the cytotoxicity of a compound, and has been used to assess the effect of BIO

and CHIR on cell cultures (Frith *et al.*, 2013; Hoffman and Benoit, 2015). This method can only inform of the terminal effect of a compound; before this point, lower concentrations of the compound will also affect the cells' health and performance, preventing normal function. Therefore, methods to assess cell performance and the cytocompatibility of a compound are arguably more informative. There are a number of widely used cell viability assays, including tetrazolim reduction assays (such as MTT), resazurin reduction assays (such as alamarBlue), and protease activity assays. Each assay measures the activity of viable cells by converting a substrate to a coloured or fluorescent product that can be detected and quantified (Riss *et al.*, 2013). The toxicity of both BIO and CHIR have been investigated using cell viability assays, notably the tetrazolim reduction MTT assay (Naujok *et al.*, 2014; Neves *et al.*, 2017) and the resazurin reduction alamarBlue assay (Hoffman, Takahata and Benoit, 2011). Comparatively resazurin reduction assays are more sensitive than tetrazolim reduction assays, and have the advantage that further tests can be performed on cells; in contrast, due to the cytotoxic nature of tetrazolim compounds (namely MTT) this assay is considered an end point assay (Riss *et al.*, 2013). To date, no published studies have investigated the effects of BIO and CHIR encapsulated in PMs upon primary BMSC cell viability, therefore doing so using the alamarBlue assay is a focus of this work, alongside the use of primary mouse derived bone marrow cells to determine the safety of the treatment for subsequent *in vivo* studies (Chapter 4 and Chapter 5 ).

Overall, to evaluate the production and pharmacological potential of polymersome encapsulated BIO and CHIR, this study uses various techniques described in the following aims section to test the hypothesis that PMs can encapsulate small molecule Wnt agonists BIO and CHIR, and deliver them *in vitro* to induce a Wnt signalling response.

## 3.2 AIMS

**The primary aim of this chapter is to develop PEG-*b*-PCL polymersomes (PMs) loaded with two types of Wnt signalling agonists using an established solvent displacement method and analyse encapsulation efficiency.**

- Develop UV-Vis as a method for detecting and calculating Wnt agonist concentrations, both free and encapsulated within PMs.
- Determine and compare the optimal PM loading concentration of small molecule Wnt agonist 6-bromo-indirubin-3'-oxime (BIO) and CHIR-99021 (CHIR).
- Determine the size and yield of PMs using Dynamic Light Scattering (DLS) and Nanoparticle Tracking Analysis (NTA).

**The second aim of this chapter is to determine the biological activity of Wnt signalling agonists BIO and CHIR *in vitro* and compare this to activity when delivered by polymersomes.**

- Measure Wnt signalling activity of free and polymersome encapsulated BIO and CHIR in a cellular activity assay (3T3 Wnt luciferase reporter cell line).
- Determine the cytocompatibility of free and polymersome encapsulated BIO and CHIR on human bone marrow stomal cells using an alamarBlue assay.
- Determine the cytocompatibility and proliferation effects of polymersome encapsulated BIO or CHIR on mouse bone marrow cells using an alamarBlue assay.

## 3.3 RESULTS

### 3.3.1 Polymersomes can successfully be produced loaded with hydrophilic small molecule Wnt agonists

#### 3.3.1.1 Developing UV-Vis as a method for detecting and calculating Wnt agonist concentration

To investigate whether Wnt-activating small molecules can be encapsulated in polymersomes (PMs), PEG(5K)-*b*-PCL(18K) polymersomes were produced loaded with Wnt activating agents BIO and CHIR using a solvent switch method, detailed in **section 2.1.** The encapsulated concentration of BIO or CHIR within PMs, post dialysis, was quantified using UV-Vis absorption spectroscopy. First, increasing concentrations of free CHIR and free BIO (5 µM to 150 µM) were measured to identify a characteristic absorption spectrum. The absorbance spectrum of CHIR has a maximum absorption peak at ~270 nm (**Figure 3.1a**). The absorption peak measurement at 273 nm was plotted against concentration to produce a standard curve (**Figure 3.1b**). For BIO, the characteristic absorbance spectrum has maximum absorption peaks at ~500 nm and ~300 nm (**Figure 3.2a**). The absorption peak measurements at 506 nm were plotted against concentration to produce a standard curve for BIO (**Figure 3.2b**). The $R^2$ values of 0.99 for both CHIR and BIO standard curves indicate high confidence in the data fit, supporting the use of absorption measurements to calculate concentration.

Absorption measurements were collected for the vehicle controls, namely DMF (used to dissolve CHIR/BIO stocks) and PBS (used to dilute CHIR for serial dilutions) (**Figure 3.3**). The absorption spectrum for DMF displays a saturated peak below 270 nm that corresponds to the saturated peak seen below 270 nm in both CHIR and BIO spectra. These peaks do not change in magnitude between sample concentrations, suggesting these are the result of DMF presence rather than a characteristic peak of CHIR/BIO.

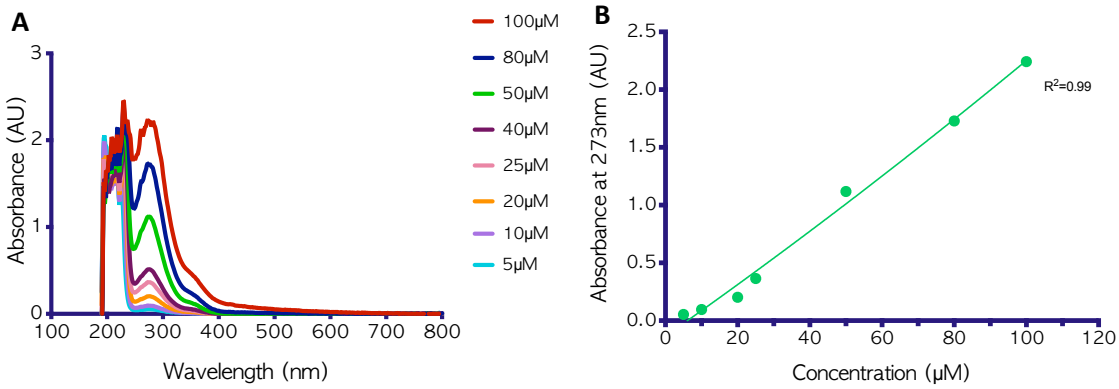


***Figure 3.1: CHIR-99021 Ultraviolet-Visible light (UV-Vis) absorbance spectra***

*A) UV-Vis absorbance spectra of increasing concentrations of CHIR diluted in phosphate buffered saline (PBS) solution. B) CHIR standard curve based on absorbance measurements at 273 nm wavelength. Data represents mean values ± standard deviation for n=3 technical repeats.*

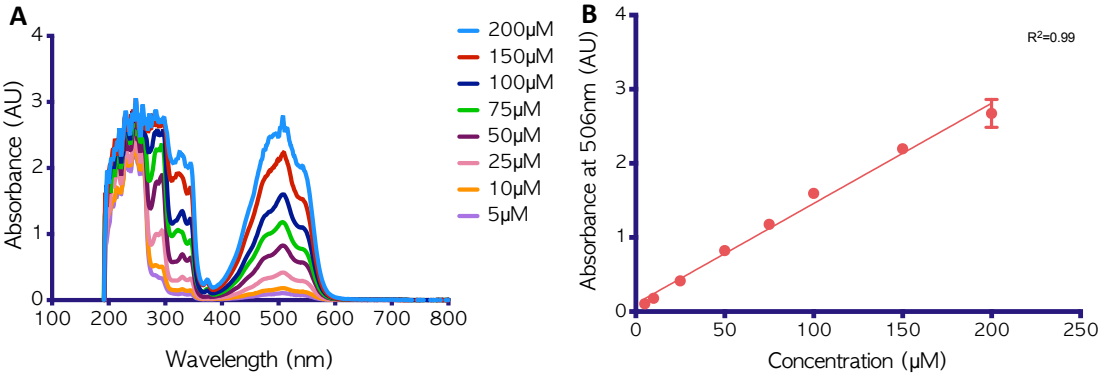


***Figure 3.2: 6-Bromo-indirubin-3'-oxime (BIO) Ultraviolet-Visible light (UV-Vis) absorbance spectra***

*A) UV-Vis absorbance spectra of increasing concentrations of BIO diluted in dimethylformamide (DMF). B) BIO standard curve based on absorbance measurements at 506 nm wavelength. Data represents mean values ± standard deviation for n=3 technical repeats.*

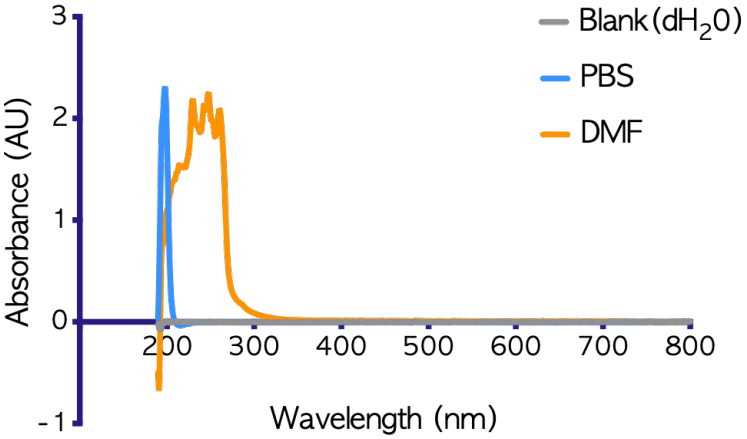


***Figure 3.3: Ultraviolet-Visible light absorbance spectra of dilutants***

*Phosphate buffered saline (PBS) solution and dimethylformamide (DMF) and distilled $H_20$ (used to blank the spectrophotometer).*

### 3.3.1.2 Determining if UV-Vis absorbance spectroscopy can be used to detect Wnt agonists encapsulated within PMs and calculate the payload dose

Having validated absorption measurements as a method for quantifying BIO and CHIR, the final concentrations of PM-encapsulated BIO (PM-BIO) and PM-encapsulated CHIR (PM-CHIR) synthesised with an initial concentration of 200 µM was measured (as depicted in the methods **Figure 2.1**). Vehicle-only PMs (i.e. encapsulating only PBS, referred to as PM-Empty) were measured to determine background spectra. Representative absorbance spectra are shown in **Figure 3.4.** Clear absorption peaks are seen above the PM-Empty spectrum, at 273 nm for PM-CHIR and 506 nm for PM-BIO. For PM-Empty, a peak is seen between 210 nm and 230 nm, with a gradual decreasing curve at higher wavelengths characteristic of scattered light. This suggests similar curves observed in PM-CHIR/PM-BIO spectra are due to the presence of the PMs themselves. This background signal was subsequently subtracted to remove any enhancement of measured absorbance and overestimation of interpolated concentration, as depicted in **Figure 3.5** and **Figure 3.6**.

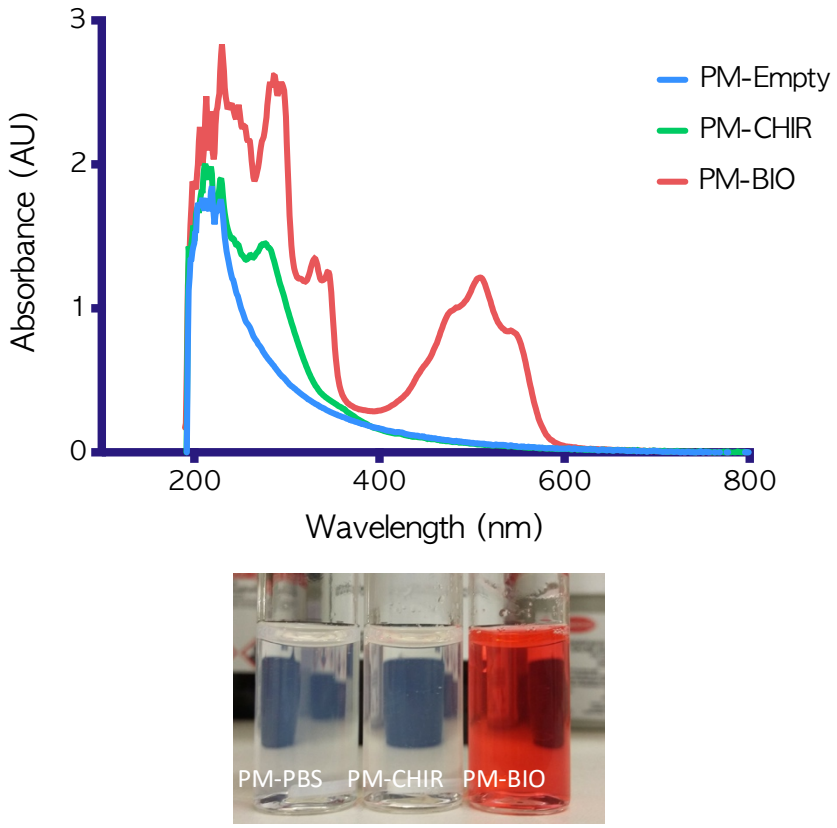


***Figure 3.4: Representative Ultraviolet-Visible light absorbance spectra of CHIR-99021 and 6-Bromo-indirubin-3'-oxime loaded (BIO) polymersomes (PMs)***

*PMs produced with an initial loading concentration of 200 µM BIO/CHIR, along with vehicle control, Phosphate Buffered Saline (PBS) loaded PMs (PM-Empty). The solutions were measured post 48 hours dialysis and at a 1 in 2 dilution with PBS. B) Representative photograph of PM solutions before dialysis.*

To confirm if the peak at 273 nm corresponded to the presence of CHIR, following the subtraction of the PM-Empty spectrum from the PM-CHIR spectrum (**Figure 3.5a**), the resultant spectrum was normalised/scaled to the spectrum for free CHIR (**Figure 3.5b**). The aligned spectral peak (in this example with a peak alignment error of 2.13%) confirms the presence of CHIR. Note the signal below 270 nm seen for free CHIR does not align with normalised PM-CHIR spectrum as this signal overlaps and is removed when PM-Empty spectra in subtracted. Subsequently the 273 nm peak absorption measurement was interpolated onto the CHIR standard curve (**Figure 3.1b**) to calculate concentration. Accounting for the PM dilution factor, a total concentration of 74.1 µM of CHIR is encapsulated within PM-CHIR in this example reading. The same analysis was performed for the PM-BIO peak at 506 nm, as this had little interference from PM-Empty absorbance (**Figure 3.6**). The final concentration of encapsulated BIO is calculated as 153.4 µM in this example reading.

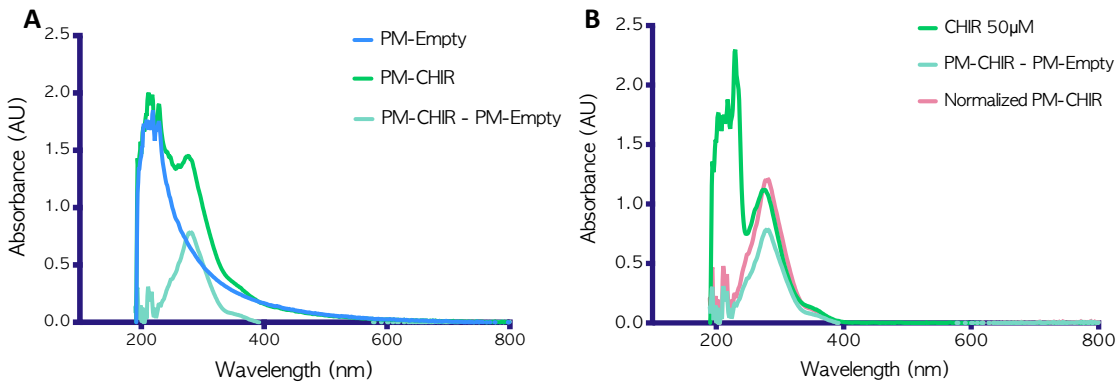


***Figure 3.5: Normalising the Ultraviolet-Visible light (UV-Vis) absorbance spectra of polymersomes (PMs) loaded with CHIR-99021 to a CHIR standard spectrum***

*A) UV-Visible light absorbance spectra of PBS loaded polymersomes (PM-Empty) and PM- CHIR both diluted 1 in 2 in PBS, plus the additional CHIR spectrum calculated by subtracting PM-Empty spectrum from the PM-CHIR spectrum. B) Spectrum of CHIR encapsulated within PMs (PM-CHIR - PM-Empty) shown alongside free CHIR 100 µM concentration spectrum and the spectrum of encapsulated CHIR normalised relative to free CHIR.*

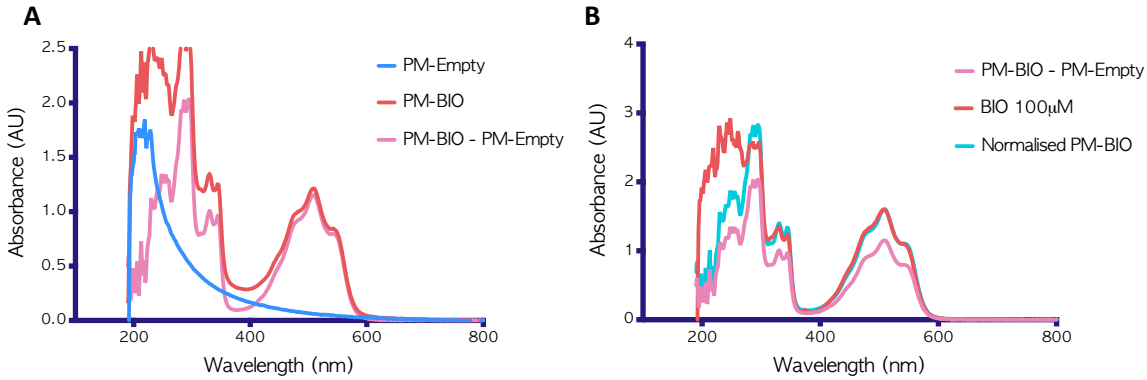


***Figure 3.6: Normalising the Ultraviolet-Visible light (UV-Vis) absorbance spectra of polymersomes (PMs) loaded with 6-bromo-indirubin-3'-oxime (BIO) to a BIO standard spectrum***

*A) UV-Vis absorbance spectrum of PMs loaded with PBS (PM-Empty) and PM-BIO both diluted 1 in 2 with PBS, plus the additional BIO spectrum calculated by subtracting PM-Empty spectrum from the PM-BIO spectrum. B) Spectrum of BIO encapsulated within PMs (PM-BIO - PM-Empty) shown alongside free BIO 100 µM concentration spectrum and spectrum of encapsulated BIO normalised relative to free BIO.*

### 3.3.1.3 Assessing if PM UV-Vis signal interferes with interpolating payload concentration

Normalised results show that PM scattering does not shift the BIO or CHIR signature peak, however this scattering from PMs could affect the absorbance magnitude and therefore the interpolated concentration. To test this a second method was employed in which PM samples were first diluted with dimethylformamide (DMF), an organic solvent that disrupts the polymersome vesicle structure (Suen and Chau, 2013), thereby releasing the encapsulated drug. **Figure 3.7** shows how diluting with DMF at a ratio of 1 in 2 successfully removed the scattering curve above 230 nm seen with Empty PMs in PBS. **Figure 3.8** shows for PM-BIO, dilution in PBS, dilution in DMF, and subtraction of PM-Empty signal all produce overlapping spectra at the peak 503 nm used in concentration calculations. For PM-CHIR diluting in DMF produces a characteristic CHIR peak at 273 nm which closely aligns with the spectra resulting from subtracting PM-Empty signal when diluted in PBS. Therefore, it can be stated that DMF removes PM scattering, however the absorbance magnitude is the same as that produced from subtracting the control PM-Empty signal when diluted in PBS.

The interpolated concentrations of BIO and CHIR in PBS vs. DMF dilutant shown in **Table 3.1** present a marginal difference, therefore validating that the presence of PMs does not affect the measured absorbance for BIO or CHIR as long as control PM-Empty spectra is subtracted. Note that in **Figure 3.7** and **Figure 3.8** UV-Vis measurements are taken using Shimadzu UV-2700i, a different machine to the Nanodrop used for all other UV-Vis measurements.

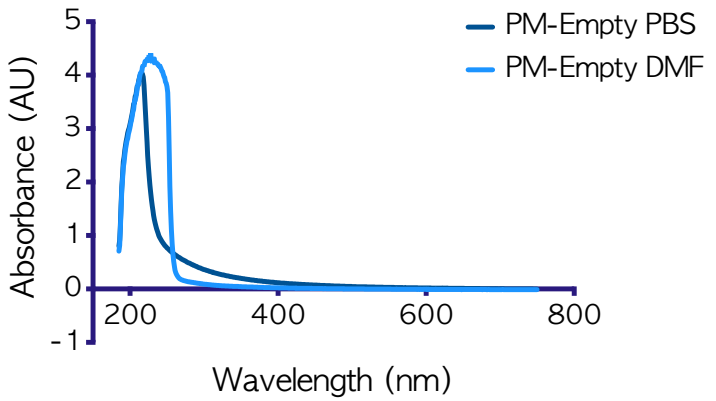


***Figure 3.7: Ultraviolet-Visible light absorbance spectrum of PMs loaded with phosphate buffered saline (PBS) (PM-Empty)***

*Diluted 1 in 2 with either PBS (dark blue) or organic solvent dimethylformamide (DMF) (light blue). Measurements taken using Shimadzu UV-2700i.*

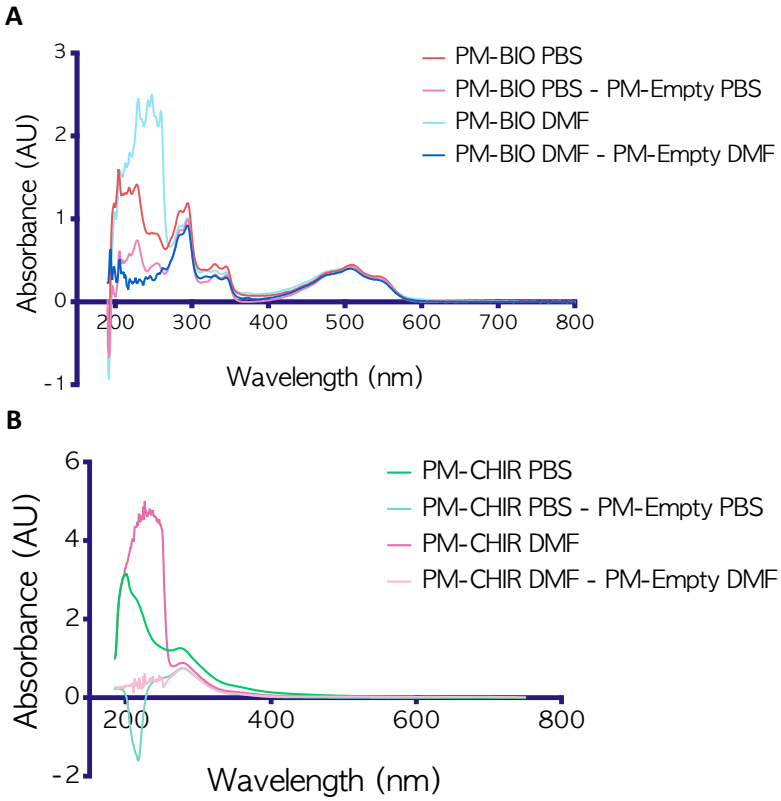


***Figure 3.8: Comparison of the ultraviolet-visible light (UV-Vis) absorbance spectroscopy spectra of polymersomes (PMs) diluted in either phosphate buffered saline (PBS) or dimethylformamide (DMF)***

*A) UV-Vis absorbance spectra of PMs loaded with 200 µM of BIO diluted 1 in 5 with either PBS (dark red) or DMF (light blue). PM-BIO minus PM-Empty spectra are also plotted for each dilutant (light red = PBS; dark blue = DMF). B) UV-Vis absorbance spectra of PMs loaded with 200 µM of CHIR diluted 1 in 2 with either PBS (dark green) or DMF (dark pink). PM-CHIR minus PM-Empty spectra are also plotted (light green = PBS; light pink = DMF). Measurements taken using Shimadzu UV-2700i.*

***Table 3.1: Comparison of polymersome payload interpolated concentration when diluted in either PBS or DMF***

*PBS interpolated concentrations taken from absorbance peaks at 503 nm for PM-BIO minus PM-Empty (light red graph A) and 273 nm for PM-CHIR minus PM-Empty (light green graph B) in figure 3.8. DMF interpolated concentrations taken from PM-BIO in DMF (light blue) and PM-CHIR in DMF (dark pink) spectra in figure 3.8.*

| | **PBS dilutant** | **DMF dilutant (% difference to PBS concentration)** |
|---|---|---|
| **PM-BIO Interpolated concentration (µM)** | 138.3 | 130.4 (5.7%) |
| **PM-CHIR Interpolated concentration (µM)** | 20.9 | 19.9 (4.8%) |

### 3.3.1.4 Investigating the efficacy of PM payload retention post dialysis

To determine whether batches of polymersomes may be produced with a consistent payload for experimental use (after dialysis), CHIR and BIO concentrations of separate batches were compared (**Figure 3.9**). PMs produced with an initial concentration of 200 µM of BIO measured a final concentration ranging from 68 µM to 173 µM with a mean concentration of 134 µM (SD 32.9 µM). PMs produced with an initial concentration of 200 µM of CHIR measured a final concentration ranging from 53 µM to 120 µM, with a mean concentration of 74 µM (SD 26.93 µM).

**Figure 3.9** shows that when PMs are produced with the same initial loading concentration of 200 µM, PM-BIO has a statistically significant higher concentration retained post dialysis compared to PM-CHIR, with a mean difference of 60.02 µM (95% CI, 22.30-97.94, *P*=0.0047). Comparison of the initial 200 µM concentration of BIO and CHIR in the PM solutions before dialysis with the final average calculated concentrations enable average percentage encapsulation efficiency to be determined: 67% for the PM-BIO solution, and 37% for the PM-CHIR solution.

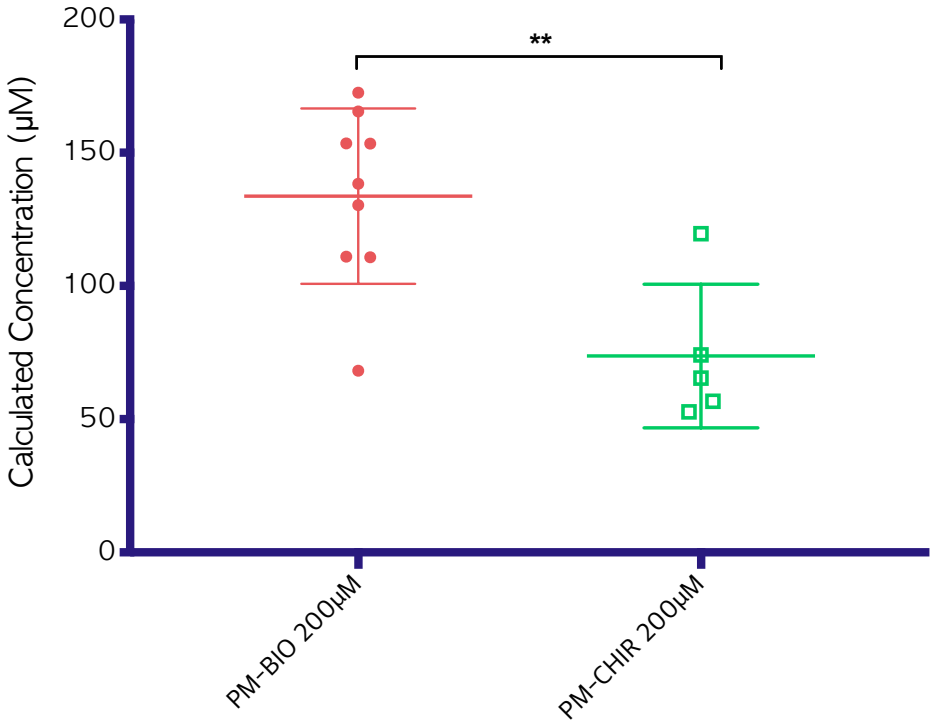


***Figure 3.9: Variation in polymersome (PM) payload calculated concentration***

*Each point plotted represents a batch of PMs produced with initial loading concentration of either 200 µM BIO (red) or 200 µM CHIR (green). The concentration was calculated from measured UV-Vis absorbance spectrum (minus PM-Empty spectrum) interpolated from standard curves and multiplied by the dilution factor. Bars represent mean ± standard deviation. **P=<0.05. Statistical significance assessed using unpaired t-test. P=0.0047.*

#### 3.3.1.5 Determining the maximum possible payload of BIO/CHIR retained by PMs post dialysis

Subsequently, to increase the payload available for release, especially for PM-CHIR, the maximum concentration of payload that can be encapsulated in these PMs was determined. Several PM-CHIR solutions were produced with increasing initial CHIR concentrations (50 μM - 2000 μM) along with vehicle control PBS loaded PMs (PM-Empty). All solutions were diluted 1 in 5 before taking absorbance measurements (**Figure 3.10**). The absorbance spectra for 100 μM PM-CHIR and above displays a peak at ~273 nm corresponding to the characteristic peak of free CHIR, thereby suggesting the presence of CHIR. Subsequently absorbance values corresponding to the 273 nm peak were subtracted from PM-Empty values and interpolated onto CHIR's standard curve (**Figure 3.1b**). After accounting for the dilution factors, the concentration of CHIR present in each PM-CHIR solution was calculated (**Figure 3.10d**). The given CHIR concentration in produced PM-CHIR solutions was plotted against the post-dialysis calculated CHIR concentration to determine a relationship (**Figure 3.10e**). With increasing initial loading CHIR concentration the resultant encapsulated CHIR concentration increases until approximately 1000 μM, at which point the loading plateaus. Together these results show that a maximum starting concentration of 1000 μM CHIR can be used to produce PMs, and above this concentration no increase in the amount of CHIR encapsulated can be achieved with this particular PM preparation.

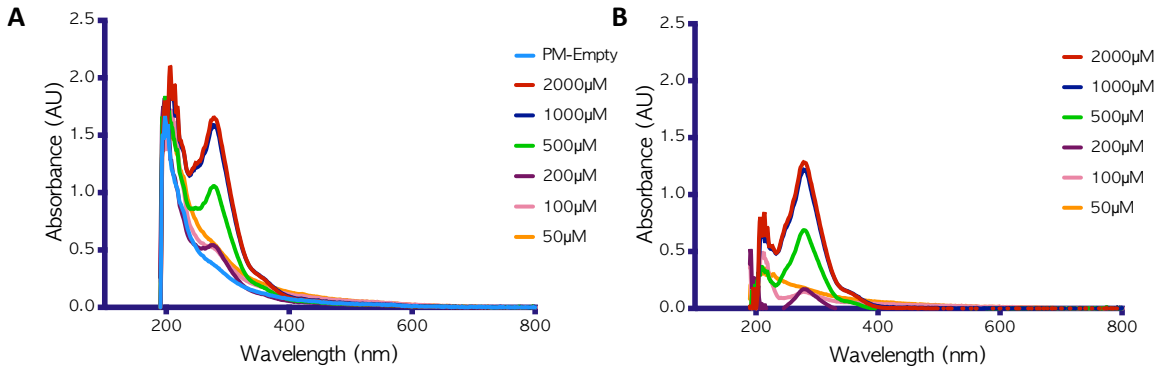


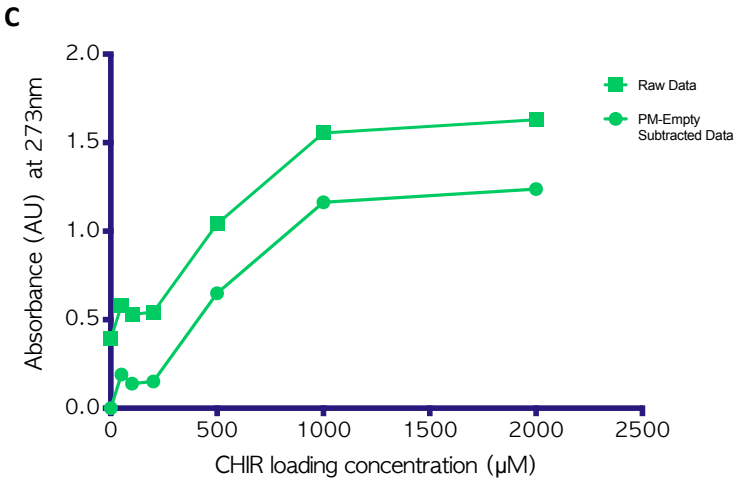


**D**

| Given CHIR Concentration (μM) | Calculated CHIR Concentration (μM) |
|---|---|
| 2000 | 292.46 |
| 1000 | 276.93 |
| 500 | 169.39 |
| 200 | 65.39 |
| 100 | 62.81 |
| 50 | 73.54 |

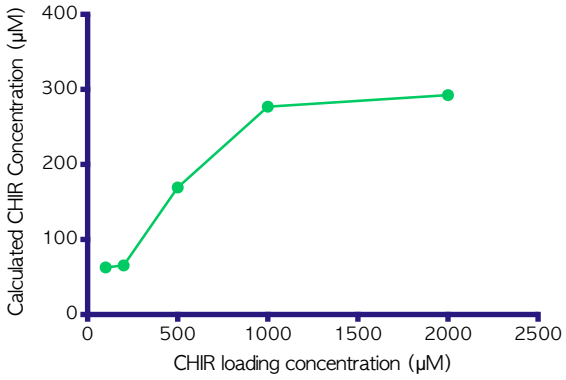


***Figure 3.10, Table 3.2: The maximum CHIR concentration encapsulation capacity for PEG(5K)-b-PCL(18K) polymersomes (PMs)***

*A) Absorbance spectra of PMs produced with increasing initial loading concentrations of CHIR. B) Absorbance spectra of PMs produced with increasing initial loading concentrations of CHIR minus PM-Empty. C) Plot of peak absorbance at 273 nm wavelength for each CHIR loading concentration with and without subtracting PM-Empty. D) Table listing concentration of CHIR encapsulated in PMs post dialysis, interpolated from CHIR standard curve (**Figure 3.1b**) using absorbance measurements in B corresponding to 273 nm. E) Plot of given CHIR concentrations in produced PM solutions vs. post dialysis calculated CHIR concentrations in PM-CHIR solutions.*

A similar relationship is observed for BIO, in which an increase in the initial loading concentration results in an increase in the post-dialysis encapsulated concentration. However, for BIO this relationship plateaus at a higher concentration of 1.5 mM to 2 mM, as seen in **Figure 3.11d**. **Figure 3.11d** uses spectral data from **Figure 3.11a** which, due to the use of a low dilution factor of 1 in 2, spectra of the highest concentrations (1.5 mM and 2 mM) contain a saturated peak. A further dilution of 1 in 10 shown in **Figure 3.11b** reveals that both 1.5 mM and 2 mM sample spectra overlap. Together these data confirm that for BIO a maximum concentration of 1.5 mM can be used to produce this formulation of PMs, after which no further gains in increasing the loading concentration to increase the encapsulated dose are made.

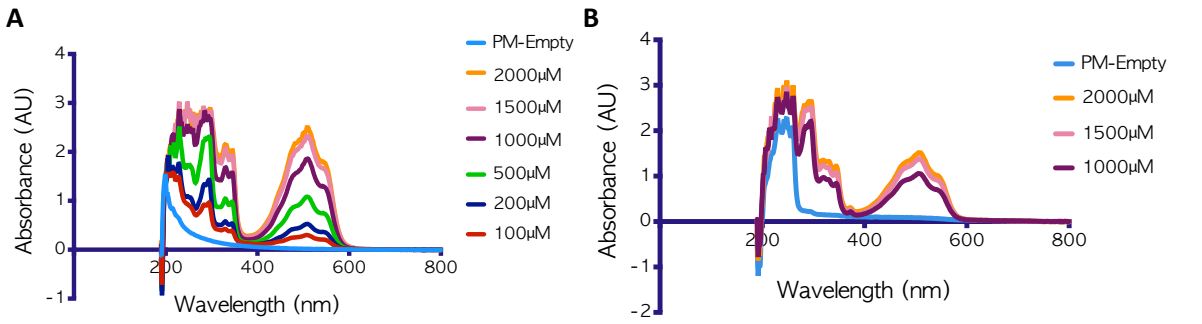


C

| Given BIO Concentration (µM) | Calculated BIO Concentration (µM) |
|---|---|
| 2000 | 360.27 |
| 1500 | 343.59 |
| 1000 | 270.88 |
| 500 | 154.20 |
| 200 | 68.67 |
| 100 | 34.03 |

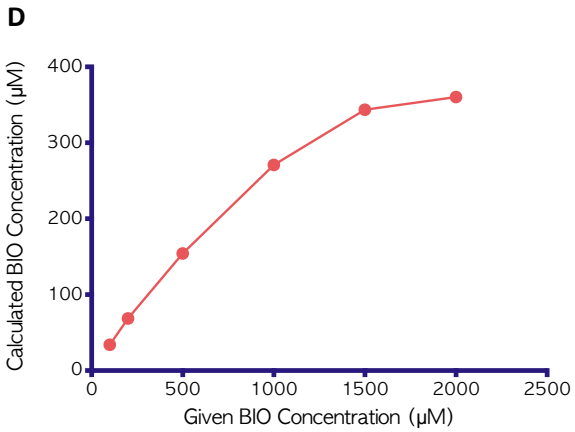


***Figure 3.11, Table 3.3: The maximum BIO concentration encapsulation capacity for PEG(5K)-b-PCL(18K) polymersomes (PMs)***

*A&B) Absorbance spectra of PMs produced with increasing initial loading concentrations of BIO diluted in PBS at a ratio of A) 1 in 2 and B) 1 in 10. C) Concentration of BIO encapsulated in PMs post dialysis, interpolated from BIO standard curve (**Figure 3.2**) using absorbance measurements in A corresponding to 506 nm. D) Plot of given BIO concentrations in produced PM solutions vs. post dialysis calculated BIO concentrations in PM-BIO solutions.*

### 3.3.2 PMs can be produced with a consistent size and yield

Having confirmed that BIO and CHIR were present in PM-BIO and PM-CHIR solutions, the effect of encapsulation of these small molecules on PM formation was then assessed. Dynamic light scattering (DLS) measurements were taken of PM-Empty, PM-CHIR, and PM-BIO solutions to determine the presence of particles, and also to ascertain their size and polydispersity characteristics, as described in **Section 2.1.3.**

DLS raw correlation plots (**Figure 3.12a**) for each sample display an equivalent exponential decay with an intercept at 0.85 and flat baseline demonstrating a good signal to noise ratio and no interference of large particles in the measurement. Measurement details listed in the size quality report reveal an automatic measurement position selected by the Zetasizer of 4.65 mm (the centre of the cuvette) (**Figure 3.12d**); this alongside the observed flat correlogram baseline (**Figure 3.12a**) further indicates no multiple scattering effects from large particles, and therefore the filter size and sample dilution used was appropriate for an accurate measurement. The overlapping start of each sample's exponential decay and gradient indicates an equivalent hydrodynamic size and polydispersity. These two characteristics are further confirmed in the distribution analysis (**Figure 3.12b,c**), in which an equivalent narrow peak is observed for all samples in intensity size distribution plots, demonstrating a low variability in size between samples and a monodisperse particle size within each sample. Cumulants analysis (**Figure 3.12d**) reveals a small difference in hydrodynamic diameter at 83.38 d.nm, 80.61 d.nm, and 80.17 d.nm for PM-Empty, PM-CHIR, and PM-BIO respectively; furthermore, a low polydispersity index measurement of less than 0.1 indicates an almost uniform-sized PM sample, and therefore a high confidence in the calculated hydrodynamic diameters. The close relationship of Z-average size to intensity distribution peak size further supports this. The Z-average (d.nm) and count rate (kcps) readings have a low standard deviation, demonstrating little change between repeat technical measurements of each sample. Therefore, no aggregation or sedimentation is detected, supporting that a stable PM preparation has been produced.

Together these data demonstrate that all synthesised PM samples contain particles that are stable at room temperature and that have a nearly uniform size. Additionally, the fact that both control (PM-Empty) and PM-BIO/CHIR solutions have similarly sized particles demonstrates that loading does not change particle size.

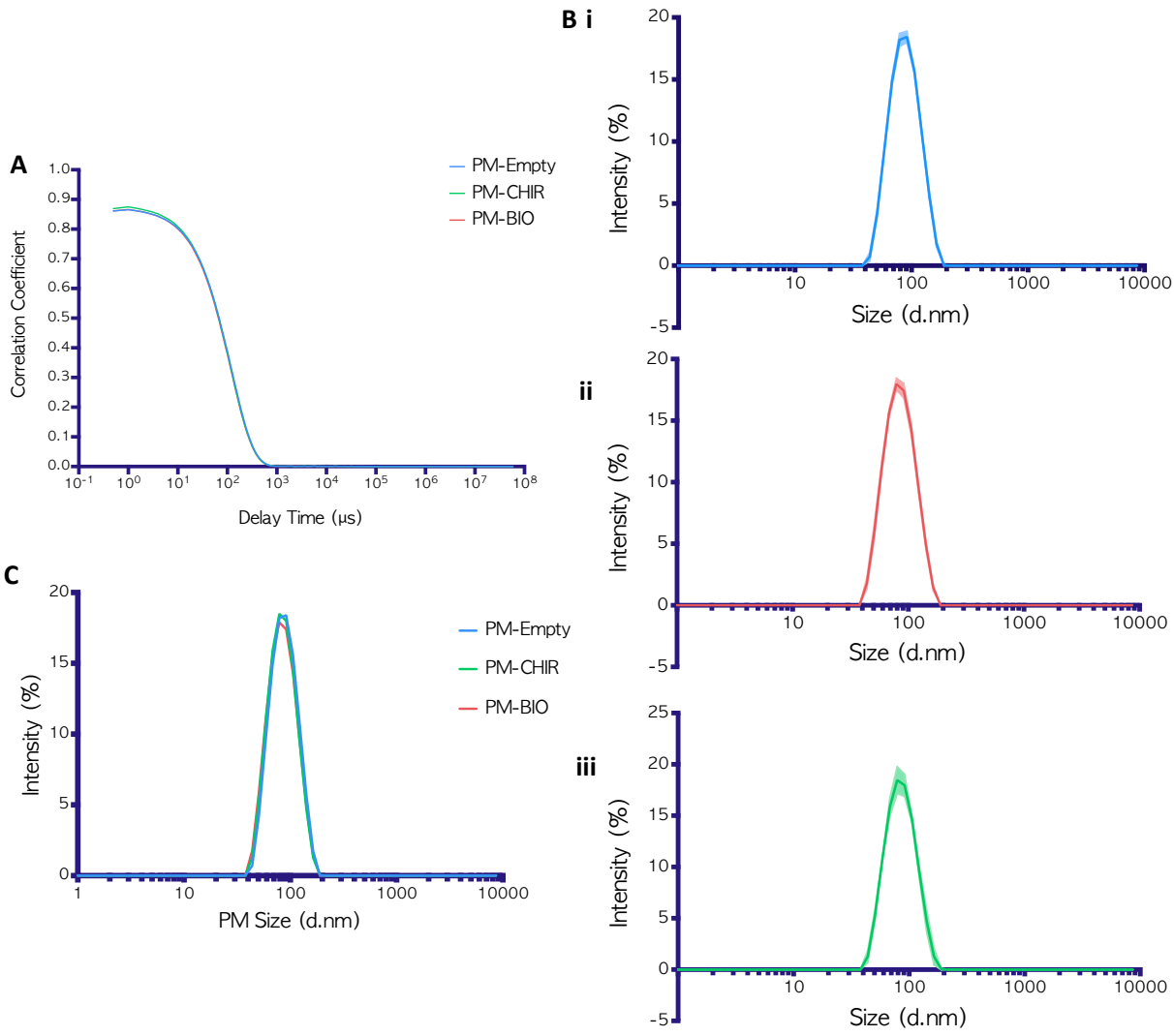


**D**

| | Z-Average (d.nm) | PdI | Count Rate (kcps) | Intensity Distribution Peak Size (d.nm) | Automated Measurement Position (mm) |
|---|---|---|---|---|---|
| **PM-Empty** | 83.38 (SD 0.28) | 0.068 (SD 0.009) | 359.57 (SD 2.76) | 90.19 (SD 0.21) | 4.65 |
| **PM-CHIR** | 80.61 (SD 0.02) | 0.073 (SD 0.019) | 333.63 (SD 0.65) | 87.42 (SD 1.20) | 4.65 |
| **PM-BIO** | 80.17 (SD 1.02) | 0.071 (SD 0.004) | 371.4 (SD 1.11) | 87.14 (SD 1.02) | 4.65 |

***Figure 3.12, Table 3.4: Representative dynamic light scattering (DLS) measurements of size and polydispersity of polymersomes encapsulating PBS (PM-Empty), CHIR, and BIO***

*Correlation function plot (A) and particle size distribution (B) of PM samples, Empty (i), CHIR (ii) and BIO (iii), diluted 1 in 10 in PBS and filtered through 0.2 µm pore filter, from DLS measurement at 173 °and 25 ℃. C) Average particle size distribution by intensity (n=3 technical repeats). D) Mean (standard deviation) hydrodynamic diameter (Z-average size d.nm) and polydispersity index (PdI) of PM samples from DLS cumulants analysis, n=3 technical repeats.*

DLS measurements were further taken of PMs produced at different times for various experiments, to check this relationship remained consistent across batches. The Z-average measurement of pooled data is shown in **Figure 3.13**. For each PM group loaded with PBS, 200 µM BIO, 200 µM CHIR, or 1 mM CHIR, some variation in size is observed: PM-Empty has a mean (SD) Z-average of 82.77 d.nm (6.65, 95% CI, 78.0-87.5), PM-BIO has a mean (SD) of 83.19 d.nm (4.83, 95% CI, 79.5-86.9), PM-CHIR 200 µM has a mean (SD) of 83.26 d.nm (6.79, 95% CI, 72.5-94.1) and PM CHIR 1 mM has a mean (SD) of 92.89 d.nm (13.81, 95% CI, 75.7-110.0). Between PM groups no statistically significant difference in hydrodynamic diameter is found (P=0.119).

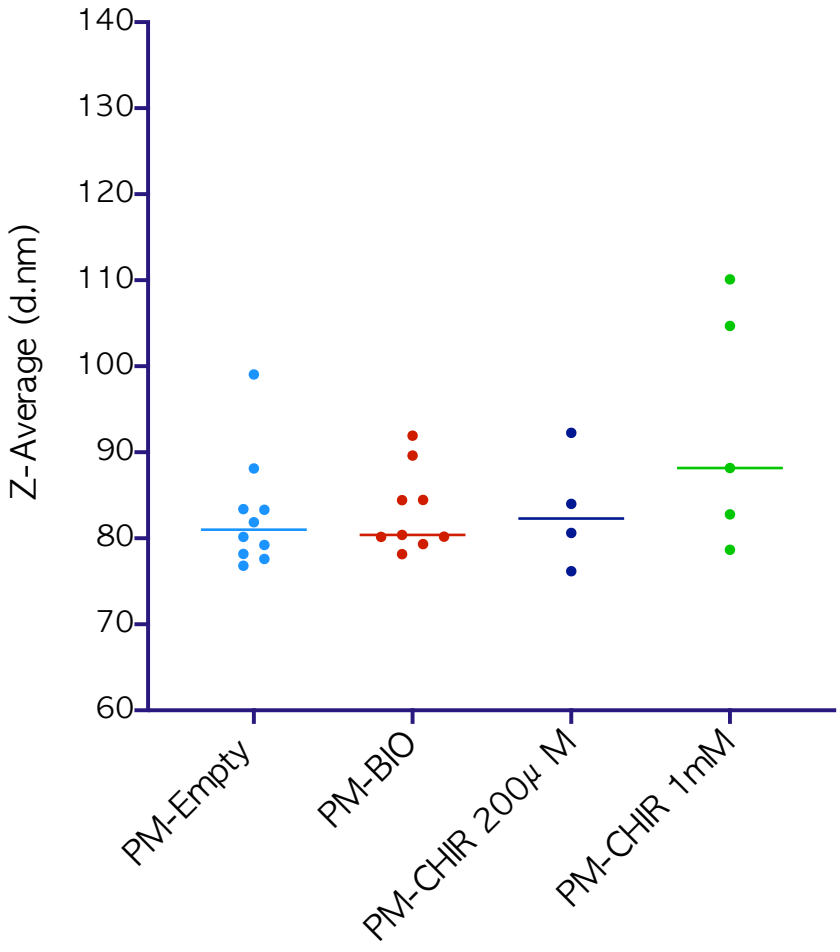


***Figure 3.13: Variation in hydrodynamic size of produced polymersomes (PMs) measured by DLS***

*PMs loaded with either PBS (PM-Empty), 200 µM BIO, 200 µM CHIR, or 1 mM CHIR, were measured post dialysis and filtering with 0.2 µm filter and diluted 1 in 10 with PBS dilutant. Dot expresses mean of n=3 technical repeat measurements from one batch of produced PMs. Bar expresses mean of pooled Z-average measurements from multiple batches of PMs. No significance between groups, P=0.119, indicated from one-way ANOVA.*

Next the amount of payload encapsulated in PMs was assessed for its effect on PM formation. DLS measurements were obtained from PM samples produced with an increasing concentration of BIO. **Figure 3.14** shows equivalent narrow size-distribution plots for each PM-BIO concentration and little variation in peak size. This consistency in size is also reflected in the DLS cumulants analysis Z-average, similar sizes ranging from 81-100 nm and Pdi values below 0.1 suggesting monodisperse samples.

**A**

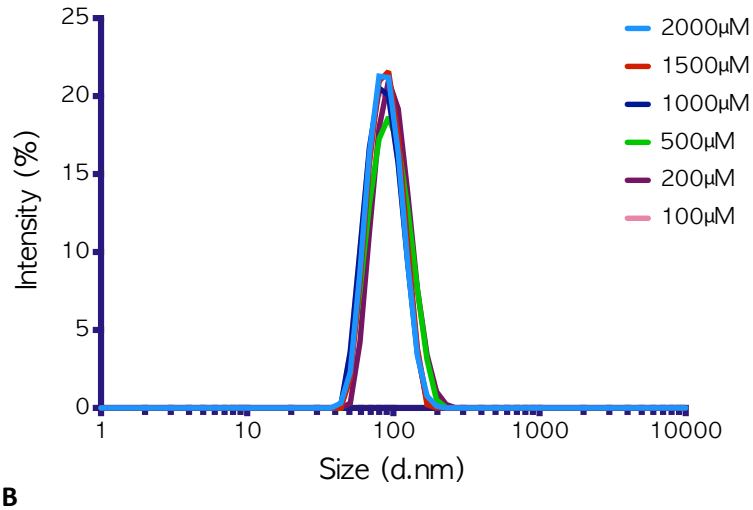


**B**

| PM-BIO Loading Concentration (µM) | Z-average (d.nm) | PdI |
|---|---|---|
| 100 | 83.57 (SD 0.36) | 0.05 |
| 200 | 100.2 (SD 1.03) | 0.16 |
| 500 | 89.95 (SD 1.05) | 0.075 |
| 1000 | 83.08 (SD 1.46) | 0.056 |
| 1500 | 85.91 (SD 0.47) | 0.044 |
| 2000 | 84.75 (SD 0.79) | 0.043 |
| PM-Empty | 81.35 (SD 0.59) | 0.06 |

***Figure 3.14, Table 3.5: Dynamic light scattering (DLS) measurements of polymersomes loaded with increasing concentrations of BIO***

*A) Particle size distribution plot of PM samples produced with increasing concentrations of BIO and measured post – dialysis, diluted 1 in10 with PBS and filtered through 0.2 µm filter. B) Table of PM samples DLS cumulants analysis, displaying mean hydrodynamic diameter (Z-average d.nm) and polydispersity index (PdI) (SD = standard deviation, n=3 technical repeats).*

#### 3.3.2.1 Determining the concentration of polymersomes present in the PM solutions

In addition to size, the yield of PMs was assessed by measuring sample concentrations using two methods: multi-angle dynamic light scattering (MADLS) and nanoparticle tracking analysis (NTA), as detailed in **section 2.1.4**. Representative results are shown in **Figure 3.15**. NTA size measurements, ranging between 71-78 nm, are smaller than the average size previously measured using DLS (**Figure 3.14**). NTA analysis shows that PM-Empty samples contain 4.3 x $10^{13}$ particles per mL of solution, whereas in solutions of loaded PMs, whether with BIO or CHIR, a decrease in concentration is observed at 2.3 x $10^{13}$ and 2.8 x $10^{13}$ particles/mL respectively. MADLS analysis of different batches of PMs gives a lower mean concentration compared to NTA analysis by a factor of 119 for PM-Empty, 267 for PM-BIO and 68 for PM-CHIR (**Figure 3.15**).

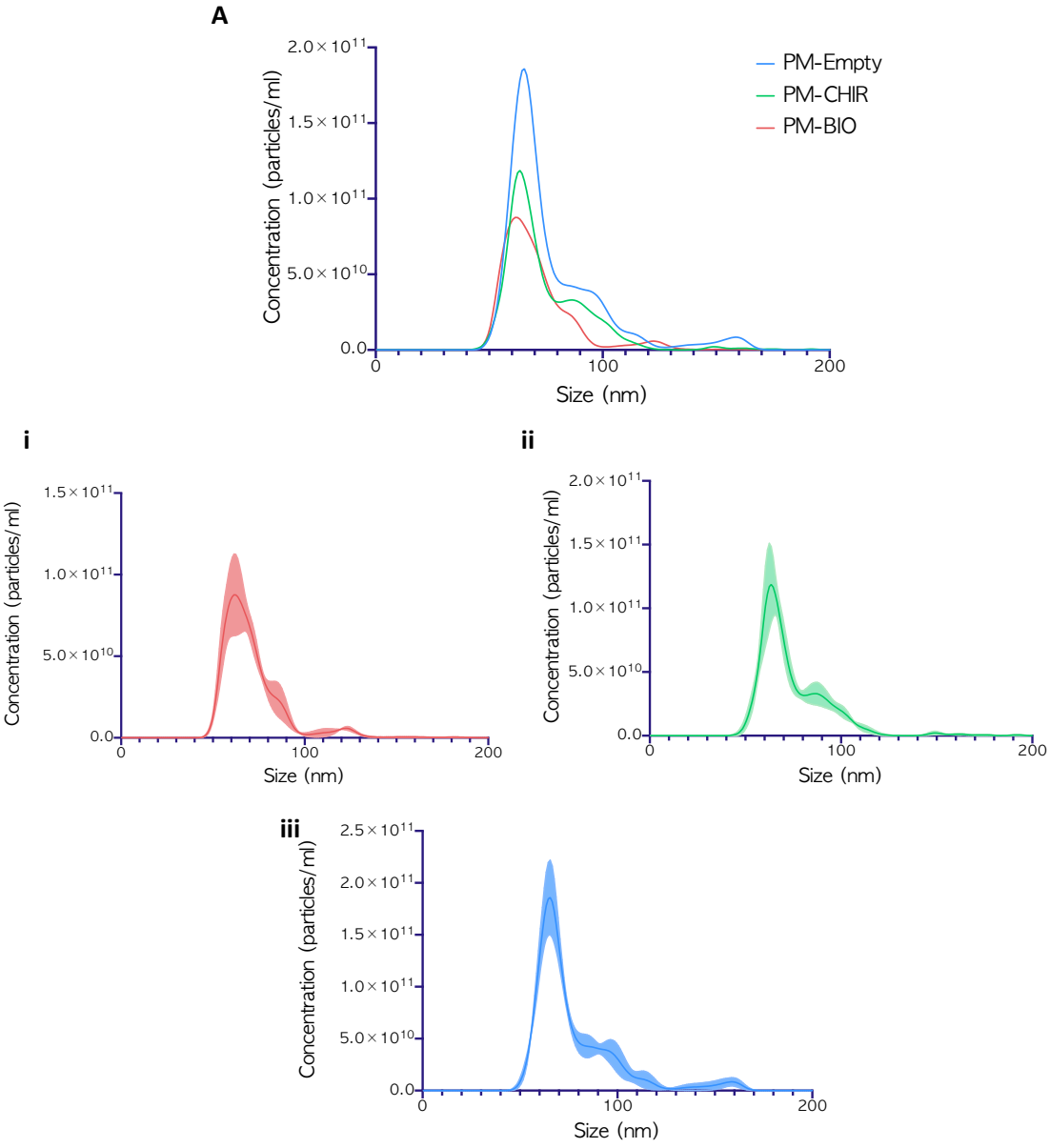


**B**

| | NTA | | MADLS | |
|---|---|---|---|---|
| | **Size (d.nm)** | **Concentration (particles/mL)** | **Size (d.nm)** | **Concentration (particles/mL)** |
| **PM-Empty** | 77.5 SD 0.2 | 4.33 x $10^{13}$ SD 5.94 x $10^{11}$ | 81.35 SD 0.35 | 3.65 x $10^{11}$ SD 2.19 x $10^{10}$ |
| **PM-BIO** | 71.2 SD 1.2 | 2.28 x $10^{13}$ SD 6.95 x $10^{11}$ | 114.1 SD 1.25 | 8.55 x $10^{10}$ SD 1.47 x $10^{10}$ |
| **PM-CHIR** | 74.3 SD 0.7 | 2.76 x $10^{13}$ SD 5.65 x $10^{11}$ | 83.90 SD 0.18 | 4.08 x $10^{11}$ SD 2.29 x $10^{10}$ |

***Figure 3.15, Table 3.6: Polymersome particle size and concentration measurements***

*A) Size vs. number distribution plots from NTA analysis of PMs loaded with (i) BIO, (ii) CHIR and (iii) PBS (PM-Empty). B) Table of measurements obtained from Nanoparticle Tracking Analysis (NTA) and multi-angle dynamic light scattering (MADLS), post production and dialysis of polymersomes loaded with either PBS (PM-Empty), BIO at 200 µM, or CHIR at 1 mM. Data mean of n=3 technical repeats, multiplied by dilution factor, SD = standard deviation.*

### 3.3.3 Polymersome-encapsulated BIO and CHIR retain their function and activate Wnt signalling in a cell line

To ascertain if PM encapsulation of BIO and CHIR alters their ability to activate Wnt signalling, free and PM-encapsulated BIO/CHIR were compared *in vitro* using a Wnt signalling activity 3T3 luciferase reporter cell line. This reporter cell expresses the firefly luciferase gene under the control of Wnt-responsive promoters TCF/LEF. Activation from exogenous Wnt signalling agonists causes production of luciferase in a dose-dependent manner, which is then quantifiable through measurement of luminescence intensity.

First the effect of free BIO and CHIR treatment on Wnt signalling activity was characterised. Reporter cells were incubated with a range of free BIO and CHIR concentrations for 17 hours, after which luminescence intensity was measured (**Figure 3.16a**)**.** In response to free BIO, there is a maximum Wnt signalling activity of 96.0 (SD 13.3) relative light units (RLU) at 2 µM. In response to free CHIR, a maximum Wnt signalling activity of 118.2 (SD 14.9) RLU is observed at 20 µM. **Figure 3.17** displays images of 3T3 cells incubated with increasing BIO and CHIR concentrations. For cells incubated with 20 µM of BIO damaged cell debris can be observed indicating cell death, which could account for the decrease in Wnt signalling visible above 5 µM of BIO in **Figure 3.16**.

Luminescence intensity was measured in response to PM-BIO and PM-CHIR at a range of dilutions (**Figure 3.16b**). PM solutions were produced with an initial concentration of 200 µM. Both PM-encapsulated BIO and CHIR show Wnt signalling activity above that of the empty vehicle and untreated cell controls. As the PM solution incubated with cells becomes more concentrated, the Wnt signalling activity increases to a maximum level of 19.5 (SD 3.6) RLU at 1 in 5 dilution for PM-BIO and a maximum level of 16.0 (SD 1.7) RLU at 1 in 2 dilution for PM-CHIR, which in the concentration range investigated does not yet reach its maximum. In comparison, PM-BIO has greater Wnt signalling activity than PM-CHIR.

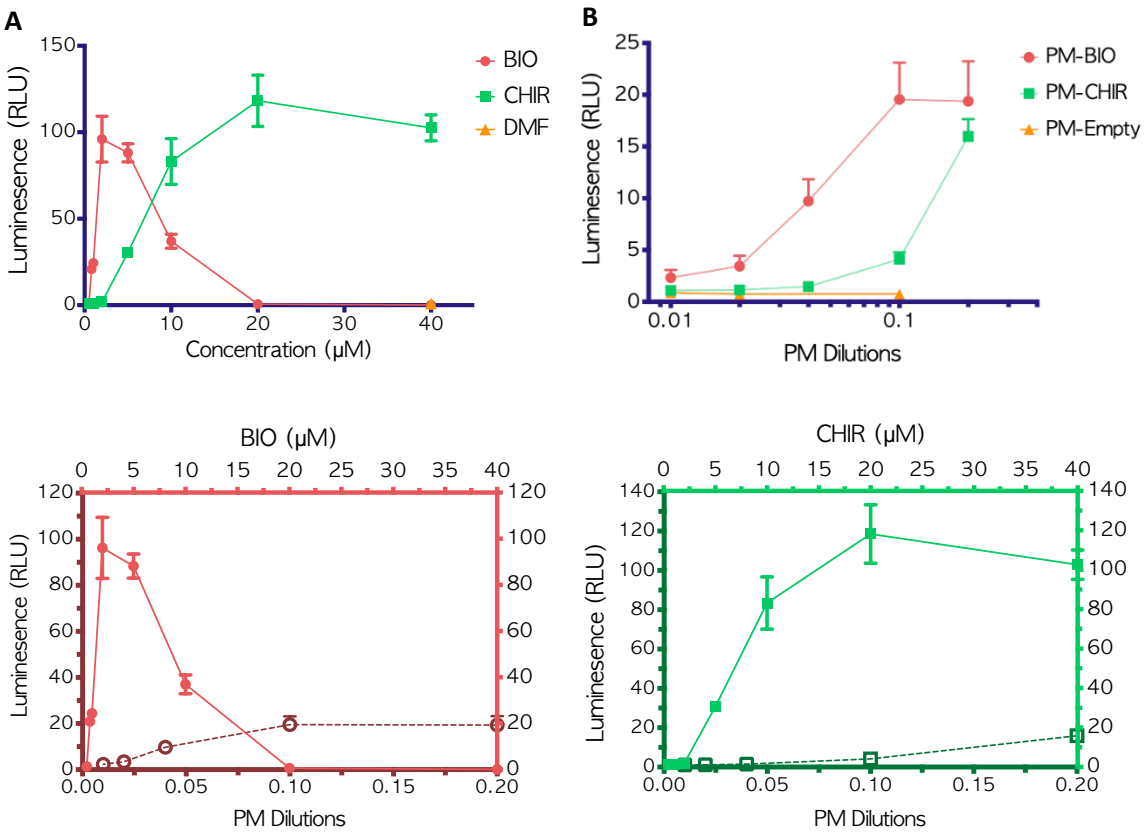


***Figure 3.16: Wnt signalling activation of 3T3 luciferase reporter cell line incubated with free and polymersome (PM) encapsulated BIO and CHIR for 24 hours***

*A) Luminescence measurements from increasing concentrations of free BIO and CHIR. Luminescence measurements from dimethylformamide (DMF), the vehicle control, are also shown. B) Luminescence intensity measurements from increasing dilutions of BIO (200 μM) or CHIR (200 μM) loaded PMs. The vehicle control, empty PM solution, measurements are also shown. Data represents mean values ± standard deviation for n=3 cell culture wells from one experiment. All data were normalised to DNA quantification and untreated cell luminescence measurements.*

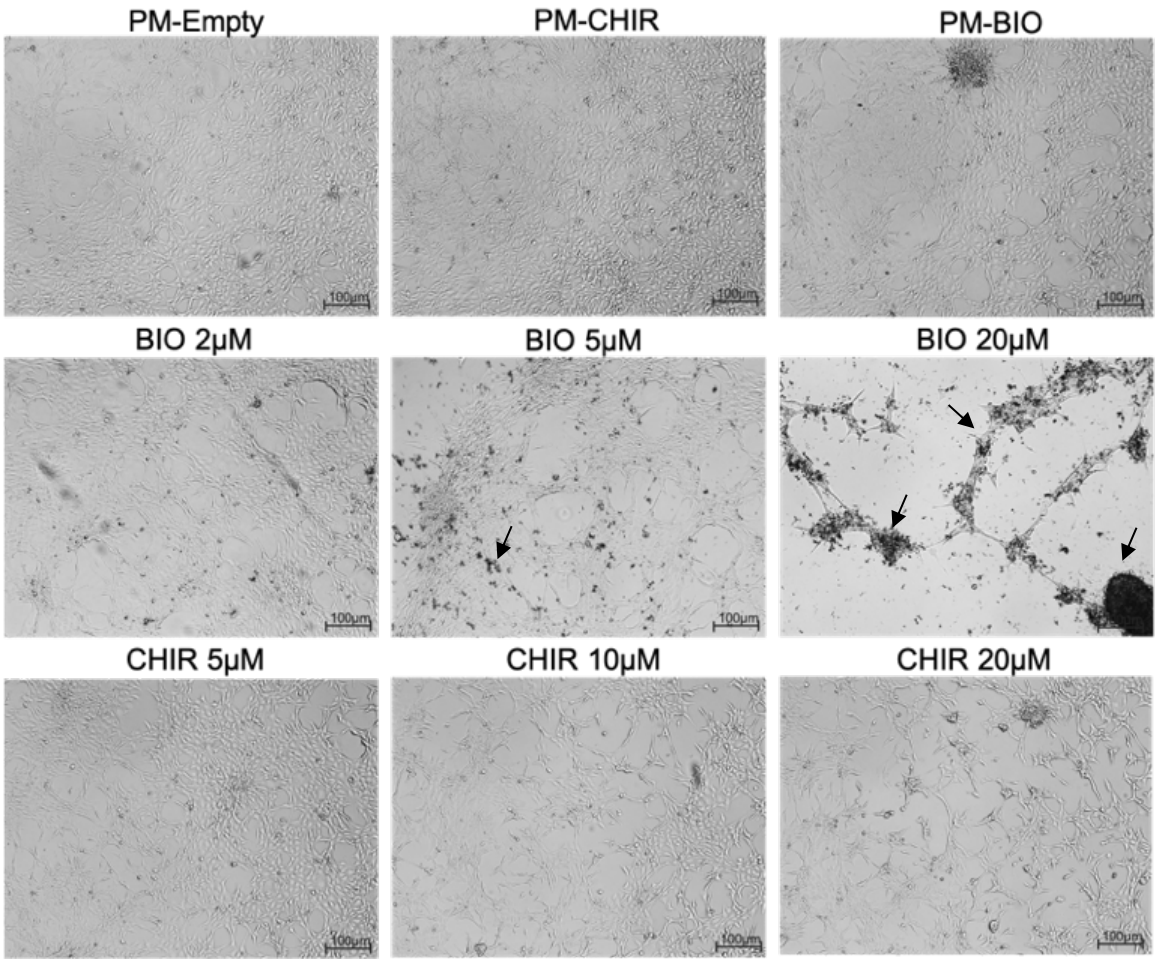


***Figure 3.17:Images of 3T3 Wnt reporter cell line cultures incubated with labelled doses of free BIO, CHIR, and filtered PMs, at a 1 in 10 dilution, for 24 hours.***

*3T3 Cells incubated with low doses of CHIR or BIO or PMs loaded with BIO or CHIR show a healthy polygonal shape and forming a monolayer. Cell incubated with high doses of CHIR or BIO show black clumps of cell debris (black arrows) and sparse areas with no cell adherence.*

### 3.3.4 Polymersome-loaded BIO and CHIR increase Wnt signalling in a dose-dependent manner

To determine if the Wnt signalling activity of PM-CHIR can be improved by altering the CHIR concentration encapsulated within PMs, PM solutions were produced with a range of initial CHIR concentrations from 50 µM to 2 mM. 3T3 Wnt reporter cell line cells were incubated for 17 hours with diluted samples of PMs before measuring luminescence intensity. With the exception of 50 µM PM-CHIR, Wnt signalling activity increases as the PM dilution decreases (**Figure 3.18a**). In comparison to free CHIR's maximum activity at a concentration of 20 µM, PM-CHIR at concentrations ≤500 µM have greater activity for 0.2 and 0.1 PM dilutions. With increasing concentrations of PM-CHIR, Wnt signalling activity also increases up to a maximum of 206.9 (SD 20.0) RLU (0.2 dilution) at 1 mM PM-CHIR, after which the activity plateaus or decreases (**Figure 3.18b**).

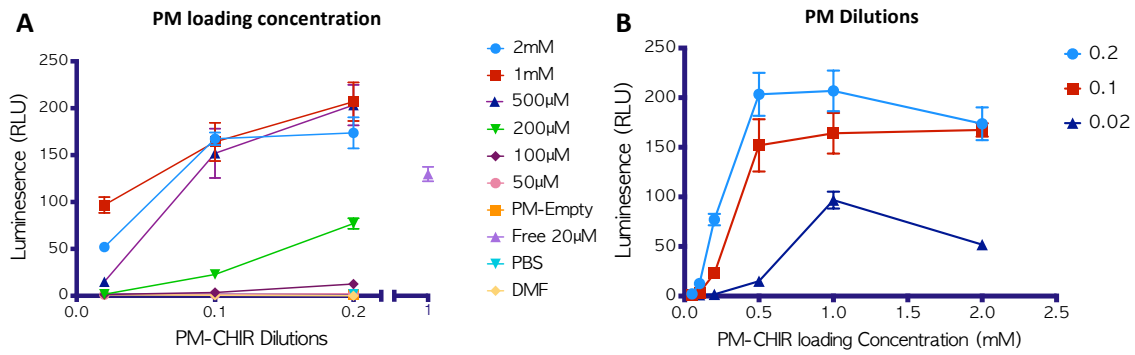


***Figure 3.18: Wnt signalling activation of 3T3 luciferase reporter cell line incubated with polymersome encapsulated CHIR (PM-CHIR) for 24 hours***

*Data presented two-ways: A) Luminescence measurements from cells incubated with increasing amounts of PM-CHIR loaded with different concentrations of CHIR. Vehicle control PM-Empty, dilutants PBS and DMF, and free CHIR at 20 µM luminescence measurements are also shown. B) Luminescence measurements from cells incubated with PM-CHIR loaded with increasing concentrations of CHIR at different dilutions of PM-CHIR. Data represents mean values ± standard deviation for n=3 cell culture wells from one experiment. All data is normalised to DNA quantification and expressed relative to untreated cell luminescence measurements.*

The same assessment was then performed on PM solutions produced with a range of initial BIO concentrations to determine if the Wnt signalling activity of PM-BIO could also be improved. **Figure 3.19** shows for 1/5 and 1/10 PM dilutions a rapid increase in Wnt signalling activity with increasing initial BIO concentration until 500 µM, after which the rate decreases and plateaus. For concentrations of 500 µM and below, as the amount of PM incubated with 3T3 cells increases Wnt signalling activity also increases. However, for 1 mM (and greater) loaded PM-BIO, Wnt signalling activity decreases with increasing amount of PMs. In comparison to free BIO with a maximum Wnt signalling activity at 5 µM, 500 µM PM-BIO at 1 in 10 and 1 in 5 PM dilutions as well as 1 mM or above PM-BIO all have equivalent or higher Wnt signalling activity.

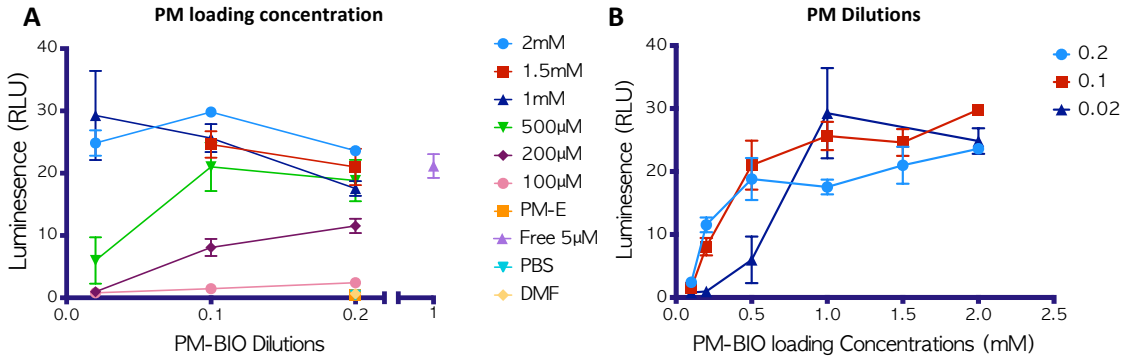


***Figure 3.19: Wnt signalling activation of 3T3 luciferase reporter cell line incubated with polymersome encapsulated BIO (PM-BIO) for 24 hours***

*A) Luminescence measurements from cells incubated with increasing amounts of PM-BIO loaded with different concentrations of BIO. Vehicle control PM-Empty, dilutants PBS and DMF, and free BIO at 5 µM luminescence measurements are also shown. B) Luminescence measurements from cells incubated with PM-BIO loaded with increasing concentration of BIO at different dilutions of PM-BIO. Data represents mean values ± standard deviation for n=3 cell culture wells from one experiment, expressed relative to untreated cell luminescence measurements.*

#### 3.3.4.1 Comparing the Wnt signalling activity of free and PM-encapsulated BIO and CHIR

Next the peak cell assay response achieved after incubation with free BIO and CHIR, and the maximum PM loading concentrations of CHIR and BIO (demonstrated in **Figure 3.18** and **Figure 3.19**), were directly compared. **Figure 3.20a** shows that PMs loaded with the maximum amount of CHIR (PM-CHIR 1 mM) have a higher Wnt signalling activity than free CHIR, with a mean difference of 21.60 RLU (95% CI, 5.6-37.6, P=0.012). This is in contrast to the relationship seen for PMs loaded with a lower CHIR concentration of 200 µM (also used in the earlier experiment shown in **Figure 3.16**) which shows PM-CHIR having a significantly lower Wnt signalling activity compared to free CHIR (P=<0.000001) (**Figure 3.20b**). This is not seen however for PM-BIO, where both 1 mM BIO and 200 µM BIO have lower Wnt signalling activity than free BIO, with a mean difference of 3.63 RLU for 1 mM (95% CI, 12.35-19.61, P=0.88) (**Figure 3.20a**) and a significant difference of 9.6 RLU for 200 µM (95% CI, 3.04-16.2, P=0.007) (**Figure 3.20b**). Additionally, when comparing the maximum PM-loaded CHIR/BIO or free CHIR and BIO, CHIR achieves a statistically significant higher Wnt signalling response (P=<0.000001 for both free and PM-loaded) (**Figure 3.20a**). Overall this shows that PM-CHIR can achieve the greater Wnt signalling response *in vitro* than PM-BIO.

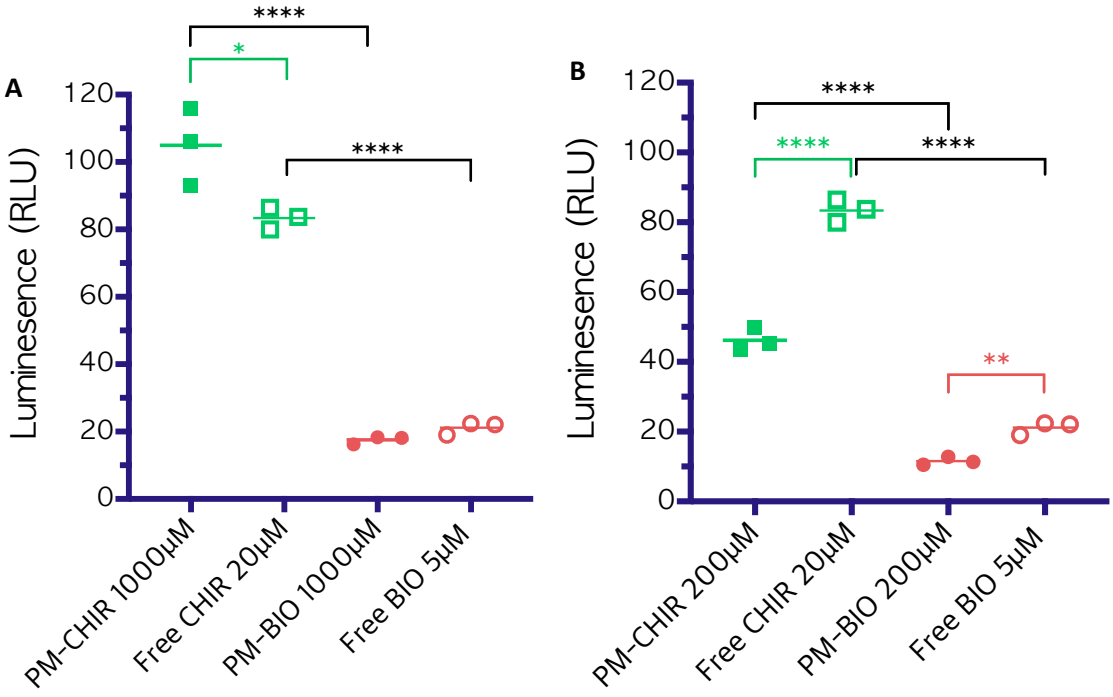


***Figure 3.20: Comparison of the maximum Wnt signalling activity induced by free and polymersome (PM)-encapsulated BIO and CHIR***

*Luminescence measurements from 3T3 Wnt luciferase reporter cells incubated with PMs loaded with either (A) 1 mM or (B) 200 µM of BIO or CHIR and free BIO or CHIR at concentrations known to give maximum activity. Data line represents mean of n=3 technical repeats and is expressed relative to untreated cell luminescence measurements. Statistical significance assessed using a one-way ANOVA with a Tukey's multiple comparisons test, *=p<0.05, ****=p<0.00001.*

### 3.3.5 PM encapsulation of BIO and CHIR improves the cytocompatibility of these compounds to human bone marrow cells

To test the cytocompatibility of polymersome-encapsulated BIO and CHIR, an *in vitro* alamarBlue cell viability assay was performed on a relevant human cell type from the bone repair microenvironment, hBMSCs. For comparison, the effect of free BIO and free CHIR on the viability of hBMSCs was also investigated. alamarBlue is an oxidation-reduction (REDOX) indicator, which both fluoresces and changes colour when resazurin is reduced to resorufin. Therefore, fluorescence intensity can be used as a readout of cell metabolic activity, where increasing fluorescence indicates reducing alamarBlue. alamarBlue fluorescence measurements are affected by both the number of cells and the length of the incubation time, therefore optimised values of these two conditions for a cell type of interest, hBMSCs, were identified by the following method. Isolated hBMSCs were seeded at a range of densities between 500 and 80,000 cells/well on a 96 well plate and incubated for 48 hours, after which alamarBlue was added and incubated at 37°C. Fluorescence measurements were then taken every hour for 8 hours. For cell seeding densities of 5000 cells/well and above, there is an increase in fluorescence intensity with respect to time for up to 4 hours of alamarBlue incubation, with the exception of the 80,000 cells/well, which has a maximum fluorescence intensity at 5 hours (**Figure 3.21a**). After these time points there is a drop in fluorescence intensity this was attributed to a lack of Oxygen and $CO_2$ control within the plate reader effecting cell metabolic activity. For subsequent experiments cells were returned to the incubator between measurements. There is a linear relationship observed between cell seeding density and alamarBlue fluorescence intensity for all time points measured; a representative plot is shown for the 4-hour measurement (**Figure 3.21c**). Linear regression analysis revealed $R^2$ of 0.99 for all time points, indicating a good data fit and that each time point is suitable for fluorescence analysis. Overall this data identifies an incubation time of 4 hours and cell seeding density of 80,000 cells/well as optimal to obtain a maximum fluorescence intensity reading; however, when taking into consideration the replicate variation and time taken for experimental cell growth, a seeding density of 20,000 cells/well and an alamarBlue incubation time of 4 hours was selected for subsequent cell viability assays.

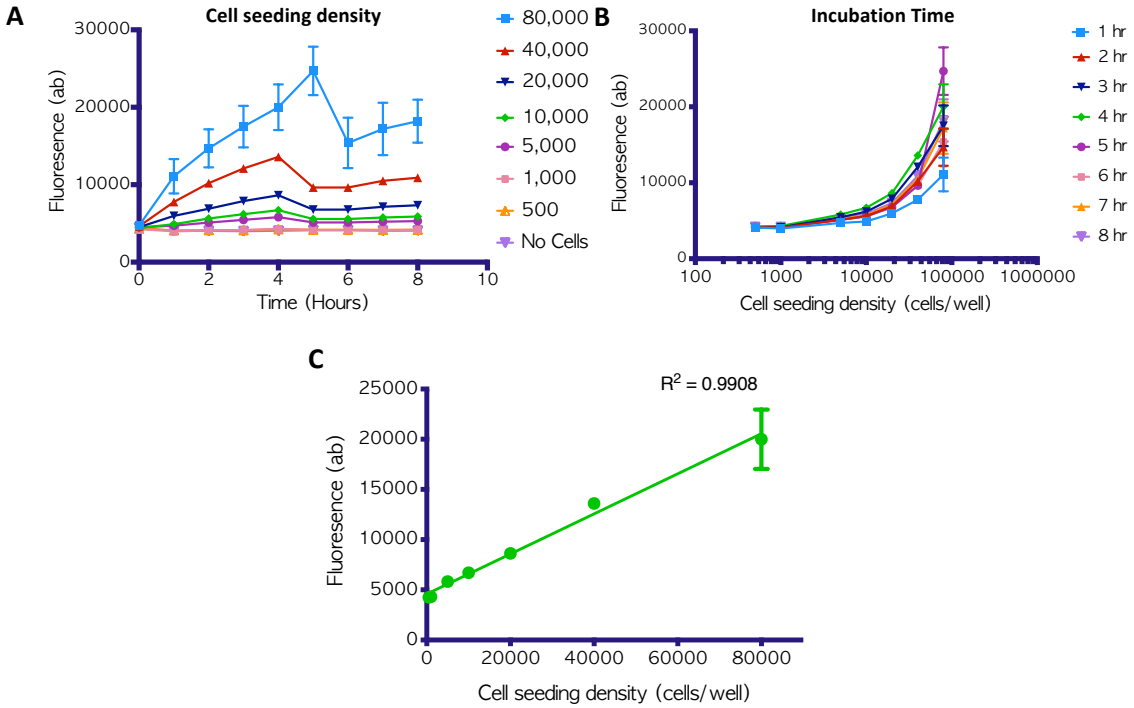


***Figure 3.21: alamarBlue fluorescence analysis of untreated human bone marrow stromal cell (hBMSC) metabolic activity***

*Fluorescence intensity measurements of hBMSCs at increasing cell densities over an 8-hour alamarBlue incubation time, presented two ways: A) grouped by density, B) grouped by incubation time. C) Fluorescence intensity measurements from increasing hBMSC cell seeding densities after a 4-hour alamarBlue incubation. Measurements taken at 37℃, between measurement cells left in machine with controlled temperature. Data represents mean values ± standard deviation for n=5 cell culture wells from one experiment.*

The optimised alamarBlue assay presented above was used to assess the metabolic activity of hBMSCs after a 24-hour exposure to increasing concentrations of free CHIR and BIO. **Figure 3.22a** shows that the activity of hBMSCs incubated with free BIO reduces in a dose-dependent manner when compared to control cells. Significantly reduced cell activity compared to control cells is observed following exposure to varying BIO concentrations as follows: 94.9% activity at 2 µM (P=0.03), 91.4% activity at 5 µM (P=0.000108), 85.3% activity at 10 µM (P=<0.0001), 72.5% activity at 20 µM (P=<0.0001), and 21.2% activity at 40 µM (P=<0.0001). For free CHIR, significantly reduced cell activity is observed at 92.5% activity for 10 µM (P=0.0052), 82.1% for 40 µM, and 55.7% for 100 µM (P=<0.0001). In comparison, free BIO with a calculated absolute half maximal inhibitory concentration ($IC_{50}$) value of 30.5 µM reduces cell metabolic activity to a greater extent than free CHIR with an undefined $IC_{50}$ within the concentration range investigated. alamarBlue fluorescence of cells incubated with DMF, the vehicle control, was measured to verify that any reduction in cell metabolic activity is the result of BIO or CHIR exposure alone. DMF has no statistically significant effect upon cell activity in comparison to control cells (**Figure 3.22a**).

Subsequently, the metabolic activity of hBMSC cells was assessed after 24-hour exposure to dialysed PM-encapsulated BIO (loaded with an initial concentration of 200 µM BIO) and PM-encapsulated CHIR (loaded with an initial concentration of 1 mM CHIR). **Figure 3.22b** shows hBMSCs incubated with PM-BIO display a significant reduction in cell activity compared to control cells: 90.1% activity for 1 in 2 PM dilution (P=0.000158), 92.2% for 1 in 5 dilution (P=0.00243), 92.01% for 1 in 10 dilution (P=0.00195), and 93.3% for 1 in 50 (P=0.0099) when. Cells incubated with PM-CHIR show a significant decrease in cell activity compared to control cells at 90.8% activity for 1 in 10 PM dilution (P=0.017). As the quantity of PM-CHIR that cells are incubated with increases, the average percentage cell activity remains between 90.0% and 98.0%. PM-Empty, the vehicle control, shows comparable cell activity to control cells, with an average percentage remaining between 96.6% and 99.3% (**Figure 3.22b**).

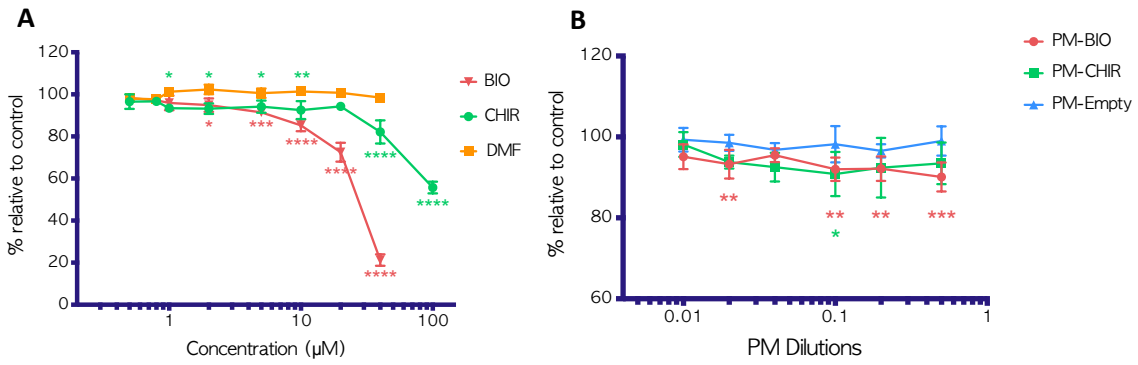


***Figure 3.22: Human bone marrow stromal cell (hBMSC) metabolic activity following exposure to free and polymersome-encapsulated BIO and CHIR***

*A) alamarBlue fluorescence measurements of hBMSCs incubated with increasing concentrations of free BIO and free CHIR and the vehicle control, Dimethylformamide (DMF). B) alamarBlue fluorescence measurements of hBMSCs incubated with increasing amounts of polymersome encapsulated BIO and CHIR. The vehicle control PM-Empty is also shown. Data is presented minus the blank control (alamarBlue and media with no cells) mean and normalised to untreated cell controls. The results represent mean values ± standard deviation for n=5 cell culture wells from one experiment. Statistical significance is assessed using one way ANOVA with Dunnett's multiple comparison test, ****=p<0.0001, *=p<0.05.*

### 3.3.6 The effects of free vs. polymersome-encapsulated BIO and CHIR on the cytocompatibility and proliferation of mouse bone marrow cells

Future progression of a BIO or CHIR loaded PM therapeutic will require assessment in an animal model, such as the mouse model described later in this thesis (**Chapter 4** ). Accordingly, the cytocompatibility of PM-BIO and PM-CHIR was assessed using primary mouse bone marrow stromal cells (mBMSC). As with the studies on hBMSCs, an optimal seeding density and alamarBlue incubation time was determined. Isolated mBMSCs (**section 2.2.4**) were seeded at increasing cell densities and measured once every hour for 8 hours, and again at 24 hours. **Figure 3.23** shows for each seeding density the level of alamarBlue fluorescence increases with time, up to 8 hours. At 24 hours a large variation in fluorescence is observed between repeat samples especially for the highest seeding density measured at 20,000 cells/well. Fluorescence increases with cell seeding density at each time point up to 8 hours. Linear regression analysis reveals for each time point up to 6 hours an $R^2$ value of 0.99, indicating any one of these incubation times would be appropriate for use in further experiments. A representative linear plot is shown for 4 hours (**Figure 3.23c**); here, the incubation time was selected for practicality in subsequent alamarBlue investigations using mBMSCs. Cell seeding at a density of 5000 cells/well was selected; this was a practical consideration to maximise the utility of available cells whilst still producing a linear increase in fluorescent signal (Figure 3.23a).

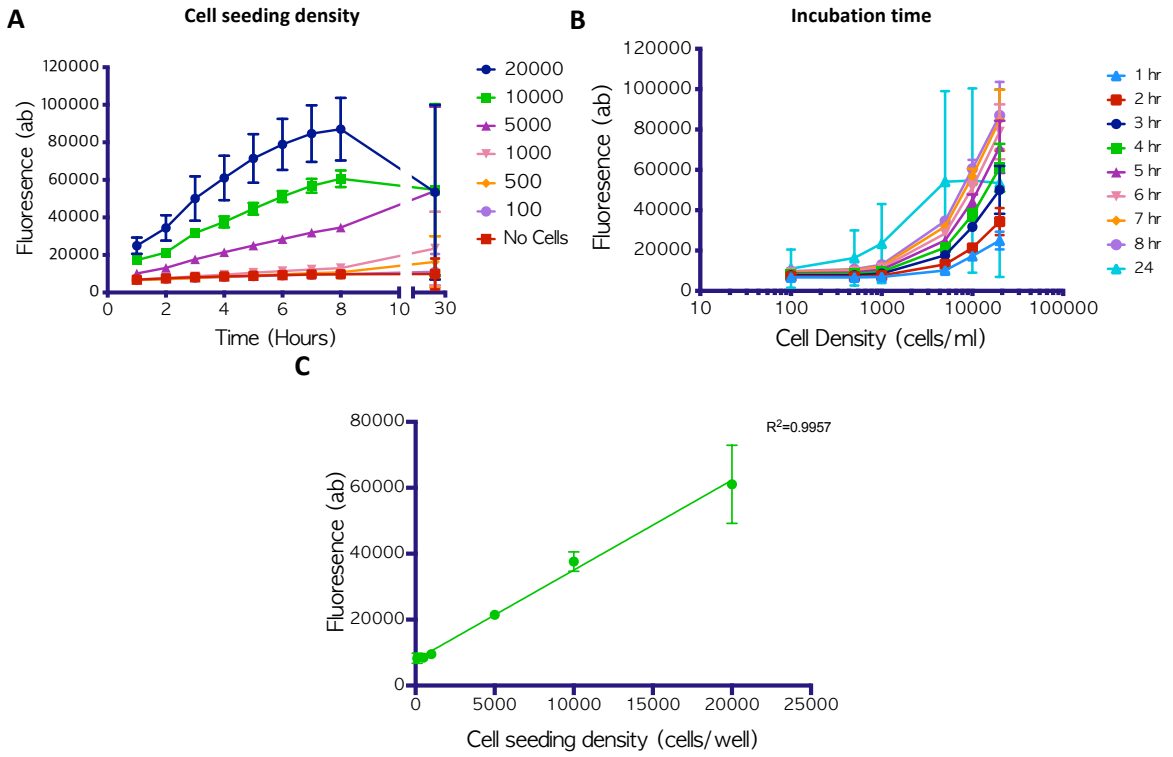


***Figure 3.23: Determining the optimum length of alamarBlue incubation and cell seeding density for primary mouse bone marrow stromal cells (mBMSCs)***

*Fluorescence intensity measurements of mBMSCs at increasing cell densities over an 8-hour alamarBlue incubation time, presented two ways: A) grouped by density, B) grouped by incubation time. C) Fluorescence intensity measurements from increasing mBMSC cell seeding densities after a 4-hour alamarBlue incubation. Measurements taken at 37℃ and between measurements plates kept in Incubator at 37℃. Data represent mean values ± standard deviation for n=5 cell culture wells from one experiment.*

The optimised alamarBlue assay presented above was used to assess the metabolic activity of mBMSCs after a 24-hour incubation with increasing concentrations of free CHIR and BIO. **Figure 3.24a** shows that both free BIO and free CHIR reduce the activity of mBMSCs in a dose-dependent manner. For BIO a significant decrease in activity compared to control cells is observed at 0% activity for 40 µM, 5.5% for 20 µM, 42.1% for 10 µM and 60.5% for 5 µM (all P=<0.0001). For cells incubated with free CHIR, there is significant decrease in activity compared to control cells, 14.3 % for 100 µM and 62.8% for 40 µM (both P=<0.0001). mBMSCs were also incubated with DMF, the dilutant used to generate stock BIO and CHIR, at a concentration equivalent to that present in diluted doses of BIO/CHIR. No statistically significant reduction in cell activity is present. In contrast, free BIO with a calculated absolute half maximal inhibitory concentration ($IC_{50}$) value of 7.6 µM reduces cell metabolic activity to a greater extent than free CHIR with an $IC_{50}$ at 65.08 µM (**Figure 3.24a**).

Next the cellular activity of mBMSCs incubated for 24 hours with PMs loaded with an initial concentration of 200 µM BIO and 1 mM CHIR was compared to control cells using the alamarBlue assay. PMs loaded with PBS (PM-Empty) were used as a vehicle control. **Figure 3.24b** shows mBMSCs incubated with a 1 in 2 dilution of all three PMs investigated have a significant reduction in activity compared to control cells. For PM-BIO the activity reduced to a level 65.5% of control cells (P=0.00097), for PM-CHIR activity it reduced to 76.9% (P=<0.0001), and for PM-Empty activity it reduced to 83.4% (P=0.00036). However, with the exception of PM-CHIR, all other PM dilutions show no significant reduction in activity. For PM-CHIR an apparently slight reduction in cell activity is observed at a 1 in 5 and 1 in 50 PM dilution - this was found to be significant (P=0.014 for 1 in 5 and P=0.036 for 1 in 50). Overall, activity of cells incubated with PMs remained above 66% of the control cell activity.

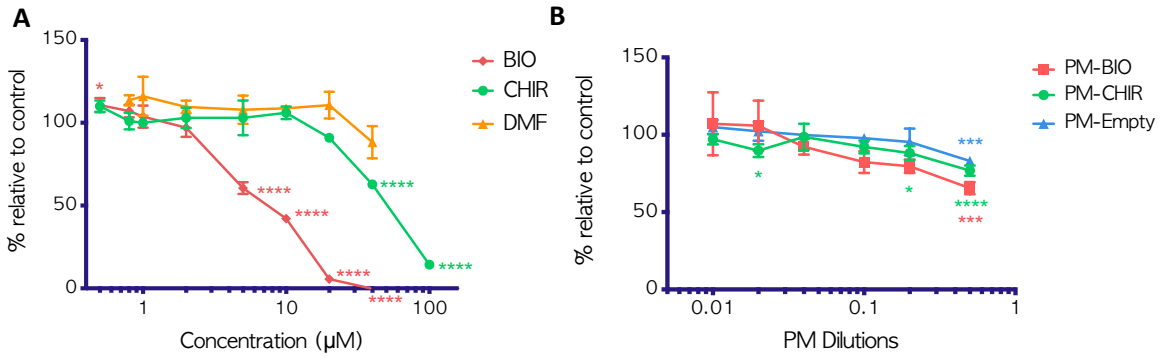


***Figure 3.24: Mouse bone marrow stromal cell (mBMSC) metabolic activity post 24-hour exposure to free or polymersome (PM) encapsulated BIO (200 µM) or CHIR (1 mM)***

*A) alamarBlue fluorescence measurements of mBMSCs incubated with increasing concentrations of free BIO and free CHIR and the vehicle control, Dimethylformamide (DMF). B) alamarBlue fluorescence measurements of mBMSCs incubated with increasing amounts of PM-encapsulated BIO and CHIR and vehicle control PM-encapsulated PBS (PM-Empty). Data is presented minus the blank control (alamarBlue and media with no cells) mean and normalised to untreated cell controls. Data represent mean values ± standard deviation for n=4 cell culture wells from one experiment. Statistical significance assessed using one way ANOVA with Dunnett's multiple comparison test, ****=p<0.0001, *=p<0.05.*

The alamarBlue assay also informs of the effect a treatment has upon cell proliferation over time. This was used to assess the effects of PM-BIO and CHIR upon mouse osteoblast proliferation. Isolated primary mouse osteoblasts (characterised by a separate *in vitro* mineralization assay with an ALP stain) were seeded at increasing densities and incubated with free BIO (2 μM), free CHIR (10 μM), PM-BIO (initial loading 200 μM), PM-CHIR (initial loading 1 mM) and PM-Empty over a period of 8 days. **Figure 3.25a** shows that the cell activity, measured by alamarBlue fluorescence, increases with time for each cell seeding density (with the exception of 2500 cells/well, which plateaus after 3 days). **Figure 3.25b** presents one data set of cell activity after incubation with BIO or CHIR compared to control cells. For BIO, a reduced rate of fluorescence increase compared to the control cells (media only) is apparent; however, the differences are not statistically significant at any timepoint. For CHIR, the rate of mean fluorescence increase over time is the same as the control.

**Figure 3.26** shows cells incubated with PM-BIO – like with free BIO – have a decreased rate of fluorescence increase over time compared to control cells (though again, the differences are not significance). For cells incubated with PM-CHIR, after 1-3 days the increase in fluorescence remains consistent compared to control cells; from 6 days onwards, an observable difference in mean fluorescence is seen, with cells incubated with CHIR increasing at a faster rate, albeit not significantly. This same effect is observed across all time points for cells incubated with PM-Empty, from 3260 (ab) difference at 1 day to 13200 (ab) difference at 8 days, with PM-Empty increasing in fluorescence at a faster rate than control cells. Significance is achieved at day 7 ($P=0.049$) and day 8 ($P=0.044$) compared to control cells.

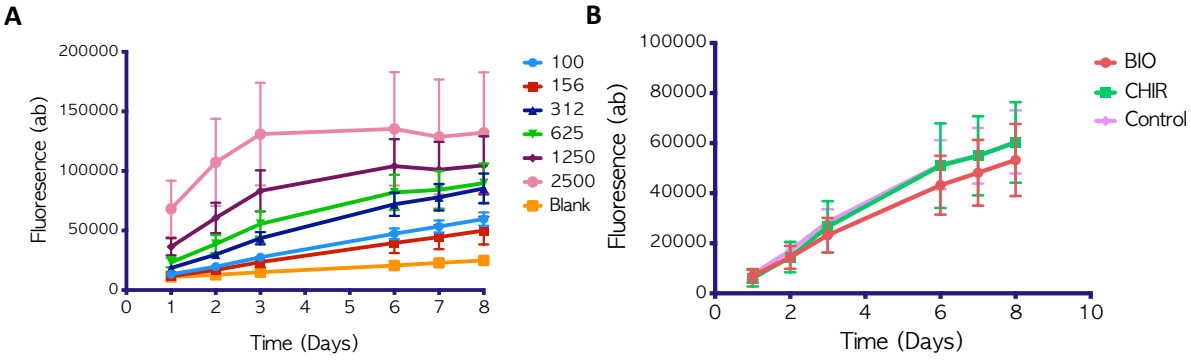


***Figure 3.25: Proliferation of mouse osteoblasts when incubated with free BIO and CHIR***

*A) Plot of alamarBlue fluorescence over 8 days for increasing cell seeding densities of primary mouse osteoblasts. B) Plot of alamarBlue fluorescence over 8 days for cells seeded at 312 cells/well and incubated with an initial dose of 5 µM free BIO (red), 10 µM free CHIR (green), or media alone (control, pink). Data represent mean values ± standard deviation for n=4 cell culture wells from one experiment.*

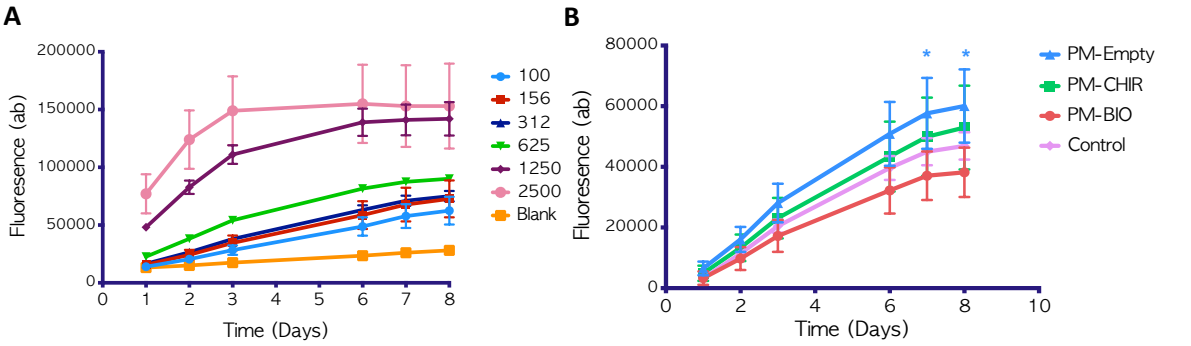


***Figure 3.26: Proliferation of mouse osteoblasts when incubated with polymersome (PM)-encapsulated BIO, CHIR, and PBS***

*A) Plot of alamarBlue fluorescence over 8 days for increasing cell seeding densities of primary mouse osteoblasts. B) Plot of alamarBlue fluorescence over 8 days for cells seeded at 312 cells/well and incubated with media alone (control) or an initial dose of 1 in 10 dilution of PMs loaded with either PBS (PM-Empty), BIO 200 µM (PM-BIO), or 1 mM CHIR (PM-CHIR). Data represent mean values ± standard deviation for n=4 cell culture wells from one experiment. Statistical significance assessed using multiple t test with Holm-Sidak method, * = p<0.05.*

## 3.4 DISCUSSION

The small molecules BIO and CHIR are Wnt signalling agonists that could be used to treat bone injuries and improve fracture outcomes. However, use of these hydrophobic reagents are limited by poor solubility and low dose toxicity. This thesis proposes that any positive therapeutic effects of BIO and CHIR would be improved by a targeted drug delivery system using polymersomes (PMs). However before testing therapeutic benefit, there is first a need to determine whether the biological activity of BIO and CHIR (particularly their ability to activate Wnt signalling) is maintained when encapsulated within PMs. There is also a need to determine what encapsulated dose is obtainable and safe for subsequent assessment of treatments.

Previously published work by Scarpa has already established that BIO can successfully be loaded into PMs and activate Wnt signalling *in vitro* (Scarpa, *et al.*, 2018). This chapter aimed to develop the characterisation of the PM delivery system and investigate the encapsulation efficiency and cytocompatibility of PM-BIO, as well as develop CHIR loaded PMs to provide an alternate Wnt-agonist treatment option for bone repair.

This chapter demonstrates the successful production of PEG-*b*-PCL polymersomes loaded with a dose of BIO or CHIR that is sufficient to induce a Wnt signalling response *in vitro.* It also demonstrates that PM delivery improves the cytocompatibility of BIO and CHIR when incubated with primary bone cells in culture.

### 3.4.1 The Wnt signalling activity of PM-BIO and PM-CHIR

There are numerous published examples of successful encapsulation of small molecules specifically within PEG-*b*-PCL nanoparticles (Grossen *et al.*, 2017), giving premise for their use in this work for the encapsulation of BIO and CHIR. At the time of writing, one other study by Scarpa, *et al.* (2018) has investigated specifically the loading of BIO into PEG-*b*-PCL nanoparticles, and reported an encapsulation efficacy of 90%, stability for 1-2 days, and successful inducement of Wnt signalling following incubation with a Wnt reporter cell line for 24 hours. Using the same reporter cell line, this chapter emulates Scarpa's results, showing successful Wnt signalling activation for PM-BIO. In addition, this chapter further demonstrates for the first time the successful loading of CHIR into PMs, and that these also induce Wnt signalling.

BIO and CHIR both interact at the ATP binding site of GSK3, indicating that both reagents competitively inhibit the targeting of β-catenin for degradation, and subsequently mimic the

activation of the Wnt signalling pathway (Meijer, Flajolet and Greengard, 2004). Previous studies have explored this and found successful Wnt signalling activation in a range of cell types including in the target tissue in this study, i.e. bone (see **section 1.7.5**). It was therefore to be expected that PM-CHIR, like PM-BIO, would induce Wnt signalling; however, the data also reveals that when loaded with the same initial concentration of reagent (200 µM), PM-BIO has a higher Wnt signalling activation than PM-CHIR.

Investigation of the Wnt signalling activity of free (i.e. unencapsulated) BIO and CHIR also displays this difference. Specifically, it was found that a greater concentration of free CHIR (20 µM) is required to achieve equivalent Wnt signalling activity of 2 µM BIO. This observation was similarly reported in other studies which used a luciferase reporter system to measure the Wnt signalling activity of BIO and CHIR in a different cell line (mouse embryonic stem cells, mESCs), and found a greater concentration of CHIR is required in comparison to BIO for significant Wnt signalling activity (Naujok *et al.*, 2014; Wu *et al.*, 2015). Additionally an *in vivo* study that compared CHIR and BIO treatment of a tooth injury also found an equivalent expression of *Axin2* (a Wnt target gene) within the injury site, when using a smaller concentration of BIO (50 nM) compared to CHIR (5 µM) (Neves *et al.*, 2017). CHIR's less potent Wnt signalling capability partly explains the lower Wnt signalling achieved after incubation with PMs; this was further affected by its lower encapsulation efficiency, described below.

### 3.4.2 The effect of encapsulation efficiency upon PM-BIO and PM-CHIR Wnt signalling

Another factor in the difference of Wnt signalling stimulated by PM-BIO and PM-CHIR is likely to be the PM encapsulation efficiency. Absorbance spectroscopy measurements revealed that across different batches of PMs, PM-BIO had a higher average encapsulation efficiency (67%) than PM-CHIR (37%). An encapsulation efficiency of less than 100% is to be expected due to the chosen production method's use of a dialysis step (**Figure 2.1**); here, unencapsulated BIO/CHIR will move from the PM-solution to the dialysate, driven by the diffusion gradient across the dialysis membrane (Modi and Anderson, 2013). However, the notable difference in the encapsulated doses measured here could also indicate a difference between the interaction of BIO and CHIR with the chemistry of the PMs themselves.

Numerous factors can influence the strength and type of drug-polymer interaction, including polymer block length, PCL crystallinity, the addition of chemical moieties, drug hydrophobicity, number of available H bonds, ionic interactions, and the encapsulation method used (Ke *et al.*, 2014; Grossen *et al.*, 2017). In a study by Liu *et al.* (2011), the effect of doxorubicin (DOX) hydrophobicity on encapsulation efficiency and release of a drug from PLA-*b*-PMPC polymersomes was investigated.

A hydrophilic variation of DOX, DOX-HCL, showed lower encapsulation and a faster release rate compared hydrophobic DOX. This and other studies suggest that molecules with greater hydrophobicity interact more strongly within the polymer region that forms the membrane. When comparing hydrophobicity, CHIR has a slightly higher XLogP3 value of 4.3 compared to BIO with a value of 3.9, suggesting CHIR would produce stronger hydrophobic interactions with the PCL polymer. The results of this chapter show an encapsulation efficiency contrary to this expectation, with PM-BIO consistently having a higher drug load. This suggests other factors have a weighted influence on encapsulation efficiency.

In a study by Shuai *et al.* (2004a), it was found that increasing the length of a PCL block results in an increase of Paclitaxel loading. Conversely in a similar experiment with Doxorubicin, Shuai found no significant increase in drug loading with increasing block length. This was attributed to a difference in hydrophobicity of the two drugs, with Doxorubicin containing polar hydroxyl and amino groups producing less hydrophobic molecules than Paclitaxel (Shuai, Ai, *et al.*, 2004b). These results indicate that for more hydrophobic molecules the amount of PCL "space" available will affect loading efficiency. In this chapter, consistent length block polymers were used (5K PEG-*b*-18k PCL). Since the available PCL therefore remains consistent, it could be inferred that the loaded molecule size will be limiting space for interactions. CHIR has a larger molecular weight (465.3 g/mol) than BIO (356.2 g/mol). As well as affecting encapsulated dose, the strength and placement of drug and polymer interactions results in different diffusion distances and will also affect the rate of drug release and subsequent Wnt signalling activity. With BIO being smaller in size and slightly less hydrophobic than CHIR, it could be reasoned that BIO has a faster release rate, contributing to its measured higher Wnt signalling activity. Further study of BIO and CHIR release rates from PMs and Wnt signalling over time would help to test this theory.

### 3.4.3 Finding the maximum PM loading dose of BIO and CHIR

A further finding of this work was that the Wnt signalling activity of PM-encapsulated BIO and CHIR reached only 20% of the maximum activity seen for free BIO (at 5 µM) and free CHIR (at 20 µM). Similarly, Scarpa *et al.* (2018) also found that in 3T3 luciferase reporter cells, after 24 hours of exposure, PM-BIO produced 40% of the maximum activity seen for free BIO (at 5 µM). Further study measuring Wnt signalling over time would determine whether this is the result of payload retention at the timepoint studied.

In order to increase the Wnt signalling activity induced by PM-BIO vs. PM-CHIR, the maximum encapsulation dose that could be achieved was investigated. The results demonstrated a relationship

between loading concentration and Wnt signalling activity which peaked at 1000 µM for CHIR and 1500 µM for BIO. Above this loading concentration, absorbance spectroscopy readings revealed a plateau in retained concentration post dialysis, suggesting the Wnt signalling activity was limited by PM loading capacity rather than any inhibitory effect within the Wnt cell assay response itself. Interestingly, in a comparison of the Wnt signalling induced by PM-BIO vs. PM-CHIR loaded with a high concentration (1 mM), PM-CHIR induced a higher level of signalling than PM-BIO, contrary to previous results. A possible explanation for this change could be differences in the relative toxicity of BIO and CHIR, discussed below.

### 3.4.4 The cytocompatibility of PM-BIO and PM-CHIR

Studies have shown that BIO and CHIR have toxic effects at high concentrations (Naujok *et al.*, 2014). In a study by Hoffman and Benoit (2014), isolated hBMSCs were incubated with BIO for 24 hours; concentrations of BIO above 5 µM resulted in cell death. Correspondingly in this chapter, free BIO at concentrations above 5 µM resulted in a clear decrease in Wnt signalling activity. Observations of the cell culture under these conditions led to the hypotheses that this change in activity was the result of cell toxicity and that PMs protect against this effect. To test this, isolated human and mouse primary bone marrow cells (relevant to the target treatment environment) were used in an alamarBlue cell metabolic activity assay to assess the toxicity of both free and PM-loaded BIO and CHIR. It is important to note that a consistent cell number in the assay was assumed, which may have affected the accuracy of the findings. An alternative would have been to perform a further PicoGreen assay to determine and normalise the results to a known cell number. Regardless, consistent with Hoffman's study it was found that incubation with 5 µM and over of free BIO caused a decrease in cell viability of human and mouse BMSCs.

Additionally, the data revealed that CHIR is less toxic than BIO at equal concentrations; this difference in cytotoxicity has been observed for other cell types. Naujok *et al.* (2014) investigated the cell viability of mouse embryonic stem cell line ES-D3 and found a 50% decrease in cell viability at 0.5 µM of BIO and at 5 µM CHIR. Using a mouse dental mesenchymal cell line (17IA4 cells), Neves *et al.* (2017) found a 50% decrease in cell viability resulted from 5 µM of CHIR yet only 50 nM of BIO. This difference in inherent toxicity could explain the greater degree of Wnt signalling observed from PM-CHIR compared to PM-BIO when PMs are loaded with equal, high, concentrations. However, the cytotoxicity study described earlier in this chapter revealed little to no decrease in cell viability when BMSCs were incubated with PM-BIO/CHIR (unlike for free BIO/CHIR). Here the cell viability remained above 70%, which ISO-10993 guidelines set as the threshold under which a substance is considered

cytotoxic; this suggests that PMs have a protective effect, reducing the toxic effects of BIO and CHIR. This effect is also demonstrated in the Wnt signalling activity results, with cells displaying no decrease in signalling when incubated with comparatively greater concentrations of reagent delivered by PMs than unencapsulated.

Of note the cytotoxicity study only assessed PMs loaded with 200 μM of BIO rather than 1 mM loading used for PM-CHIR. At this lower loading concentration, for cells incubated with more concentrated samples of PMs, a significant decrease in cell metabolic activity was observed for PM-BIO (although not below the threshold 70%, as mentioned previously). It could therefore be predicted that at higher loading concentrations the cell metabolic activity would reduce further, again supporting the theory that BIO's toxicity led to the lower Wnt signalling induced by PM-BIO compared to PM-CHIR.

In addition to investigating cell viability, the alamarBlue assay was used to investigate the effects of PM-BIO/CHIR upon cell growth. Previous studies have demonstrated the ability of both BIO (Hoffman and Benoit, 2015) and CHIR (Narcisi *et al.*, 2016) to increase cell proliferation of mesenchymal stem cells (MSCs). Hoffman and Benoit (2015) reported that incubation of MSCs with 2 μM or 5 μM of BIO leads to cell number increases of 1.5- and 2.5-fold respectively compared to control cells. In this chapter, 5 μM of free BIO was used and resulted in a slight decrease in cell growth (although not significant) compared to control cells. This difference could be accounted for by the use of different cell sources: in the previously-discussed cell viability study, 5 μM of BIO was found to decrease cell viability to a greater extent in mouse BMSCs compared to human. Narcisi *et al.* (2016) reports that MSC exposure to 2.5 μM or 5 μM of CHIR-99021 results in a statistically significant increase in proliferation. In this chapter, the use of 10 μM of CHIR resulted in no difference to cell proliferation. Toxicity studies show that at this concentration cell activity starts to decrease. Further work using a lower concentration would reveal if the selected concentration was too high, with resultant toxic effects offsetting any proliferative effects. Notably at the lowest BIO concentration investigated (0.5 μM) there is a significant increase in activity compared to that seen in control cells. This demonstrates that concentration is important in balancing cell activity/growth vs. inhibition of cell activity/toxicity.

It was expected that, as in the cell viability study, PMs would have protective effect enabling BIO/CHIR to increase cell growth. Unexpectedly a similar effect was observed to that seen for free BIO/CHIR, in which cell growth slightly decreased following incubation with PM-BIO and remained consistent with the control following incubation with PM-CHIR. It may be that the PM loading dose of BIO/CHIR used in this study was again sufficient to have negatively impacted cell activity, leading to

reduced rate of cell growth over time. More specifically, the previously-discussed toxicity study demonstrated that cell metabolic activity decreased (especially for PM-BIO) after 24 hours exposure; over time, this decrease may therefore be enough to affect longer term cell growth.

It is also interesting to note that exposure of cells to the vehicle control, PM-Empty, resulted in an increase in the rate of cell growth. A possible explanation for this effect is that, once taken up by a cell, the biodegradable products of the polymersome induces a cell proliferation response. This effect was studied by Zhu *et al.* (2019), who found that PCL-*b*-PE increases the proliferation of primary dermal fibroblasts and attributed this to an observed down regulation of p21 and p53 cell cycle regulator genes. In further *in vivo* studies this effect will be important to consider in the variety of cell types which may take up PMs.

Collectively this data demonstrates PMs enable delivery of a higher concentration of BIO/CHIR whilst reducing their toxic effects, but also that this apparent protective effect has a limit. Additionally, the synthesised PM-BIO and PM-CHIR doses were found to not be cytotoxic to hBMSCs or mBMSCs and, despite there being no significant increase in cell proliferation, they did not inhibit cell growth of mouse osteoblasts, thereby achieving some evidence of their safety as a treatment. These data, alongside data from an *in vivo* study by Scarpa (2016) using the same mouse model and PM synthesis, suggest that the PM-BIO and PM-CHIR doses tested are safe for future *in vivo* investigation. As well as assessment of the impact of BIO/CHIR treatment upon cell metabolic activity and growth, future work could benefit from assessing its impact upon mouse osteoblast protein production (such as ALP or collagen) and direct measures of apoptosis, to provide further insight into how treatment affects cell health.

### 3.4.5 The characteristics of developed PMs

In addition to successfully encapsulating BIO or CHIR, for PMs to be used as a therapeutic delivery system it is also essential that they are produced having a stable uniform size. The size of PMs will affect the amount of payload encapsulated, hence variations in size may lead to dosage variations. Size also affects cellular uptake, extraversion (and hence circulation time), and organ distribution *in vivo*. Therefore producing PMs of a consistent size is crucial to ensure later accurate measurement of the distribution and therapeutic effects of PM-BIO/CHIR.

Using DLS, the presence of uniformly sized particles was confirmed in both control (PM-Empty) and PM-BIO/CHIR solutions, with an average PM hydrodynamic size of 83-93 nm. Furthermore, there was low variability in size (81-100 nm) when PMs were loaded with different concentrations of payload. A

small degree of size variability when encapsulating BIO or CHIR is to be expected, due to their additional electrostatic forces interacting with polymer chain association (Brinkhuis, Floris and van Hest, 2011). Scarpa *et al.* (2018) used the same solvent switch production method and polymer chemistry used in this study, and reported an average size of 63 $\pm$ 26 nm from DLS measurements; this result further supports the reproducibility of this production method. However, it is important to note that DLS size calculations assume a solid spherical configuration, whereas polymersomes are known to have a flexible and fluidic membrane that can be subject to compressive forces affecting size measurements (Brinkhuis, Floris and van Hest, 2011). Therefore the calculated size must be taken as representative and measurement conditions must be kept consistent to enable batch to batch comparisons.

In addition to consistent size, a high yield of PMs is desired, as this will also affect the delivered dose. NTA analysis revealed an average concentration of 2-3 x $10^{13}$ cells/mL for PMs loaded with BIO or CHIR, and 4 x $10^{13}$ cells/mL for empty (PBS loaded) PMs. This result again closely corresponds to NTA measurements recorded by Scarpa *et al*. (2018), wherein BIO loaded PMs produced in the same manner used in this work had an average concentration of 1.5 x $10^{13}$ cells/mL; however, no measurement of how this compared to the concentration of PM-Empty is reported. In this chapter, a second method of MADLS was used to assess particle concentration, which measured lower average concentrations of 8.5 x $10^{10}$ and 4 x $10^{11}$ cells/mL for BIO and CHIR loaded PMs respectively, and 3.6 x $10^{11}$ cells/mL for PM-Empty. A difference between the results reported by NTA and MADLS is to be expected, as each method utilises different techniques to capture particle movement and different algorithms from which concentration is calculated. Indeed, for size measurements, NTA produces a number-weighted distribution whereas DLS provides an intensity-weighted distribution, and hence the NTA results display a smaller size relative to DLS results. An experiment which compared these two methods for the concentration analysis of a liposome formulation found that MADLS was suited to higher concentration measurements where NTA was more suited to lower concentrations (Malvern Panalytical Limited, 2018). Furthermore, results were obtained from PMs produced on separate occasions, and since DLS and UV-vis grouped data shows that small inter-batch variations in size and payload is expected, this could be a contributing factor to the observed difference. A better way to compare readings in future would be to measure the same PM preparation with both methods and measure several dilutions to determine a linear range where the concentration results may overlap.

Overall, the results presented in this chapter have shown successful formation of uniformly sized particles loaded with either BIO or CHIR. However, the methods used in this study are subject to some limitations, as discussed below.

### 3.4.6 Study limitations

The size (which may range from nm to µm scale) and yield of synthesised PMs is dependent on the method of production (LoPresti *et al.*, 2009). It is known that the ratio of hydrophilic to hydrophobic polymer segments directs a higher yield of a polymersome vs. polymeric micelle formation (Brinkhuis, Floris and van Hest, 2011), however the spontaneous self-assembly nature of the solvent switch PM production technique used in this work makes it likely that both morphologies are present in the PM solutions; separation is only possible through further purification steps. Visual techniques such as TEM imaging could be used in future to confirm the production of a specific PM morphology.

The chosen strategy for measuring encapsulated concentrations also has some limitations. Firstly, it is known that CHIR has a peak absorption at low (~270 – 289 nm) wavelengths (Francis, 2014) which correspond to the region where PM light scatter is observed (PM-Empty spectrum, **Figure 3.4**), thereby possibly interfering with detection of low CHIR concentrations. This was particularly evident for the 50 µM PM-CHIR solution in which no peak could be observed at 277 nm above the PM-Empty curve **(Figure 3.10**). Secondly, UV-Vis spectroscopy has a limited detection range, whereby measuring non-diluted PM solutions produces saturation whilst measurements of very low concentrations of encapsulated compounds are subject to large degrees of noise. Therefore alternative methods to UV-Vis are recommended for future experiments to further determine encapsulation efficiency; one example is HPLC, which has a higher range of sensitivity than UV-Vis and hence enables detection over a greater range of concentrations (Siddiqui, Alothman and Rahman, 2017).

In addition, it is important to note that the experimental approach used only provides calculated concentrations of the PM solution as a whole, and cannot distinguish the signals of encapsulated CHIR/BIO from those of any free CHIR/BIO that remains within the solution post-dialysis (Modi and Anderson, 2013). This could be improved by employing an ultracentrifugation step to separate PMs from free solution.

Furthermore, note that absorbance spectroscopy is only able to measure in solutions. Specifically, any BIO or CHIR which has precipitated will be under-represented in the resultant measurements. Nevertheless, the results demonstrate successful encapsulation of BIO/CHIR. This can be verified as it is expected that the dialysis process removes the majority of free BIO/CHIR from a solution;

therefore, if the PM solutions contained no encapsulated BIO/CHIR, this would result in post-dialysis absorbance measurements showing negligible BIO/CHIR characteristic peaks. A control measurement of free BIO/CHIR post-dialysis would further support this. However, due to their hydrophobic properties, BIO and CHIR precipitate in the absence of a polymer (pictured in **supplementary Figure S 1**), resulting in a solution not suited to spectrophotometry.

The chosen method for measuring Wnt activity also has some limitations. Specifically, the assay used only expresses luciferase upon TCF/LEF promoter activation and therefore cannot distinguish which signalling events cause activation. The TCF/LEF promoter is a known downstream target of Wnt signalling and hence it is assumed BIO/CHIR, known to inhibit GSK-3β, is activating this pathway; this could be supported by comparing the dose response in the presence of a natural Wnt ligand. In addition, when maximum Wnt signalling activity is reached, this assay cannot distinguish whether this is caused by cells having reached their maximum ability to express luciferase, or whether the dose response does increase further but luminescence detection is saturated.

For the alamarBlue assays, primary cells were utilised. One limitation in the use of human-derived bone marrow cells is that the growth and performance of these cells can exhibit patient-to-patient variability. The samples used in this research are taken from an elderly patient, and their medical history is not recorded; it is therefore unclear whether underlying mechanisms from patient-specific medical conditions are a factor in the low metabolic activity recorded. On the other hand, with the use of a greater number of samples, this study has the potential to provide insight into human variation in response to BIO/CHIR treatment, highlighting if individual underlying mechanisms can impact treatment activity.

Finally, it is important to note the toxicity information can only go so far in informing how safe a therapeutic will be in clinical use. Clinical studies of cancer-targeting PM treatments have found differences in animal and human toxicity effects. For example, in studies employing cyclodextrin polymer-based nanoparticles loaded with siRNA, there was evidence of liver and kidney toxicity in pre-clinical animal data, however in a subsequent human clinical trial, markers of cytotoxicity did not change (Zuckerman *et al.*, 2014).

### 3.4.7 Conclusions and future work

This work presents the first known investigation of the Wnt activity of nanoparticle-encapsulated CHIR. Following on from this, it would be useful to investigate Wnt signalling activity within a cell type relevant to a bone injury environment: for example, primary human BMSCs which contain

unselected SSCs, a target cell type for this treatment. Furthermore, the ability of PM-BIO and PM-CHIR to activate Wnt signalling needs to be validated *in vivo;* this is discussed in **Chapter 5** .

Overall, this chapter has demonstrated that PEG-*b*-PCL polymersomes can successfully be produced loaded with varying concentrations of small molecules BIO or CHIR. These PMs have a uniform size and can be produced with a sufficient yield to induce a Wnt signalling response within a cell line. Importantly, PMs were shown to protect cells from BIO or CHIR's toxic effects, particularly enabling delivery of a higher dose of these Wnt agonists. Ultimately these tested characteristics have shown PM-BIO and PM-CHIR to be a safe and easily reproducible treatment that can successfully activate Wnt signalling; these treatments can hence be used in further *in vivo* tests to assess their potential therapeutic benefits for improving fracture outcomes, as described in the following chapters.

# CHAPTER 4

## THE LOCALISATION AND QUANTIFICATION OF POLYMERSOME UPTAKE OVER TIME IN A MOUSE INJURY MODEL

### 4.1 INTRODUCTION

Nanoparticle (NP) delivery has the potential to increase the bioavailability of a drug at a target site and reduce off-target effects. For this thesis, polymersomes (PMs) have been selected to control the delivery of a Wnt agonist as a treatment to improve fracture outcome. In chapter 3 it was shown that synthesised polyethylene glycol (5k)-polycaprolactone copolymer (18k) (PEG-*b*-PCL) PMs can be loaded with small molecule Wnt agonists (BIO and CHIR), and that these successfully induce a Wnt signalling response whilst reducing toxicity *in vitro*. The efficacy of this treatment *in vivo* will require successful delivery of the Wnt agonist payload to the target fracture site. In addition to delivery efficiency, for eventual clinical translation it is also important to both understand the pharmacokinetics and resultant biosafety (i.e. the effects from all PM-organ interactions) and establish sufficient clearance. It is therefore necessary to have methods which determine the specific localisation and uptake of synthesised PMs within an *in vivo* bone injury model, at a whole body, organ, and cellular level, ideally in real time.

For a bone injury model, a mono-cortical 1 mm drill hole defect to a mouse femur was selected for use in this research as an ethical alternative to standard open- or closed-fracture models (Monfoulet *et al.*, 2010; He *et al.*, 2011), benefitted by their reproducibility and reduced morbidity rates. Additionally, this model is mechanically more stable than standard closed or open fractures, which is reflected by the mice being able to walk freely post-injury without the need of a supportive device.

In this thesis, PEG-*b*-PCL PMs (characterised in **section 3.3.2**) were selected as the drug delivery vehicle. The incorporation of PEG, also referred to as polyethylene oxide (PEO), is known to increase PM circulation time *in vivo* (Gref, Minamitake, Peracchia, Trubetskoy, Torchilin and Langerll, 1994). PEG is a synthetic polymer that has antifouling properties and, in particular, prevents protein adsorption and opsonisation of NPs (Owens and Peppas, 2006). Opsonisation is a process of the innate immune system that labels foreign antigens and makes them more susceptible to uptake by macrophages of the mononuclear phagocytic system (MPS) (formerly known as the

'reticuloendothelial system' (RES) (Frank and Fries, 1991)), predominantly by the Kupffer cells of the hepatic sinusoids (Bertrand and Leroux, 2012). Photos *et al.* (2003) studied PEGylated NP circulation time by collecting plasma samples at set timepoints from rats injected with fluorescently labelled NPs; the NPs were visualised and quantified with fluorescence microscopy. Photos found differences in circulation time amongst NPs produced with different PEG molecular weights. This molecular weight affects the configuration and thickness of PEG's neutrally-charged brush configuration resulting from its self-assembly in an aqueous solution, which is thought to restrict protein interaction (LoPresti *et al.*, 2009).

In the literature, different sizes of PEG-*b*-PCL nanoparticles ranging between 20 and 200 nm have been synthesised (some conjugated with targeting ligands) and their biodistribution investigated. Within the first 48 hours following intravenous (IV) injection, PMs were located within the liver, spleen, and kidneys (Liu, Zeng and Allen, 2007; Schädlich *et al.*, 2011; Xin *et al.*, 2011; Cho *et al.*, 2012; Gu *et al.*, 2013; Asem *et al.*, 2016; Wang *et al.*, 2016; Grossen *et al.*, 2017). This shows that NPs in a range of sizes will distribute into these tissues, each of which have roles in the body's clearance systems. In each of these studies, the biodistribution of PMs is assessed using *in vivo* fluorescent imaging.

This thesis focuses on using PMs to deliver a payload to a bone injury site. Within the published literature, *in vivo* fluorescent imaging has also been used to assess NP accumulation within bone tissue. A number of studies synthesise NPs with specific bone-targeting moieties with the aim of enhancing accumulation; examples include bisphosphonate ligands which bind to the bone mineral hydroxyapatite (Swami *et al.*. 2014), or ligands which target tartrate-resistant acid phosphatase (TRAP) found on bone surfaces (Wang *et al.*, 2017; Lavrador, Gaspar and Mano, 2018). On the other hand, NPs (including PEG-*b*-PCL PMs) have also been found to accumulate in bone tissue passively. Asem *et al.* (2016) synthesised PEG-*b*-PCL micelles and, 48 hours following IV injection, observed accumulation at the region of the femur using NIR fluorescence imaging. This study used PMs conjugated with a fluorescent probe that enables PM identification whilst still encapsulating the desired payload for further study. However, this conjugation step, which for clinical use will not be necessary, can also influence both the chemistry and size of the PM, ultimately affecting *in vivo* uptake and distribution. An alternative approach is to synthesise PMs loaded with a fluorescent representative payload. This approach cannot locate PMs themselves, however it will inform of where PMs have localised and released a payload. Wang *et al.* (2016) used this approach to determine the biodistribution of the fluorescent dye DiD encapsulated in PEG-*b*-PCL micelles within a mouse model with induced arthritis; they also observed PM accumulation within the hind leg. *In vivo*

fluorescent imaging detects scattered light from the surface of an animal; therefore to precisely localise NP accumulation to particular tissues, *ex vivo* imaging is required. Wang *et al.* (2016) used this method to confirm PEG-*b*-PCL can accumulate in bone tissue passively. These data cumulatively suggest PEG-*b*-PCL can passively accumulate within bone tissue, and that *in vivo* and *ex vivo* fluorescent imaging could be used to assess the passive distribution of PEG-*b*-PCL following a bone injury.

At least two studies have investigated polymeric nanoparticle biodistribution in a mouse model with a bone injury. Low *et al.* (2015) synthesised a polymeric micelle conjugated with BIO, the treatment payload, and used radioiodination to enable visualisation with single photon emission computed tomography and micro computed tomography (SPECT-µCT) imaging. BIO-micelles were IV-injected 2 weeks following the bone injury, and the greatest accumulation at the target injury site was observed 24 hours following injection. Wang *et al.* (2017) used *in vivo* fluorescent imaging to assess the biodistribution of PSMA-*b*-PS polymeric micelles, either alone (non-targeted) or conjugated with a TRAP-binding peptide (targeted), both of which were loaded with an NIR dye. These NPs were injected recto-orbitally 3 days post-fracture, and accumulation of both targeted and non-targeted NPs at the target fracture site peaked by 48 hours post-injection; targeted NPs had 2-fold greater accumulation.

At the time of writing, only published work by Scarpa (Scarpa, 2016) has investigated the biodistribution of PEG-*b*-PCL PMs with a focus on assessing distribution in an injured mouse model. Here, DiR loaded PEG-*b*-PCL PMs (PM-DiR) were administered to mice with drill hole fractures; using IVIS, an *in* vivo fluorescent imaging system, it was found that IV-injected PMs do reach the target fracture site. Scarpa assessed the accumulation of PMs with respect to time following injection immediately after an injury and found localisation at the injury site 24 hours post injection, which persisted for at least 10 days. However, it is not yet known how the temporal delivery of PMs impacts their distribution following injection. Although robust accumulation of PMs was seen from immediate injection following bone fracture, this 'window of opportunity' may not be convenient for clinical application – it is often the case that a fracture patient will present several hours after injury. Bone fractures can be separated into several overlapping phases: haematoma formation, replacement of haematoma with granulation tissue, and cartilage deposition and/or bony deposition (Einhorn and Gerstenfeld, 2014). It is possible that later time points during fracture healing might also lead to passive accumulation of PMs to the target fracture site. For instance, the inflammatory phase of bone fracture healing leads to overt blood vessel formation (Claes, Recknagel and Ignatius, 2012; Schell *et al.*, 2017), in some cases leading to enhanced blood flow (Tomlinson, Shoghi and Silva,

2014) within the early repair phase of fracture healing. This time window may therefore also present an opportunity to administer PMs and achieve passive accumulation to the target, bone.

Another unanswered question is the mechanism by which PMs accumulate at fracture sites. Passive targeting strategies have been built upon the 'enhanced permeability and retention' (EPR) effect theory, in which hyperpermeable tumour vasculature combined with impaired lymphatic draining enables particles large enough to avoid renal clearance to be entrapped and retained (Matsumura and Maeda, 1986). This theory relies on the assumption that nanosized objects escape blood vessels particularly in regions with low blood velocity and fenestrations; such features are found in developing vasculature following injury and in tumours (Maeda, 2015; Narum *et al.*, 2019), and in damaged vasculature immediately following injury. Long circulating PMs have been shown to accumulate in this proposed manner (Cho *et al.*, 2012; Jia *et al.*, 2015; Miller *et al.*, 2015).

Another mechanism to consider for the accumulation of PMs and other nanosized objects is cell-mediated uptake. The retention of NPs in clearance tissues is hypothesised to largely be the result of phagocytic uptake by resident macrophages. This is evidenced from several sources: NP biodistribution studies, which have shown high accumulation to MPS organs (Gref, Minamitake, Peracchia, Trubetskoy, Torchilin and Langer, 1994; Moghimi, Hunter and Andresen, 2012; Gustafson *et al.*, 2015); *in vitro* studies of varying NP characteristics, such as size and charge; resultant isolated macrophage uptake; and also associated blood circulation times *in vivo* (Alexis *et al.*, 2008). In tumour tissue it has been shown that tumour associated macrophages take up NPs to a greater extent than other cell types present (Miller 2015 and Dai 2018). Approaches which rely on inhibiting the activity of the MPS, for example by removing Kupffer cells from the liver, have shown this leads to an increase in the accumulation of NPs in tumours. For example Tavares *et al.* (2017) found that pre-administration of mice with clodronate liposomes led to an increase in circulation time and tumour accumulation of AuNPs. Similarly, clodronate liposome pre-treatment has been found to decrease the liver accumulation and prolong the circulation time of liposomes (Hu, Van Rooijen and Liu, 1996; Van Rooijen and Van Kesteren-Hendrikx, 2002). This method of macrophage depletion could be used to assess changes in PM accumulation and possibly promote uptake away from the liver to the target bone site.

Additionally to tissue resident macrophages, blood associated macrophages in circulation have also been suggested to have a role in NP uptake (Batrakova, Gendelman and Kabanov, 2011; Baumann *et al.*, 2013). Following injury, local and systemically recruited macrophages play a key role throughout the inflammatory and repair processes. Local environmental factors have been shown to alter

macrophage phenotypes and function, which in turn could affect NP uptake (Gustafson *et al.*, 2015). How the presence of an injury may affect possible phagocytic PM uptake *in vivo* therefore warrants further investigation.

In summary, to evaluate if PMs present a viable drug delivery system to target a bone injury, this study uses IVIS analysis of a fluorescent payload to test the hypothesis that PMs will passively accumulate at a target bone injury site when systemically administered either immediately or with a delay post injury formation. Additionally, to gain some mechanistic understanding of cellular PM uptake *in vivo*, clodronate liposome induced depletion of macrophages is used to test the hypothesis that the depletion of macrophages will change PM uptake distribution *in vivo,* reducing liver accumulation and promoting accumulation to a target bone injury site.

## 4.2 AIMS

**The first aim of this chapter is to localise and quantify polymersome uptake in a mouse bone injury model following immediate and delayed systemic injection.**

- Produce a 1 mm unilateral drill defect to the femur of mice and characterise it at set time points post injury.
- Localise and quantify IV injected PM-DiR uptake at a whole body and tissue level within healthy mice and mice with a bone injury.
- Assess the effect of delaying IV injection of PM-DiR upon its uptake at a whole body and tissue level in a mouse bone injury model.

**The second aim of this chapter is to determine the effects of systemically depleting macrophages upon the uptake of polymersomes in a healthy and injured mouse model.**

- Assess macrophage depletion in the liver of mice treated with a single dose of clodronate using immunohistochemistry.
- Localise and quantify PM-DiR uptake at a whole body and tissue level within healthy mice and mice with a bone injury following a dose of clodronate.

## 4.3 RESULTS

Within the clinic it is likely that not all fracture types will be assessed and treated immediately. It is therefore important to understand how a delayed treatment might affect successful PM delivery of a payload. To inform of an optimal time at which to administer PM treatment following a bone injury for maximum accumulation and resultant effect, a mouse drill hole bone injury model was used in a series of experiments utilising IVIS imaging to assess PM distribution *in vivo*. These experiments form a continuation of studies previously published within our lab by Scarpa (2016), who used the same injury model to assess PM uptake over time and established that PMs have a peak accumulation at a bone injury site 48 hours following IV injection given within 1 hour of surgery. This data informed the experimental design presented here, specifically the practice of consistently imaging at 48 hours post injection of PMs. The experiments presented in this chapter involved determining PM distribution in mice with a bone injury and healthy controls to confirm method reproducibility, as well as comparing PM at the target bone injury site when PMs are administered at a later timepoint. Finally, the impact of macrophage depletion on PM distribution was assessed in both non-injured and injured mice.

Following Scarpa, (2016), PMs were produced loaded with DiI and DiR fluorescent dyes in order to detect and semi-quantify PMs. DiR as a near infrared dye is particularly suited to IVIS imaging with an excitation and emission range that is not impaired by overlap with the absorption spectrum of haemoglobin (Frangioni, 2003). Furthermore, both DiR and DiI are hydrophobic, enabling incorporation with the PCL chains of the produced PMs. The relationship between amount of dye loaded and sufficient fluorescent signal *in vivo* was previously assessed by Scarpa: of the DiR loading concentrations investigated, 0.1 mg/mL produced the most intense subcutaneous fluorescent reading (Scarpa, 2016), and therefore this loading dose was also used in this study. DLS analysis confirmed successful formation of uniformly sized particles with a Z average of 83.52 d.nm for PMs loaded with DiR and 123.1 d.nm for dual loaded PMs (**Figure 4.1**).

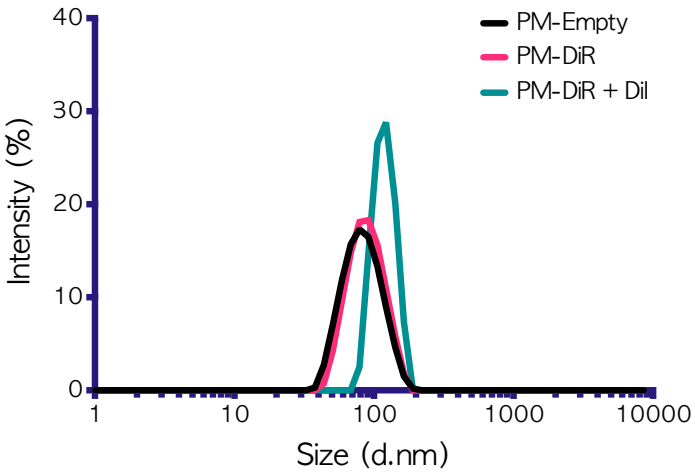


| | Z-average (d.nm) | PDI |
|---|---|---|
| **PM-Empty** | 78.18 | 0.076 |
| **PM-DiR** | 83.52 | 0.065 |
| **PM-DiI & DiR** | 123.1 | 0.329 |

***Figure*** 4.1***, Table*** 4.1***: Representative dynamic light scattering (DLS) measurements of fluorescent dye DiR- and DiI-loaded polymersome size and polydispersity.***

*A) Average particle size distribution by intensity of PM samples, diluted 1 in 10 in PBS and filtered through 0.2 µm pore filter, from DLS measurement at 173 ° and 25 ℃ (n=3 technical repeats). B) Mean (standard deviation) hydrodynamic diameter (Z-average size d.nm) and polydispersity index (PdI) of PM samples from DLS cumulants analysis (n=3 technical repeats).*

### 4.3.1 Establishing repair timings in control mouse bone injury model

First the repair timings for the chosen mouse bone injury model were established to better inform which administration timepoints to assess. Histological staining of femurs extracted 0, 7, and 10 days post injury are shown in **Figure 4.2**. On day 0 a haematoma is observed spanning the cortical bone gap and partially filling the marrow cavity beneath, distinguished particularly by GT orange stain and H&E red/deep pink stain of erythrocytes. These images also confirm the surgical technique used successfully created a unilateral defect with a hole bored though one cortical wall and partially into the marrow cavity. Some broken fragments of mature bone (stained bright red/orange in Tetrachrome) can be seen pushed into this marrow cavity. At day 7 woven bone is seen within the marrow cavity peripherally to the cortical gap and fibrous tissue bridges the gap. Tetrachrome stain identifies osteoid in pale blue and sparse areas of mineralised bone in bright red. At day 10 woven bone bridges the cortical gap and fills the marrow cavity beneath, spreading beyond the initial drill site. Polscope imaging reveals multi directional fibres characteristic of immature woven bone yet to be remodelled to an ordered lamella structure (an example of ordered lamella bone can be seen at the intact cortical bone beside the drill site at day 0).

At days 7 and 10, woven bone surrounds variously sized medullary spaces, some of which could be identified as blood vessels with a lining of stained cell nuclei (likely endothelial cells) and containing red stained blood cells in H&E sections (**Figure 4.2**). There is also evidence in literature that for a rodent bone injury model, angiogenesis occurs from at least 3-11 days post fracture (Rundle *et al.*, 2006; Lu *et al.*, 2008). Together, these factors informed the selection of day 7 as a second experimental timepoint in which to assess any effect of delaying PM administration upon its distribution post injury, hypothesising that with increased vessel formation PMs would be able to transport to target injury site.

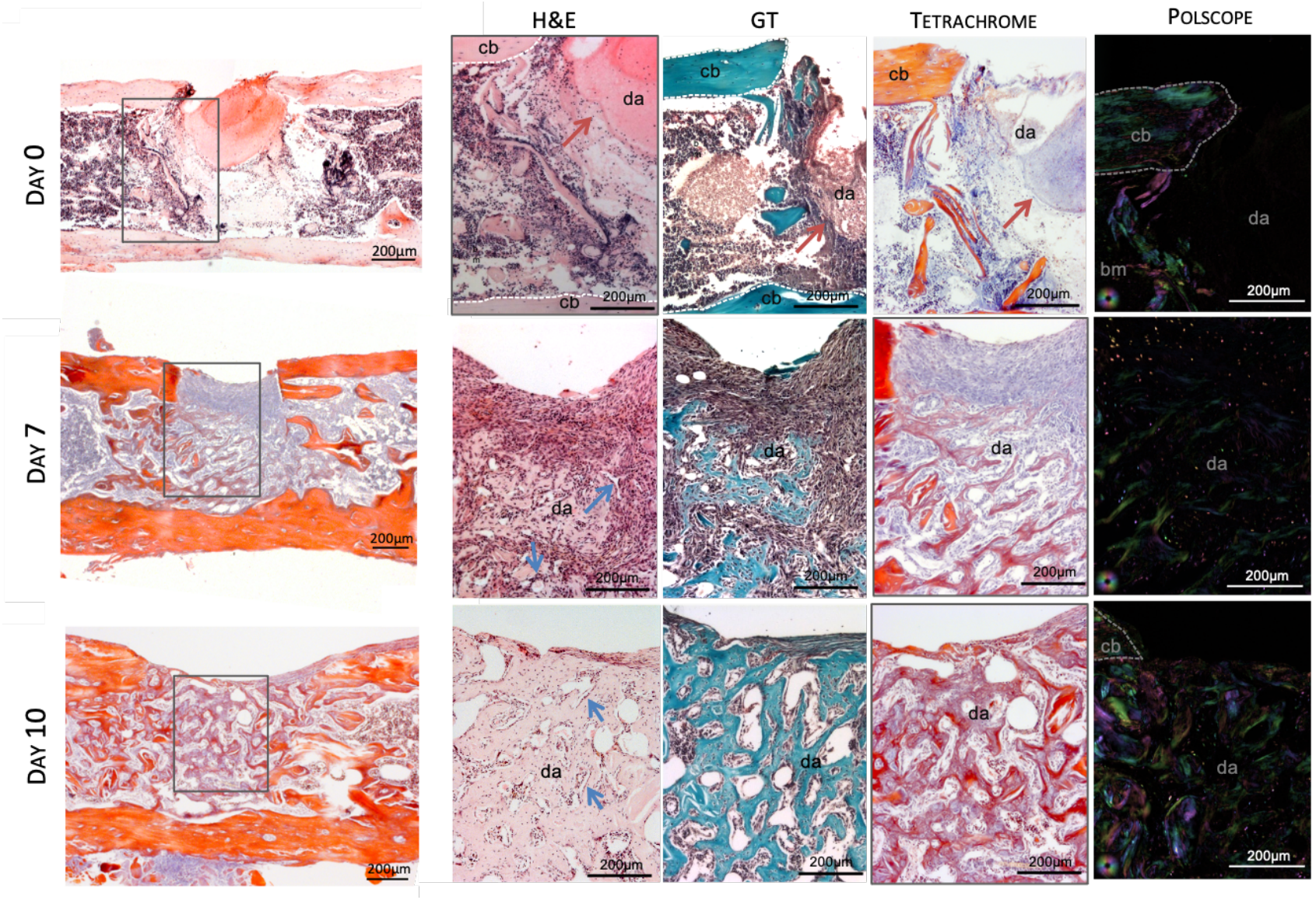
H&E
GT
TETRACHROME
POLSCOPE
DAY 0
DAY 7
DAY 10
cb
da
bm
200µm

***Figure 4.2: Histology of a unilateral drill defect to the femur of a mouse, repair over time***

*Hematoxylin & Eosin (H&E), Goldner's Trichrome (GT) and Tetrachrome staining, and non-stained polscope imaged sections, of male MF1 mice femurs extracted 0, 7, and 10 days post creation of a 1 mm drill hole defect. Cortical bone (cb) wall adjacent to drill hole site is labelled and distinguished by white dotted border, beneath which is bone marrow and bone fragment debris. In day 0, haematoma formation is marked by red arrows. The defect area (da) is filled progressively with granular tissue, osteoid, and woven bone, producing a callus. In days 7 and 10 H&E, example blood vessels are marked by blue arrows. The formed bones' various collagen orientations have birefringence which is detected in polscope images and is depicted by a colour wheel spectrum. Surgery and tissue extraction performed by Dr Edoardo Scarpa. Tissue processing, staining, and analysis performed by Alethia Hailes. H&E and Tetrachrome images re-published with permission from* (Scarpa, 2016).

### 4.3.2 PMs passively accumulate at a target injury site when injected IV

Before assessing the effects of delaying PM administration following injury upon its distribution *in vivo*, a reference study to establish the effect of a bone injury upon PM distribution *in vivo* was performed as a continuation to Scarpa's (2016) initial studies previously mentioned. Here, both injured and non-injured mice were injected IV with PM-DiI/DiR and 48 hours following PM administration, DiR fluorescence was imaged and quantified using IVIS. Whole-body images show two main sites of DiR fluorescent signal, measured by radiant efficiency ([p/sec/cm$^2$/sr]/[µW/cm$^2$]), situated in regions corresponding to the liver in both injured and non-injured mice; in mice with the bone injury, a high accumulation of DiR can also be seen at the site of injury (**Figure 4.3**). In comparison, the mean PM-DiR signal at the leg region is significantly higher for injured mice than uninjured mice (95% CI, 4.1 x $10^8$-5.1 x $10^{10}$, P=0.048), increasing from 1.4 x $10^{10}$ to 4.0 x $10^{10}$. However, for the liver region there is no significant difference between means (P=0.99), suggesting that bone injury does not affect liver accumulation of PMs.

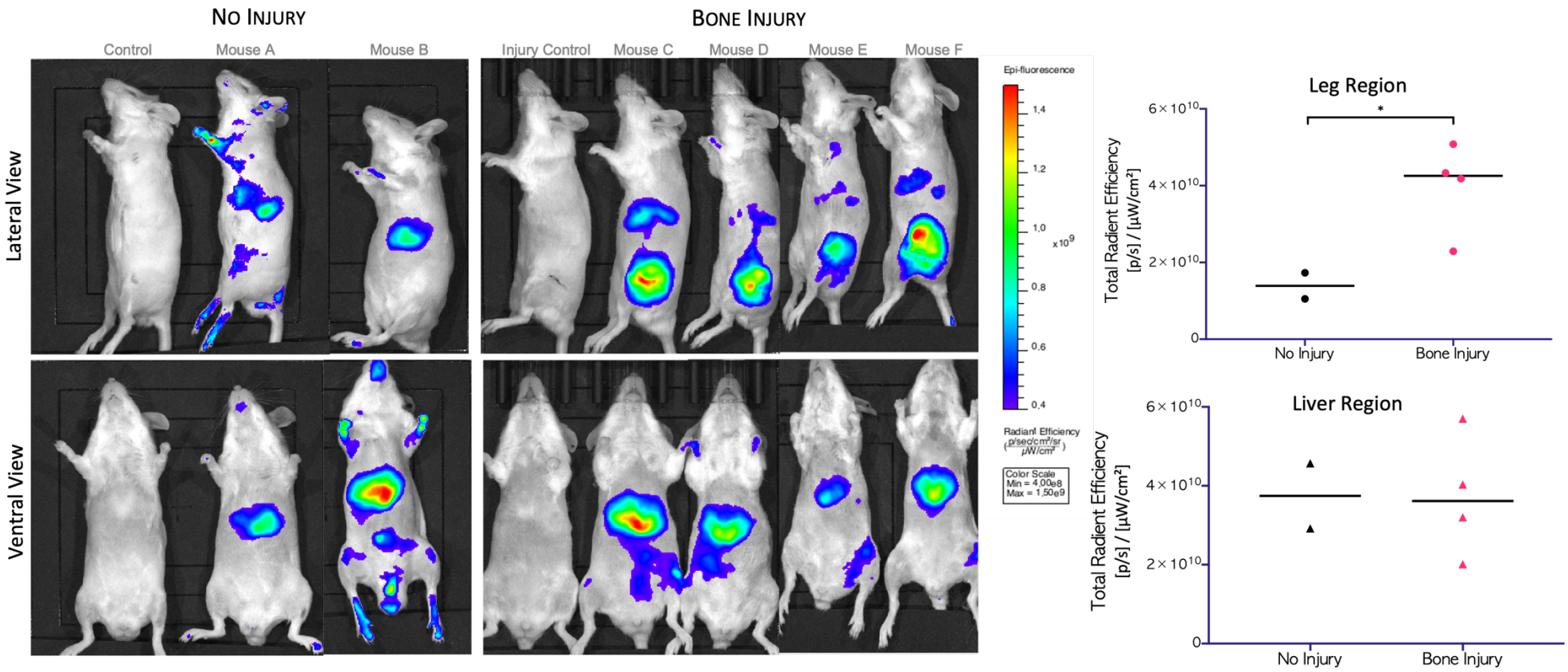


***Figure 4.3: In vivo imaging system (IVIS) analysis of polymersome-loaded fluorescent DiR (PM-DiR), whole body distribution in healthy mice and mice with a bone injury***

*Lateral and ventral view whole body IVIS images of female MF1 mice 48 hours post IV injection of PM-DiR (200 µL). For mice with a bone injury PM-DiR was administered 1 hour following a drill-hole surgery to the left femur. DiR fluorescence is measured in radiant efficiency ([p/sec/cm$^2$/sr]/[µW/cm$^2$]). Control mice (first left in each image) received no injection. Graphs display quantitative analysis of DiR fluorescence within a selected leg (lateral view) and liver (ventral view) regions of interest. Bars represent mean of n=2 (non-injured) and n=4 (injured) experimental subject repeats. Statistical significance assessed using un-paired t-test, *=p<0.05.*

To further identify specific anatomical locations of DiR accumulation, organs were extracted and imaged. Within uninjured tissues (**Figure 4.4)**, DiR accumulation is notably highest within the liver for both injured and non-injured mice. DiR fluorescence is also present within the spleen, and with the exception of the heart a smaller amount is measured in all other tissues extracted. In comparison between injured and non-injured mice, there was a slight increase in DiR accumulation within the liver and spleen, although not significant (P=0.37 & P=0.35). As the fluorescence signal from the liver dominated other tissues, isolated images of the tissue from the surgical site were subsequently taken in order to quantify accumulation in this target area independently (**Figure 4.5**). Image analysis revealed a markedly greater accumulation of DiR signal within the skin compared to other tissues, particularly in mice with a bone injury. In comparison between injured and non-injured mice, there is a significant increase in DiR signal present within the muscle of injured mice (95% CI, $3.2 \times 10^7$-$1.4 \times 10^8$, P=0.013) by a factor of ~6.5, as well as in the left femur (95% CI, $4.3 \times 10^7$-$1.6 \times 10^8$, P=0.0089) by a factor of ~2.3.

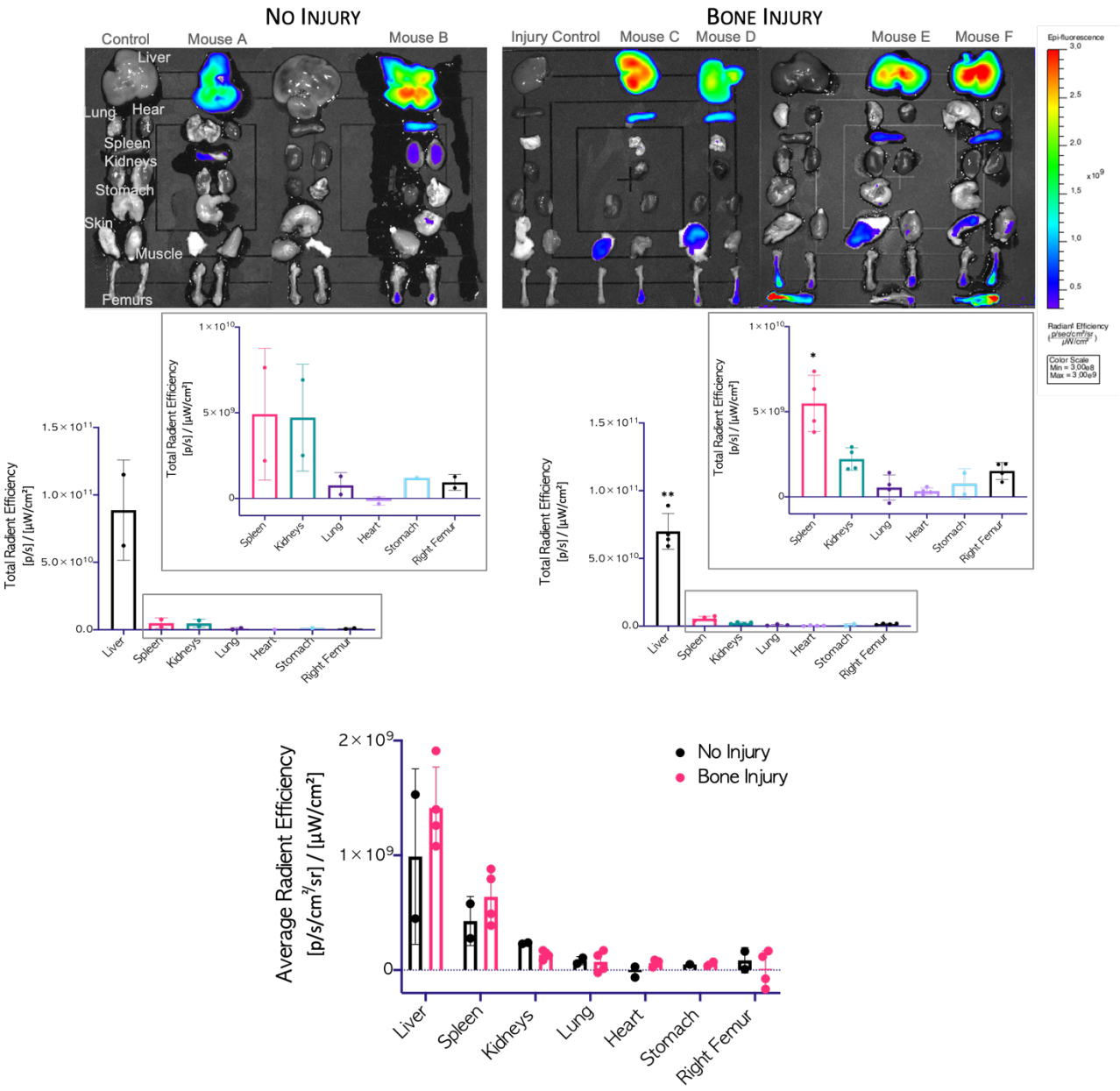


***Figure 4.4: In vivo imaging system (IVIS) analysis of polymersome-loaded fluorescent DiR (PM-DiR) distribution in uninjured tissues extracted from healthy mice and mice with a bone injury***

*IVIS images of organs extracted from female MF1 mice 48 hours post IV injection of PM-DiR (200 µL). For mice with a bone injury PM-DiR was administered 1 hour following a drill-hole surgery to the left femur. DiR fluorescence is measured in radiant efficiency ([p/sec/cm²/sr]/[µW/cm²]). Control mice (first left in each image) received no injection. Graphs display quantitative analysis of DiR fluorescence from selected organ regions of interest. Bars represent mean ± standard deviation of n=2 (non-injured) and n=4 (injured) experimental subject repeats. Statistical significance assessed using a matched one-way ANOVA for tissue comparison and unpaired t-test for no injury vs. bone injury comparison, *=p<0.05, **=p<0.005.*

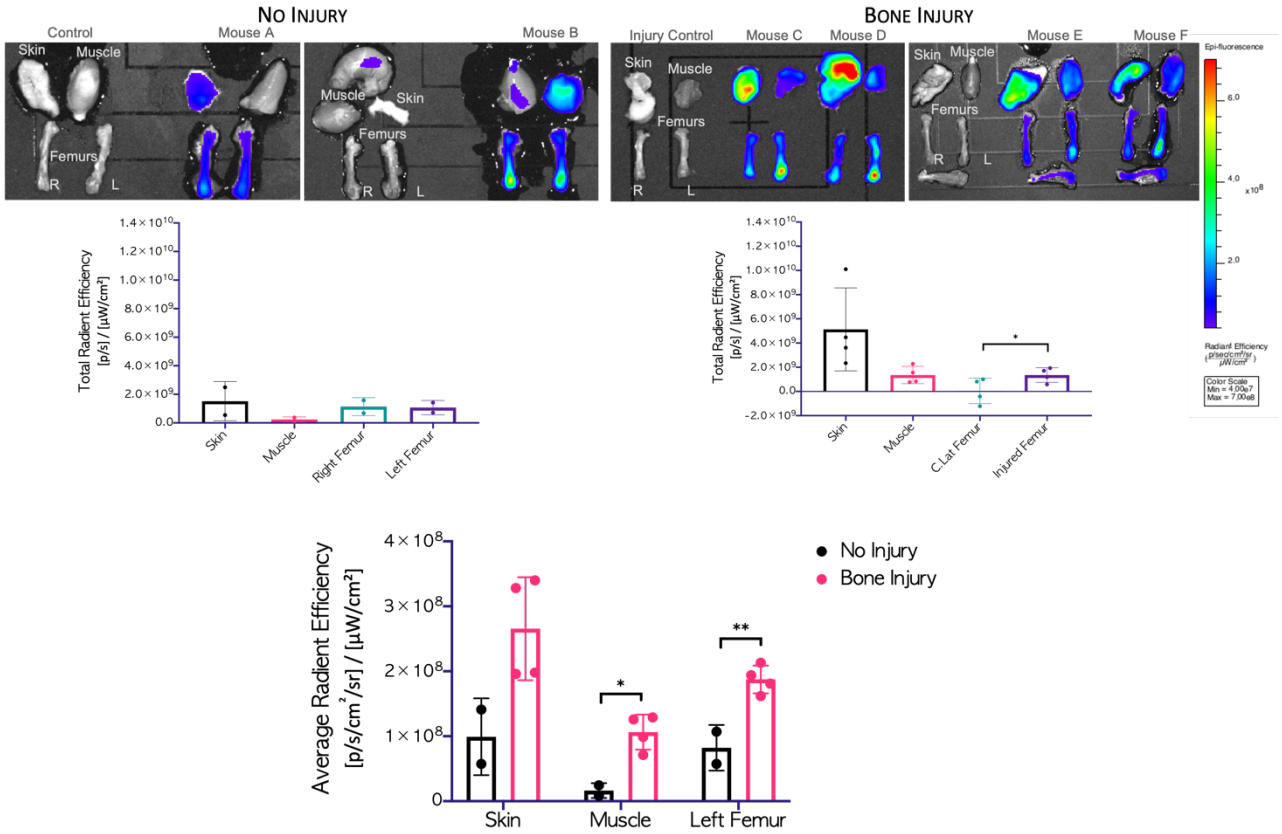


***Figure 4.5: In vivo imaging system (IVIS) analysis of polymersome-loaded fluorescent DiR (PM-DiR) distribution in surgical site tissue extracted from healthy mice and mice with a bone injury***

*IVIS images of left leg skin and muscle and both femurs extracted from female MF1 mice 48 hours post IV injection of PM-DiR (200 µL). For mice with a bone injury PM-DiR was administered 1 hour following a drill-hole surgery to the left femur. DiR fluorescence is measured in radiant efficiency ([p/sec/cm²/sr]/[µW/cm²]). Control mice (first left in each image) received no injection. Graphs display quantitative analysis of DiR fluorescence from selected organ regions of interest. Bars represent mean ± standard deviation of n=2 (non-injured) and n=4 (injured) experimental subject repeats. Statistical significance assessed using a matched one-way ANOVA for tissue comparisons and unpaired t-test for no injury vs. bone injury comparison, *=p<0.05, **=p<0.005.*

Visually in the femurs of mice with a bone injury in **Figure 4.5**, a distinction in DiR accumulation can be seen between the right and left femurs, which is not apparent in the femurs of uninjured mice. To quantify and investigate this in more detail, images were obtained of extracted femurs alone (**Figure 4.6**). For non-injured mice, the DiR signal measured within the contralateral femurs is equivalent to the corresponding injured femur. Conversely for injured mice there is a significant two-fold increase in DiR signal within the injured femur compared to the contralateral femur (95% CI, $6.05 \times 10^8$-$3.4 \times 10^8$, P=0.0005). Comparing the left/injured femur between healthy and injured mice, there is again a significant two-fold greater amount of DiR accumulation for injured mice (95% CI, $1.0 \times 10^9$-$2.6 \times 10^7$, P=0.04).

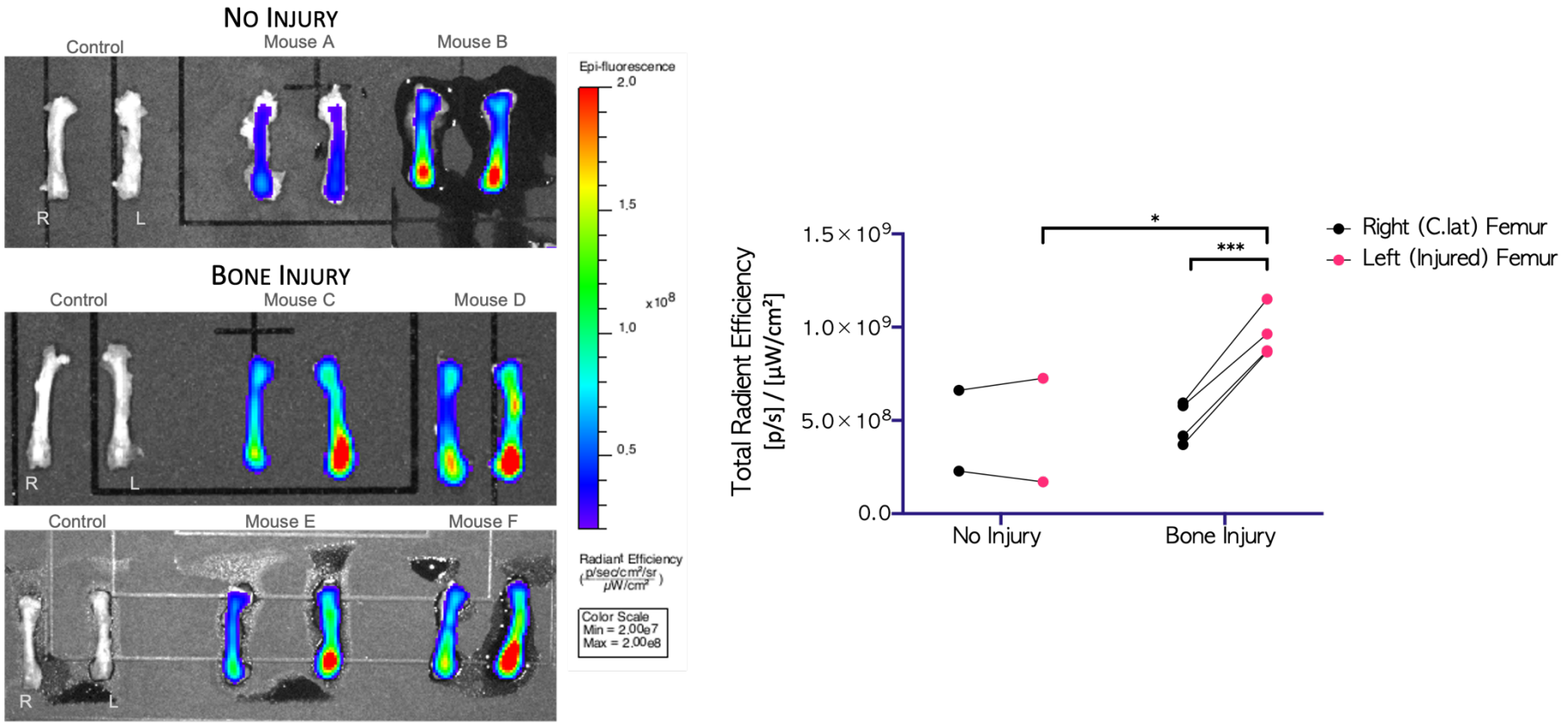


***Figure 4.6: In vivo imaging system (IVIS) analysis of polymersome-loaded fluorescent DiR (PM-DiR) distribution in extracted femurs of healthy mice and mice with a bone injury***

*IVIS images of femurs extracted from female MF1 mice 48 hours post IV injection of PM-DiR (200 µL). For mice with a bone injury PM-DiR was administered 1 hour following a drill-hole surgery to the left femur. DiR fluorescence is measured in radiant efficiency ([p/sec/cm$^2$/sr]/[µW/cm$^2$]). Control mice (first left in each image) received no injection. Graphs display quantitative analysis of DiR fluorescence from selected organ regions of interest. Bars represent mean ± standard deviation of n=2 (non-injured) and n=4 (injured) experimental subject repeats. Statistical significance assessed using a two-way ANOVA with a Sidak multiple comparison test, *=p<0.05, ***=p<0.0005.*

To confirm that the signal distribution is the result of PM delivery, control mice administered with DiR alone were also imaged. Due to the hydrophobic properties of DiR molecules, IV delivery required the presence of a lipid suspension (DSPC-PEG40s) (DiR-Lipid). **Figure 4.7** shows that in both whole-body and extracted organ image analysis, DiR-Lipid showed significantly greater accumulation to the liver compared to mice given PM-DiR (P=0.0019 (whole body) & P=0.0012 (organ)). As well as the liver, for mice treated with DiR-Lipid a significantly greater amount of DiR fluorescence can also be seen within the spleen (P=0.002). Images of extracted femurs alone show mice treated with DiR-Lipid have a slightly greater degree of DiR accumulation within the femur compared to healthy mice treated with PM-DiR, although not to a significant extent (P=0.30).

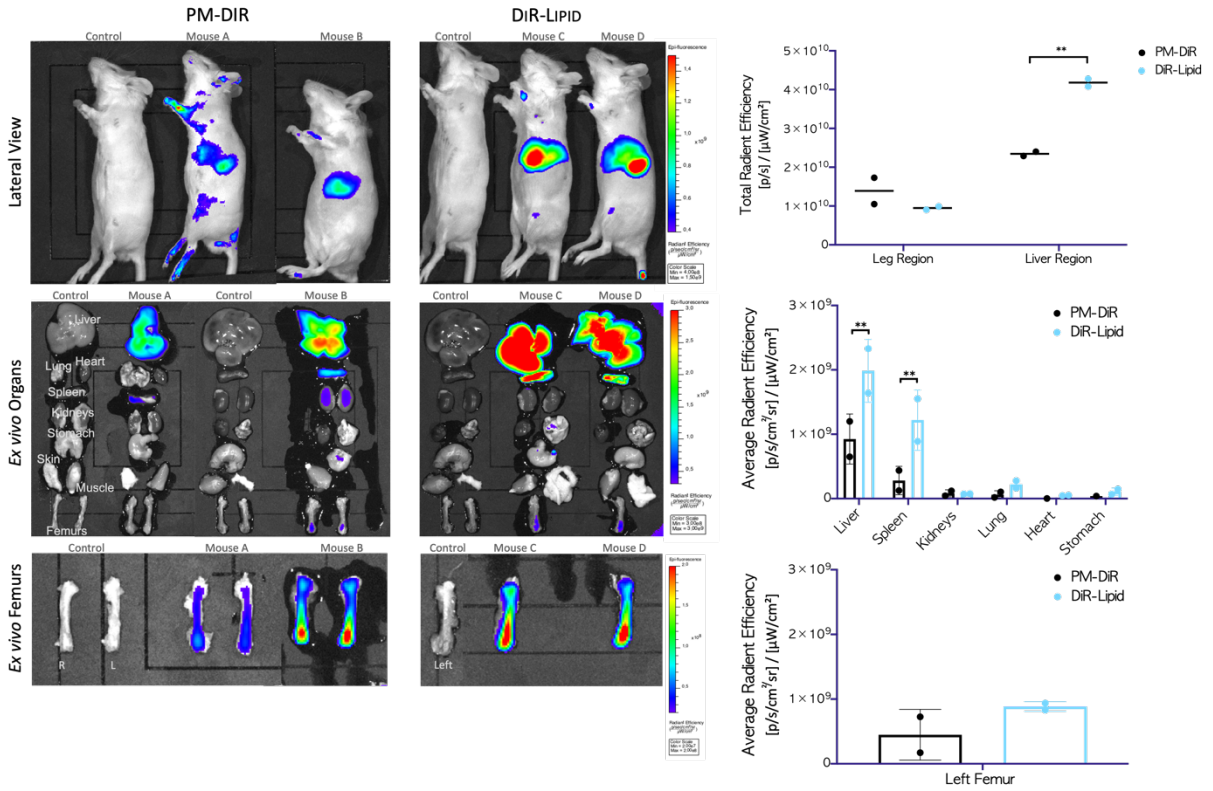


***Figure 4.7: In vivo imaging system (IVIS) analysis of polymersome-loaded fluorescent DiR (PM-DiR) and lipid-conjugated DiR (DiR-Lipid) distribution in vivo***

*IVIS images of whole body, extracted organs, and extracted femurs of female MF1 mice 48 hours post IV injection of either PM-DiR (200 µL) or DiR-Lipid (200 µL). DiR fluorescence is measured in radiant efficiency ([p/sec/cm$^2$/sr]/[µW/cm$^2$]). Control mice (first left in each image) received no injection. Graphs display quantitative analysis of DiR fluorescence from selected regions of interest. Bars represent mean ± standard deviation of n=2 experimental subject repeats. Statistical significance assessed using un-paired t-test, **=p<0.005.*

### 4.3.3 PM whole body and organ distribution is affected by timing of PM delivery post injury

To understand how the *in vivo* distribution of PMs following a bone injury might be affected by the timing of injection post injury, mice were IV injected with PMs encapsulating DiR (PM-DiR) and PMs encapsulating DiI (PM-DiI) either 1 hour (day 0) or 7 days (day 7) following bone injury. 48 hours following PM administration, DiR fluorescence was imaged and quantified using IVIS. Whole-body images show DiR fluorescent signal in regions corresponding to the location of the liver and the injured femur for both day 0 and day 7 injection timepoints (**Figure 4.8**). No fluorescent signal above that of autofluorescence is detected in control mice, which received no injection. Quantitative measurements from the selected regions of interest in whole-body images reveal a significant 44% mean decrease in DiR fluorescence at the lateral leg region (95% CI, $3.1 \times 10^{10}$-$3.8 \times 10^{9}$, P=0.0181) between day 0 and day 7. For the dorsal leg region there was a significant mean decrease of 56% (95% CI, $1.7 \times 10^{10}$-$4.7 \times 10^{9}$, P=0.0035) between day 0 and day 7; for the ventral liver region there is negligible change between the two timepoints (**Figure 4.8**).

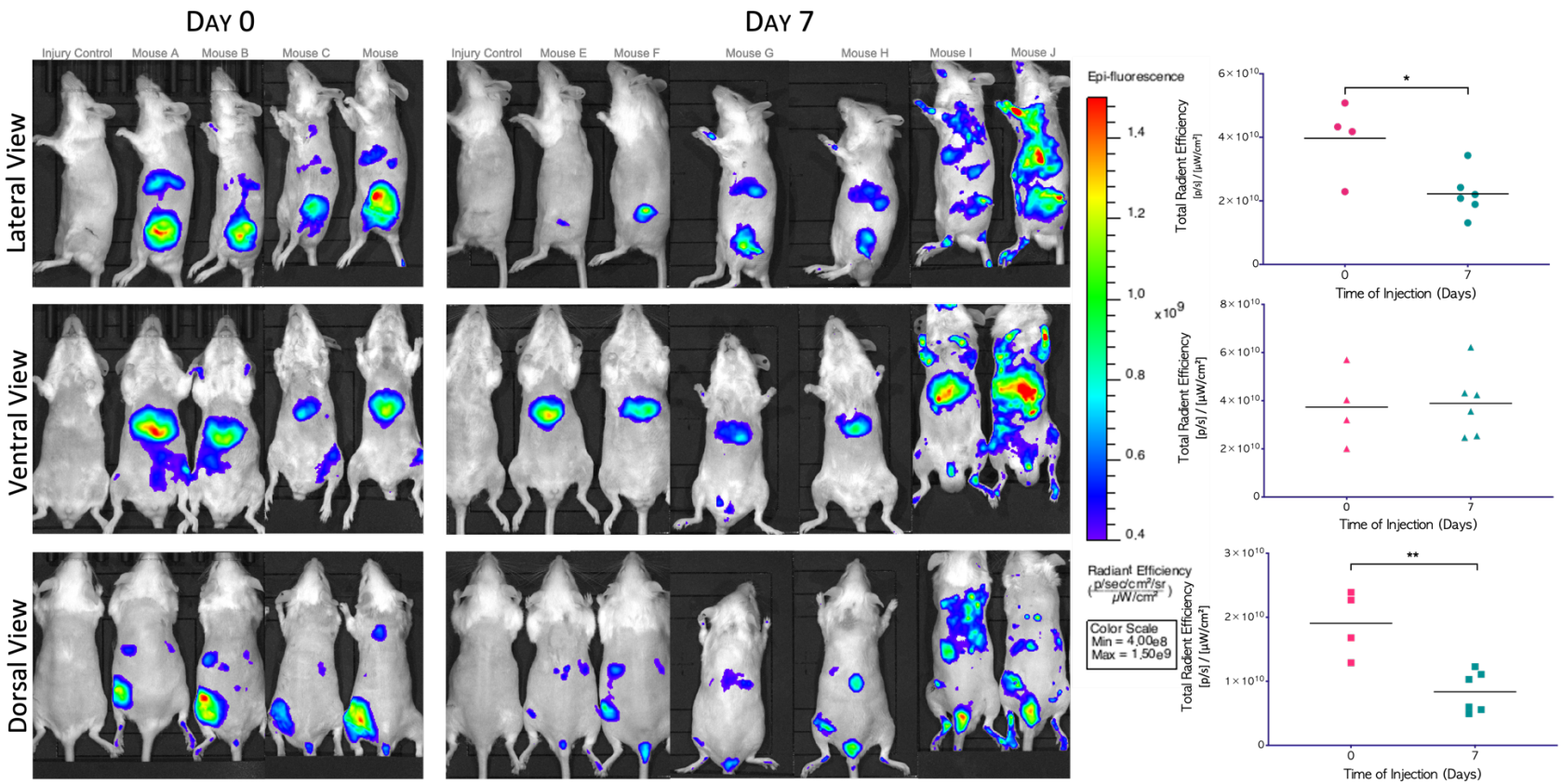


***Figure 4.8: In vivo imaging system (IVIS) analysis comparing the immediate and delayed systemic treatment of fluorescent DiR-loaded polymersomes (PM-DiR) on their whole-body distribution in mice with a bone injury***

*Whole body IVIS images of female MF1 mice injected IV with DiR polymersomes at either 1 hour (day 0) or 7 days (day 7) following a drill-hole injury to the left femur. Images were acquired 48 hours after each of these time points. DiR fluorescence is measured by total radiant efficiency ([p/sec/cm2/sr]/[µW/cm2]). Control mice (first left in each image) received no injection. Graphs display quantitative analysis of DiR fluorescence within a selected region of interest of the ventral view liver region and lateral and dorsal view leg region. Horizontal lines represent the mean of n=4 (day 0) and n=6 (day 7) experimental subject repeats. Statistical significance assessed using unpaired t-test. *=p<0.05.*

Next, to further ascertain the anatomical location and distribution of DiR signal, key tissues that play a key role in NP clearance, or that are present near the surgical site, were extracted and imaged. Images of distal/non-surgical site tissues show, for both injection timepoints, DiR fluorescence most intensely within the liver, followed by the spleen. DiR signal is also present within the kidneys, stomach, and contralateral femur. Negligible to no measurable signal is associated with the lung tissue and heart (**Figure 4.9**). In a comparison between mice given PMs at day 0 vs. day 7 post injury, there is no significant difference in DiR accumulation in any of the uninjured tissues, however for day 7 a slight reduction is observed in the liver and spleen ($P=0.49$ & $P=0.12$).

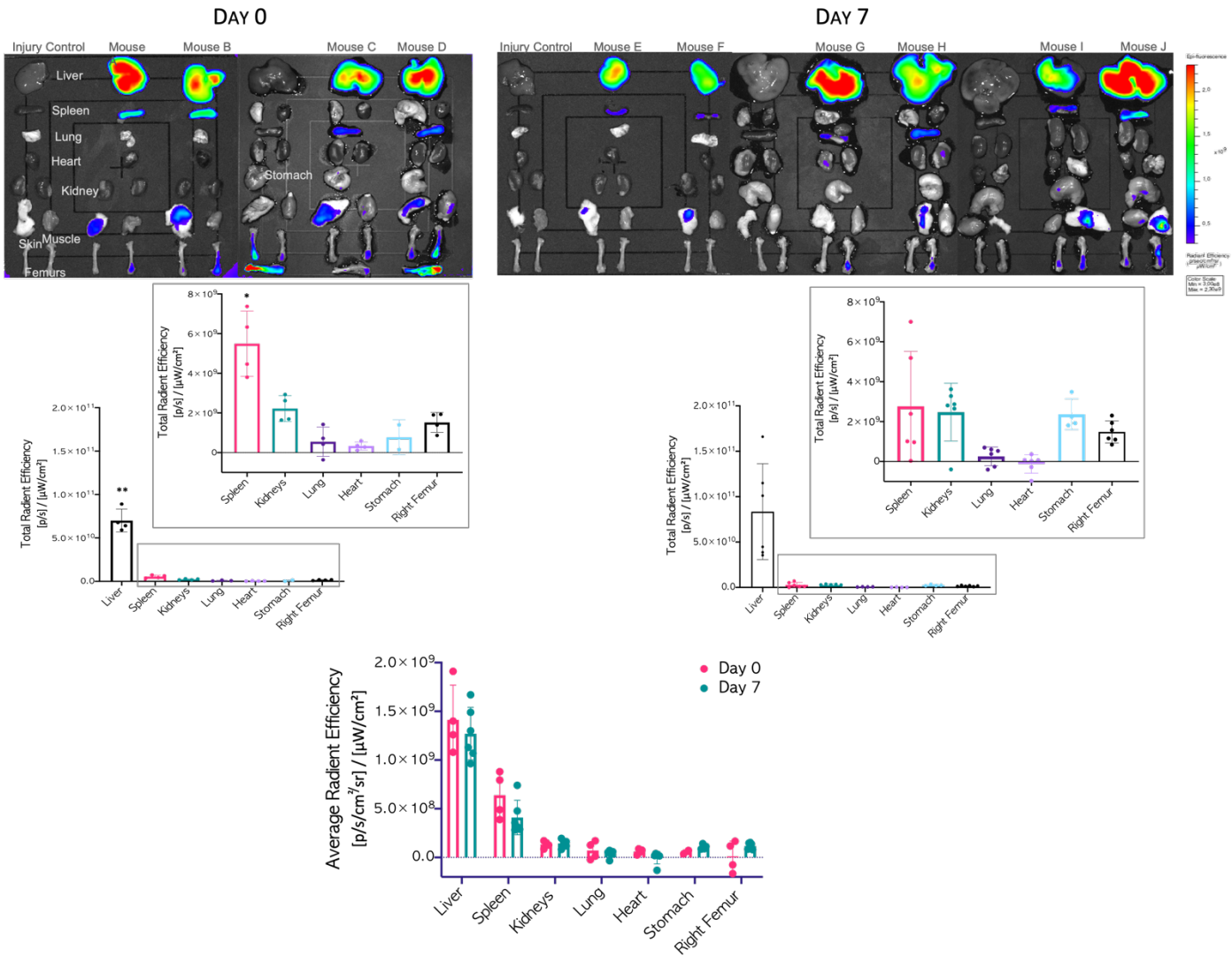


***Figure 4.9: In vivo imaging system (IVIS) analysis of fluorescent DiR-loaded PM distribution within extracted organ tissues***

*IVIS images of tissues (labelled on image) extracted 48 hours following IV injection of PMs encapsulating DiR at either 1 hour (day 0) or 7 days post drill-hole injury to the left femur. DiR fluorescence is measured by radiant efficiency ([p/sec/cm2/sr]/[µW/cm2]). Controls (first left in each image) received no injection. Graphs display quantitative analysis of DiR fluorescence within selected organ regions of interest. Bars represent mean ± standard deviation of n=4 (day 0) and n=6 (day 7) experimental subject repeats. Statistical significance assessed using a matched one-way ANOVA for tissue comparisons and unpaired t-test for day 0 vs. day 7 administration comparison. *=p<0.05, **=p<0.005.*

### 4.3.4 IV administered PMs passively accumulate at a target bone injury site when injected at different timepoints post injury

Next to determine whether the PMs can reach the target bone injury site following immediate or delayed administration, further images of injured tissue from the surgical site (**Figure 4.10**) as well as the femurs alone (**Figure 4.11**) were taken and analysed.

In **Figure 4.10** for both day 0 and day 7 a greater amount of DiR fluorescence is located at the skin compared to the muscle and femurs, however for day 7 this is to a statistically significant extent (P=0.04 for skin vs. muscle, P=0.05 for skin vs. C.Lat femur). At day 7 a slightly greater amount of DiR signal is present at the injured femur compared to the muscle and contralateral femur (although not statistically significant, P=0.06 & P=0.12 respectively). In contrast, at day 0 no clear signal difference is observed between the injured femur and muscle, although there is significantly more signal in the injured compared to the contralateral femur (P=0.03). In direct comparison between days 0 and 7, the muscle tissue shows a significant mean decrease in DiR signal (P=0.02); a slight mean decrease in DiR signal within the remaining tissues is seen, with the exception of the contralateral femur which exhibits a slight mean signal increase.

In **Figure 4.11** DiR signal is seen to again accumulate to a greater extent within the injured femur compared to the contralateral femur at both timepoints, although this difference is significant for day 0 only (P=0.013 for day 0, P=0.06 for day 7). In comparison between day 0 and day 7 for both the injured femur and contralateral femur no significant difference in quantified DiR fluorescence is seen (P=0.07 for injured and P=0.67 for C.Lat).

For mice given a PM injection at day 0, the injured femur was further examined for localised PMs by sectioning and fluorescent imaging. **Figure 4.12** shows punctate DiI fluorescence (represented in red) within the drill defect area at both 7 days and 10 days following surgery.

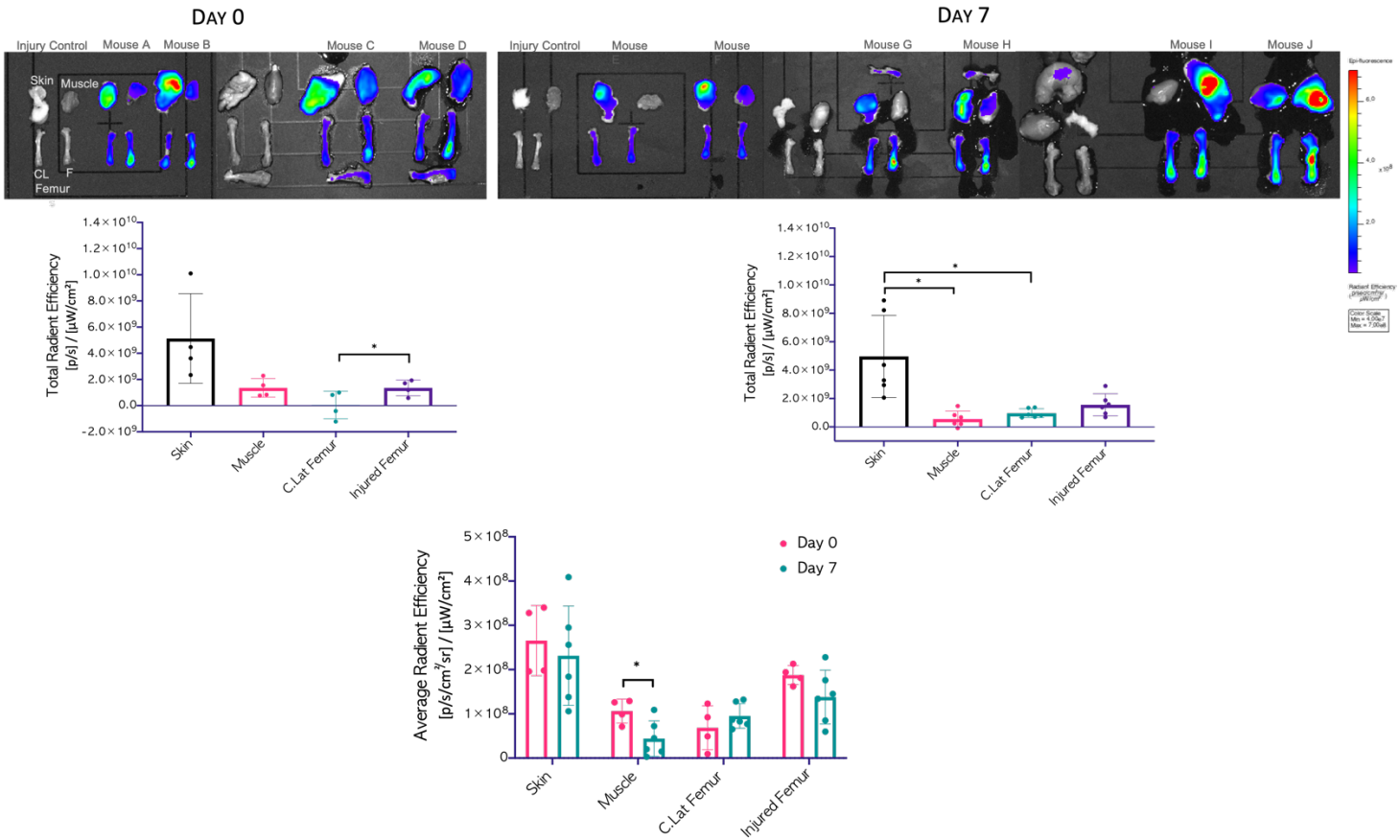


***Figure 4.10: In vivo imaging system (IVIS) analysis of fluorescent DiR-loaded polymersome (PM) distribution within tissue extracted from the surgery site***

*IVIS images of tissues (labelled on image) extracted 48 hours following IV injection of PMs encapsulating DiR at either 1 hour (day 0) or 7 days post drill-hole injury to the left femur. DiR fluorescence is measured by radiant efficiency ([p/sec/cm2/sr]/[µW/cm2]). Controls (first left in each image) received no injection. F = fractured femur, CL = contralateral femur. Graphs display quantitative analysis of DiR fluorescence within selected tissue regions of interest. Bars represent mean ± standard deviation of n=4 (day 0) and n=6 (day 7) experimental subject repeats. Statistical significance assessed using a matched one-way ANOVA for tissue comparisons and unpaired t-test for day 0 vs. day 7 administration comparison. *=p<0.05, **=p<0.005.*

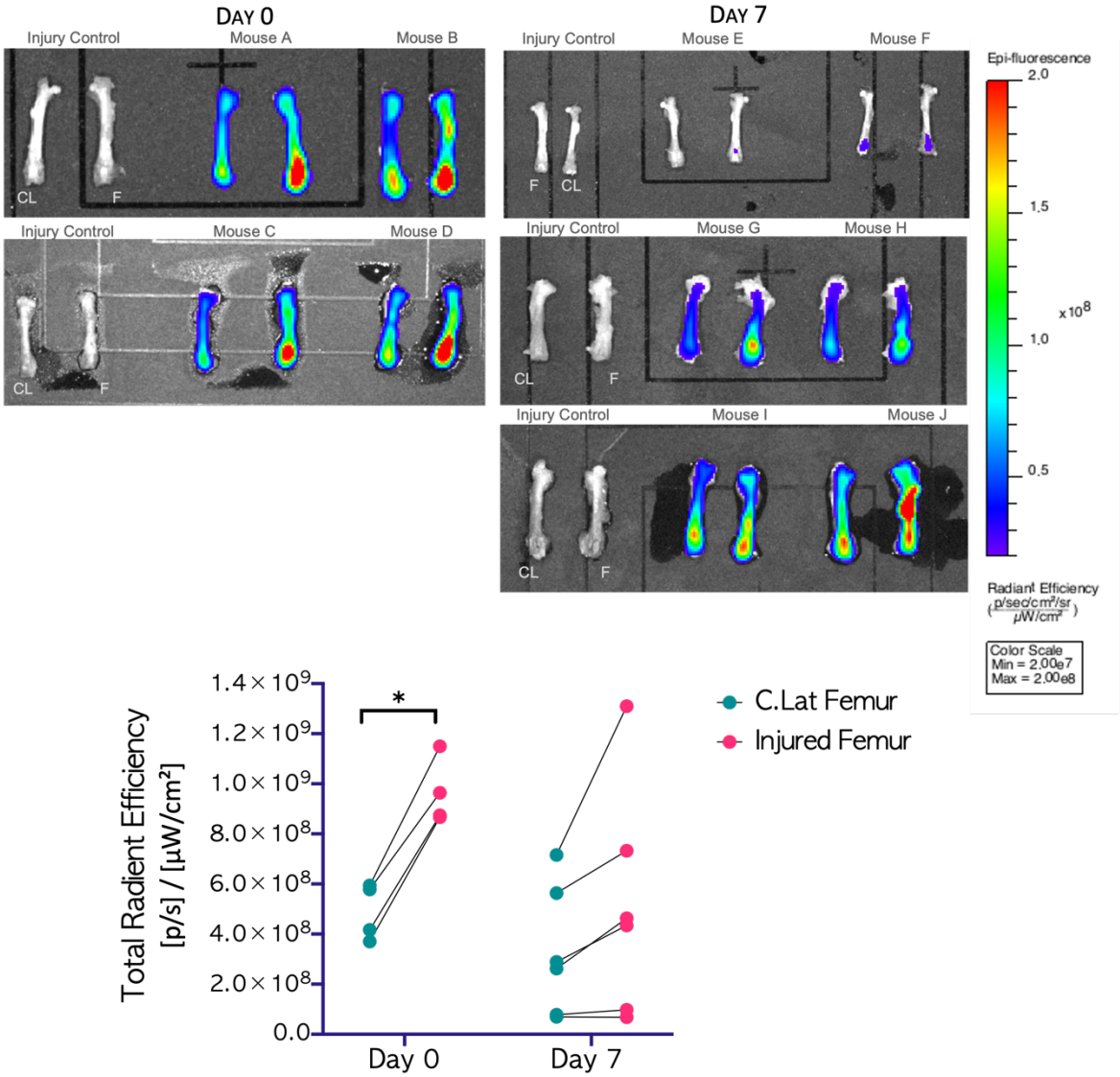


***Figure 4.11: In vivo imaging system (IVIS) analysis of fluorescent DiR-loaded polymersome (PM) distribution within extracted femurs***

*IVIS images of injured (F) and contralateral (CL) femurs extracted 48 hours following IV injection of PMs encapsulating DiR at either 1 hour (day 0) or 7 days post drill-hole injury to the left femur. DiR fluorescence is measured by radiant efficiency ([p/sec/cm2/sr]/[µW/cm2]). Controls (first left in each image) received no injection. Graphs display quantitative analysis of DiR fluorescence within a selected femur region of interest. Bars represent mean ± standard deviation of n=4 (day 0) and n=6 (day 7) experimental subject repeats. Statistical significance assessed using a matched two-way ANOVA with Sidak's multiple comparison test, *=p<0.05.*

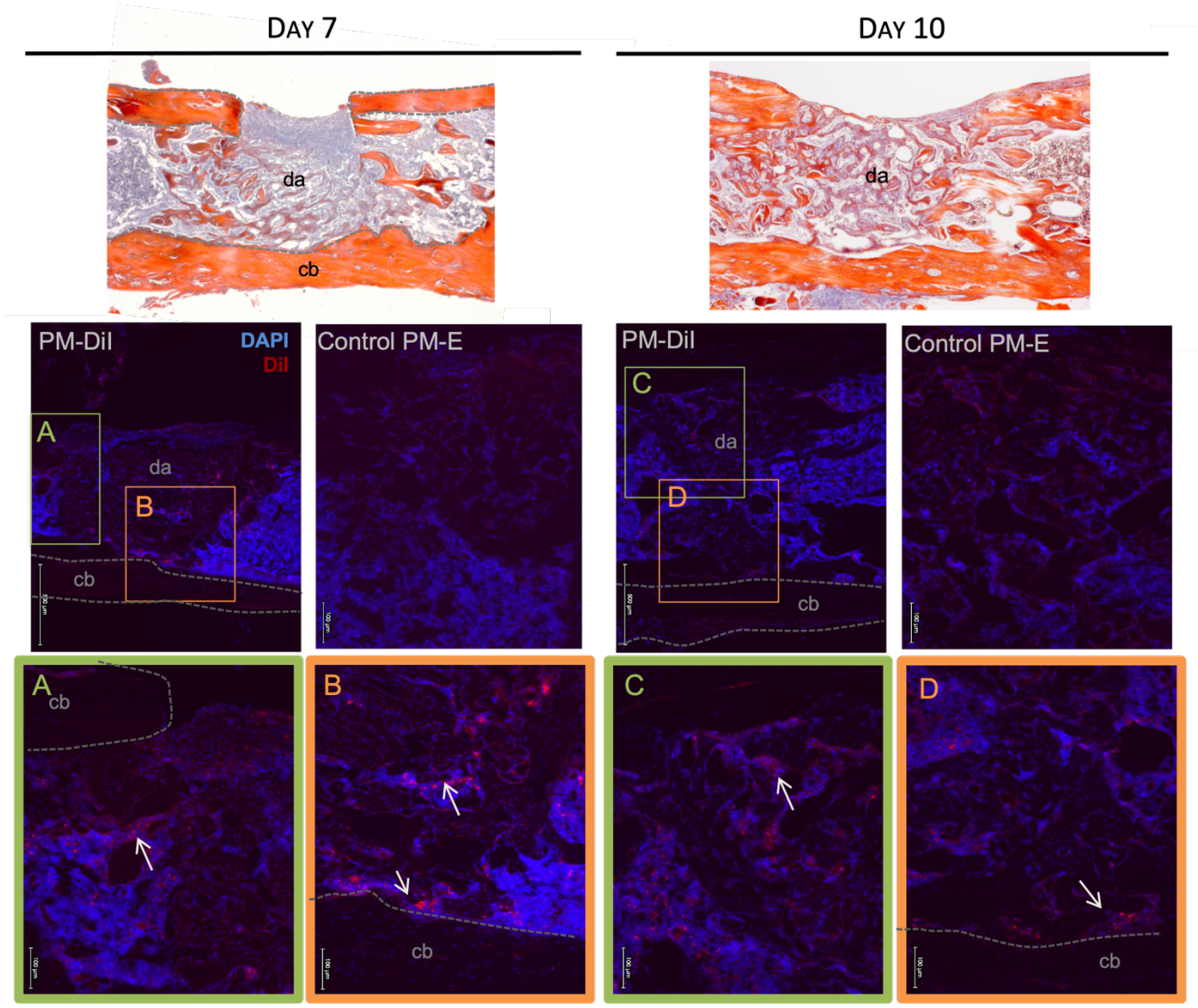


***Figure 4.12: Fluorescent imaging of DiI-loaded polymersome (PM) accumulation within an injured mouse femur***

*Top row shows representative tetrachrome stained histological 7 µm sections of injured male MF1 mice femurs extracted 7 and 10 days post-surgery. Middle row shows fluorescent images of injured femur sections extracted §from mice 7 and 10 days following surgery and IV treatment with either PM-DiR/DiI or control PM-Empty (PM-E). Bottom row shows higher magnification images of two defect areas outlined in green and orange. White arrows highlight areas of fluorescent DiI accumulation, represented in red. Cell nuclei stained with DAPI shown in blue. Identifiable features of cortical bone (cb) and defect area (da) are labelled. Surgery and extraction performed by Dr Edoardo Scarpa. IV injection performed by Vikki English. Tissue processing, staining, and analysis performed by Alethia Hailes. Tetrachrome and one day 7 fluorescent image re-published with permission from* (Scarpa, 2016)

### 4.3.5 PMs accumulate in the liver with no acute signs of toxicity

Liver samples from mice injected with PM-DiR/DiI at day 0 were extracted 7 days following injury and analysed by histological examination for localised PMs and signs of liver toxicity. Histological examination of sections stained with hematoxylin and eosin (H&E) revealed overall a normal morphology. More specifically, the gross hepatic structure (namely portal triads and central vein) in sections from both control and PM-DiR/DiI treated mice are apparent, labelled in **Figure 4.13**. Hepatocytes appear to be similarly sized between the two subjects, indicating no obvious signs of hypertrophy; furthermore, there is no apparent increase in the number of cells showing signs of hyperplasia (i.e. dividing or binucleated). High frequency of white space within and between cells was observed, which could designate fatty change (steatosis, indicated by lipid vacuoles) or hepatocyte glycogen accumulation (indicated by a central nucleus and clear cytoplasm with indistinct vacuoles (ground glass effect)). However here these were attributed to freezing artifacts as opposed to gross fat or glycogen accumulation as they are present in both control and treated mice and are not focused to one area. These artifacts make it difficult to distinguish any subtle changes which may have resulted from mice undergoing injury and PM administration.

Fluorescent images showed DiI accumulation within the liver tissue of mice treated with PM-DiR/DiI 7 days prior. Punctate spots of DiI fluorescence are seen associated near/within cells both with large granular nuclei likely hepatocytes and cells with small oblong nuclei likely Kupffer cells.

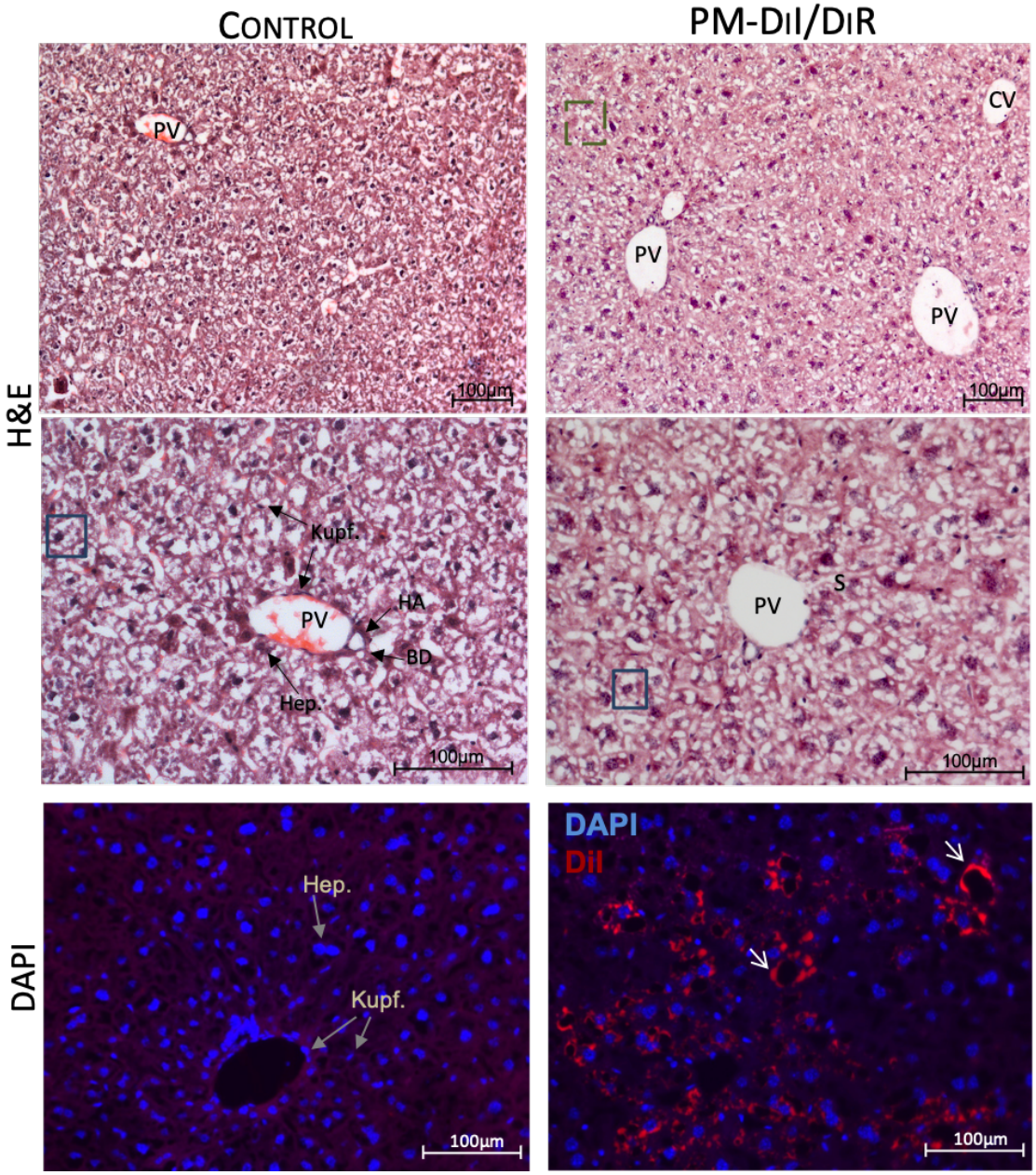


***Figure 4.13: Histological sections of male MF1 mouse livers extracted 7 days following a bone injury and IV administration of polymersome (PM)-DiR/DiI***

*Top two rows show representative bright field images at two magnifications of 7 µm thick mouse liver cryo-sections stained with hematoxylin and eosin (H&E). Sections show a normal liver tissue structure with identifiable features labelled. Portal triad units comprised of portal vein (PV), bile duct (BD), and hepatic artery (HA), surround and connect to a central vein (cv) via sinusoids (s), together forming a haptic lobule. Dark purple staining of nuclei reveals identifiable cell types labelled, namely Hepatocytes (Hep.), with larger granular nuclei, and Kupffer cells (Kupf.), with smaller oblong nuclei, associated near sinusoids. The blue box surrounds features of some cellular glycogen accumulation and the green box surrounds some fatty/lipid deposits. Bottom row shows representative fluorescent images of mouse liver sections stained with DAPI (blue) to identify cell nuclei, and DiI accumulation is shown in red. Surgery and tissue extraction performed by Dr Edoardo Scarpa. IV injection performed by Vikki English. Tissue processing, staining, and analysis performed by Alethia Hailes. Images re-published with permission from* (Scarpa, 2016).

### 4.3.6 Clodronate treatment successfully depletes phagocytic cells in the liver

IVIS analysis shows a high degree of PM-DiR accumulation within the liver, therefore in an effort to increase PM accumulation at the target bone injury site, the effect of systemically depleting macrophages upon PM distribution *in vivo* was investigated. First a (5 mg/mL, 250 µl) dose of clodronate liposomes was selected, based on literature, and tested for any Kupffer cell depletion within the liver of mice with a bone injury. F4/80 immunohistochemical staining of livers, extracted 4 days following treatment, revealed a positive stain on sections extracted from mice treated with control PBS liposomes whereas no stain was observed for mice treated with clodronate-liposomes. Example sections are shown in **Figure 4.14**; for the complete set of subject mice liver sections see **supplementary section S.2.** The positive stain overlayed cells with small oblong shaped nuclei and which are distributed characteristically of Kupffer cells. The clodronate dose used here was therefore considered adequate for achieving macrophage depletion in subsequent experiments.

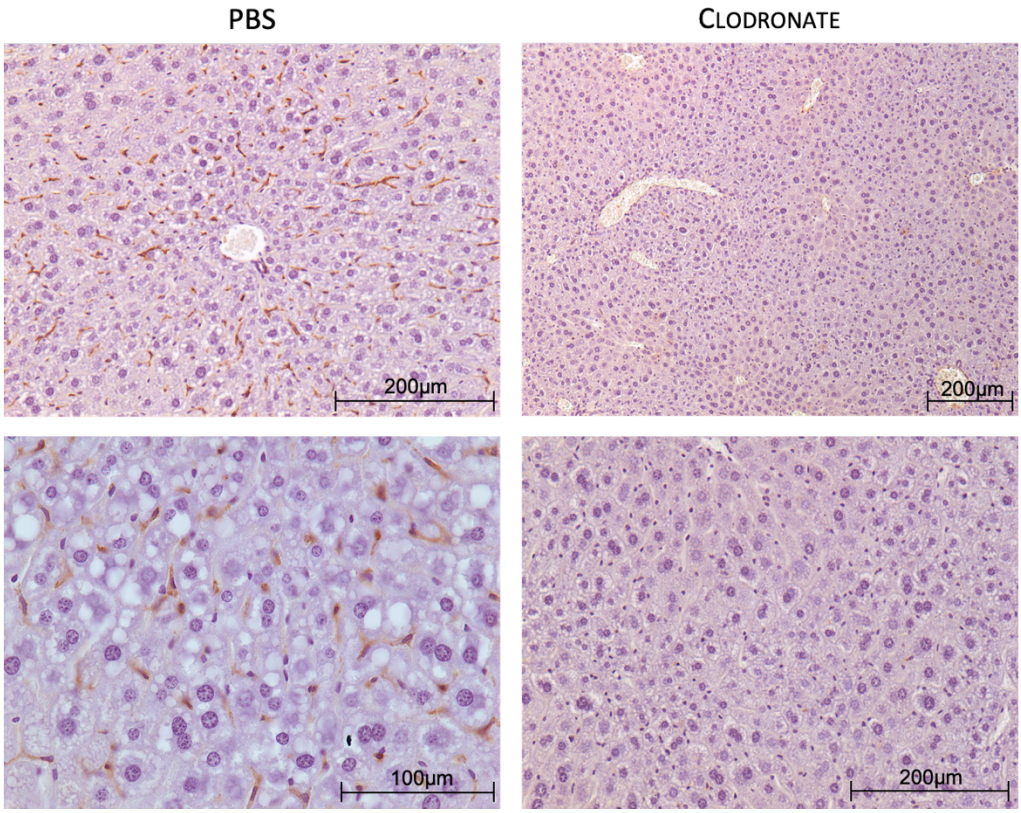


***Figure 4.14: Histological sections of mouse liver tissue immunohistochemically stained with anti-F4/80 following treatment with clodronate or PBS liposomes***

*Representative images of 7 µm thick mouse liver sections extracted from male MF1 mice (with a bone injury) 96 hours following IV injection of 250 µL of either clodronate (5 mg/mL) or vehicle control PBS liposomes. PBS images show positive F4/80 DAB stain, in brown, surrounding cells with small oblong nuclei, stained dark purple by hematoxylin, indicative of Kupffer cells. Clodronate images show no positive stain for Kupffer cells.*

### 4.3.7 Clodronate treatment affects PM liver accumulation

Having established successful Kupffer cell depletion from the use of clodronate, next any subsequent effect on PM distribution was investigated in healthy mice without a bone injury. To test the hypothesis that Kupffer cell depletion leads to a reduced PM liver accumulation, mice were administered clodronate liposomes or PBS liposome control two days prior to IV administration of PM-DiR. 48 hours later DiR fluorescence was imaged and quantified using IVIS. Due to surgical complication, detailed in **methods section 2.3.4**, this study lacks sufficient subject numbers for statical analysis and is therefore considered a preliminary study.

Whole body image analysis of the liver region of interest as well as image analysis of extracted livers both reveal a marked decrease in DiR fluorescence signal in mice pre-treated with clodronate (**Figure 4.15**). As a measurable change was achieved the clodronate dose was deemed appropriate for further experimental use.

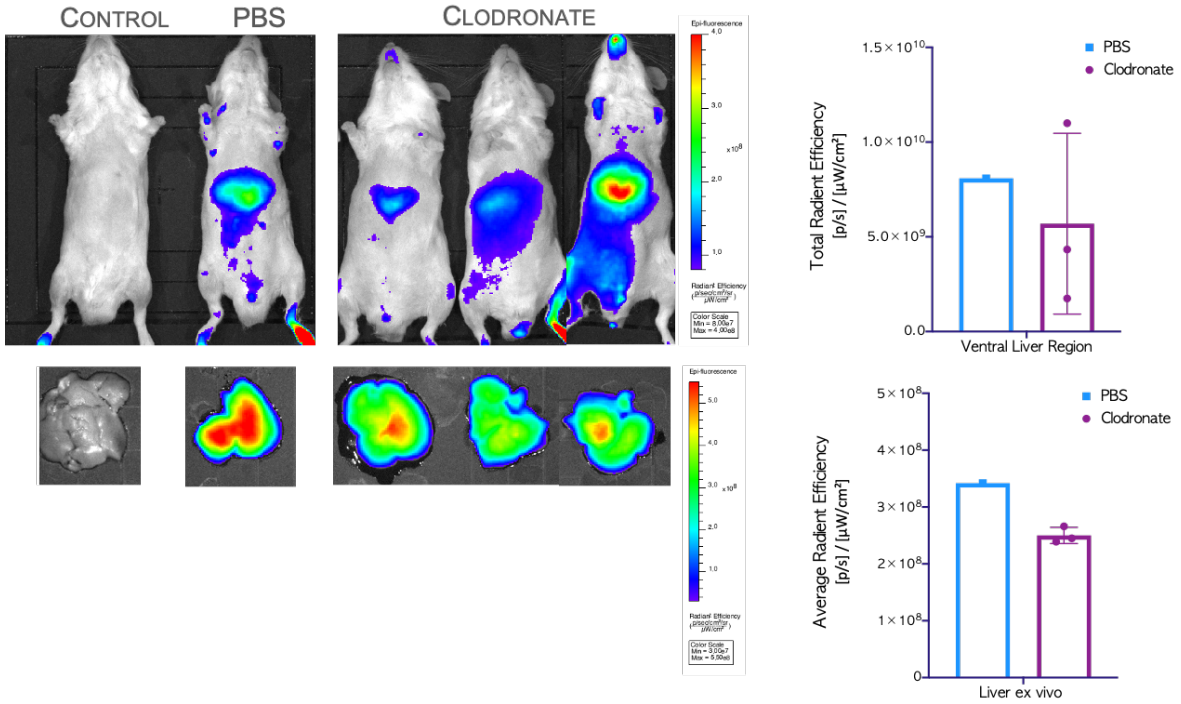


***Figure 4.15: IVIS image analysis of polymersome (PM)-DIR accumulation to the liver in mice pre-treated with clodronate***

*Images show whole body and extracted liver of male MF1 mice 48 hours following IV injection of PM-DiR/DiI (200 µL, 9.8 µM DiR-loaded PMs). 48 hours prior, mice also received 250 µL IV injection of either clodronate (5 mg/mL) (n=3) liposomes or vehicle control, PBS liposomes (n=1). Control mice received no injections. DiR fluorescence is measured by radiant efficiency ([p/sec/cm2/sr]/[µW/cm2]). Graphs display quantitative analysis of DiR fluorescence within a selected region of interest surrounding the liver. Bars represent mean ± standard deviation.*

As well as assessing for any change to liver accumulation, tissues were extracted for *ex vivo* analysis of clodronate pre-treatment effect upon PM distribution. **Figure 4.16** shows an increase in DiR signal within the spleen, lung, and both femurs of mice pre-treated with clodronate compared to PBS control.

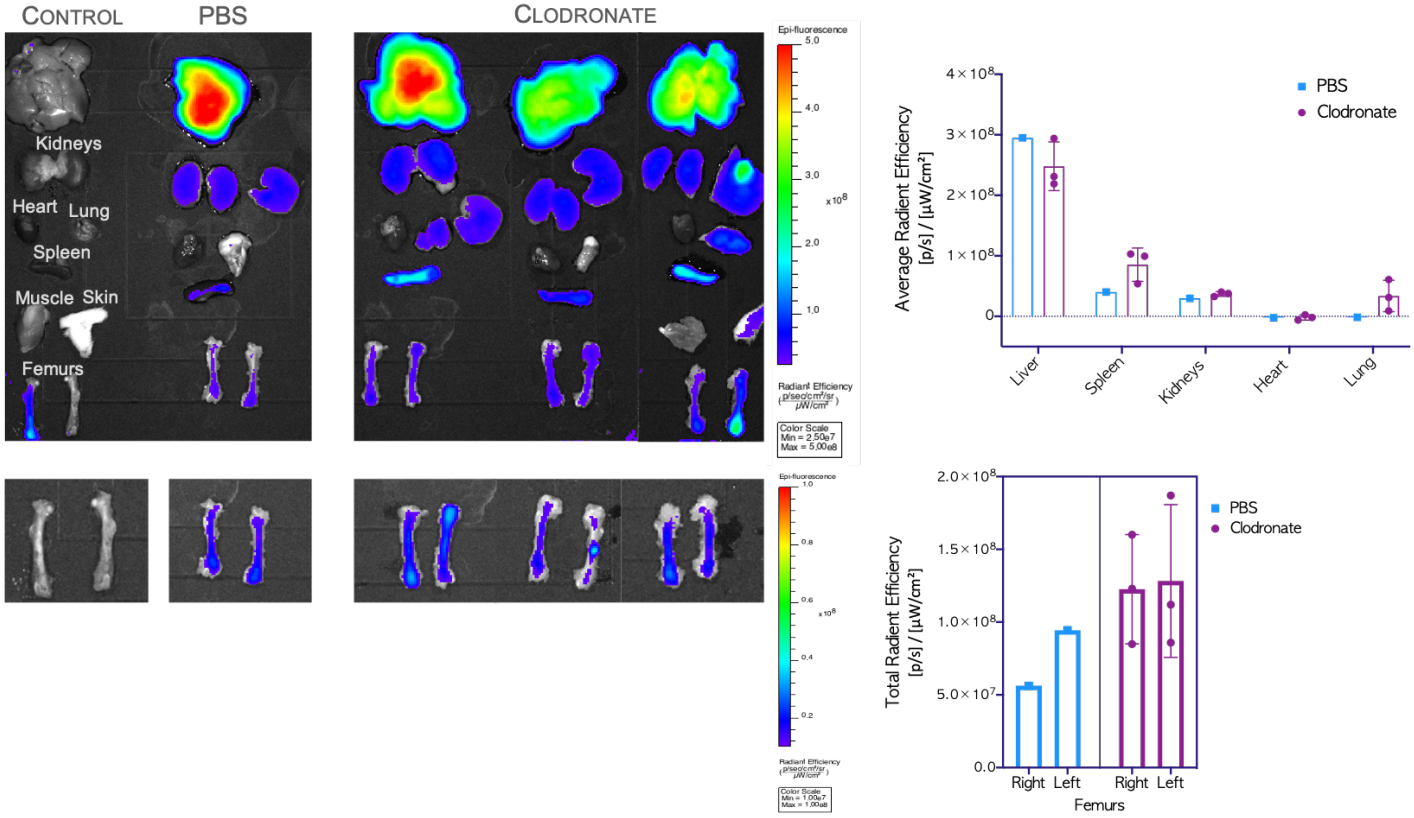


***Figure 4.16: IVIS image analysis of polymersome (PM)-DIR accumulation to the organs of mice pre-treated with clodronate***

*Images show extracted organs (labelled) of male MF1 mice 48 hours following IV injection of PM-DiR/DiI (200 µL, 9.8 µM DiR-loaded PMs). 48 hours prior, mice also received 250 µL IV injection of either clodronate (5 mg/mL) (n=3) liposomes or vehicle control, PBS liposomes (n=1). Control mice received no injections. DiR fluorescence is measured by radiant efficiency ([p/sec/cm2/sr]/[µW/cm2]). Graphs display quantitative analysis of DiR fluorescence within a selected region of interest surrounding the organ. Bars represent mean ± standard deviation.*

### 4.3.8 The effect of clodronate treatment on PM localisation post injury

Next the effect of clodronate treatment upon PM localisation in mice with a bone injury was assessed. To test the hypothesis that macrophage depletion leads to reduced PM liver accumulation and subsequent increased bone injury accumulation, clodronate or PBS liposomes were administered IV to mice, 2 days before surgery and PM-DiR injection. Whole body IVIS images taken 48 hours following PM-DiR administration show DiR fluorescent signal accumulation at the target injury site. Analysis of the injury site from both dorsal (**Figure 4.17**) and lateral (**Figure 4.18**) views reveal that mice treated with clodronate have less DiR accumulation compared to controls. In the lateral view (**Figure 4.18**) a significant decrease is measured from $1.3 \times 10^{11}$ to $7.7 \times 10^{10}$ (95% CI, $7.6 \times 10^{9}$-$9.1 \times 10^{10}$, P=0.03). Contrary to the results from non-injured mice, ventral view analysis (**Figure 4.19**) shows for mice pre-treated with clodronate there is an increase in DiR signal over the region corresponding to the liver, although not to a statistically significant extent (P=0.11).

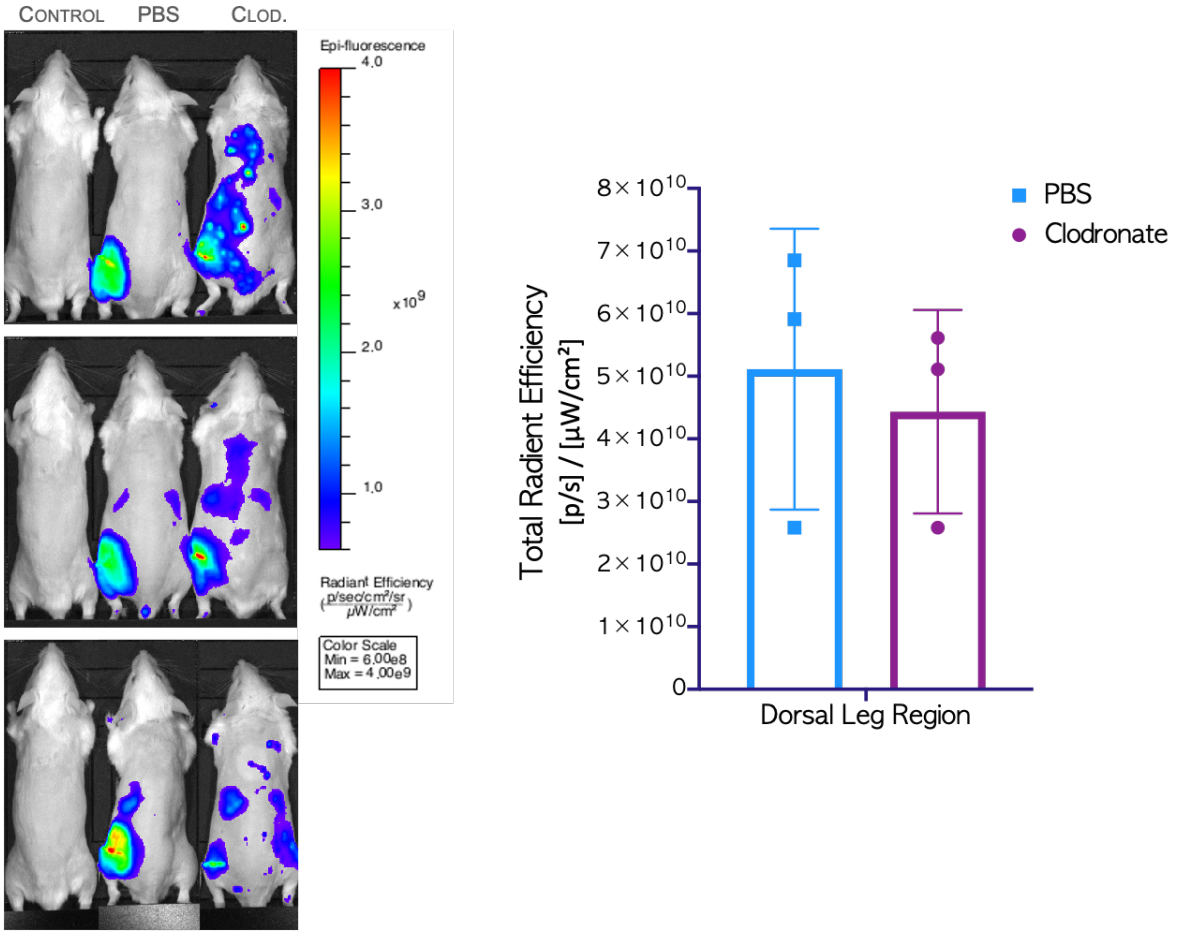


***Figure 4.17: Dorsal IVIS image analysis of polymersome (PM)-DiR distribution in mice with a bone injury and pre-treated with clodronate liposomes***

*Whole body dorsal view images of male MF1 mice 48 hours post IV injection of PM-DiR (200 µL) following surgery to produce a drill-hole injury to the left femur. 48 hours prior to surgery, mice also received 250 µL IV injection of either clodronate (5 mg/mL) (n=3) liposomes or vehicle control, PBS liposomes (n=3). Control mice received no injections. DiR fluorescence is measured by radiant efficiency ([p/sec/cm2/sr]/[µW/cm2]). Graphs display quantitative analysis of DiR fluorescence within a selected region of interest surrounding the injured leg. Bars represent mean ± standard deviation. Statistical significance assessed using an unpaired t-test, *=p<0.05.*

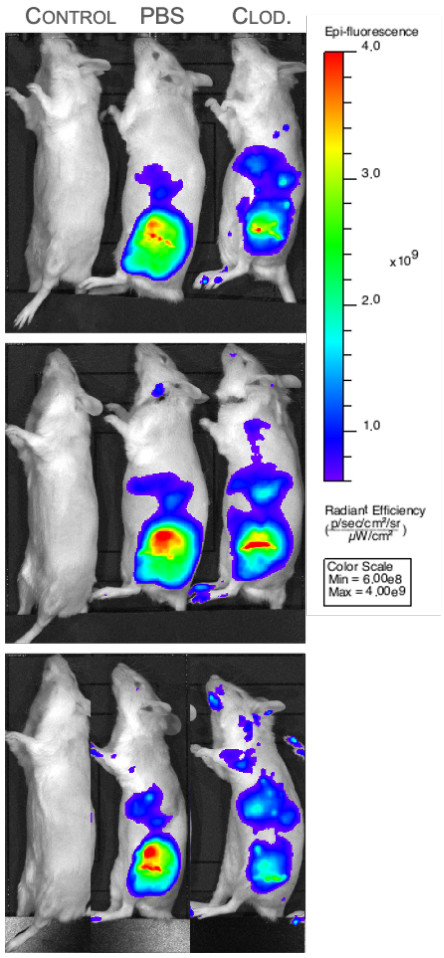


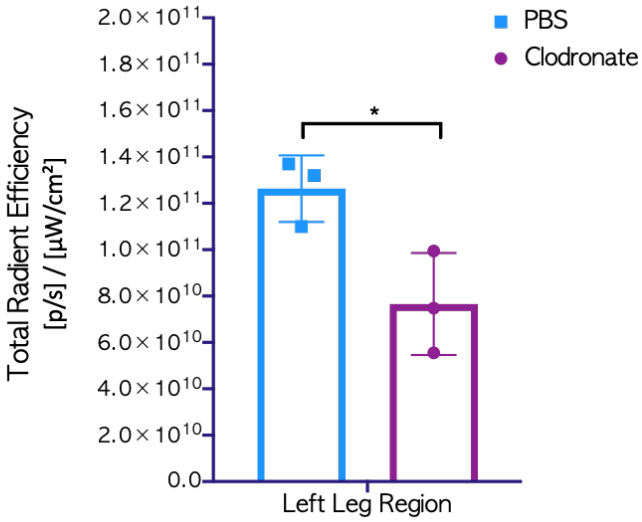


***Figure 4.18: Lateral view IVIS image analysis of polymersome (PM)-DiR distribution in mice with a bone injury and pre-treated with clodronate liposomes***

*Whole body left view images of male MF1 mice 48 hours post IV injection of PM-DiR (200 µL) following surgery to produce a drill-hole injury to the left femur. 48 hours prior to surgery, mice also received 250 µL IV injection of either clodronate (5 mg/mL) (n=3) liposomes or vehicle control, PBS liposomes (n=3). Control mice received no injections. DiR fluorescence is measured by radiant efficiency ([p/sec/cm2/sr]/[µW/cm2]). Graphs display quantitative analysis of DiR fluorescence within a selected region of interest surrounding the injured leg. Bars represent mean ± standard deviation. Statistical significance assessed using an unpaired t-test, *=p<0.05.*

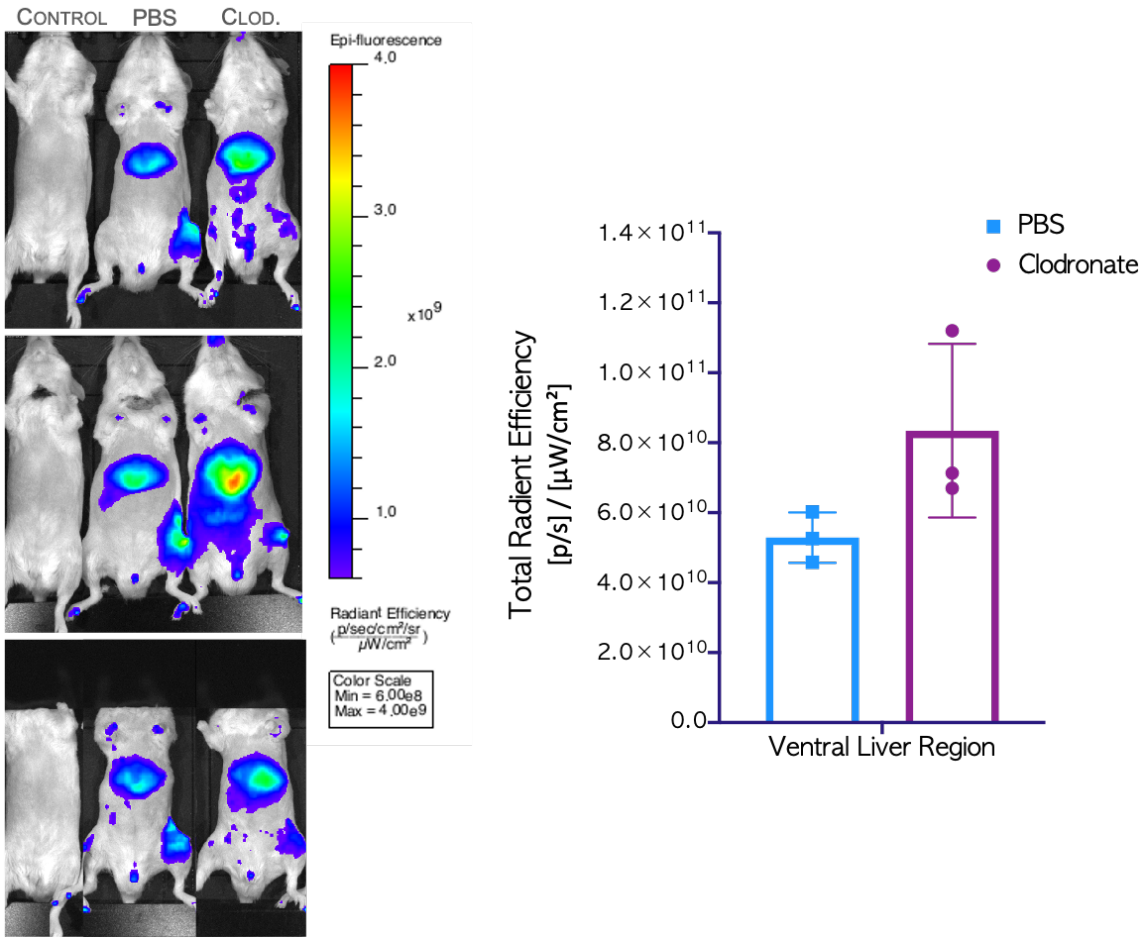


***Figure 4.19: Ventral view IVIS image analysis of polymersome (PM)-DiR distribution in mice with a bone injury and pre-treated with clodronate liposomes***

*Whole body ventral view images of male MF1 mice 48 hours post IV injection of PM-DiR (200 µL) following surgery to produce a drill-hole injury to the left femur. 48 hours prior to surgery, mice also received 250 µL IV injection of either clodronate (5 mg/mL) (n=3) liposomes or vehicle control, PBS liposomes (n=3). Control mice received no injections. DiR fluorescence is measured by radiant efficiency ([p/sec/cm2/sr]/[µW/cm2]). Graphs display quantitative analysis of DiR fluorescence within a selected region of interest surrounding the liver. Bars represent mean ± standard deviation. Statistical significance assessed using an unpaired t-test, *=p<0.05.*

To further examine PM distribution, as with the previous experiments, tissues were extracted and imaged. For both PBS control and clodronate treated mice, a similar DiR signal distribution between each tissue was observed, with the greatest signal again residing within the liver, followed by the injured skin and spleen.

In comparison between clodronate and PBS treated mice, consistent with the observed relationship in the whole-body analysis, a greater amount of DiR signal is measured within the liver of clodronate treated mice, although not to a statistically significant extent (P=0.12) (**Figure 4.20**). The other extracted organs – namely the spleen, kidneys, lung, and stomach – of mice pre-treated with clodronate show slightly higher DiR signal compared to PBS controls. The skin and muscle from the injury site however shows the opposite, with clodronate treated mice having a lower DiR accumulation.

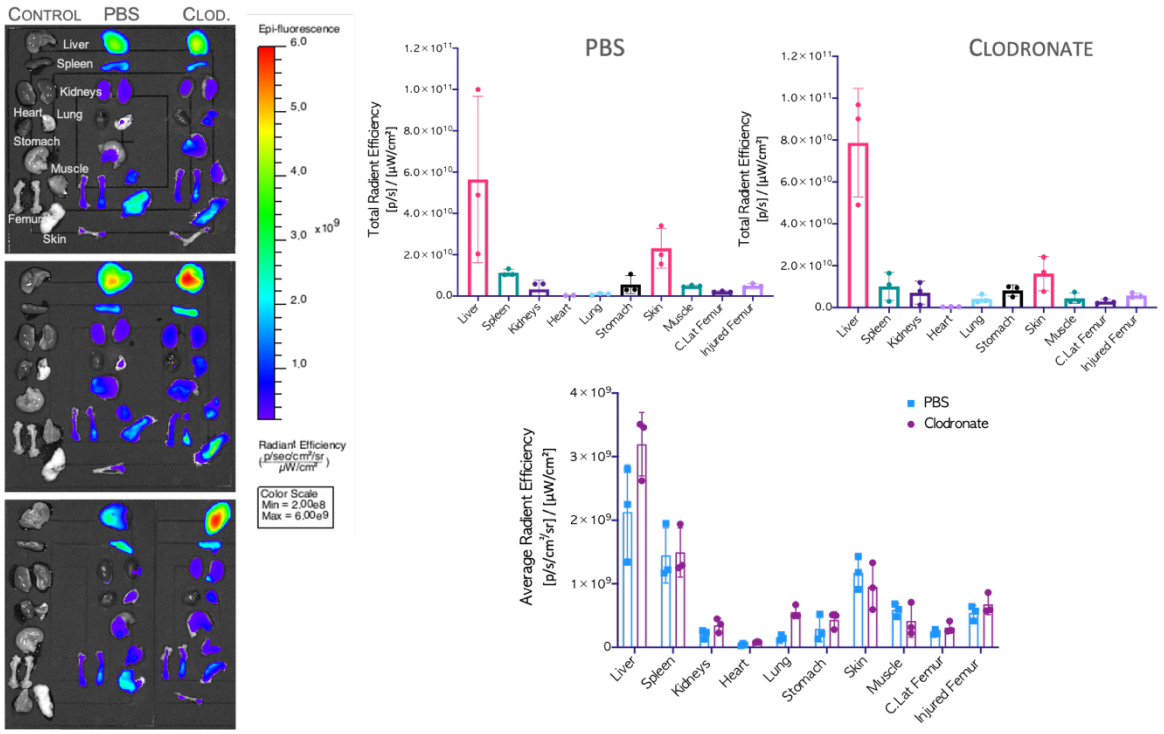


***Figure 4.20: IVIS analysis of polymersome (PM)-DiR distribution within extracted organs of mice with a bone injury and pre-treated with clodronate liposomes***

*Images of extracted organs (labelled) from male MF1 mice 48 hours post IV injection of PM-DiR (200 µL) following surgery to produce a drill-hole injury to the left femur. 48 hours prior to surgery, mice also received 250 µL IV injection of either clodronate (5 mg/mL) (n=3) liposomes or vehicle control, PBS liposomes (n=3). Control mice received no injections. DiR fluorescence is measured by radiant efficiency ([p/sec/cm2/sr]/[µW/cm2]). Graphs display quantitative analysis of DiR fluorescence within a selected region of interest surrounding the organ. Bars represent mean ± standard deviation. Statistical significance assessed using matched one-way AVONA for tissue type variation and unpaired t-test for PBS vs. clodronate comparison, *=p>0.05.*

Image analysis of extracted femurs (**Figure 4.21**) shows both injured and contralateral femurs from mice pre-treated with clodronate have a slightly higher DiR signal, although not significant (C.Lat P=0.23, injured P=0.38). For both treatment groups a significantly higher amount of DiR is present within the injured femur compared to the contralateral femur (P=0.001 for both PBS and Clod). Image analysis of fractured femurs alone (**Figure 4.22**) shows negligible differences between DiR signal from clodronate and control groups.

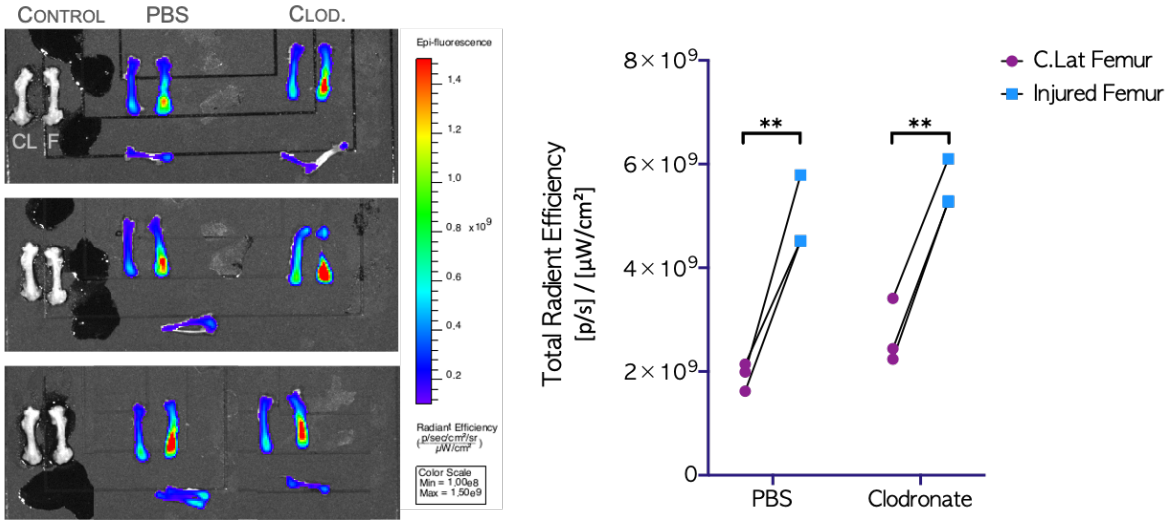


***Figure 4.21: IVIS analysis of polymersome (PM)-DiR distribution within extracted femurs from mice with a bone injury and pre-treated with clodronate liposomes***

*Images of extracted femurs from male MF1 mice 48 hours post IV injection of PM-DiR (200 µL) following surgery to produce a drill-hole injury to the left femur. 48 hours prior to surgery, mice also received 250 µL IV injection of either clodronate (5 mg/mL) (n=3) liposomes or vehicle control, PBS liposomes (n=3). Control mice received no injections. DiR fluorescence is measured by radiant efficiency ([p/sec/cm2/sr]/[µW/cm2]). Graphs display quantitative analysis of DiR fluorescence within a selected region of interest surrounding the injured femur (F) or contralateral femur (CL). Bars represent mean ± standard deviation. Statistical significance assessed using matched two-way ANOVA, **=p>0.005.*

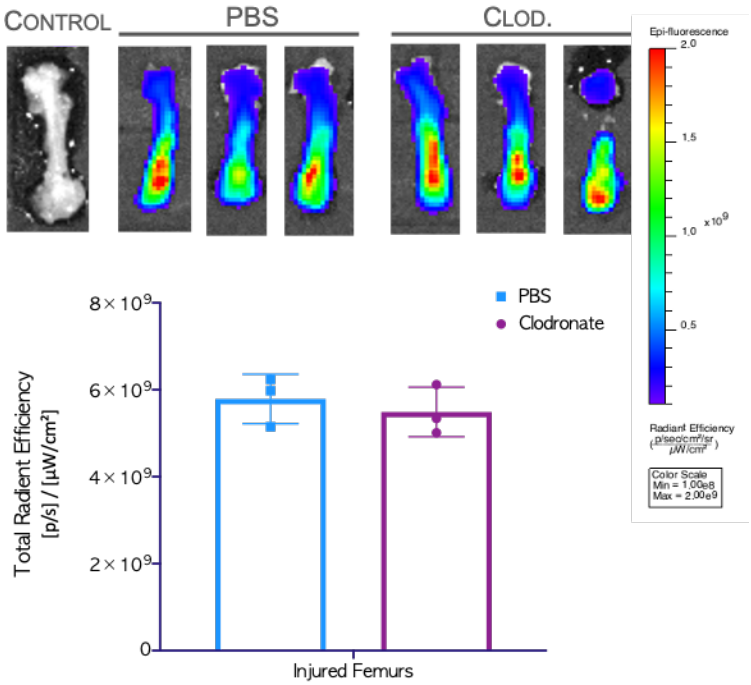


***Figure 4.22: IVIS analysis of polymersome (PM)-DiR distribution within extracted injured femurs from mice pre-treated with clodronate liposomes***

*Images of extracted left injured femurs from male MF1 mice 48 hours post IV injection of PM-DiR (200 µL) following surgery to produce a drill-hole injury to the left femur. 48 hours prior to surgery, mice also received 250 µL IV injection of either clodronate (5 mg/mL) (n=3) liposomes or vehicle control, PBS liposomes (n=3). Control mice received no injections. DiR fluorescence is measured by radiant efficiency ([p/sec/cm2/sr]/[µW/cm2]). Graphs display quantitative analysis of DiR fluorescence within a selected region of interest surrounding the femur. Bars represent mean ± standard deviation. Statistical significance assessed using an unpaired t-test, *=p<0.05.*

## 4.4 DISCUSSION

The efficacy of PM delivery of Wnt agonists for improving fracture outcome will be dependent upon the successful delivery of a sufficient working dose of payload to the target fracture site. Furthermore, a full understanding of the biodistribution and clearance of the PM delivery system is necessary for future clinical translation. It is therefore important to detect and quantify the specific localisation and uptake of synthesised PMs *in vivo*, particularly within a bone injury model.

In this chapter a fluorescent representative payload and *in vivo* imaging system (IVIS) was used to semi-quantify and track PM biodistribution in living mice following a bone fracture. It was demonstrated that PMs passively accumulate at a target injury site 48 hours following administration either 1 hour or 7 days post bone injury. In addition, clodronate liposomes were used to determine the effect of macrophage depletion on PM biodistribution, thereby giving further insight into cell specific functions for nanoparticle uptake. PM accumulation at a target bone injury site was found to not significantly change following the depletion of macrophages.

The data presented in this chapter provide evidence that polymersome nanoparticles are a potential method of facilitating passive accumulation of a drug at a bone injury site. This section discusses each of the above findings in turn.

### 4.4.1 PMs passively accumulate at a target bone site

The drug delivery strategy used in this thesis relies on PMs (the drug carrier), administered IV, to passively accumulate at target bone injury site (passive targeting). Several nanoparticle properties, namely shape, size, composition (i.e. PEGylation), molecular weight, and charge affect PM biodistribution *in vivo.* It was expected that some of the systemically injected dose of PMs would accumulate within bone tissue due to the incorporation of PEG, the measured size of produced PMs (60-120 nm), and the established literature of drug clearance systems *in vivo* – notably that the bone marrow forms a key part in the mononuclear phagocyte system (Bertrand and Leroux, 2012).

One study by Porter *et al.* (1992) which focuses particularly on particle accumulation to the femoral bone marrow demonstrated that, at 24 hours post IV administration to rabbits, particles coated with PEG and particles below 150 nm show greater affinity for bone marrow accumulation compared to larger or uncoated particles. Notably both of these traits are present in the PMs used in the study presented in this chapter. There are few studies which use a polymeric vesicle-based drug delivery system to passively target bone. Of note, a study by Swami *et al.* (2014) used fluorescently labelled

PEG-PLGA-Alexa647 sized between 150-200 nm, and found accumulation in the femurs of healthy mice 24 hours following IP administration. Similarly, a study by Özcan *et al.* (2011) used PEG-PBLG-FITC sized between 40-80 nm, and found fluorescence within the femurs of healthy Wistar rats 24 hours following IV injection. In the experiments reported in this chapter, a slightly later time point of 48 hours was chosen. Nevertheless, at this time point, like in studies by these authors, PMs accumulated to bone tissue, not only in healthy mice femurs but also in mice with injured bones as well as their contralateral femurs.

One difference between the experiments presented in this chapter and the aforementioned research is that a fluorescent representative payload was tracked, rather than the particle itself through the conjugation of a fluorescent tag to the polymer. A study by Adjei *et al.* (2016) also used an NIR dye, in this case to track neutrally charged PVA-PLGA particles (less than 150 nm), and found these particles had the greatest accumulation to mouse skeletons, particularly the vertebrae, pelvis, and long bones, compared to charged and larger particles. Here, particle localisation was found in the marrow but not calcified regions of the tibiae by *ex vivo* IVIS imaging (Adjei *et al.*, 2016). Similarly in this chapter's results, fluorescent imaging of injured bone sections revealed payload signal exclusively within the marrow cavity and not at the cortical wall. Upon reaching the bone marrow vessels, it is thought that nanoparticles extravasate either via intercellular gaps which lack a basement membrane (similar to the sinusoids of the liver) or via phago-endocytic uptake throughout the endothelium. Vessels in cortical bone lined by endothelial cells are thought to have no phago-endocytic activity (Sarin, 2010), possibly accounting for the observed absence of particles here. Of note there is some ambiguity over the types of gaps present at bone marrow capillaries, thereby affecting transport of particular sized molecules. Further research into this will help to improve nanotherapeutic development and potential. To this end, recent advances in intravital imaging may provide insight within live subjects in real-time (Miller and Weissleder, 2017; Reismann *et al.*, 2017).

Particle accumulation within bone tissue has also been measured in other studies which target drug delivery to bone using a specific bone targeting moiety (active targeting), such as alendronate (ALD) or acidic oligopeptides. This active targeting has often resulted in increased accumulation to bone; for example, in a study by Swami *et al.* (2014) ALD conjugated particles exhibited a 9.6 fold increase in bone accumulation (Swami *et al.*, 2014). Özcan *et al.* (2011) found greater bone accumulation of FITC labelled PEG-PBLG-ALD than particles without ALD, but also found the active targeted particles accumulated more so to bone surface than bone marrow. Similarly, Wang *et al.* (2006) found more accumulation to the endocortical surface using an active targeted polymer conjugate (HPMA-

Aspartate peptide), whereas the control (passive targeted particles) accumulated within the bone marrow along sinusoids.

However, it is important to consider which cells present in this micro-environment might be exposed to the released therapeutic payload. Collectively the data reported in this chapter, as well as the literature cited, provides evidence that passively targeted particles accumulate primarily to the bone marrow, whereas active targeting mechanisms accumulate primarily at the bone's surface. The drug delivery system used in this thesis aims to influence SSCs with a Wnt activating payload; these cells preside in the bone marrow (Bianco and Robey, 2004), and therefore passive accumulation to the bone marrow may be more beneficial for this therapeutic strategy.

### 4.4.2 PMs passively accumulate to a bone injury

Unlike in other studies, the data in this chapter show bone marrow PM accumulation at the site of a bone defect. Skeletal injury is associated with disruption to the vascular network at the injured bone and surrounding soft tissue, leading to loss of circulating material to the haematoma. The local and systemic response to inflammation also affects vascular permeability (Levy *et al.*, 2006). Indeed, bone injury has been shown to increase blood flow in a rodent model for at least the first 14 days post injury and cause local vasodilation, which may affect delivery of blood-borne circulating agents (Tomlinson, Shoghi and Silva, 2014).

On this basis, it was hypothesised that early IV administration would result in an increased passive accumulation of PMs to the bone injury site compared to intact bones. Histological assessment of the injury model at day 0 confirmed a haematoma formation, suggesting damaged vasculature and an inflammatory response. When comparing PM bone localisation in injured vs. non-injured mice, whole body images show an increased signal within the injured mice; however, *ex vivo* analysis revealed that accumulation within the skin is primarily responsible for this observed difference. Within the target injured femurs there was a slight increase in PM accumulation between healthy and injured mice, but not to a significant extent. This result only partially supports findings from Scarpa's previous work related to this study, using the same PM-DiR and injury protocols: here, when comparing the femurs from sham control mice to mice with a bone injury, a significantly greater DiR signal was present within the injured femur. However, like Scarpa, a clear increase in accumulation to injured femurs was observed compared to contralateral femurs. Again, this supports the notion that an injury causes local accumulation through formation of the haematoma.

In addition to causing vasodilation, inflammation mobilises phagocytic cells. Jia *et al.* (2015) administered NIR-dye labelled PEG-simvastatin conjugate micelles and observed passive targeting to a bone injury site for at least 7 days. FACs analysis of cells isolated from the fracture callus showed positive particle signal in cells also positive for Ly-6G (myeloid derived cells), F4/80 (macrophage marker), Ly-6B (monocytes and neutrophils), and CD44 (osteoblast/clast/cytes) (Jia *et al.*, 2015). It is possible that resident macrophages within the bone marrow increase their particle uptake activity in response to injury, resulting in the higher accumulation compared to the contralateral femur accumulation.

IVIS image analysis further revealed that PM payloads passively accumulated at the target fracture site whether injected 0 or 7 days following injury, albeit with reduced accumulation to the whole surgical site when the injection was given 7 days post injury. As discussed previously, this may be due to the continued increased blood flow and vascular permeability changes that occur during injury healing. Using a rat bone injury model, Tomlinson *et al.* (2014) found a 22-33% increase in flow rate at 0-14 days post bone injury. In addition, Tomlinson *et al.* assessed vasodilation and found an increase in arterial area up to 3 days post bone injury; mast cell infiltration (indicating increased permeability) was also significantly greater from 1 day to at least 14 days post injury compared to controls (Tomlinson, Shoghi and Silva, 2014). Together these data support the notion that changes in vascular permeability may promote nanoparticle accumulation to a bone injury site for a period of at least 7 days. Future experiments may seek to address the degree of permeability in a bone fracture through, for example, administration of NPs that vary in size, to determine the degree of size-dependent accumulation.

The clinical translation of EPR principles has highlighted marked variability in successful nanoparticle tumour accumulation due to heterogeneity of tumours, namely vascularly permeability, lymphatic drainage, blood perfusion rates, interstitial pressure, ECM density, and composition. Similarly, in bone repair there are complex microenvironment changes, in different regions, at different rates, which likely affect not only vessel permeability, but also ECM density and phagocytic cell activity. Each of these factors may in turn affect the movement and uptake of particles. Detailed understanding of how these injury-induced environmental changes affect particle uptake *in vivo* is required.

### 4.4.3 The bulk of PMs accumulate to the liver

Aside from accumulation to the target bone injury, IVIS analysis showed that the largest accumulation of PM payload was within the liver. Several studies which also use systemically

administered PEG-*b*-PCL of various ratios and sizes have also demonstrated this observation. Asem *et al.* (2016), administering fluorescent tagged PEG-PCL micelles (sized 212 nm) to a healthy mouse, report highest accumulation in the liver at 48 hours. Using the same method employed in this chapter's experiments (i.e. DiR loading and IVIS imaging), Cho *et al.* (2012) record liver accumulation of PEG5k-*b*-PCL10k micelles (31.9 and 47.06 nm) at 96 hours post IV to be second highest to tumour accumulation. Using an alternative method of radio labelling, Liu, Zeng and Allen (2007) studied the distribution MePEG5k-*b*-PCL5k micelles (56 nm) at several timepoints post IV, including 48 hours, and consistently found that the liver retains the highest accumulation of particles. Each of these studies also report uptake within the spleen and kidneys, as is seen in this chapter's results.

When comparing uninjured mice and mice with a bone injury, the change in PM accumulation to the liver was negligible – if not slightly increased in the injured model. Drawing firm conclusions here is limited by a lack of sufficient subject numbers. However, evidence from the literature on changes to liver activity following a distal bone injury have shown that Kupffer cells are significantly activated within 24 hours, as measured by increases in their production and release of cytokines such as IL-6 and IL-10 (Levy *et al.*, 2006); by 3 days post injury, this effect subsides (Matsutani *et al.*, 2007; Neunaber *et al.*, 2013). Schirmer *et al.* (1988) investigated liver blood flow rates in a rat following a femur fracture both with and without soft tissue injury. Here it was found that in fracture subjects with minimal soft tissue injury (surgically induced fracture rather than blunt force trauma), the liver blood flow has returned to normal levels after 24 hours (Schirmer *et al.*, 1988). This suggests that for the injury model used in this chapter, 48 hours post injury liver perfusion and Kupffer cell activity, both factors associated with NP accumulation as previously discussed, likely have returned to near normal state, accounting for the minor change in liver uptake compared to non-injured controls.

### 4.4.4 The effect of macrophage depletion upon PM localisation *in vivo*

Liver sinusoidal endothelial cells lack a basement membrane and contain fenestrations with pore sizes ranging from 100-150 nm (Zhang *et al.*, 2016), thereby allowing NPs in circulation to extravasate to the liver tissue. It is widely suggested that Kupffer cells are responsible for nanoparticle retention in this tissue. Accordingly, to determine whether the liver-specific accumulation observed in this chapter's experiments could be reduced, clodronate liposomes were used to deplete these cells. It was also hypothesised that reducing liver accumulation might promote injury-specific accumulation in a similar manner to that seen in tumour nanoparticle accumulation post clodronate liposomes treatment (Tavares *et al.*, 2017). Liposome encapsulated clodronate has been used as a tool for regulating macrophage activity *in vivo*, and – depending on the administration route used – can

deplete subpopulations of macrophages in particular tissues. Specifically intravenous injection has been shown to target macrophages present within the liver, spleen (Van Rooijen and Van Kesteren-Hendrikx, 2002; van Rooijen and Hendrikx, 2010), and bone marrow (Schlundt *et al.*, 2018).

Previous studies have employed depletion techniques and studied the subsequent effects upon nanoparticle accumulation. Hu, Van Rooijen and Liu (1996) showed that clodronate liposomes, IV injected 24 hours before radiolabelled NP (liposome) IV injection, reduced liver accumulation at 4 and 36 hours post NP injection regardless of NP size, composition, or the clodronate dose. Laverman *et al.* (2001) showed that clodronate liposomes, IV injected 48 hours before radiolabelled PEG-liposome administration, reduced liver accumulation of a second dose of NPs administered 2 weeks following the first. Similarly, in the experiments using healthy/uninjured mice reported in this chapter, a decrease in liver PM accumulation (measured by DiR) was seen 48 hours post NP IV administration (96 hours post clodronate treatment).

Unlike the previous studies, this chapter further investigated PM accumulation to the bone. Here, clodronate pre-treatment in uninjured mice showed an increase in PM accumulation to the femurs. With lower uptake by the liver, a greater systemic dose is available for other organs with permeable vasculature to take up. This was also seen by Tavares *et al.* (2017), where a 4-fold decrease in gold nanoparticle liver accumulation coincided with a clodronate-dose-dependent increase in accumulation to the spleen, as well as increased accumulation to a tumour by a factor of 142. In this chapter, an increase in signal in the spleen was also observed in addition to the aforementioned femur increase. The use of a single dose of clodronate liposomes in this chapter was expected to only partially deplete macrophages in the bone marrow, based on previous studies (van Rooijen and Hendrikx, 2010; Schlundt *et al.*, 2018), thus possibly enabling uptake of the increased systemic dose. Further IHC & FACs assessment of macrophage depletion within the femurs would confirm the extent of depletion within this tissue.

Conversely in mice with a bone injury, despite confirming clodronate liposome pre-injection fully depleted the macrophage population in the livers of treated mice, a corresponding decrease in liver DiR accumulation was not found. Instead, accumulation to the liver increased, along with no significant change in accumulation to bone.

This observation is surprising. Although not in an injury model, Tavares *et al.* (2017) studied the role of macrophages in the uptake of nanoparticles within a mouse tumour model, a distal site of NP uptake. Like the experiments in this chapter, macrophages were depleted with clodronate liposomes 48 hours before injecting various NPs and the tissue accumulation was quantified with IVIS, however

ICP-MS was also used and assessment was at a slightly earlier time point of 24 hours (Tavares *et al.*, 2017). As previously mentioned, liver accumulation decreased following clodronate pre-treatment, whilst accumulation of nanoliposomes, silica nanoparticles, and silver nanoparticles at the tumour site increased by factors of 2, 5, and 7, respectively. Although formed of different materials to the PMs used in this chapter, the particles used by Tavares were fixed to 100 nm size and had surface PEG ligands, similar to the PMs used in this thesis. Collectively this suggests that the major difference of an injury/inflamed state may be responsible for the opposing results seen in this chapter. These findings are limited by a lack of experimental replicates; further work to increase N numbers in line with NC3R recommended power calculations would draw out any statistically significant difference.

Tavares also notes that despite macrophage depletion leading to increased NP accumulation to the tumour site, the overall delivery efficacy was only 2% of the injected dose. This leaves open questions as to what other cell types in the liver and other organs are responsible for sequestering dose away from the target site. There is a general consensus that NPs are predominantly sequestered by macrophages through recognition of surface opsonins. This theory is based on observed liver and spleen uptake at a whole organ level, histological knowledge that the liver contains 80-90% of the macrophage population of the body (Bertrand and Leroux, 2012) and that Kupffer cells are known to line the sinusoid capillaries encountering blood borne particles, and *in vitro* studies investigating PEGylation and opsonisation effects upon uptake in cell culture (Gref, Minamitake, Peracchia, Trubetskoy, Torchilin and Langer, 1994; Moghimi, Hunter and Andresen, 2012). These studies have left questions open as to what extent protein and cell interactions occur *in vivo* (Papini, Tavano and Mancin, 2020).

Using intravital microscopy imaging methods, Miller *et al.* (2015) demonstrated live *in vivo* that PEG-PLGA (IV injection) are extensively taken up by macrophages within a tumour model. However, studies which properly investigate uptake at a cellular level, especially across multiple particle sizes and compositions within liver tissue, are sparse. Zhang reviews much of the available literature that does investigate further liver cell types which uptake NP. Notably hepatocytes in the hepatobiliary clearance system are able to scavenge particles up to 150-200 nm which have extravasated into the space of Disse after evading Kupffer cell engulfment. There is also evidence showing liver sinusoidal endothelial cells take up smaller sized NPs. It is possible that the particles used in this thesis, being less than 150 nm, are able to move into this space. In the fluorescent imaging results from this chapter, nanoparticles, identified by DiI, are seen localised within cells that are distributed and contain nuclei associated with hepatocytes. This evidence suggests that attributing the observed sequestering of NPs in clearance organs to only macrophages may be limiting. It is possible that for

injured and clodronate depleted subjects, in the absence of competition from Kupffer cells other cell types responding to the inflammatory state may be responsible for the greater uptake of PMs observed. Further study using immunohistochemistry to assess any co-localisation of payload signal to resident hepatocyte and macrophage markers in injured vs. non-injured subjects would confirm this theory. Distinguishing which cell types are responsible for PM uptake *in vivo* would help to identify which cell types may be affected by the Wnt agonists encapsulated in the PM-treatment, as well as provide insight to benefit future NP designs to potentially avoid off-target accumulation and clearance.

### 4.4.5 Study limitations and future work

With more extensive reference measurements, IVIS imaging has the potential to quantify the payload dose reaching the target injury site. Additionally, not fully utilised in this study is its ability to track biodistribution in real time within the same animal, and combine this with µCT for 3D imaging. Tracking PM accumulation within the same mouse at multiple timepoints would be beneficial to reduce biological variation and extensively map particle localisation *in vivo* in real time; this has not yet been possible in the current study due to project licence restrictions.

In addition, use of fluorescently tagged PMs would enable dual tracking of vehicle and payload (Miller *et al.*, 2015). This would be useful to understand firstly the payload release rate and dose within tissues which retain PMs, but also the tissue retention time and clearance of PMs themselves. Each of these will impact potential side-effects and help to establish treatment windows. Furthermore a long-term *in vivo* study which assesses PM retention and effects upon tissue toxicity such as liver morphology and performance would also be of benefit.

Since passive targeting is impacted by vascular extravasation mechanisms, it would also be interesting to compare bone injury uptake in an aged mouse model, enabling understanding of delivery efficiency within various vascular conditions likely encountered in clinic. This could ultimately inform of how dose might be optimised for different conditions. However, note that species differences in vasculature will limit translation of NP localisation in humans. For example, rodents do not have a Harversian remodelling system like humans; more specifically, their vasculature is in series rather than parallel network (Lavrador, Gaspar and Mano, 2018), and their hepatic sinusoid pore sizes differ (humans 180 nm vs. rodents 280 nm).

Research into facilitating PM access across the barrier between vasculature and bone marrow, for example using vascular mediator drugs or through the addition of active bone targeting moieties, could also improve treatment success.

### 4.4.6 Conclusion

Overall this chapter has demonstrated that systemic administration of PEG-*b*-PCL within a time window of a least 7 days post injury can successfully deliver a payload to a bone injury site, primarily to the bone marrow. Through using IVIS to track a payload *in vivo*, a further understanding of this type of nanoparticle's biodistribution in the context of a bone injury has been gained. It is apparent that clearance systems, phagocytic or otherwise, reduce the amount of available payload at a target bone injury site. An understanding is required of whether the available dose at the injury site is sufficient to cause a measurable effect; this is explored in the next chapter.

# CHAPTER 5

## THE BIOLOGICAL ACTIVITY OF POLYMERSOMES LOADED WITH THE SMALL MOLECULE WNT AGONIST BIO IN A MOUSE INJURY MODEL

### 5.1 INTRODUCTION

Pharmaceutical treatments for fracture repair have potential to increase healing rates and reduce complication such as non-unions. To date surgically implanted scaffolds with rhBMP-2 (InFUSE®) or rhBMP-7 (OP-1®) are the only approved drug-based treatment for non-unions (Krishnakumar *et al.*, 2017); however as discussed in **section 1.6**, BMP treatment has several limitations, including heterotopic bone formation side effects, and the requirement of surgical implantation. Other approved bone regenerative drug therapies have focused primarily on decreasing the risk of osteoporosis related fragility fractures. Here antiresorptive agents such as the bisphosphonate alendronate, and anabolic agents such as recombinant parathyroid hormone (teriparatide), are traditionally prescribed (Hoang-Kim *et al.*, 2009). Anabolic agents, including the more recently-approved therapy Romosozumab (an antibody that inhibits sclerostin), have potential for use in promoting general fracture repair (Saag *et al.*, 2017), yet a recent trial found use of Romosozumab in hip fracture treatment did not improve outcomes compared to placebo (Schemitsch *et al.*, 2020). Thus, clinically available drug therapies for improving fracture outcome are sparse, driving the development of alternatives.

The Wnt signalling pathway has a well-established and important function in bone growth, homeostasis, and repair following a bone injury, as discussed in **section 1.7**. Necessary for both osteogenesis and early chondrogenesis during repair *in vivo* (Chen and Alman, 2009), it is hence an attractive target for drug therapies to enhance bone healing and improve fracture outcome. This thesis explores the therapeutic benefit of small molecule Wnt agonists BIO and CHIR within a polymersome (PM)-controlled delivery system.

As detailed in **section 1.7.5**, research has already been performed into determining the effects of free BIO and free CHIR treatment upon human BMSCs *in vitro*. These small molecules were found to induce Wnt signalling, as determined by increased *AXIN2* expression (Frith *et al.*, 2013; Scarpa *et al.*, 2018); additionally PM-BIO was found to promote and sustain *AXIN2* expression for a longer duration

than free BIO (Scarpa *et al.*, 2018). *In vitro* studies have however also revealed a complex and contradictory set of results regarding BIO and CHIR's success at promoting osteogenesis. What is not clear is whether Wnt signalling is required to be active for all stages involved in osteogenesis, i.e. throughout progenitor differentiation into a mature osteoblast phenotype with the capability to produce a mineralised bone matrix. Importantly, these results are from a cell type taken out of its natural environment, hence removed from the many autocrine and paracrine signals from other neighbouring cell types which would otherwise direct stem cell proliferation and differentiation. Putting a Wnt agonist into this repair environment will affect multiple cell types that have roles in repair and influence the overall local secretome environment. Therefore, it is ultimately important to understand what effect BIO/CHIR treatment has *in vivo* and in particular within an injured bone model, and whether controlling delivery via PMs will impact this.

So far only Scarpa, (2016) has begun to investigate the effects of PM-BIO treatment on a mouse bone injury model, and found from µCT measurements comparable extent and rate of healing compared to controls. This work hence leaves open opportunities for further research, to ascertain what features, such as loading dose, may have limited any measurable therapeutic efficacy of PM-BIO.

To test therapeutic efficacy upon bone healing, as well as assessing gross changes such as bone density (µCT measurements) or healing progression (histological assessment), it is useful to measure changes at a level corresponding to the therapeutic's direct target, i.e. changes to signalling *in vivo*. At the time of writing, no published studies have investigated Wnt signalling or osteogenic signalling changes *in vivo* after BIO/CHIR treatment. However, Wang *et al.* (2017) has studied an alternative Wnt agonist (AZD2858) using an *Axin2* reporter mouse to evidence canonical Wnt signalling activation at a bone injury site. This method has the advantage of identifying spatial and temporal information in bone sections. However, in terms of measuring therapeutic efficacy it is a semi-quantitative method at best and also requires *ex vivo* analysis, rather than providing true *in vivo* information during real time within a live subject.

Other methods to confirm Wnt induction and osteogenesis *ex vivo* include qPCR, which has the advantage of being a quantitative method for assessing therapeutic efficacy. Furthermore, it has long been used in literature to understand temporal expression following a bone injury as described in **section 1.4**. These temporal studies highlight key genes known to be regulated in repair that could be monitored for changes following treatment. For example, *Axin2,* a known gene target of Wnt signalling activation (Jho *et al.*, 2002, Ramakrishnan and Cadigan, 2017), has previously been used as a reliable readout of the Wnt signalling activation of Wnt-responsive cells in both liver tissue (Wang *et al.*, 2015) and bone tissue (Ransom *et al.*, 2016). *Dkk1* is also an established Wnt signalling target

(Niida *et al.*, 2004) expressed within bone tissue (Baron and Kneissel, 2013). If the level of *Axin2* and *Dkk1* gene expression is sufficient to induce production of proteins, these act as negative regulators of the Wnt signalling pathway (Monroe *et al.*, 2012), therefore an increase in *Axin2* and *Dkk1* expression infers subsequent downregulation of the Wnt signalling pathway. For identifying osteogenic signalling, gene expression markers such as *Runx2* and *Osx/Sp7* have been established as key regulators of osteoblast differentiation (Kaback *et al.*, 2008). *Runx2* in particular has been identified as a regulator for progenitor cell differentiation into chondrocyte or osteoblast lineages and therefore indicates endochondral and/or intramembranous based bone formation (Komori, 2018). As such *Axin2*, *Dkk1*, and *Runx2* provide useful markers to assess if PM-delivered Wnt agonists can induce Wnt and osteogenic signalling *in vivo*.

It is notable that the gene expression studies which investigate Wnt related signalling changes post bone injury lack information within the first 72 hours after treatment (see **Figure 1.9**). This phase of healing involves inflammatory signaling and haematoma formation known to be essential for initiating bone formation. Therefore, treatment application and assessment within this time period is a focus of investigation in this chapter. Additionally, this early time window is of particular interest due to a previous PM localisation study which identified that the greatest accumulation at the target injury site occurs 48 hours post-injury (Scarpa, 2016).

From the review of the literature, no published studies have yet studied if PM-delivery of CHIR can achieve Wnt signalling activation *in vivo*. However, for this study BIO became the first primary focus over CHIR due to its higher potency as a Wnt agonist and more extensive prior study.

Overall to evaluate if PM-BIO has potential as a treatment to improve fracture outcome, this study uses qPCR analysis to test the hypothesis that a single dose of PM-encapsulated BIO can induce Wnt signalling activity and osteogenic differentiation *in vivo*. This study also begins to inform of the optimal dose and time after injury at which to apply treatment.

## 5.2 AIMS

**The first aim of this chapter is to determine the biological activity of BIO loaded polymersomes *in vivo* by assessing expression of Wnt signalling target genes in tissues of high PM accumulation, within 48 hours post IV administration.**

- Compare the relative gene expression of Wnt target gene *Axin2* over time in mouse fibroblast cells incubated with BIO.
- Assess the relative gene expression of Wnt target gene Axin2 over time in mouse bone marrow cells incubated with CHIR.
- Optimise qPCR assay for measuring the relative expression of genes of interest using mouse fibroblasts treated with BIO.
- Assess the relative gene expression of Wnt target genes in the liver and bone marrow of mice treated with PM-BIO.
- Assess the relative gene expression of osteogenic genes in the bone marrow of mice treated with PM-BIO.

**The second aim of this chapter is to determine the biological activity of BIO-loaded polymersomes within a mouse bone injury model, within 48 hours post IV administration.**

- Assess the relative gene expression of Wnt target genes in the livers and bone marrow of mice treated with PM-BIO.
- Assess the relative gene expression of osteogenic genes in the bone marrow of mice treated with PM-BIO.

## 5.3 RESULTS

The ability of polymersome-encapsulated BIO to activate Wnt signalling *in vivo*, and specifically at a bone injury site, was evaluated by measuring Wnt gene expression changes using RT-qPCR. The following genes that are activated downstream of Wnt signalling, referred to as Wnt target genes, were selected for investigation: *Axin2*, a negative regulator of the Wnt signalling pathway which is expressed directly upon Wnt signalling activation (Jho *et al.*, 2002); and *Dkk1*, also a negative feedback inhibitor (Niida *et al.*, 2004). In addition, the effect of PM-BIO on the expression of an osteogenic gene – *Runx2*, which induces osteoblast differentiation and is activated downstream of Wnt signalling activation (Zou *et al.*, 2006) – was also selected for investigation. In order to assess Wnt signalling activity *in vivo* using qPCR analysis, primer pairs were designed for Wnt target and osteogenic genes, as well as various reference (housekeeping) genes (all primer sequences are listed in **Table 2.1**). Once designed, the efficiency of these primers needed to be tested, to determine their suitability for future experimental use.

### 5.3.1 Primer efficiency testing for genes of interest

To test primer efficiency, serial dilutions of a positive source cDNA (from mouse fibroblasts incubated with BIO for 6 hrs) were analysed by RT-qPCR with the newly designed primers. Raw qPCR data plots of normalised fluorescence (ΔRn) against PCR cycle number show amplification of a cDNA sequence, an example of which is shown for *Gapdh* reference gene primer in **Figure 5.1a**. Negative control samples that contain no cDNA template show no amplification. Within the exponential phase of ΔRn a threshold of 0.2 was selected; corresponding cycle numbers ($C_T$) were then plotted against cDNA concentration to create a standard curve, an example of which is shown for *Gapdh* in **Figure 5.1b**. Linear regression analysis of the standard curve was then performed; resultant $R^2$ values ranging between 0.99 and 0.95 indicate a high confidence in the data fit (**Figure 5.1b**). The given slope value was then used to calculate efficiency $E$ (%) using the equation given by Pfaffl (2001), detailed in **section 2.4.6**. An example standard curve and efficiency calculation is shown for *Gapdh* in **Figure 5.1c**; other primer efficiency data is given in supplementary material **section S.4**. Note that the high dilutions for some primers have not been plotted due to having an undetermined $C_T$ value or a $C_T$ value of 35 or above, which are considered likely to contain primer dimers and non-specific binding products and are therefore discounted.

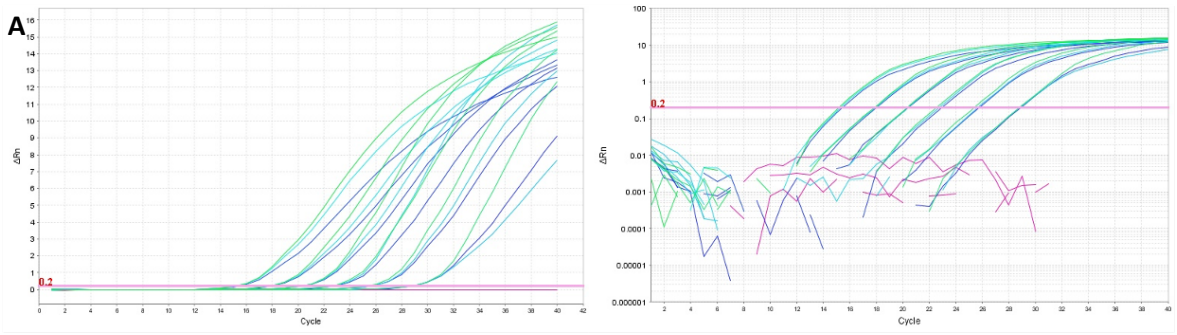


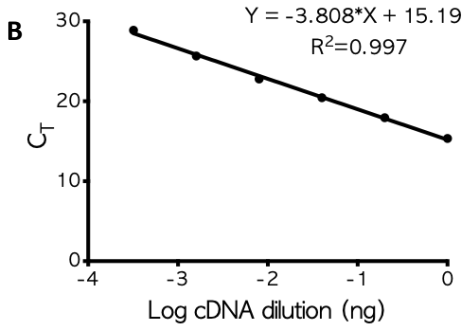


C

$$E\ (\%) = \left(10^{\left(\frac{-1}{-3.808}\right)} - 1\right) \times 100$$

$$E\% = 83.0$$

***Figure 5.1: Gapdh reference gene primer efficiency***

*A) Amplification plot normalised to a passive reference dye (Rn) and minus the instrument and baseline signal (ΔRn), expressed using both log (right) and non-log (left) scales. B) Standard curve of the log concentration of template cDNA diluted 5-fold against qPCR cycle number ($C_T$) from 0.2 fluorescence threshold (red line in (A)). Data presented is the mean and standard deviation of n=3 repeat diluted template samples. C) Percentage primer efficiency calculated using the standard curve slope value.*

To validate the observed amplification of cDNA related to specific primer target sequences, qPCR melt curve analysis and agarose gel electrophoresis of the qPCR product was performed. An example data set is shown for *Gapdh* in **Figure 5.2**, and other primers are shown in supplementary material **section S.4**.

Raw qPCR data plots of normalised fluorescence signal (Rn) against temperature (°C) show the melting temperature at which double-stranded cDNA sequences separate to single-stranded cDNA, identified by a sudden decrease in fluorescence (**Figure 5.2a**). The derivative plot of this melt curve shows a single prominent peak indicating the presence of a single amplified transcript product (**Figure 5.2b**). Negative non-template controls (NTCs) displayed no prominent melt curve peak at the same scale as the template sample, suggesting no primer dimers were produced, hence verifying that samples with cDNA would be free of false-positive signals (**Figure 5.2c**). Any primers having a prominent negative control melt curve peak were discounted at this stage, except when that peak corresponded to qPCR amplification plots above a cycle number of 35.

Following electrophoresis, imaged agarose gels display a prominent band at a size (defined by the base pair number (bp) marker (**Figure 5.2c**)) that corresponds to the expected *Gapdh* product length listed in **Table 2.1**. Note the faint second band observed below the main band is likely due to the presence of single-stranded DNA present within the qPCR product following the additional melt curve thermal cycle. This is supported by the absence of secondary peaks in the qPCR melt curves, which would otherwise suggest a non-specific amplification product. Any primers which displayed multiple bands, bands not corresponding to the expected weight, or bands within the negative control (NTC), were discounted at this stage. Note that for some of the primers shown in **section S.4**, additional faint bands are present for high dilutions; this is likely due to low template and high primer ratios causing primer dimers.

Together data from melt curve analysis and agarose gel electrophoresis confirmed the amplification of a single product with the target gene's sequence length, rather than non-specific cDNA amplification or primer dimerization. This therefore validates the observed results and subsequent primer efficiency calculations.

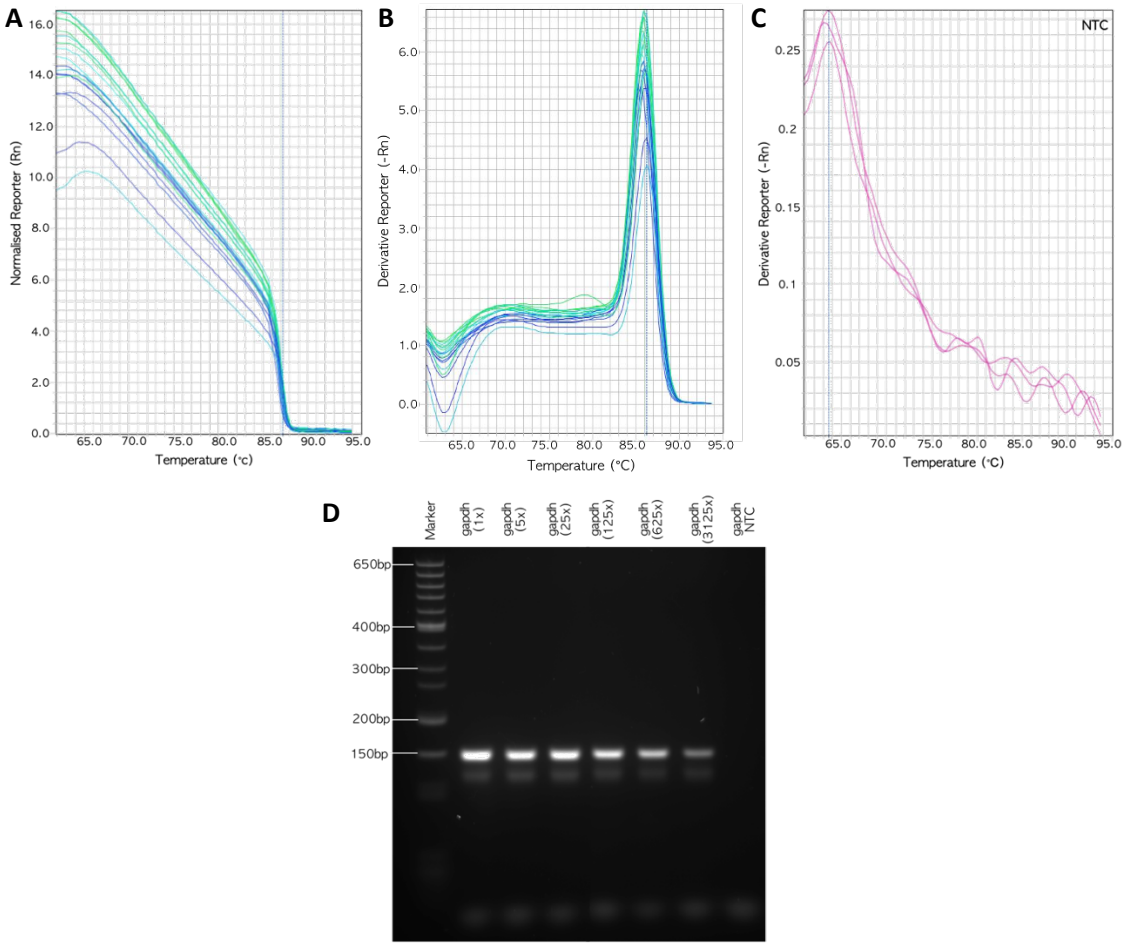


***Figure 5.2: Gapdh reference gene primer validation***

*qPCR amplification product melt curve (A) and derivative melt curve (B), both displaying a melting temperature of 86.23°C for Gapdh. C) The derivative melt curve of the non-template control (NTC) negative control wells. D) Agarose gel image of qPCR amplification products with DNA ladder of 25-60 bp length markers.*

A further test was performed to determine which of the designed reference (housekeeping) primers would be most suitable for use as the reference gene for normalisation in relative expression analysis. Genes were selected based on the criteria that expression remained consistent across all experimental tissue types and conditions, i.e. injured or non-injured mice. Control tissue samples not exposed to any treatment were used to assess reference gene expression. **Figure 5.3** shows that, of all the reference genes investigated, *B2m* has the highest expression variation across tissue types and therefore was discounted from further use. Additionally, *Polr2a* was discounted due to the primer validation melt curve analysis showing multiple expression peaks (**Figure S 9**). Of the remaining reference genes, a variation of at least one cycle number ($C_T$) is present between injured and non-injured bone marrow samples. Since +/- 0.5 $C_T$ results in a 2-fold variation in expression, two reference genes were used in experimental runs and their relative expression analyses were compared.

Overall, the primer validation steps described here determined which primer designs were suitable for further experimental use. When comparing the efficiency of the reference genes (e.g. 83% for *Gapdh*) against some of the target genes (*Dkk1* and *Runx2),* a difference of over 5% was observed. Therefore all future qPCR analysis used the Pfaffel method (Pfaffl, 2001), which accounts for differences in reference and target primer efficiencies in relative expression calculations (equation shown in **section 2.4.7**).

| | Liver | Bone marrow | Liver (injured) | Bone marrow (injured) |
|---|---|---|---|---|
| ***Gapdh*** | 14.87±0.09 | 15.03±0.19 | 15.04±0.21 | 16.43±0.14 |
| ***Tbp*** | 24.46±0.09 | 23.44±0.02 | 24.46±0.008 | 24.81±0.11 |
| ***B2m*** | 14.31±0.31 | 16.58±0.16 | 14.39±0.11 | 17.66±0.12 |
| ***Eif3f*** | 19.09±0.96 | 18.40±0.23 | 18.97±0.91 | 20.11±0.39 |
| ***Polr2a*** | 23.04±0.08 | 21.81±0.10 | 23.44±0.10 | 23.60±0.05 |
| ***Axin2*** | 25.97±0.02 | 29.54±0.18 | 26.53±0.04 | 30.79±0.14 |

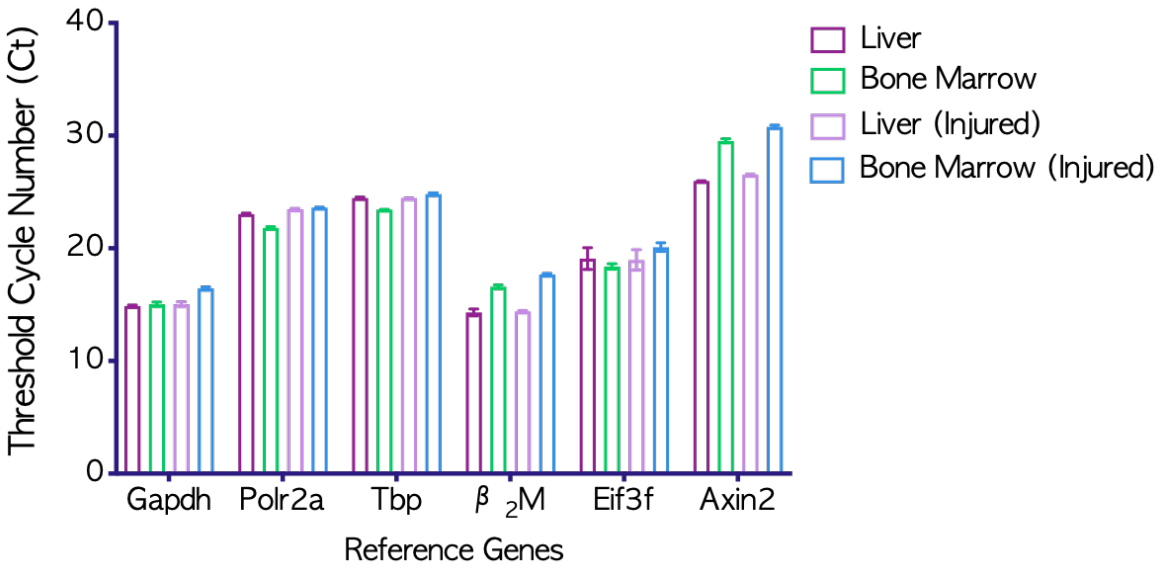


***Figure 5.3, Table 5.1: Expression of reference genes within control tissue samples***

*Table and graph display the same data of reference gene expression levels: RT-qPCR cycle number at a set threshold within the liver tissue and flushed bone marrow samples extracted from mice both with and without a bone injury. Wnt target gene Axin2 is also included for reference of a gene expected to change with varying conditions. Data expressed as mean ± standard deviation of n=3 technical repeats from the same sample.*

### 5.3.2 BIO can activate Wnt signalling in primary cells and signalling decreases with time

To test if the GSK3 inhibitor BIO could increase expression of Wnt-responsive genes in primary mouse cells, primary mouse fibroblasts were incubated with BIO (5 µM) for varying lengths of time, and their resultant level of *Axin2* activity was assessed (**Figure 5.4**). A schematic of this experiment can be found in methods **Figure 2.9** and the extracted RNA purity and yield is reported in supplementary **Table S 1**. RT-qPCR analysis revealed 6-hour exposure to BIO produced the highest expression of *Axin2* out of the timepoints investigated, and this sample was subsequently selected for further use as the positive control with which to test selected primer efficiencies.

Further to producing a sufficient positive control, this experiment also showed that incubation of primary mouse cells with a single dose of BIO results in increased Wnt signalling which peaks at 6 hours and then decreases at 12 hours, with this decrease persisting at 24 hours. The same experiment was subsequently performed with 5 µM CHIR which showed little change to *Axin2* expression relative to control untreated cells, and thereby less expression compared to 5 µM BIO 6-hour exposure. This may indicate that the selected CHIR concentration is below a threshold required to activate gene expression of *Axin2* Wnt inhibitor.

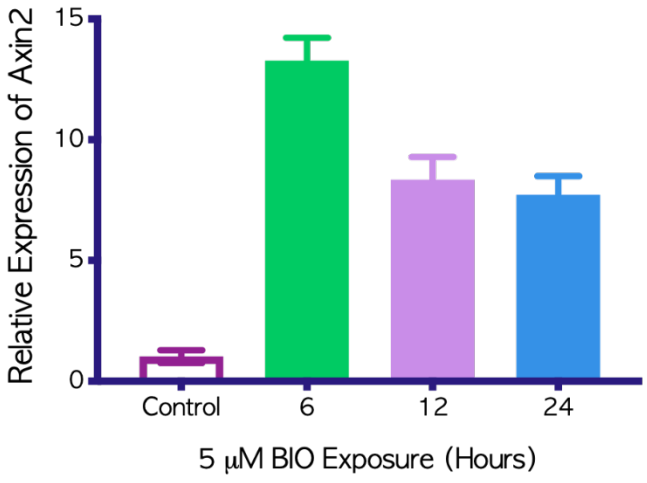


***Figure 5.4: Relative expression of Axin2 in mouse fibroblasts treated with Wnt agonist BIO***

*Primary mouse fibroblast cells were incubated with 5 µM BIO for 6, 12, or 24 hours before lysing and extracting RNA for RT-qPCR analysis. Cells with no treatment, lysed at 24-hour timepoint, served as the control. Readings represent Axin2 expression relative to the control and normalised to Gapdh Reference gene expression. Bars represent the mean ± standard deviation of n=3 technical RT-qPCR repeats.*

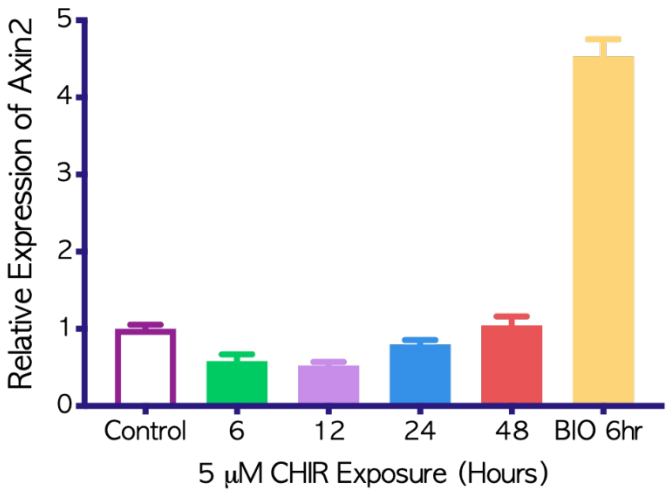


***Figure 5.5: Relative expression of Axin2 in mouse bone marrow cells treated with Wnt agonist CHIR***

*Primary mouse bone marrow cells were incubated with 5μM CHIR for 6, 12, or 24 hours before lysing and extracting RNA for RT-qPCR analysis. Cells with no treatment served as the control. Readings represent Axin2 expression relative to the control and normalised to Gapdh Reference gene expression. Bars represent the mean ± standard deviation of n=3 technical RT-qPCR repeats.*

### 5.3.3 Mice treated with PM-BIO show no increased Wnt signalling *in vivo*

To determine if PM-BIO induces Wnt signalling *in vivo*, validated primers were used to assess the relative expression of *Axin2* and *Dkk1* (Wnt signalling related genes) in healthy, uninjured mice following IV administration of PM-BIO. Liver and bone marrow tissues were extracted from mice at 24- and 48-hours following PM administration, and their gene expression was compared with controls which received PM-Empty. These timepoints and tissues were selected based on data in the previous chapter which showed marked accumulation of PMs in the liver tissue at 48 hours (**Figure 4.4**). A schematic of this experiment is visible in the bottom half of **Figure 5.6** (which is repeated from Figure 2.10), and the extracted RNA purity and yield are reported in supplementary **Table S 1.**

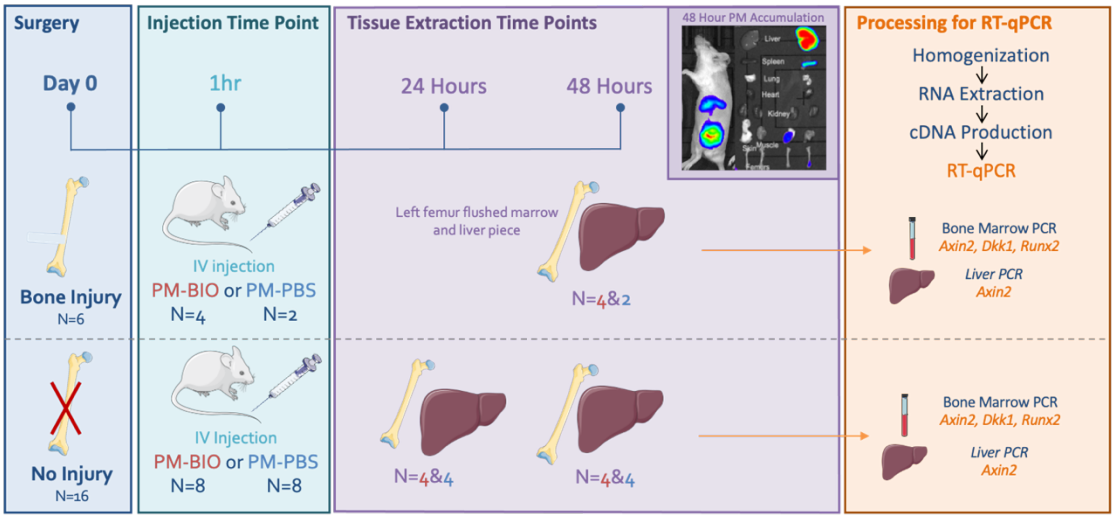


***Figure 5.6: Experimental plan for RT-qPCR analysis of polymersome (PM)-BIO treatment 24- and 48-hours following administration to female MF1 mice with and without a bone injury***

*PM-BIO subjects highlighted in red. Control PM-Empty/PBS subjects highlighted in blue. (Figure reproduced from methods* ***section 2.4.2****). (Parts of this figure's graphics are credited to smart.servier.com)*

**Figure 5.7** shows within extracted liver tissues, mice treated with PM-BIO had no statistically significant change in *Axin2* expression in comparison to the control at either 24- or 48-hours post treatment. This is apparent for the relative expression when normalised to either *Gapdh* (P=0.53) or *Eif3f* (P=0.40) reference genes.

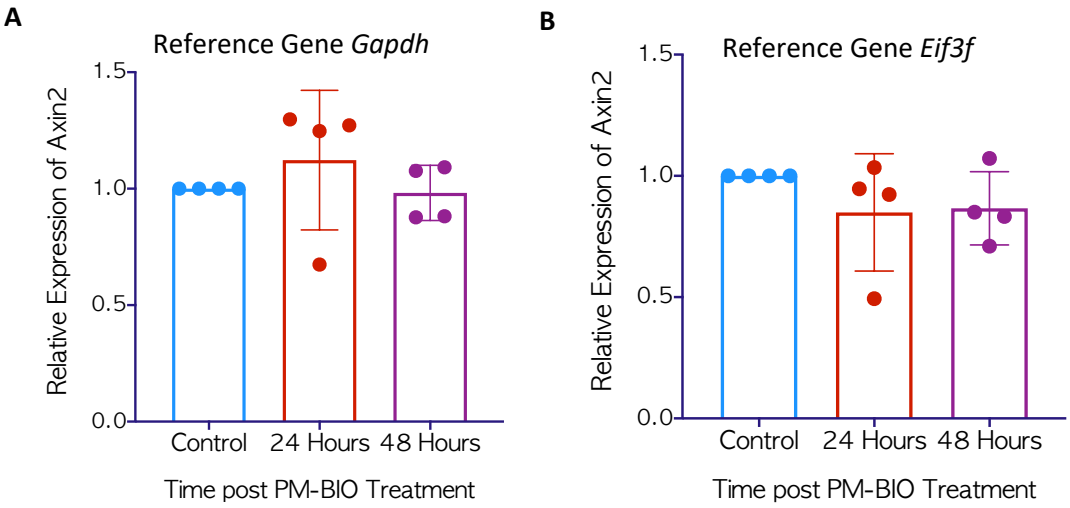


***Figure 5.7: Relative expression of Axin2 over time in liver tissue extracted from healthy female MF1 mice treated with polymersome (PM)-BIO***

*Axin2 expression relative to Gapdh reference gene (A) and Eif3f reference gene (B) normalised to mean of controls which received PM-Empty IV. Graphs displayed mean ± standard deviation of n=4 mice. Statistical significance assessed using one way ANOVA with Dunnett's Multiple comparisons test.*

The same relationship is seen within the extracted bone marrows (**Figure 5.8**), where no statistically significant change in *Axin2* expression exists between control mice and PM-BIO treatment (P=0.33 for *Gapdh* and P=0.32 for *Eif3f*). However, for one of the four mice the bone marrow samples did show a notable increase in *Axin2* expression, 2.5 times that of the control expression. Another gene associated with Wnt signalling activation, *Dkk1*, was also investigated (**Figure 5.8c**). Within the bone marrow no change in the mean expression was measured between control and PM-BIO treated mice (P=0.74). However, a wide variation in individual responses is observed, with one subject showing increased *Dkk1* expression.

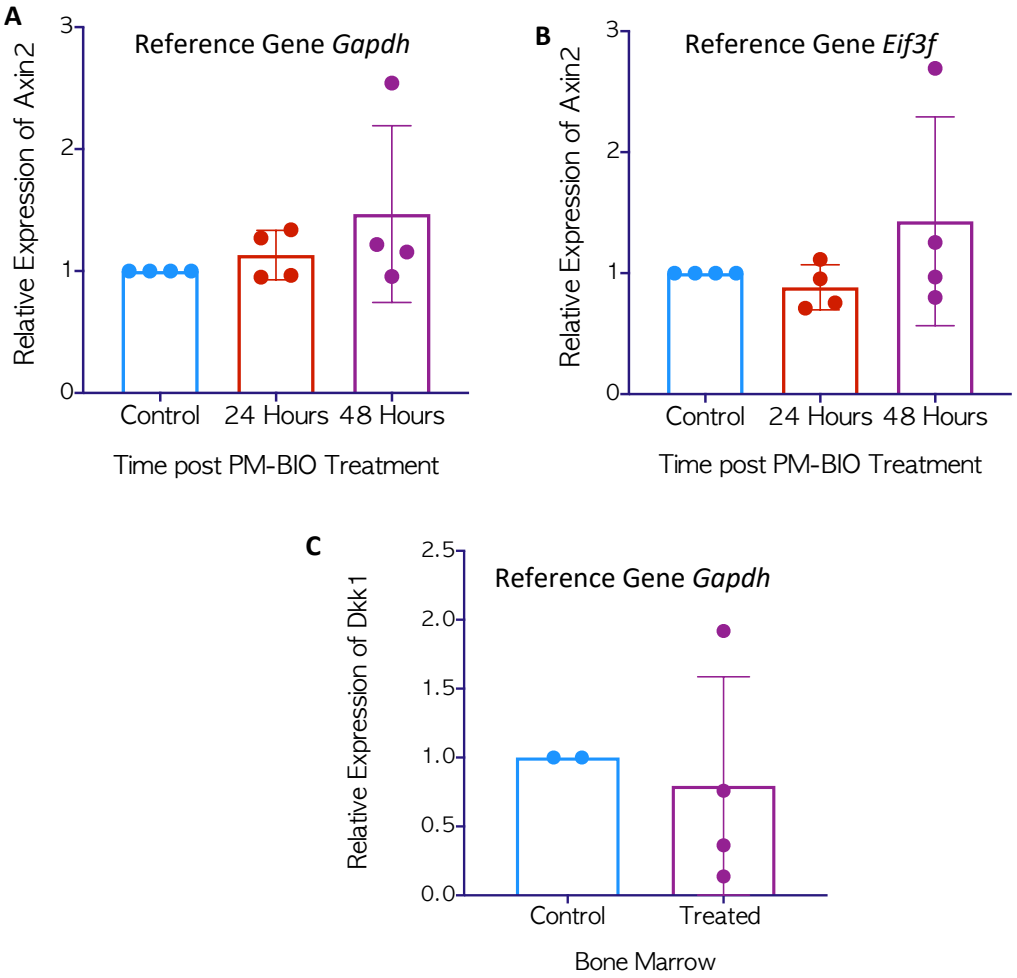


***Figure 5.8: Relative expression of Wnt target genes over time within the bone marrow of female MF1 mice treated with polymersome (PM)-BIO***

*Axin2 expression relative to Gapdh reference gene (A) and Eif3f reference gene (B) normalised to mean of controls which received PM-Empty IV. C) 48-hour post IV PM-BIO Dkk1 expression relative to Gapdh reference gene and normalised to controls. Graphs display mean ± standard deviation of n=4 (Axin2) or n=2 (Dkk1) mice. Statistical significance assessed using one way ANOVA with Dunnett's Multiple comparisons test for Axin2 (A&B) and unpaired t-test for Dkk1 (C).*

### 5.3.4 Mice with a bone injury treated with PM-BIO show no increase in Wnt signalling

Since the intended use of PM-BIO in this thesis is the treatment of bone injuries, next qPCR was used to assess the relative expression of Wnt target genes following PM treatment, this time in mice modelling a bone injury, created as detailed in methods **section 2.4.2**. Tissue from both the liver (as a site of high PM accumulation in mice with a bone injury) and bone marrow from the injured femur was extracted 48 hours following IV treatment of 200 µL PM-BIO or 200 µL PM-Empty (the control group). A schematic of this experiment is visible in the top half of **Figure 5.6**.

**Figure 5.9** shows that in mice with a bone injury, *Axin2* expression slightly decreases within the liver following PM-BIO treatment; this is to a statistically significant extent when normalised to *Efi3f* reference gene (P=0.02), but not when normalised to *Gapdh* (P=0.39).

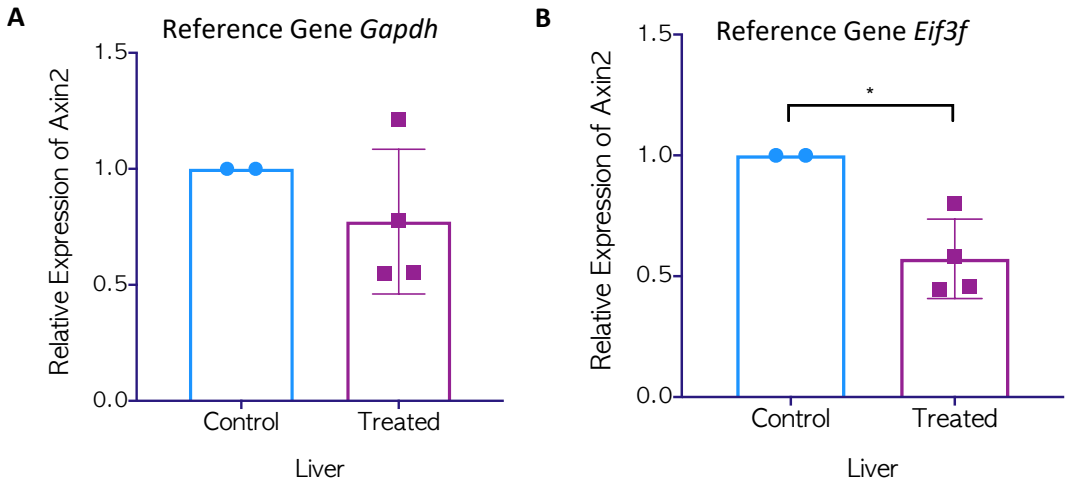


***Figure 5.9: Relative expression of Axin2 in liver tissue extracted from female MF1 mice with a bone injury 48 hours following polymersome (PM)-BIO IV treatment***

*Axin2 expression relative to Gapdh reference gene (A) and Eif3f reference gene (B) normalised to mean of controls which received PM-Empty IV. Graphs display mean ± standard deviation of n=4 (treated) and n=2 (control) mice. Statistical significance assessed using unpaired t-test, *=p<0.05.*

**Figure 5.10a** shows that within the bone marrow of the injured femur, *Axin2* expression is not significantly different between PM-BIO treated mice and controls (P=0.65). Note for this tissue type only expression relative to *Gapdh* reference gene is shown, because raw $C_T$ analysis revealed the *Eif3f* reference gene to be significantly affected by treatment (shown in **supplementary section S.4**). **Figure 5.10b** shows a significant decrease in *Dkk1* expression within the bone marrow of mice treated with PM-BIO compared to controls (P=0.0014).

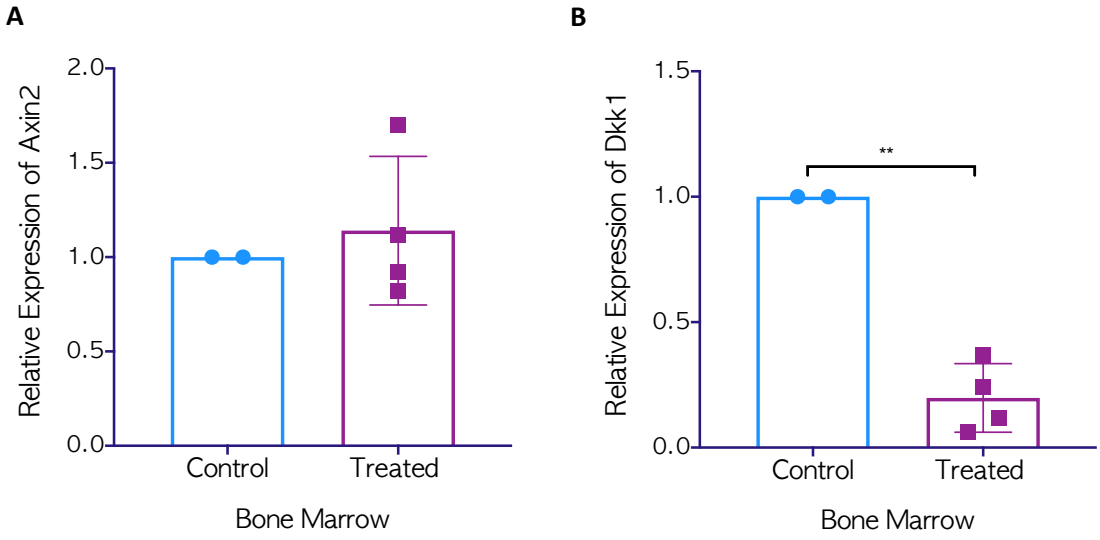


***Figure 5.10: Relative expression of Wnt target genes in bone marrow extracted from female MF1 mice with an injured femur 48 hours following polymersome (PM)-BIO IV treatment***

*(A) Axin2 expression relative to Gapdh reference gene and normalised to mean of controls which received PM-Empty IV. (B) Dkk1 expression relative to Gapdh reference gene and normalised to controls. Graphs display mean ± standard deviation of n=4 (treated) and n=2 (control) mice. Statistical significance assessed using unpaired t-test, **=p<0.005.*

### *5.3.5* Mice treated with PM-BIO show osteogenic signalling *in vivo*

Wnt signalling has been shown to be essential for osteoblast differentiation (Zou *et al.*, 2006), which in turn is integral to successful bone repair. Therefore the induction of osteogenesis following PM-BIO treatment was also investigated, by measuring the relative expression of osteogenic gene *Runx2* in extracted bone marrow samples from mice both with and without a bone injury.

**Figure 5.11** shows a statistically significant decrease in *Runx2* expression within the bone marrow of uninjured mice following PM-BIO treatment (P=0.04). However for injured mice a statistically significant increase in *Runx2* expression is measured following PM-BIO treatment (P=0.009).

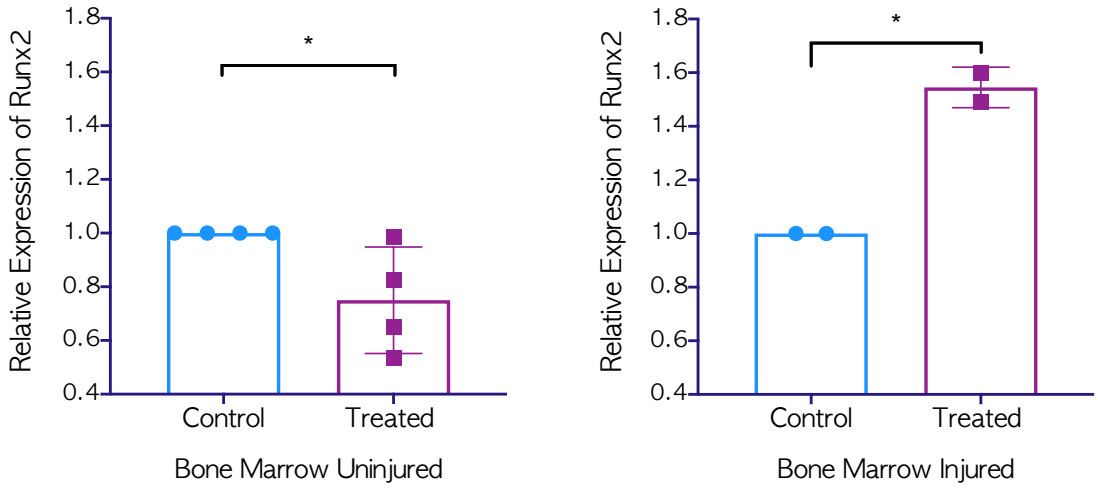


***Figure 5.11: Relative expression of Runx2 in bone marrow of female MF1 mice with and without a bone injury 48 hours following polymersome (PM)-BIO IV treatment***

*Runx2 expression relative to Gapdh reference gene and normalised to controls given PM-Empty IV. Graphs display mean ± standard deviation of n=4 (uninjured) and n=2 (injured) mice. Statistical significance assessed using unpaired t-test, *=p<0.05.*

## 5.4 DISCUSSION

Polymersome controlled delivery of a Wnt agonist has the potential to promote bone formation in the treatment of fractures. In chapter 3 it was established that PM-BIO and PM-CHIR can successfully activate Wnt signalling in an *in vitro* cell line, and in chapter 4 significant accumulation of PMs was found at both fracture sites and other tissues after injection. This chapter aimed to determine whether IV treatment of PMs loaded with BIO can activate the Wnt signalling pathway and promote osteogenic gene activation *in vivo* in these tissues, in mice with and without a bone injury.

RT-qPCR analysis was used to detect changes in gene expression resulting from a single dose of PM-BIO. It was found that:

- PM-BIO did not stimulate the expression of Wnt target genes in the tissues where PM accumulation occurred in uninjured mice.
- PM-BIO induced disparate effects on Wnt target gene expression in injured mice, which was tissue-dependent.
- PM-BIO upregulated osteogenic *Runx2* gene expression in bone marrow of injured mice and downregulated it in uninjured mice.

These findings are discussed in the following sub sections.

### 5.4.1 Wnt signalling in an un-injured bone model

The results presented in this chapter demonstrate that PM-BIO, at the dose administered (200 µL IV), has no significant impact upon Wnt target gene (*Axin2* and *Dkk1*) expression within the liver or bone tissue of a non-injured mouse. This result is surprising and contradictory to *in vitro* studies which have measured the response of isolated human bone marrow cells to free BIO and PM-BIO treatment. Huang *et al.* (2018) showed *in vitro* that free BIO at concentrations of 1 µM and 2 µM induces *AXIN2* expression. Similarly Scarpa *et al.* (2018) found both free BIO at 2 µM and PM-BIO treatment increased *AXIN2* expression. Also in this chapter, 5 µM of free BIO increased *Axin2* expression in primary cells isolated from mice (a more relevant cell source for the *in vivo* model used here). However, a reason for this observed difference could be that the available dose directly exposed to isolated mouse cells is likely greater than that within the liver or the bone marrow *in vivo*. For example, from the *in vivo* IVIS experiments described in **section 4.3** it can be calculated that approximately 85% of the total dose of PM-BIO accumulates in the liver; in this *in vivo* experiment, that implies 170 µl of the injected 200 µM solution is acting on the extracted liver tissue, compared

to a 2000 µl dose a 5 µM solution acting on only 450,000 cells *in vitro*. Further experiments which test the change in Wnt gene expression from a range of administered doses and even PMs loaded with higher concentrations of BIO would confirm if the local available dose is the limiting factor in these results.

Notably as with all *in vitro* studies the findings of these studies are limited, and can lack *in vivo* translation due to the absence of the multiple signalling feedback mechanisms present in an *in vivo* environment. However, they provide the best currently-available prediction for the effect of a GSK-3β inhibitor upon Wnt gene expression, as *in vivo* evidence within healthy bone tissue is limited. In one *in vivo* study, Clément-Lacroix *et al.* (2005) administered lithium, another GSK-3 inhibitor, to mice and measured a 4-fold increase in *Axin2* expression within isolated healthy bone marrow tissue compared to the control. Again, this finding is contrary to the consistent expression of *Axin2* seen in this chapter's study. However, this difference could be due to Clement-Lacroix's use of genetically altered Lrp5 KO mice – which arguably have a reduced baseline level of Wnt signalling, making upregulation more apparent – as well as use of a long-sustained treatment rather than a single dose.

An added complexity in the data presented here is the uncertainty over what amount of BIO has been released from PMs at the chosen 48-hour time point, and whether this reaches a high enough local concentration to induce signalling. In a study by Scarpa *et al.* (2016), PM release kinetics were investigated *in vitro*. Scarpa *et al.* used fluorescein, a self-quenching fluorophore that only fluoresces upon release from PM encapsulation, to quantify payload release over time. Within 1 hour of exposure to cells, PMs were found to release their payload intracellularly, and at 24 hours, over 90% of cells contained the released payload (Scarpa *et al.*, 2016). These data suggest PM uptake and payload release is a gradual process, and that at 48 hours, the maximum BIO concentration may have been released *in vivo*. However further research is required into PM release kinetics *in vivo* to ascertain whether similar PM uptake and drug release rates occur, and hence whether this assumption is correct. For example, an experiment which differentially labels the payload and the PM carrier, and tracks their spatial separation over time may give insight into local released payload concentration.

An alternative explanation for the observed lack of response may be that a response occurred but at a different time. More specifically, PM-BIO treatment may have activated Wnt signalling, yet at the chosen tissue extraction time point, feedback mechanisms may have already regulated Wnt signalling back to control levels. Mechanisms to control Wnt signalling are essential in bone homeostasis to avoid skeletal overgrowth (Brunkow *et al.*, 2001). In bone homeostasis, *Dkk1* and *Axin2* are known to be key negative regulators of Wnt signalling, yet at 24- and 48-hours post-

treatment no clear mean change in expression is observed (although a wide variation in individual subject responses is present). *In vitro* exposure of lithium (40 mM) to a 293T cell line at times from 2-10 hours saw an increase in *Dkk1* after only 6 hours of exposure, in which time *Axin2* expression also gradually increased (Niida *et al.*, 2004). This indicates Wnt treatment has an immediate effect upon expression. With knowledge from previous work by Scarpa that PMs accumulate at tissues within 2 hours post injection (Scarpa, 2016), it is possible a homeostatic state may have been reached by 24 and 48 hours post-treatment. A future experiment in which expression is measured within the first few hours post-treatment would confirm if induced Wnt signalling is achieved in healthy tissue at a fast rate like that seen *in vitro*.

### 5.4.2 Wnt signalling in an injured bone model

This chapter also assessed treatment response in an injured state, in which signalling and feedback mechanisms change from homeostasis to driving repair. Within a mouse with a bone injury the measured Wnt target gene expression in response to PM-BIO treatment had two distinct effects: *Axin2* expression remained relatively unchanged, and *Dkk1* expression significantly decreased. This finding was again contrary to expectations that Wnt signalling would increase in response to treatment, possibly again due to the aforementioned reasons of available dose and also choice of extraction timepoint. In an *in vivo* study by Wang *et al.* (2017), the Wnt signalling response at a bone injury site resulting from NP-encapsulated GSK-3β inhibitor (AZD2858) IV treatment was also investigated. Here, increased Wnt signalling activity above controls was seen via a LacZ reporter mouse (expressed upon β-catenin TCF/LEF activation) at 2 and 4 weeks following one dose of treatment given 3 days post injury (Wang *et al.*, 2017). This finding suggests early GSK3-β treatment affects Wnt signalling expression later in the healing process; further study of later extraction timepoints following PM-BIO treatment would be required to confirm this.

An additional factor to consider is the selection of a Wnt signalling inhibitor being used as a readout of Wnt activity. As a TCF target, *Dkk1* expression is known to increase following Wnt signalling activation. In a study of gene expression following repair, control samples with no treatment showed *Dkk1* expression increase 7 days following injury, peaking at 10 days post-injury (Kakar *et al.*, 2007). This suggests the chosen time point of 48 hours post-injury may be too soon to see an increase in *Dkk1* expression.

However, there is also evidence to suggest *Dkk1* expression is repressed during early fracture healing, despite Wnt signalling activation. The results in this chapter show *Dkk1* expression below control levels, which suggests PM-BIO may act upon an additional mechanism to suppress *Dkk1*

expression. A possible explanation for this suppression could be an increase in the activity of the transcription factor Msx2. In the multipotent mesenchymal C3H10T1/2 cell line, Msx2 was found to selectively downregulate the association of RNA polymerase II with the *Dkk1* gene, and is also thought to have inhibitory interactions with other *Dkk1* translational activators (Cheng *et al.*, 2008). There is also evidence to suggest *Msx2* expression is increased by canonical Wnt signalling (Zhai *et al.*, 2011; Lieven *et al.*, 2014), therefore *Dkk1* transcription and expression could be finely regulated downstream of Wnt signalling action via PM-BIO alongside other influential transcription factors and signalling pathways (Grotewold and Rüther, 2002). However, these findings are from developmental and *in vitro* studies and therefore further research is required to see if these same mechanisms occur during fracture repair. It is possible that alternative GSK-3 related pathways that may be activated by PM-BIO might also influence downstream *Dkk1* transcription regulation, thereby downregulating expression. In retrospect, with Wnt signalling activation being essential for fracture healing progression, the use of an alternative expression readout which isn't an inhibitor of the pathway, such as β-catenin nuclear localisation, would be of benefit to future study.

Although in this chapter only an injury to the bone is induced, this insult is also known to impact the environment within the liver, as evidenced from a measured increase in inflammatory response within isolated Kupffer cells following a bone fracture (Neunaber *et al.*, 2013). As a site of the highest PM accumulation in the IVIS localisation study of chapter 4, the effect of PM-BIO treatment upon Wnt signalling within liver tissue was also measured. The results revealed a slight decrease in *Axin2* expression, suggesting PM-BIO causes a downregulation of Wnt signalling within the liver, which is contrary to the increase that would be expected from a Wnt agonist. This unexpected result may be attributed to the complex crosstalk between inflammatory and Wnt signalling pathways. Wnt signalling is known to have both anti-inflammatory and pro-inflammatory functions, and conversely inflammatory factors such as NF-kB are known to promote or inhibit Wnt signalling (Ma and Hottiger, 2016). There is evidence to suggest NF-kB activation inhibits TCF activity via upregulation of LZTS2 in liver cells (Cho *et al.*, 2008), although this is observed within cancerous liver cells so may not reflect signalling effects in healthy tissue. Nevertheless, the agonistic effect of PM-BIO may not be enough to overcome inflammatory signalling effects at this time point, due to either the concentration or the timing of exposure. Further research is therefore required to understand Wnt signalling in healthy liver tissue with a raised inflammatory state.

### 5.4.3 Increase to osteogenic signalling

In administering a PM-BIO treatment to induce Wnt signalling in a controlled manner, this treatment is expected to promote downstream activation of osteogenesis, as seen upon Wnt activation *in vitro* (Janeczek *et al.*, 2015). Expression of the transcription factor *Runx2* is regarded as an early indicator of osteogenic differentiation in both bone development and repair (Day *et al.*, 2005; Kim *et al.*, 2007), and therefore qPCR measurements of *Runx2* were used to assess the effects of PM-BIO treatment upon osteoblast differentiation in both non-injured and injured bone. The results showed that PM-BIO treatment had a slight decreasing effect upon *Runx2* expression in non-injured bone at 48 hours post-treatment. This is contradictory to results seen *in vitro* with extracted hBMSCs showing an increased expression of *Runx2* following exposure to PM-BIO and free BIO (Clough *et al.*, 2018; Scarpa *et al.*, 2018). A number of reasons mentioned earlier in this discussion may explain this disparity, including available local dose and *in vivo* homeostatic feedback mechanisms not present *in vitro*. However of these, the actions of homeostasis to reduce excessive bone formation seems more likely, as conversely in subjects with an injured bone an increase in *Runx2* expression is observed. The observation of downstream *Runx2* expression at the investigated timepoint (48 hours) further supports earlier discussion that PM-BIO does successfully induce Wnt signalling, and hence that other signalling mechanisms present in an injured state may be keeping inhibitor (*Axin2* and *Dkk1*) expression supressed. It is worth noting that *Runx2* injured data is taken from a low biological repeat number of n=2 mice; accordingly, the observed results do not have statistical power and may not be truly representative. Further biological repeats are needed to confirm this theory.

### 5.4.4 Conclusions, study limitations, and future work

Overall the findings presented in this chapter demonstrate the first measured *in vivo* expression of Wnt target genes and osteogenic markers during early fracture repair in response to a Wnt agonist treatment. In addition to informing of treatment effectiveness, this study provides measurements of the effects of one treatment administration time point (straight after injury) and treatment dose (200 µl of PMs loaded with 200 µM BIO) which can be used in future work to determine the optimal timing and dosage. Future study of expression changes in response to free BIO will be required to determine if PM delivery affects the response to treatment. Since PMs have been shown to improve bioavailability of a therapeutic at the target site as well as reducing toxicity (Nicolas *et al.*, 2013), it could therefore be hypothesised that PM delivery will increase the treatment effects in comparison to free treatment alone.

One limitation to the experimental method used in this chapter is that RT-qPCR shows gene expression within pieces of tissue rather than at a cellular level across the whole tissue. It is therefore possible that early Wnt signalling activation is occurring in certain cells reached by PMs, however possibly not to a measurable extent over control levels. Here methods of ISH or use of Wnt signalling reporter mice could be of benefit, providing cellular level spatial detail of any Wnt signalling in comparison to untreated controls. In addition to confirming whether any increase in the expression of genes relates to inferred effects, inclusion of additional methods to assess related protein expression such as western blot analysis, IHC, and histological stains to confirm differentiated states would be beneficial to future work.

Finally, it is worth noting that this study has focused on investigating only one osteoblast differentiation marker. The occurrence of osteoblast differentiation could be further supported using additional markers found in mature osteoblasts, such as Osterix (*Osx/Sp7*), an indirect Wnt target gene activated by *Runx2*. Additionally, there exist many other mechanisms which could be affected by the activation of Wnt signalling that have not yet been investigated, such as chondrogenesis, cell proliferation, or cell migration. All of these mechanisms can impact fracture outcome, and hence warrant further investigation of their own in future. Furthermore, this discussion highlights a lack of information within literature regarding the *in vivo* temporal expression of Wnt target genes following a bone injury, particularly from 0-3 days post-injury. Future analysis comparing injured and non-injured expression would further understanding of this area, informing future Wnt-based treatment interventions.

# CHAPTER 6

## GENERAL DISCUSSION AND FUTURE WORK

Bone fracture incidence and management of repair outcomes is a prevalent medical issue with high financial costs and losses to quality of life and productivity. Pharmaceutical interventions to promote repair have long held promise for improving fracture outcomes, but the only notable success is in the management of osteoporosis-related fracture prevention. Therapeutic candidates such as Wnt agonists are often limited by side effects which result in failure at the risk/benefit analysis stage. Nanoparticle delivery systems may provide a solution to issues that are due to the delivery route and formulation. Nanoparticles alter the biodistribution and pharmacokinetics of small-molecule drugs, enabling large dose delivery of drugs to a targeted diseased tissue, thereby potentially improving the therapeutic's efficacy and reducing systemic toxicity.

This research set out to develop a polymersome drug delivery therapeutic for the controlled and localised delivery of a Wnt agonist to a bone injury site, in order to promote bone repair and ultimately improve fracture healing outcomes.

This thesis achieved this by:

- Successfully producing stable PEG-*b*-PCL polymersomes loaded with BIO and CHIR.
- Demonstrating that these polymersomes induce Wnt signalling in a reporter cell line and in primary tissue-derived cells.
- Showing that PM delivery improves the cytocompatibility of BIO and CHIR to primary bone cells.
- Demonstrating that either immediate or delayed (7 day) IV administration of PMs results in passive accumulation at a target bone injury site.
- Demonstrating that PM accumulation at a target bone injury is not significantly altered when the *in vivo* macrophage population is depleted.
- Showing that IV treatment with a single dose of PM-BIO results in the disparate *in vivo* gene expression of Wnt signalling inhibitors depending on the presence of a bone injury, as well as the induction of early osteogenic gene expression at the intended bone injury site.

## 6.1 SUMMARY OF FINDINGS

The aim of chapter 3 was to test the hypothesis that PMs can encapsulate small molecule Wnt agonists BIO and CHIR and deliver them *in vitro* to induce a Wnt signalling response. This was achieved by producing PMs with a range of loading concentrations of BIO and CHIR and measuring encapsulation efficiency using UV-Vis spectroscopy. Subsequently the ability of PM-BIO and PM-CHIR to induce Wnt signalling was measured using a Wnt signalling activated luciferase reporter cell line. Initial safety testing of the PMs for *in vivo* experimental use was evaluated by determining the cytotoxicity of PM-BIO and PM-CHIR on primary bone cells using an alamarBlue reporter assay. It was determined that BIO and CHIR can be encapsulated within PMs at a sufficient dose to induce Wnt signalling *in vitro,* and that delivery in PMs protects cells from the otherwise toxic effects of high BIO/CHIR concentrations. This work is the first to produce PMs loaded with CHIR and assess their biological activity in comparison to free CHIR as well as to PM-BIO. It was interesting to find that encapsulated CHIR induced the greatest Wnt signalling response, despite its free form having a lower potency than BIO. CHIR was selected for investigation as a candidate Wnt agonist due to reports of greater cytocompatibility compared to BIO (Naujok *et al.*, 2014), which this study has also seen not only for free CHIR but also PM-CHIR. Overall, PMs enable delivery of greater doses of reagents whilst reducing toxicity.

Chapter 4 tested the hypothesis that PMs will passively accumulate at a target bone injury site when administered systemically either immediately or after a post-injury delay. The study was carried out using a mouse bone injury model. PMs with a fluorescent representative payload were delivered IV either immediately or 7 days post induction of the injury. Localised PM accumulation measured by fluorescence intensity was quantified across the whole body of the mouse and in isolated tissues using IVIS image analysis. PMs were found to passively accumulate at a target bone injury site within 48 hours following systemic injection regardless of whether given immediately post injury or after delivery delayed by 7 days. This finding demonstrates that PMs as a drug delivery system can be used for the targeted administration of pharmaceuticals for promoting fracture healing. These findings also have the important and useful outcome that clinical application could be achieved within a treatment administration window of at least 7 days following injury. Accumulation was also observed in skin and muscle around the injury site. This indicates that PMs may be used in targeting treatment for repair of other injuries, such as skin and soft tissue damage. The largest accumulation of PM was measured in the liver. Although this may be a disadvantage for systemically administering PMs intended to target bone, it may present an opportunity for the delivery of pharmaceuticals purposed for treating hepatic injury or disease.

The aim of chapter 5 was to test the hypothesis that PM-encapsulated BIO can induce Wnt signalling activity and osteogenic differentiation *in vivo.* RT-qPCR was used to assess Wnt targets (*Axin2* and *Dkk1*) and osteogenic (*Runx2*) gene expression in extracted tissues of high PM accumulation from mice with and without a bone injury, extracted within 48 hours following PM-BIO administration. PM-BIO treatment induced variable changes to the *in vivo* gene expression of Wnt signalling inhibitors depending on the presence of a bone injury, as well as the induction of early osteogenic *Runx2* gene expression at a target injured bone. This is preliminary evidence that there is an early window of opportunity in which controlled delivery of a Wnt agonist has a positive osteoinductive effect, which could lead to early increased bone formation, potentially improving fracture outcomes in the longer term.

## 6.2 LIMITATIONS OF THE RESEARCH AND INDICATIONS FOR FURTHER EXPERIMENTS

There are a number of limitations to the presented studies, and for a PM-Wnt agonist therapeutic to progress towards translation to the clinic, further experiments are required. Key aspects of this future work are discussed in the following sections, which consider three key areas of assessment required for clinical translation.

***Delivery system efficiency***

This research has shown that PMs can deliver biologically active Wnt agonists BIO and CHIR, which are then bioavailable and safer to use. However, this research highlights a need to fully test the effects of a selected therapeutic when delivered by PMs. In the case of BIO and CHIR, two molecules with similar hydrophobicity and known interaction with GSK-3β (Naujok *et al.*, 2014), delivery by PMs resulted in variable Wnt signalling, which also differed to the free compounds. The precise chemical and biophysical interaction of BIO/CHIR with PMs appears to alter the cellular response to the compound; the factors that control this change are unknown and difficult to predict. Future research aimed at understanding how PMs facilitate cell uptake and affect intracellular chemical processing would be useful not only to this research, but also other future PM-delivered therapeutics. Here live cell uptake imaging and intracellular tracking techniques may prove useful (Miller and Weissleder, 2017; Sun *et al.*, 2019).

***Safe clearance***

This research has established that PMs can accumulate at the site of an induced injury in a bone; however, unanswered questions remain regarding how long PMs persist at sites of accumulation and, importantly for clinical safety, how efficiently PMs are cleared from the body. A future long-term study which tracks both PMs and their payload separately over time in the same subject, using IVIS SpectrumCT, would further ascertain tissue-specific accumulation, and show both when and where PM payload is released and cleared. The inclusion of blood and urine sampling would also be useful to inform of pharmacokinetics.

Additionally, the use of visually tagged BIO/CHIR (e.g. with fluorescence) could enable biodistribution to be tracked, whilst also giving therapeutic efficiency information from μ-CT imaging analysis of bone repair over time. The use of liposome-mediated delivery as a control would also be insightful, answering whether PM-specific features provide benefits over this more commonly used alternative delivery vehicle (Matoori and Leroux, 2020).

Detailed analysis of PM uptake at a cellular level, informing which cells in an injury environment may be affected by a PM-delivered therapeutic, is also needed. IVIS imaging lacks the resolution for this type of study, however alternative methods of fluorescent IHC identifying specific cell markers in whole mouse or extracted tissue sections could be used. Determining co-localisation of these cellular markers with a fluorescently labelled payload and/or PM structure directly could inform of cell-specific uptake in sites of accumulation. In parallel, cytometric analysis of flushed bone marrow and extracted blood and urine samples could enable estimation of cell-specific PM uptake and provide some insight into the pharmacokinetics.

The issue of off-target liver accumulation raises concern over how a PM-delivered therapeutic might then influence liver signalling and long-term function, perhaps in more subtle ways not examined in toxicity studies. Moving forward, assessment of signalling activation in high PM accumulation tissue with mass arrays may be of benefit to better understand potentially problematic off-target effects.

The issue of large off-target liver accumulation sequestering the therapeutic dose away from bone could be overcome by investigating methods to increase bone targeting. The addition of bone-specific targeting moieties to PM structure such as alendronate has shown some success in other studies (Özcan *et al.*, 2011; Swami *et al.*, 2014). Alternatively, a strategy of direct application could be employed. One such strategy could be through the use of implanted biomaterials, which is another area of significant current research in promoting regeneration of various tissues, including bone (Gaharwar, Singh and Khademhosseini, 2020). However, to date there have only been a few successful clinical applications (e.g. Dermagraft and Apligraf), and this delivery strategy commonly requires invasive surgery. A less invasive alternative could be the direct injection of PMs to an injury site; similarly to systemic administration, this strategy can be employed at any time, but could overcome the aforementioned mass liver clearance issue. However it is a less attractive clinical option as it would require guided delivery in a specialist clinical setting, an issue that is avoided with systemically delivered moieties.

***Achieving the intended treatment effect***

Ultimately for clinical use, PM delivery of a Wnt agonist needs to result in a measurable and therapeutically efficient response which promotes bone healing. This thesis presents evidence from PCR analysis that PM-BIO treatment induces a response within bone. Evidence of induced Wnt signalling was however inconclusive, limited by the study design and time available to perform further PCR runs. Further study could benefit from the inclusion of multiple extraction timepoints which would help to ascertain whether the window of significant Wnt signalling may have been

missed. Furthermore, use of a mass PCR array would be beneficial in order to assess multiple Wnt gene targets rather than just inhibitors, which are possibly affected by other injury-activated signalling pathways. Similarly, inclusion of multiple osteogenic gene expression markers would determine whether osteogenesis has occurred. Future work should assess changes to the gene expression associated with chondrogenesis and angiogenesis, as Wnt signalling induction may have a paracrine effect upon the signalling of other cells present at the injury site.

Using the same experimental parameters as used in this thesis, Scarpa has also shown that PM-BIO treatment results in no significant change to bone healing progression, assessed by μ-CT and histological analysis (Scarpa, 2016). Combined these data suggest that PM-BIO, at the given dose, has a subtle effect and that perhaps these study designs are limited by the dose selected. A study to investigate healing progression following administration of multiple doses or PMs loaded with a higher initial concentration of BIO should be considered. The effect of PM-CHIR treatment upon *in vivo* signalling and bone repair progression was not investigated; however, findings described in chapter 3 suggest that PM-CHIR treatment may be a safer and more efficient alternative to PM-BIO.

PCR is a tissue destructive method, which prevents parallel measurement of tissue morphology. A possible alternative which would localise the signals within the tissue would be to use ISH and IHC staining of sequential tissue sections. Although less quantitative and lower throughput, this strategy would enable visualisation of gene expression (for Wnt, osteogenesis, and other repair related genes), cell identification with cell specific markers, and histological assessment of repair stages. Inclusion of fluorescence staining of labelled PMs could simultaneously inform of PM uptake as previously described.

There is a need for more effective methods to uncover specific cell signalling factor production spatially and temporally *in vivo.* Within this thesis, the treatment effects upon the entire local cellular environment within the target area is unknown and would take extensive lab time with IHC and PCR techniques looking at one feature at a time. An alternative omics approach could be used, in which biopsies from sites of PM accumulation are assessed. With an ever-growing reference atlas for cell identification and function, combined omics techniques (including genomics, epigenomics, transcriptomics, proteomics, and metabolites) would provide detailed information of specific cellular changes over time resulting from both a bone injury and treatment (Gaharwar, Singh and Khademhosseini, 2020).

Further to techniques for establishing cell signalling, for future studies of PM-BIO/CHIR's therapeutic efficacy, μ-CT and histology could be used for the assessment of gross bone formation and rate of

repair. Additionally, techniques such as polscope imaging may be used to assess more subtle improvements in the quality of the newly formed bone. Using these techniques, future studies could then address several other questions, such as: whether a local injection strategy gives better results than systemic injection; whether injuries to other bone sites (such as calvaria) are as responsive to treatment; and what the window of opportunity is for treatment (i.e. whether delaying treatment administration affects bone healing outcomes).

An aspect which may have limited significant results is whether Wnt agonist treatment is enough of a driving force to improve healing in an arguably already efficient, healthy subject. An alternative would be to test treatment efficacy using a model where repair is less efficient such as in an aged animal or a non-union model.

Finally, it may be found that, regardless of optimisation, the chosen strategy of inducing Wnt signalling alone may not promote significant measurable improvements to bone healing. Here, there are other molecules which could be investigated for their potential to promote fracture repair, which could also benefit from PM-controlled delivery; examples include previously researched therapeutics BMPs and PTH, which were hindered by off-target effects (Aspenberg, 2013; Arzeno, Wang and Huddleston, 2018). Another option could be to load anabolic drugs currently used in osteoporosis treatment. For instance, in a recent trial Romosozumab was found to not improve the healing of hip fractures over the placebo (Schemitsch *et al.*, 2020), however with PM delivery a higher dose could be administered, possibly improving outcomes. There could also be potential for repurposing currently used drugs such as the statin Simivastin. In dentistry research, Simivastin treatment has been found to promote both bone regeneration and soft tissue healing, and also infection control by reducing inflammation (Gupta, Del Fabbro and Chang, 2019). PMs could enable targeted delivery of Simivastin to bone injuries whilst reducing side effects. Alternatively, instead of loading PMs with drug compounds, PMs could be used for the delivery of RNA-based therapeutics (Mitragotri *et al.*, 2015). This strategy has the advantage of theoretically inducing cells to produce an excess of more than one signalling factor crucial to fracture repair. For instance, anti-inflammatory, osteoinductive, and angiogenic signalling could be induced simultaneously to improve fracture outcome.

A schematic of a potential future experiments combining the suggestions discussed in this section is shown in Figure 6.1.

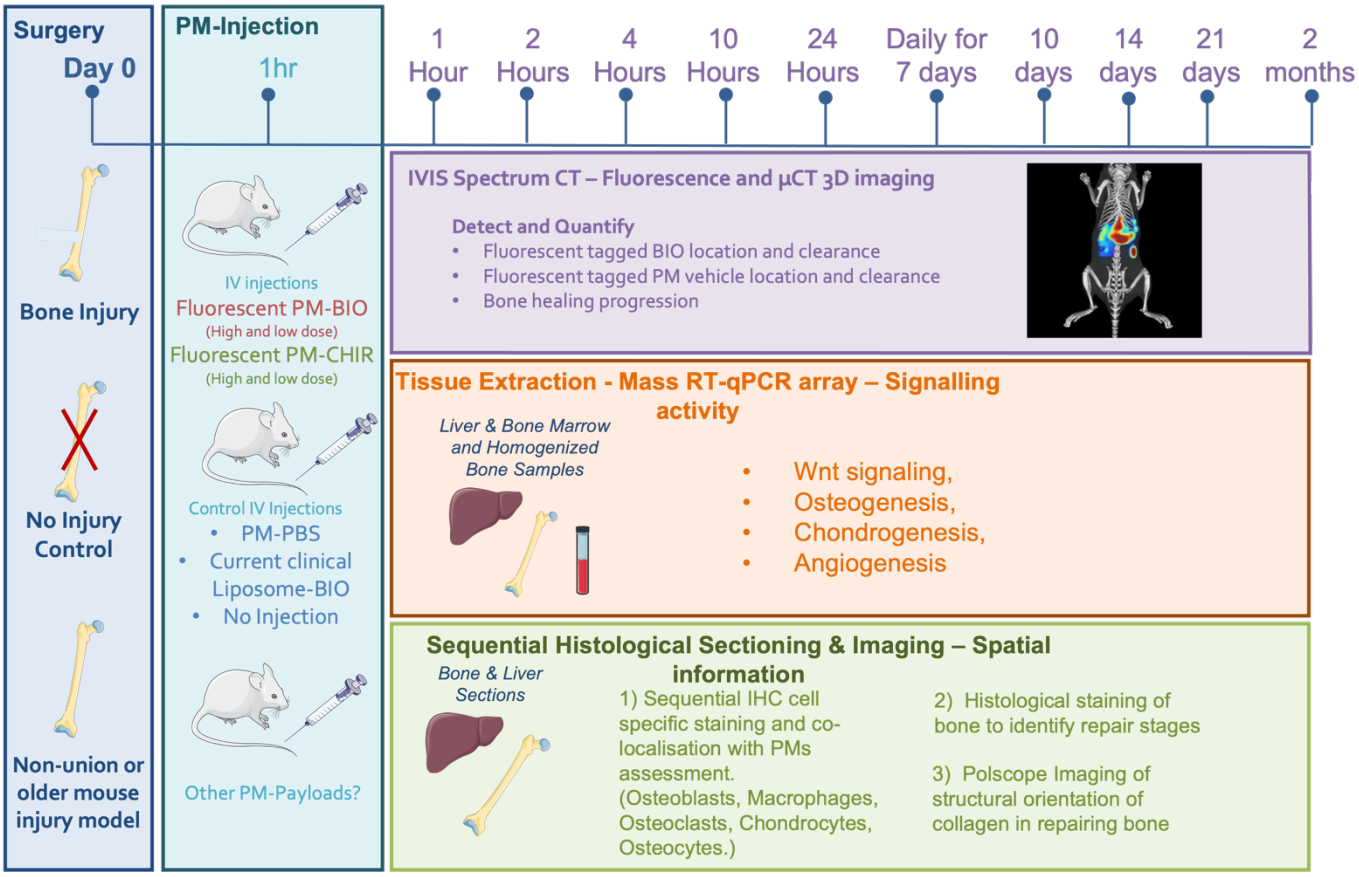


***Figure 6.1: Potential Future Experiment Schematic***

*(Parts of this figure's graphics are credited to smart.servier.com)*

## 6.3 FUTURE RESEARCH POTENTIAL

The research presented in this thesis has highlighted the potential of PMs as delivery agents. It has demonstrated the effects of delivery of two Wnt agonists on isolated cells and in an *in vivo* bone injury site. In both systems pharmacological activity of the agonists was retained, and importantly, PM-encapsulated delivery of the Wnt agonists was associated with improved cytocompatibility. Delivery of a PM Wnt agonist *in vivo* induced early osteogenesis, thereby providing a viable bone-promoting therapeutic which may (after more robust testing) be suitable as part of a strategy to improve outcomes after a fracture.

That PM delivery changes how a cell responds to a compound provides an opportunity for molecules that have been previously deemed unviable, due to poor cell uptake or toxicity, to be used via PM delivery. This includes compounds that may be considered peripheral, but which are important in tissue repair, such as antibiotics (Rizzello *et al.*, 2017). The findings from this work adds BIO and CHIR to the library of otherwise insoluble or toxic drugs which can now be used by polymersome nanoparticle facilitated delivery for treatment.

PMs loaded with GSK-3β inhibitors hold potential not only for bone fracture treatment but also in other treatment fields. Inhibitors of GSK-3β have been investigated in the regulation of glucose metabolism as a treatment for diabetes (Meijer, Flajolet and Greengard, 2004), reducing neuronal apoptosis in the treatment of neurological traumas such as stroke and epilepsy (Frame and Cohen, 2001), as well as increasing cardiomyocyte regeneration for the treatment of AMI (Fan *et al.*, 2020). PM-controlled delivery of BIO or CHIR could therefore be of therapeutic benefit in these conditions with further research.

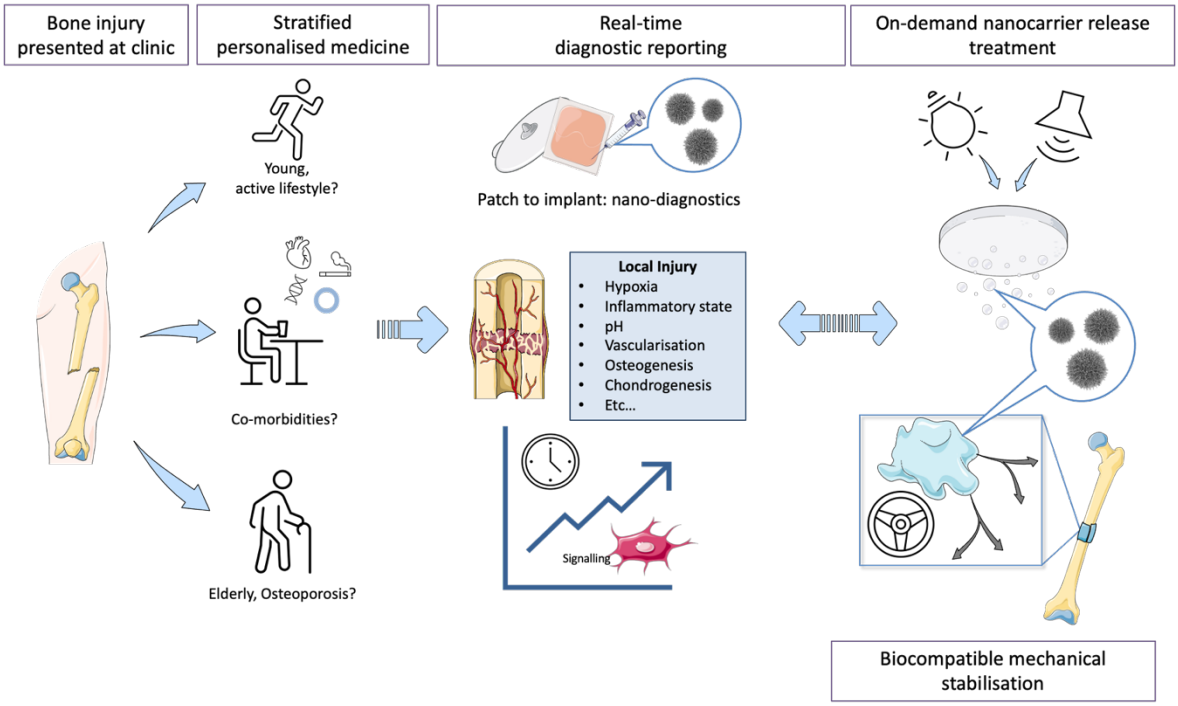


***Figure 6.2: Schematic of future uses for nanomedicine in bone injury treatment***

*(Parts of this figure's graphics are credited to smart.servier.com)*

Looking to the future of fractures and treatment to improve tissue repair, it is likely that no single intervention will result in optimal outcomes. In the clinic, an apparently identical injury (e.g. fracture of the femur) can present in different patients and in turn have variable outcomes. A non-union injury in an elderly patient with osteoporosis, patients with co-morbidities such as cardiovascular disease and diabetes, and young, otherwise fit patients, are likely to require different management. There is a need for stratified personalised treatment plans with real-time detection of the essential signalling pathways to identify cases where the cell signalling in an injured bone is e.g. under or overactive. Ideally this detection could be coupled with on-demand release of factors to compensate, in turn optimising repair efficiency. The synergistic use of nanotechnologies holds promise for making this theranostic based medicine possible (**Figure 6.2**). For example, in the field of diagnostics, nano-implants and nanobot-based diagnostic technologies (Christodoulides *et al.*, 2012; Jeelani *et al.*, 2014) could enable detection of multiple signalling factors reporting on the local injury environment, e.g. hypoxic conditions. The research in this thesis has identified that there is window of at least 7 days in which PMs are able to reach a bone injury site after IV delivery; this could be exploited to report on the state of repair at the injury site, or even different regions of the injury site. To take diagnostic information and assign a personalised treatment plan, further research is still required to fully map the signalling that occurs across the period of repair, especially across a heterogenous

population. Detailed mapping could result in a data driven/algorithmic strategy to apply appropriate treatments for boosting or inhibiting signalling pathways at the appropriate points in the repair site. For on-demand drug release strategies, technologies involving acoustic stimulated (Mannaris *et al.*, 2020), light-responsive (Thang *et al.*, 2019), and magnetic field–responsive nanocarriers, amongst others have been investigated (Luo *et al.*, 2018). Regeneration therapies need more innovation not only pharmaceutically but also in engineering. At present screws and plates are required for aiding stability during bone repair yet these can disrupt important early repair and hematoma signalling (Schell *et al.*, 2017). Engineered biocompatible alternatives such as grafts with controllable nanorobotics for directed movement and nanocarriers for on-demand release of therapies could better support the ideal mechanical and signalling repair environment. Challenges remain for these strategies to function effectively when translated to a physiological environment. The ideal would be to combine technologies from multiple disciplines to create a biocompatible nanodevice which is simultaneously: controllable and tracible for movement, able to detect and report on biomarkers in an environment, responsive to stimuli to release therapeutic cargo, and harmlessly removable from the body.

Getting this research from the lab to the clinic requires a huge multidisciplinary effort that we must continue to strive towards, for it holds exciting potential to restore people from suffering life-altering injuries to living fulfilling lives.

# LIST OF REFERENCES

Adjei, I.M., Sharma, B., Peetla, C. and Labhasetwar, V. (2016) 'Inhibition of bone loss with surface-modulated, drug-loaded nanoparticles in an intraosseous model of prostate cancer', *Journal of Controlled Release*, 232, pp. 83–92. doi:10.1016/j.jconrel.2016.04.019.

Alexis, F., Pridgen, E., Molnar, L.K. and Farokhzad, O.C. (2008) 'Factors affecting the clearance and biodistribution of polymeric nanoparticles', *Molecular Pharmaceutics*, 5(4), pp. 505–515. doi:10.1021/mp800051m.

Anselmo, A.C. and Mitragotri, S. (2014) 'Cell-mediated delivery of nanoparticles: Taking advantage of circulatory cells to target nanoparticles', *Journal of Controlled Release*, 190, pp. 531–541. doi:10.1016/j.jconrel.2014.03.050.

Arzeno, A., Wang, T. and Huddleston, J.I. (2018) 'Abundant heterotopic bone formation following use of rhBMP-2 in the treatment of acetabular bone defects during revision hip arthroplasty', *Arthroplasty Today*, 4(2), pp. 162–168. doi:10.1016/j.artd.2017.12.004.

Asem, H., Zhao, Y., Ye, F., Barrefelt, Å., Abedi-Valugerdi, M., El-Sayed, R., El-Serafi, I., Abu-Salah, K.M., Hamm, J., Muhammed, M. and Hassan, M. (2016) 'Biodistribution of biodegradable polymeric nano-carriers loaded with busulphan and designed for multimodal imaging', *Journal of Nanobiotechnology*, 14(1), pp. 1–16. doi:10.1186/s12951-016-0239-0.

Aspenberg, P. (2013) 'Parathyroid hormone and fracture healing.', *Acta orthopaedica*, 84(1), pp. 4–6. doi:10.3109/17453674.2013.771301.

Bakker, A.D. and Klein-Nulend, J. (2012) 'Osteoblast isolation from murine calvaria and long bones', *Methods in Molecular Biology*, 816, pp. 19–29. doi:10.1007/978-1-61779-415-5_2.

Bao, Q., Chen, S., Qin, H., Feng, J., Liu, H., Liu, D., Li, A., Shen, Y., Zhao, Y., Li, J. and Zong, Z. (2017) 'An appropriate Wnt/β-catenin expression level during the remodeling phase is required for improved bone fracture healing in mice', *Scientific Reports*, 7(1), pp. 1–11. doi:10.1038/s41598-017-02705-0.

Baron, R. and Kneissel, M. (2013) 'WNT signaling in bone homeostasis and disease: from human mutations to treatments', *Nature Medicine*, 19(2), pp. 179–192. doi:10.1038/nm.3074.

Batrakova, E. V, Gendelman, H.E. and Kabanov, A. V (2011) 'Cell-mediated drug delivery', *Expert Opinion Drug Delivery*, 8(4), pp. 415–433.

Baumann, D., Hofmann, D., Nullmeier, S., Panther, P., Dietze, C., Musyanovych, A., Ritz, S., Landfester, K. and Mailänder, V. (2013) 'Complex encounters: Nanoparticles in whole blood and their uptake into different types of white blood cells', *Nanomedicine*, 8(5), pp. 699–713. doi:10.2217/nnm.12.111.

Behonick, D.J., Xing, Z., Lieu, S., Buckley, J.M., Lotz, J.C., Marcucio, R.S., Werb, Z., Miclau, T. and Colnot, C. (2007) 'Role of matrix metalloproteinase 13 in both endochondral and intramembranous ossification during skeletal regeneration.', *PloS one*, 2(11), p. e1150. doi:10.1371/journal.pone.0001150.

Bennett, C.N., Longo, K.A., Wright, W.S., Suva, L.J., Lane, T.F., Hankenson, K.D. and MacDougald, O.A. (2005) 'Regulation of osteoblastogenesis and bone mass by Wnt10b.', *Proceedings of the National Academy of Sciences of the United States of America*, 102(9), pp. 3324–9. doi:10.1073/pnas.0408742102.

Bennett, C.N., Ross, S.E., Longo, K.A., Bajnok, L., Hemati, N., Johnson, K.W., Harrison, S.D. and MacDougald, O.A. (2002) 'Regulation of Wnt signaling during adipogenesis', *Journal of Biological Chemistry*, 277(34), pp. 30998–31004. doi:10.1074/jbc.M204527200.

Bertrand, N. and Leroux, J.C. (2012) 'The journey of a drug-carrier in the body: An anatomo-physiological perspective', *Journal of Controlled Release*, pp. 152–163. doi:10.1016/j.jconrel.2011.09.098.

Bianco, P. and Robey, P.G. (2004) 'Skeletal Stem Cells', *Handbook of Stem Cells*, 2, pp. 415–424. doi:10.1016/B978-012436643-5/50129-2.

Bielby, R., Jones, E. and McGonagle, D. (2007) 'The role of mesenchymal stem cells in maintenance and repair of bone', *Injury Internation Journal of the care of the injured.*, 38(S1), pp. S26–S32. doi:10.1016/j.injury.2007.02.007.

Boer, J. De, Siddappa, R., Gaspar, C., Apeldoorn, A. Van, Fodde, R. and Blitterswijk, C. Van (2004) 'Wnt signaling inhibits osteogenic differentiation of human mesenchymal stem cells', *Bone*, 34, pp. 818–826. doi:10.1016/j.bone.2004.01.016.

Boland, G.M., Perkins, G., Hall, D.J. and Tuan, R.S. (2004) 'Wnt 3a promotes proliferation and suppresses osteogenic differentiation of adult human mesenchymal stem cells', *Journal of Cellular Biochemistry*, 93(6), pp. 1210–1230. doi:10.1002/jcb.20284.

Bolander, M.E. (1992) 'Regulation of Fracture Repair by Growth Factors (43410A)', *Proceedings of the Society for Experimental Biology and Medicine*, 200(2), pp. 165–170. doi:10.3181/00379727-200-43410A.

Bostrom, M.P.G., Lane, J.M., Berberian, W.S., Missri, A.A.E., Tomin, E., Weiland, A., Doty, S.B., Glaser, D. and Rosen, V.M. (1995) 'Immunolocalization and expression of bone morphogenetic proteins 2 and 4 in fracture healing', *Journal of Orthopaedic Research*, 13(3), pp. 357–367. doi:10.1002/jor.1100130309.

Brinkhuis, R.P., Floris, R.P.J.T. and van Hest, J.C.M. (2011) 'Polymeric vesicles in biomedical applications', *Polymer Chemistry*, 2(7), pp. 1449–1462. doi:10.1039/c1py00061f.

Brownlow, H.C., Reed, A. and Simpson, A.H.R.W. (2002) 'The vascularity of atrophic non-unions.', *Injury*, 33(2), pp. 145–50.

Brunkow, M.E., Gardner, J.C., Van Ness, J., Paeper, B.W., Kovacevich, B.R., Proll, S., Skonier, J.E., Zhao, L., Sabo, P.J., Fu, Y., Alisch, R.S., Gillett, L., Colbert, T., Tacconi, P., Galas, D., Hamersma, H., Beighton, P., Mulligan, J., Niikawa, N., *et al.* (2001) 'Bone dysplasia sclerosteosis results from loss of the SOST gene product, a novel cystine knot-containing protein.', *American journal of human genetics*, 68(3), pp. 577–89. doi:10.1086/318811.

Buckiová, D., Ranjan, S., Newman, T.A., Johnston, A.H., Sood, R., Kinnunen, P.K., Popelář, J., Chumak, T. and Syka, J. (2012) 'Minimally invasive drug delivery to the cochlea through application of nanoparticles to the round window membrane', *Nanomedicine*, 7(9), pp. 1339–1354. doi:10.2217/nnm.12.5.

Ceradini, D.J., Kulkarni, A.R., Callaghan, M.J., Tepper, O.M., Bastidas, N., Kleinman, M.E., Capla, J.M., Galiano, R.D., Levine, J.P. and Gurtner, G.C. (2004) 'Progenitor cell trafficking is regulated by hypoxic gradients through HIF-1 induction of SDF-1', *Nature Medicine*, 10(8), pp. 858–864. doi:10.1038/nm1075.

Chen, Y. and Alman, B.A. (2009) 'Wnt pathway, an essential role in bone regeneration', *Journal of Cellular Biochemistry*, 106(3), pp. 353–362. doi:10.1002/jcb.22020.

Chen, Y., Whetstone, H.C., Lin, A.C., Nadesan, P., Wei, Q., Poon, R. and Alman, B.A. (2007) 'Beta-catenin signaling plays a disparate role in different phases of fracture repair: Implications for therapy to improve bone healing', *PLoS Medicine*, 4(7), pp. 1216–1229. doi:10.1371/journal.pmed.0040249.

Cheng, C.J., Tietjen, G.T., Saucier-Sawyer, J.K. and Saltzman, W.M. (2015) 'A holistic approch to targeting disease with polymer nanoparticles', *Nature Reviews Drug Discovery*, 14(3), pp. 239–247. doi:110.1016/j.bbi.2017.04.008.

Cheng, S.L., Shao, J.S., Cai, J., Sierra, O.L. and Towler, D.A. (2008) 'Msx2 exerts bone anabolism via canonical Wnt signaling', *Journal of Biological Chemistry*, 283(29), pp. 20505–20522. doi:10.1074/jbc.M800851200.

Cho, H., Indig, G.L., Weichert, J., Shin, H.C. and Kwon, G.S. (2012) 'In vivo cancer imaging by poly(ethylene glycol)-b-poly(ε-caprolactone) micelles containing a near-infrared probe', *Nanomedicine: Nanotechnology, Biology, and Medicine*, 8(2), pp. 228–236. doi:10.1016/j.nano.2011.06.009.

Cho, H.H., Song, J.S., Yu, J.M., Yu, S.S., Choi, S.J., Kim, D.H. and Jung, J.S. (2008) 'Differential effect of NF-κB activity on β-catenin/Tcf pathway in various cancer cells', *FEBS Letters*, 582(5), pp. 616–622. doi:10.1016/j.febslet.2008.01.029.

Cho, S.W., Soki, F.N., Koh, A.J., Eber, M.R., Entezami, P., Park, S.I., van Rooijen, N. and McCauley, L.K. (2014) 'Osteal macrophages support physiologic skeletal remodeling and anabolic actions of parathyroid hormone in bone', *Proceedings of the National Academy of Sciences*, 111(4), pp. 1545–1550. doi:10.1073/pnas.1315153111.

Cho, T.-J., Gerstenfeld, L.C. and Einhorn, T.A. (2002) 'Differential temporal expression of members of the transforming growth factor β superfamily during murine fracture healing', *Journal of Bone and Mineral Research*, 17(3), pp. 513–520. doi:10.1359/jbmr.2002.17.3.513.

Choy, M.H.V., Wong, R.M.Y., Chow, S.K.H., Li, M.C., Chim, Y.N., Li, T.K., Ho, W.T., Cheng, J.C.Y. and Cheung, W.H. (2020) 'How much do we know about the role of osteocytes in different phases of fracture healing? A systematic review.', *Journal of orthopaedic translation*, 21, pp. 111–121. doi:10.1016/j.jot.2019.07.005.

Christodoulides, N., Pierre, F.N., Sanchez, X., Li, L., Hocquard, K., Patton, A., Muldoon, R., Miller, C.S., Ebersole, J.L., Redding, S., Yeh, C.K., Furmaga, W.B., Wampler, D.A., Bozkurt, B., Ballantyne, C.M. and McDevitt, J.T. (2012) 'Programmable bio-nanochip technology for the diagnosis of cardiovascular disease at the point-of-care.', *Methodist DeBakey cardiovascular journal*. Methodist DeBakey Heart & Vascular Center, pp. 6–12. doi:10.14797/mdcj-8-1-6.

Chung, R., Cool, J.C., Scherer, M.A., Foster, B.K. and Xian, C.J. (2006) 'Roles of neutrophil-mediated inflammatory response in the bony repair of injured growth plate cartilage in young rats', *Journal of Leukocyte Biology*, 80(6), pp. 1272–1280. doi:10.1189/jlb.0606365.

Claes, L., Recknagel, S. and Ignatius, A. (2012) 'Fracture healing under healthy and inflammatory conditions', *Nature Reviews Rheumatology*, 8(3), pp. 133–143. doi:10.1038/nrrheum.2012.1.

Clark, D., Brazina, S., Yang, F., Hu, D., Hsieh, C.L., Niemi, E.C., Miclau, T., Nakamura, M.C. and Marcucio, R. (2020) 'Age-related changes to macrophages are detrimental to fracture healing in mice', *Aging Cell*, 19(3), p. e13112. doi:10.1111/acel.13112.

Clarke, B. (2008) 'Normal bone anatomy and physiology.', *Clinical journal of the American Society of Nephrology : CJASN*, 3, pp. 131–139. doi:10.2215/CJN.04151206.

Clarkin, C.E. and Gerstenfeld, L.C. (2013) 'VEGF and bone cell signalling: An essential vessel for communication?', *Cell Biochemistry and Function*, 31(1), pp. 1–11. doi:10.1002/cbf.2911.

Clément-Lacroix, P., Ai, M., Morvan, F., Roman-Roman, S., Vayssière, B., Belleville, C., Estrera, K., Warman, M.L., Baron, R. and Rawadi, G. (2005) 'Lrp5-independent activation of Wnt signaling by lithium chloride increases bone formation and bone mass in mice.', *Proceedings of the National Academy of Sciences of the United States of America*, 102(48), pp. 17406–11. doi:10.1073/pnas.0505259102.

Clough, B.H., Zeitouni, S., Krause, U., Chaput, C.D., Cross, L.M., Gaharwar, A.K. and Gregory, C.A. (2018) 'Rapid Osteogenic Enhancement of Stem Cells in Human Bone Marrow Using a Glycogen-Synthease-Kinase-3-Beta Inhibitor Improves Osteogenic Efficacy In Vitro and In Vivo', *Stem Cells Translational Medicine*, pp. 1–12. doi:10.1002/sctm.17-0229.

Colnot, C., Thompson, Z., Miclau, T., Werb, Z. and Helms, J.A. (2003) 'Altered fracture repair in the absence of MMP9.', *Development (Cambridge, England)*, 130(17), pp. 4123–33. doi:10.1242/dev.00559.

*Complications from Fractures. Information and treatment | Patient* (no date). Available at: https://patient.info/doctor/complications-from-fractures#nav-1 (Accessed: 14 April 2021).

Dawson, J.I. and Oreffo, R.O.C. (2008) 'Bridging the regeneration gap: Stem cells, biomaterials and clinical translation in bone tissue engineering', *Archives of Biochemistry and Biophysics*, 473(2), pp. 124–131. doi:10.1016/j.abb.2008.03.024.

Day, T.F., Guo, X., Garrett-Beal, L. and Yang, Y. (2005) 'Wnt/β-catenin signaling in mesenchymal progenitors controls osteoblast and chondrocyte differentiation during vertebrate skeletogenesis', *Developmental Cell*, 8(5), pp. 739–750. doi:10.1016/j.devcel.2005.03.016.

Dickson, K., Katzman, S., Delgado, E. and Contreras, D. (1994) 'Delayed unions and nonunions of open tibial fractures. Correlation with arteriography results.', *Clinical orthopaedics and related research*, (302), pp. 189–93.

Dimitriou, R., Tsiridis, E. and Giannoudis, P. V. (2005) 'Current concepts of molecular aspects of bone healing', *Injury*, 36(12), pp. 1392–1404. doi:10.1016/j.injury.2005.07.019.

Discher, B.M., Won, Y.Y., Ege, D.S., Lee, J.C., Bates, F.S., Discher, D.E. and Hammer, D.A. (1999) 'Polymersomes: tough vesicles made from diblock copolymers.', *Science (New York, N.Y.)*, 284(5417), pp. 1143–1146. doi:10.1126/science.284.5417.1143.

Duan, Y., Beck, T.J., Wang, X.F. and Seeman, E. (2003) 'Structural and Biomechanical Basis of Sexual Dimorphism in Femoral Neck Fragility Has Its Origins in Growth and Aging', *Journal of Bone and Mineral Research*, 18(10), pp. 1766–1774. doi:10.1359/JBMR.2003.18.10.1766.

Eckardt, H., Ding, M., Lind, M., Hansen, E.S., Christensen, K.S. and Hvid, I. (2005) 'Recombinant human vascular endothelial growth factor enhances bone healing in an experimental nonunion model', *Journal of Bone and Joint Surgery - British Volume*, 87-B(10), pp. 1434–1438. doi:10.1302/0301-620X.87B10.16226.

Edgar, C.M., Chakravarthy, V., Barnes, G.L., Kakar, S., Gerstenfeld, L.C. and Einhorn, T.A. (2007) 'Autogenous regulation of a network of bone morphogenetic proteins (BMPs) mediates the osteogenic differentiation in murine marrow stromal cells', *Bone*, 40(5), pp. 1389–1398. doi:10.1016/j.bone.2007.01.001.

Einhorn, T. a. and Gerstenfeld, L.C. (2014) 'Fracture healing: mechanisms and interventions', *Nature Reviews Rheumatology*, 11(1), pp. 45–54. doi:10.1038/nrrheum.2014.164.

Einhorn, T.A. (1998) 'The cell and molecular biology of fracture healing', *Clinical Orthopaedics and Related Research*, (355S), pp. 7–21. doi:10.1097/00003086-199810001-00003.

Fan, C., Oduk, Y., Zhao, M., Lou, X., Tang, Y., Pretorius, D., Valarmathi, M.T., Walcott, G.P., Yang, J., Menasche, P., Krishnamurthy, P., Zhu, W. and Zhang, J. (2020) 'Myocardial protection by nanomaterials formulated with CHIR99021 and FGF1', *JCI insight*, 5(12), pp. 1–19. doi:10.1172/jci.insight.132796.

Farhat, G.N. and Cauley, J.A. (2008) 'The link between osteoporosis and cardiovascular disease', *Clinical Cases in Mineral and Bone Metabolism*, 5(1), pp. 19–34.

Farokhzad, O.C. and Langer, R. (2006) 'Nanomedicine: Developing smarter therapeutic and diagnostic modalities', *Advanced Drug Delivery Reviews*, 58(14), pp. 1456–1459. doi:10.1016/j.addr.2006.09.011.

Frame, S. and Cohen, P. (2001) 'GSK3 takes centre stage more than 20 years after its discovery.', *The Biochemical journal*, 359, pp. 1–16. doi:10.1042/0264-6021:3590001.

Francis, R.M.J. (2014) *Proliferation of Adult Human Small Intestinal Epithelial Stem Cells by a GSK-3beta; Inhibitor, CHIR99021 Encapsulated in Poly Lactic-co-Glycolic Acid Nanoparticles.* UCLA.

Frangioni, J. V. (2003) 'In vivo near-infrared fluorescence imaging', *Current Opinion in Chemical Biology*, 7(5), pp. 626–634. doi:10.1016/j.cbpa.2003.08.007.

Frank, M.M. and Fries, L.F. (1991) 'The role of complement in inflammation and phagocytosis', *Immunology Today*, 12(9), pp. 322–326. doi:10.1016/0167-5699(91)90009-I.

Friedlaender, G.E., Perry, C.R., Cole, J.D., Cook, S.D., Cierny, G., Muschler, G.F., Zych, G.A., Calhoun, J.H., LaForte, A.J. and Yin, S. (2001) 'Osteogenic protein-1 (bone morphogenetic protein-7) in the treatment of tibial nonunions: A prospective, randomized clinical trial comparing rhOP-1 with fresh bone autograft', *Journal of Bone and Joint Surgery*, 83, pp. S151–S158.

Frith, J.E., Titmarsh, D.M., Padmanabhan, H. and Cooper-White, J.J. (2013) 'Microbioreactor array screening of wnt modulators and microenvironmental factors in osteogenic differentiation of mesenchymal progenitor cells', *PLoS ONE*, 8(12), pp. 1–15. doi:10.1371/journal.pone.0082931.

Frost, H.M. (1989) 'The Biology of Fracture Healing', *Clinical Orthopaedics and Related Research*, 248(NA;), p. 294???309. doi:10.1097/00003086-198911000-00046.

Fu, X., Han, B., Cai, S., Lei, Y., Sun, T. and Sheng, Z. (2009) 'Migration of bone marrow-derived mesenchymal stem cells induced by tumor necrosis factor-α and its possible role in wound healing', *Wound Repair and Regeneration*, 17(2), pp. 185–191. doi:10.1111/j.1524-475X.2009.00454.x.

Gaharwar, A.K., Singh, I. and Khademhosseini, A. (2020) 'Engineered biomaterials for in situ tissue regeneration', *Nature Reviews Materials*, 5(9), pp. 686–705. doi:10.1038/s41578-020-0209-x.

Gardner, M.J., van der Meulen, M.C.H., Demetrakopoulos, D., Wright, T.M., Myers, E.R. and Bostrom, M.P. (2006) 'In vivo cyclic axial compression affects bone healing in the mouse tibia', *Journal of orthopaedic research : official publication of the Orthopaedic Research Society*, 24(8), pp. 1679–1686. doi:10.1002/JOR.20230.

Gerstenfeld, L.C., Cho, T.J., Kon, T., Aizawa, T., Tsay, A., Fitch, J., Barnes, G.L., Graves, D.T. and Einhorn, T.A. (2003) 'Impaired Fracture Healing in the Absence of TNF-α Signaling: The Role of TNF-α in Endochondral

Cartilage Resorption', *Journal of Bone and Mineral Research*, 18(9), pp. 1584–1592.

Gerstenfeld, L.C., Cullinane, D.M., Barnes, G.L., Graves, D.T. and Einhorn, T.A. (2003) 'Fracture healing as a post-natal developmental process: Molecular, spatial, and temporal aspects of its regulation', *Journal of Cellular Biochemistry*, 88(5), pp. 873–884. doi:10.1002/jcb.10435.

Ghoroghchian, P.P., Li, G., Levine, D.H., Davis, K.P., Bates, F.S., Hammer, D.A. and Therien, M.J. (2006) 'Bioresorbable Vesicles Formed through Spontaneous Self-Assembly of Amphiphilic Poly(ethylene oxide)-block-polycaprolactone.', *Macromolecules*, 39(5), pp. 1673–1675. doi:10.1021/ma0519009.Bioresorbable.

Gibbs, D.M.R., Black, C.R.M., Hulsart-Billstrom, G., Shi, P., Scarpa, E., Oreffo, R.O.C. and Dawson, J.I. (2016) 'Bone induction at physiological doses of BMP through localization by clay nanoparticle gels', *Biomaterials*, 99, pp. 16–23. doi:10.1016/j.biomaterials.2016.05.010.

Glass, G.E., Chan, J.K., Freidin, A., Feldmann, M., Horwood, N.J. and Nanchahal, J. (2011) 'TNF-α promotes fracture repair by augmenting the recruitment and differentiation of muscle-derived stromal cells', *Proceedings of the National Academy of Sciences of the United States of America*, 108(4), pp. 1585–1590. doi:10.1073/pnas.1018501108.

Gong, T., Xie, J., Liao, J., Zhang, T., Lin, S. and Lin, Y. (2015) 'Nanomaterials and bone regeneration.', *Bone research*, 3, p. 15029. doi:10.1038/boneres.2015.29.

Govender, S., Csimma, C., Genant, H.K., Valentin-Opran, A., Amit, Y., Arbel, R., Aro, H., Atar, D., Bishay, M., Börner, M.G., Chiron, P., Choong, P., Cinats, J., Courtenay, B., Feibel, R., Geulette, B., Govender, S., Gravel, C., Haas, N., *et al.* (2002) 'Recombinant human bone morphogenetic protein-2 for treatment of open tibial fractures a prospective, controlled, randomized study of four hundred and fifty patients', *Journal of Bone and Joint Surgery - Series A*, 84(12), pp. 2123–2134. doi:10.2106/00004623-200212000-00001.

Grafe, I., Alexander, S., Peterson, J.R., Snider, T.N., Levi, B., Lee, B. and Mishina, Y. (2018) 'TGF-b Family Signaling in Mesenchymal Differentiation', *Cold Spring Harbor Perspectives in Biology*, 10, pp. 1–49. doi:10.1101/cshperspect.a022202.

Gref, R., Minamitake, Y., Peracchia, M.T., Trubetskoy, V., Torchilin, V. and Langer, R. (1994) 'Biodegradable long-circulating polymeric nanospheres', *Science*, 263(5153), pp. 1600–1603. doi:10.1126/science.8128245.

Gref, R., Minamitake, Y., Peracchia, M.T., Trubetskoy, V., Torchilin, V. and Langerll, R. (1994) 'Biodegradable Long-Circulating Polymeric Nanospheres ILlauana Upon solvent evaporation , the', *Science*, 263(January), pp. 1600–1603.

Grossen, P., Witzigmann, D., Sieber, S. and Huwyler, J. (2017) 'PEG-PCL-based nanomedicines: A biodegradable drug delivery system and its application', *Journal of Controlled Release*, 260, pp. 46–60. doi:10.1016/j.jconrel.2017.05.028.

Grotewold, L. and Rüther, U. (2002) 'The Wnt agonist Dickkopf-1 is regulated by Bmp signalling and c-Jun and modulates programmed cell death.', *The EMBO Journal*, 21, pp. 966–975.

Grundnes, O. and Reikerås, O. (1993) 'the Importance of the Hematoma for Fracture Healing in Rats', *Acta Orthopaedica*, 64(3), pp. 340–342. doi:10.3109/17453679308993640.

Gu, G., Xia, H., Hu, Q., Liu, Z., Jiang, M., Kang, T., Miao, D., Tu, Y., Pang, Z., Song, Q., Yao, L., Chen, H., Gao, X. and Chen, J. (2013) 'PEG-co-PCL nanoparticles modified with MMP-2/9 activatable low molecular weight protamine for enhanced targeted glioblastoma therapy', *Biomaterials*, 34(1), pp. 196–208. doi:10.1016/j.biomaterials.2012.09.044.

Guan, L., Rizzello, L. and Battaglia, G. (2015) 'Polymersomes and their applications in cancer delivery and therapy', *Nanomedicine*, 10(17), pp. 2757–2780.

Gupta, S., Del Fabbro, M. and Chang, J. (2019) 'The impact of simvastatin intervention on the healing of bone, soft tissue, and TMJ cartilage in dentistry: a systematic review and meta-analysis', *International Journal of Implant Dentistry*, 5(1). doi:10.1186/s40729-019-0168-4.

Gustafson, H.H., Holt-Casper, D., Grainger, D.W. and Ghandehari, H. (2015) 'Nanoparticle uptake: The phagocyte problem', *Nano Today*. Elsevier B.V., pp. 487–510. doi:10.1016/j.nantod.2015.06.006.

Habel, J., Ogbonna, A., Larsen, N., Cherré, S., Kynde, S., Midtgaard, S.R., Kinoshita, K., Krabbe, S., Jensen, G.V.,

Hansen, J.S., Almdal, K. and Hèlix-Nielsen, C. (2015) 'Selecting analytical tools for characterization of polymersomes in aqueous solution', *RSC Adv.*, 5(97), pp. 79924–79946. doi:10.1039/C5RA16403F.

Hadjiargyrou, M., Ahrens, W. and Rubin, C.T. (2000) 'Temporal Expression of the Chondrogenic and Angiogenic Growth Factor CYR61 During Fracture Repair', *Journal of Bone and Mineral Research*, 15(6), pp. 1014–1023. doi:10.1359/JBMR.2000.15.6.1014.

Hadjiargyrou, M., Lombardo, F., Zhao, S., Ahrens, W., Joo, J., Ahn, H., Jurman, M., White, D.W. and Rubin, C.T. (2002) 'Transcriptional profiling of bone regeneration. Insight into the molecular complexity of wound repair.', *The Journal of biological chemistry*, 277(33), pp. 30177–30182. doi:10.1074/jbc.M203171200.

Hankenson, K.D., Gagne, K. and Shaughnessy, M. (2015) 'Extracellular signaling molecules to promote fracture healing and bone regeneration', *Advanced Drug Delivery Reviews*, 94, pp. 3–12. doi:10.1016/j.addr.2015.09.008.

Hashimoto, J., Yoshikawa, H., Takaoka, K., Shimizu, N., Masuhara, K., Tsuda, T., Miyamoto, S. and Ono, K. (1989) 'Inhibitory effects of tumor necrosis factor alpha on fracture healing in rats', *Bone*, 10(6), pp. 453–457. doi:10.1016/8756-3282(89)90078-1.

Hauser, C.J., Zhou, X., Joshi, P., Cuchens, M.A., Kregor, P., Devidas, M., Kennedy, R.J., Poole, G. V. and Hughes, J.L. (1997) 'The immune microenvironment of human fracture/soft-tissue hematomas and its relationship to systemic immunity', *Journal of Trauma - Injury, Infection and Critical Care*, 42(5), pp. 895–904. doi:10.1097/00005373-199705000-00021.

Hausman, M.R., Schaffler, M.B. and Majeska, R.J. (2001) 'Prevention of fracture healing in rats by an inhibitor of angiogenesis.', *Bone*, 29(6), pp. 560–4.

He, Y.X., Zhang, G., Pan, X.H., Liu, Z., Zheng, L.Z., Chan, C.W., Lee, K.M., Cao, Y.P., Li, G., Wei, L., Hung, L.K., Leung, K.S. and Qin, L. (2011) 'Impaired bone healing pattern in mice with ovariectomy-induced osteoporosis: A drill-hole defect model', *Bone*, 48(6), pp. 1388–1400. doi:10.1016/j.bone.2011.03.720.

Hernlund, E., Svedbom, A., Ivergård, M., Compston, J., Cooper, C., Stenmark, J., McCloskey, E. V., Jönsson, B. and Kanis, J.A. (2013) 'Osteoporosis in the European Union: Medical management, epidemiology and economic burden: A report prepared in collaboration with the International Osteoporosis Foundation (IOF) and the European Federation of Pharmaceutical Industry Associations (EFPIA)', *Archives of Osteoporosis*, 8(136), pp. 1–115. doi:10.1007/s11657-013-0136-1.

Hess, K., Ushmorov, A., Fiedler, J., Brenner, R.E. and Wirth, T. (2009) 'TNFα promotes osteogenic differentiation of human mesenchymal stem cells by triggering the NF-κB signaling pathway', *Bone*, 45(2), pp. 367–376. doi:10.1016/j.bone.2009.04.252.

Hill, T.P., Später, D., Taketo, M.M., Birchmeier, W. and Hartmann, C. (2005) 'Canonical Wnt/β-catenin signaling prevents osteoblasts from differentiating into chondrocytes', *Developmental Cell*, 8(5), pp. 727–738. doi:10.1016/j.devcel.2005.02.013.

Hoang-Kim, A., Gelsomini, L., Luciani, D., Moroni, A. and Giannini, S. (2009) 'Fracture healing and drug therapies in osteoporosis', *Clinical Cases in Mineral and Bone Metabolism*, 6(2), pp. 136–143.

Hoeppner, L.H., Secreto, F.J. and Westendorf, J.J. (2009) 'Wnt Signaling as a Therapeutic Target for Bone Diseases', 13(4), pp. 485–496. doi:10.1517/14728220902841961.Wnt.

Hofbauer, L.C., Khosla, S., Dunstan, C.R., Lacey, D.L., Boyle, W.J. and Riggs, B.L. (2000) 'The roles of osteoprotegerin and osteoprotegerin ligand in the paracrine regulation of bone resorption', *Journal of Bone and Mineral Research*, 15(1), pp. 2–12. doi:10.1359/jbmr.2000.15.1.2.

Hoffman, M.D. and Benoit, D.S.W. (2015) 'Agonism of Wnt/β-catenin signaling promotes mesenchymal stem cell (MSC) expansion.', *Tissue Eng Regen Med*, 9(11), pp. 1–25. doi:10.1002/term.1736.Agonism.

Hoffman, M.D., Takahata, M. and Benoit, D.S.W. (2011) '6-Bromoindirubin-3'-oxime (BIO) induces proliferation of human mesenchymal stem cells (hMSCs)', *2011 IEEE 37th Annual Northeast Bioengineering Conference (NEBEC)*, pp. 1–2. doi:10.1109/NEBC.2011.5778684.

Hoggatt, J. and Pelus, L.M. (2011) 'Mobilization of hematopoietic stem cells from the bone marrow niche to the blood compartment.', *Stem cell research & therapy*, 2(2), p. 13. doi:10.1186/scrt54.

Hu, D.P., Ferro, F., Yang, F., Taylor, A.J., Chang, W., Miclau, T., Marcucio, R.S. and Bahney, C.S. (2017) 'Cartilage to bone transformation during fracture healing is coordinated by the invading vasculature and induction of the core pluripotency genes', *Development (Cambridge)*, 144(2), pp. 221–234. doi:10.1242/dev.130807.

Hu, Q., Van Rooijen, N. and Liu, D. (1996) 'Effect of macrophage elimination using liposome-encapsulated dichloromethylene diphosphonate on tissue distribution of liposomes', *Journal of Liposome Research*, 6(4), pp. 681–698. doi:10.3109/08982109609039921.

Huang, X., Zhong, L., Hendriks, J., Post, J.N. and Karperien, M. (2018) 'The Effects of the WNT-Signaling Modulators BIO and PKF118-310 on the Chondrogenic Differentiation of Human Mesenchymal Stem Cells', *International Journal of Molecular Sciences*, 19(2), p. 561. doi:10.3390/ijms19020561.

Janeczek, A.A., Scarpa, E., Horrocks, M.H., Tare, R.S., Rowland, C.A., Jenner, D., Newman, T.A., Oreffo, R.O.C., Lee, S.F. and Evans, N.D. (2017) 'PEGylated liposomes associate with Wnt3A protein and expand putative stem cells in human bone marrow populations', *Nanomedicine*, 12(8), pp. 845–863. doi:10.2217/nnm-2016-0386.

Janeczek, A.A., Tare, R.S., Scarpa, E., Moreno-Jimene, I., Rowland, C.A., Jenner, D., Newman, T.A., Oreffo, R.O.C. and Evans, N.D. (2015) 'Transient Canonical Wnt Stimulation Enriches Human Bone Marrow Mononuclear Cell Isolates for Osteoprogenitors', *Stem Cells*, 34(2), pp. 418–430.

Jeelani, S., Jagat Reddy, R.C., Maheswaran, T., Asokan, G.S., Dany, A. and Anand, B. (2014) 'Theranostics: A treasured tailor for tomorrow', *Journal of Pharmacy and Bioallied Sciences*. Medknow Publications, p. S6. doi:10.4103/0975-7406.137249.

Jho, E., Zhang, T., Domon, C., Joo, C., Freund, J. and Costantini, F. (2002) 'Wnt / β -Catenin / Tcf Signaling Induces the Transcription of Axin2 , a Negative Regulator of the Signaling Pathway Wnt / ß-Catenin / Tcf Signaling Induces the Transcription of Axin2 , a Negative Regulator of the Signaling Pathway', *Molecular and Cellular Biology*, 22(4), pp. 1172–1183. doi:10.1128/MCB.22.4.1172.

Jia, Z., Zhang, Y., Chen, Y.H., Dusad, A., Yuan, H., Ren, K., Li, F., Fehringer, E. V., Purdue, P.E., Goldring, S.R., Daluiski, A. and Wang, D. (2015) 'Simvastin prodrug micelles target fracture and improve healing', *Journal of Controlled Release*, 23(200), pp. 23–34. doi:10.1038/jid.2014.371.

Johnell, O. and Kanis, J.A. (2006) 'An estimate of the worldwide prevalence and disability associated with osteoporotic fractures', *Osteoporosis International*, 17(12), pp. 1726–1733. doi:10.1007/s00198-006-0172-4.

Johnson, N.A., Jeffery, J., Stirling, E., Thompson, J. and Dias, J.J. (2019) 'Effects of deprivation, ethnicity, gender and age on distal radius fracture incidence and surgical intervention rate', *Bone*, 121(December 2018), pp. 1–8. doi:10.1016/j.bone.2018.12.018.

Johnston, A.H., Dalton, P.D. and Newman, T.A. (2010) 'Polymersomes, smaller than you think: Ferrocene as a TEM probe to determine core structure', *Journal of Nanoparticle Research*, 12(6), pp. 1997–2001. doi:10.1007/s11051-010-9886-5.

Joyce, M.E., Terke, R.M., Jingushi, S. and Bolander, M.E. (1990) 'Role of Transforming Growth Factor-β in Fracture Repair', *Annals of the New York Academy of Sciences*, 593(1), pp. 107–123. doi:10.1111/j.1749-6632.1990.tb16104.x.

Kaback, L.A., Soung, D.Y., Naik, A., Smith, N., Schwarz, E.M., O'Keefe, R.J. and Drissi, H. (2008) 'Osterix/Sp7 Regulates Mesenchymal Stem Cell Mediated Endochondral Ossification', *Journal of cellular physiology*, 214, pp. 173–182. doi:10.1002/JCP.

Kakar, S., Einhorn, T.A., Vora, S., Miara, L.J., Hon, G., Wigner, N.A., Toben, D., Jacobsen, K.A., Al-Sebaei, M.O., Song, M., Trackman, P.C., Morgan, E.F., Gerstenfeld, L.C. and Barnes, G.L. (2007) 'Enhanced chondrogenesis and Wnt signaling in PTH-treated fractures', *Journal of Bone and Mineral Research*, 22(12), pp. 1903–1912. doi:10.1359/jbmr.070724.

Ke, X., Ng, V.W.L., Ono, R.J., Chan, J.M.W., Krishnamurthy, S., Wang, Y., Hedrick, J.L. and Yang, Y.Y. (2014) 'Role of non-covalent and covalent interactions in cargo loading capacity and stability of polymeric micelles', *Journal of Controlled Release*, 193, pp. 9–26. doi:10.1016/j.jconrel.2014.06.061.

Kegelman, C.D., Nijsure, M.P., Moharrer, Y., Pearson, H.B., Dawahare, J.H., Jordan, K.M., Qin, L. and Boerckel, J.D. (2021) 'YAP and TAZ Promote Periosteal Osteoblast Precursor Expansion and Differentiation for Fracture Repair', *Journal of Bone and Mineral Research*, 36(1), pp. 143–157. doi:10.1002/jbmr.4166.

Kennell, J.A. and MacDougald, O.A. (2005) 'Wnt signaling inhibits adipogenesis through ??-catenin-dependent and -independent mechanisms', *Journal of Biological Chemistry*, 280(25), pp. 24004–24010. doi:10.1074/jbc.M501080200.

Kim, J.-B., Leucht, P., Lam, K., Luppen, C., Ten Berge, D., Nusse, R. and Helms, J.A. (2007) 'Bone regeneration is regulated by wnt signaling.', *Journal of bone and mineral research : the official journal of the American Society for Bone and Mineral Research*, 22(12), pp. 1913–1923. doi:10.1359/jbmr.070802.

Klop, C., van Staa, T.P., Cooper, C., Harvey, N.C. and de Vries, F. (2016) 'The epidemiology of mortality after fracture in England: variation by age, sex, time, geographic location, and ethnicity', *Osteoporosis International*, 28(1), pp. 161–168. doi:10.1007/s00198-016-3787-0.

Kolar, P., Gaber, T., Perka, C., Duda, G.N. and Buttgereit, F. (2011) 'Human Early Fracture Hematoma Is Characterized by Inflammation and Hypoxia', *Clinical Orthopaedics and Related Research*, 469, pp. 3118–3126. doi:10.1007/s11999-011-1865-3.

Kolar, P., Schmidt-Bleek, K., Schell, H., Gaber, T., Toben, D., Schmidmaier, G., Perka, C., Buttgereit, F. and Duda, G.N. (2010) 'The early fracture hematoma and its potential role in fracture healing', *Tissue Eng Part B Rev*, 16(4), pp. 427–434. doi:10.1089/ten.TEB.2009.0687.

Komatsu, D.. and Hadjiargyrou, M. (2004) 'Activation of the transcription factor HIF-1 and its target genes, VEGF, HO-1, iNOS, during fracture repair', *Bone*, 34(4), pp. 680–688. doi:10.1016/J.BONE.2003.12.024.

Komiya, Y. and Habas, R. (2014) 'Wnt signal transduction pathways', *Organogenesis*, 4(2), pp. 68–75. doi:10.4161/org.4.2.5851.

Komori, T. (2018) 'Runx2, an inducer of osteoblast and chondrocyte differentiation', *Histochemistry and Cell Biology*, pp. 1–11. doi:10.1007/s00418-018-1640-6.

Kon, T., Cho, T.-J., Aizawa, T., Yamazaki, M., Nooh, N., Graves, D.T., Gerstenfeld, L.C. and Einhorn, T.A. (2001) 'Expression of osteoprotegerin, receptor activator of NF-κB ligand (osteoprotegerin ligand) and related proinflammatory cytokines during fracture healing', *Journal of Bone and Mineral Research*, 16(6), pp. 1004–1014. doi:10.1359/jbmr.2001.16.6.1004.

Kostenuik, P. and Mirza, F.M. (2017) 'Fracture Healing Physiology and the Quest for Therapies for Delayed Healing and Nonunion', *J Orthopedic Research*, 35, pp. 213–223. doi:10.1002/jor.23460.

Kramer, I., Halleux, C., Keller, H., Pegurri, M., Gooi, J.H., Weber, P.B., Feng, J.Q., Bonewald, L.F. and Kneissel, M. (2010) 'Osteocyte Wnt/beta-catenin signaling is required for normal bone homeostasis.', *Molecular and cellular biology*, 30(12), pp. 3071–85. doi:10.1128/MCB.01428-09.

Krause, U., Harris, S., Green, A., Ylostalo, J., Zeitouni, S., Lee, N. and Gregory, C.A. (2010) 'Pharmaceutical modulation of canonical Wnt signaling in multipotent stromal cells for improved osteoinductive therapy', *Proceedings of the National Academy of Sciences*, 107(9), pp. 4147–4152. doi:10.1073/pnas.0914360107.

Krishnakumar, G.S., Roffi, A., Reale, D., Kon, E. and Filardo, G. (2017) 'Clinical application of bone morphogenetic proteins for bone healing: a systematic review', *International Orthopaedics*, 41(6), pp. 1073–1083. doi:10.1007/s00264-017-3471-9.

Kubota, K., Sakikawa, C., Katsumata, M., Nakamura, T. and Wakabayashi, K. (2002) 'Platelet-derived growth factor BB secreted from osteoclasts acts as an osteoblastogenesis inhibitory factor', *Journal of Bone and Mineral Research*, 17(2), pp. 257–265. doi:10.1359/jbmr.2002.17.2.257.

Kumar, S., Wan, C., Ramaswamy, G., Clemens, T.L. and Ponnazhagan, S. (2010) 'Mesenchymal stem cells expressing osteogenic and angiogenic factors synergistically enhance bone formation in a mouse model of segmental bone defect.', *Molecular therapy : the journal of the American Society of Gene Therapy*, 18(5), pp. 1026–1034. doi:10.1038/mt.2009.315.

Lange, J., Sapozhnikova, A., Lu, C., Hu, D., Li, X., Miclau, T. and Marcucio, R.S. (2010) 'Action of IL-1β during fracture healing', *Journal of Orthopaedic Research*, 28(6), pp. 778–784. doi:10.1002/jor.21061.

Laverman, P., Carstens, M.G., Boerman, O.C., Dams, E.T.M., Oyen, W.J.G., Van Rooijen, N., Corstens, F.H.M. and Storm, G. (2001) 'Factors affecting the accelerated blood clearance of polyethylene glycol-liposomes upon repeated injection', *Journal of Pharmacology and Experimental Therapeutics*, 298(2), pp. 607–612.

Lavrador, P., Gaspar, V.M. and Mano, J.F. (2018) 'Stimuli-responsive nanocarriers for delivery of bone therapeutics – Barriers and progresses', *Journal of Controlled Release*, 273, pp. 51–67. doi:10.1016/j.jconrel.2018.01.021.

Le, A.X., Miclau, T., Hu, D., Helms, J.A. and A. (2001) 'Molecular aspects of healing in stabilized and non-stabilized fractures', *Journal of Orthopaedic Research*, 19(1), pp. 78–84. doi:10.1016/S0736-0266(00)00006-1.

Leal, J., Gray, A.M., Prieto-Alhambra, D., Arden, N.K., Cooper, C., Javaid, M.K. and Judge, A. (2016) 'Impact of hip fracture on hospital care costs: a population-based study', *Osteoporosis International*, 27(2), pp. 549–558. doi:10.1007/s00198-015-3277-9.

Leucht, P., Jiang, J., Cheng, D., Liu, B., Dhamdhere, G., Fang, M.Y., Monica, S.D., Urena, J.J., Cole, W., Smith, L.R., Castillo, A.B., Longaker, M.T. and Helms, J.A. (2013) 'Wnt3a reestablishes osteogenic capacity to bone grafts from aged animals.', *The Journal of bone and joint surgery. American volume*, 95(14), pp. 1278–88. doi:10.2106/JBJS.L.01502.

Levy, R.M., Prince, J.M., Yang, R., Mollen, K.P., Liao, H., Watson, G.A., Fink, M.P., Vodovotz, Y. and Billiar, T.R. (2006) 'Systemic inflammation and remote organ damage following bilateral femur fracture requires Toll-like receptor 4', *American Journal of Physiology - Regulatory Integrative and Comparative Physiology*, 291(4), pp. 970–976. doi:10.1152/ajpregu.00793.2005.

Li, A., Xia, X., Yeh, J., Kua, H., Liu, H., Mishina, Y., Hao, A. and Li, B. (2014) 'PDGF-AA Promotes Osteogenic Differentiation and Migration of Mesenchymal Stem Cell by Down-Regulating PDGFRa and Derepressing BMP-Smad1/5/8 Signaling', *PLoS ONE*, pp. 1–21. doi:10.1371/journal.pone.

Lieven, O., Dronka, J., Burmü Hl, S. and Rüther, U. (2014) 'Differential Binding of Lef1 and Msx1/2 Transcription Factors to Dkk1 CNEs Correlates with Reporter Gene Expression In Vivo', *PLoS ONE*, 9(12), pp. 1–23. doi:10.1371/journal.pone.0115442.

Lin, C.-Y., Chang, Y.-H., Sung, L.-Y., Chen, C.-L., Lin, S.-Y., Li, K.-C., Yen, T.-C., Lin, K.-J. and Hu, Y.-C. (2014) 'Long-term tracking of segmental bone healing mediated by genetically engineered adipose-derived stem cells: focuses on bone remodeling and potential side effects.', *Tissue engineering. Part A*, 20(9–10), pp. 1392–1402. doi:10.1089/ten.TEA.2013.0314.

Liu, G.Y., Lv, L.P., Chen, C.J., Liu, X.S., Hu, X.F. and Ji, J. (2011) 'Biocompatible and biodegradable polymersomes for pH-triggered drug release', *Soft Matter*, 7(14), pp. 6629–6636. doi:10.1039/c1sm05308f.

Liu, J., Zeng, F. and Allen, C. (2007) 'In vivo fate of unimers and micelles of a poly(ethylene glycol)-block-poly(caprolactone) copolymer in mice following intravenous administration', *European Journal of Pharmaceutics and Biopharmaceutics*, 65(3), pp. 309–319. doi:10.1016/j.ejpb.2006.11.010.

Loi, F., Córdova, L.A., Pajarinen, J., Lin, T. hua, Yao, Z. and Goodman, S.B. (2016) 'Inflammation, fracture and bone repair', *Bone*, 86, pp. 119–130. doi:10.1016/j.bone.2016.02.020.

Loots, G.G., Kneissel, M., Keller, H., Baptist, M., Chang, J., Collette, N.M., Ovcharenko, D., Plajzer-Frick, I. and Rubin, E.M. (2005) 'Genomic deletion of a long-range bone enhancer misregulates sclerostin in Van Buchem disease.', *Genome research*, 15(7), pp. 928–35. doi:10.1101/gr.3437105.

Lopas, L. a., Belkin, N.S., Mutyaba, P.L., Gray, C.F., Hankenson, K.D. and Ahn, J. (2014) 'Fractures in Geriatric Mice Show Decreased Callus Expansion and Bone Volume', *Clinical Orthopaedics and Related Research®*, 472(11), pp. 3523–3532. doi:10.1007/s11999-014-3829-x.

LoPresti, C., Lomas, H., Massignani, M., Smart, T. and Battaglia, G. (2009) 'Polymersomes: nature inspired nanometer sized compartments', *Journal of Materials Chemistry*, 19(22), p. 3576. doi:10.1039/b818869f.

Low, S.A., Galliford, C. V., Jones-Hall, Y.L., Roy, J., Yang, J., Low, P.S. and Kopeček, J. (2017) 'Healing efficacy of fracture-targeted GSK3 β inhibitor-loaded micelles for improved fracture repair', *Nanomedicine*, 12, pp. 185–193.

Low, S.A., Galliford, C. V., Yang, J., Low, P.S. and Kopeček, J. (2015) 'Biodistribution of Fracture-Targeted GSK3β Inhibitor-Loaded Micelles for Improved Fracture Healing', *Biomacromolecules*, 16(10), pp. 3145–3153. doi:10.1021/acs.biomac.5b00777.

Lu, C., Hansen, E., Sapozhnikova, A., Hu, D., Miclau, T. and Marcucio, R.S. (2008) 'Effect of age on vascularization during fracture repair', *Journal of Orthopaedic Research*, 26(10), pp. 1384–1389.

doi:10.1002/jor.20667.

Lu, C., Huang, S., Miclau, T., Helms, J.A. and Colnot, C. (2004) 'Mepe is expressed during skeletal development and regeneration', *Histochemistry and Cell Biology*, 121(6), pp. 493–499. doi:10.1007/S00418-004-0653-5.

Lu, C., Miclau, T., Hu, D., Hansen, E., Tsui, K., Puttlitz, C. and Marcucio, R.S. (2005) 'Celluar basis for age-related changes in fracture repair.', *Journal of Orthopaedic Research*, 23(6), pp. 1300–1307. doi:10.1016/j.orthres.2005.04.003.1100230610.Cellular.

Luo, M., Feng, Y., Wang, T. and Guan, J. (2018) 'Micro-/Nanorobots at Work in Active Drug Delivery', *Advanced Functional Materials*, 28(25), pp. 1–23. doi:10.1002/adfm.201706100.

Ma, B. and Hottiger, M.O. (2016) 'Crosstalk between wnt/β-catenin and NF-κB signaling pathway during inflammation', *Frontiers in Immunology*, 7(378), pp. 1–14. doi:10.3389/fimmu.2016.00378.

Maeda, H. (2015) 'Toward a full understanding of the EPR effect in primary and metastatic tumors as well as issues related to its heterogeneity', *Advanced Drug Delivery Reviews*, 91, pp. 3–6. doi:10.1016/j.addr.2015.01.002.

Malvern Panalytical Limited (2018) *Characterizing the size and concentration of liposomes using multi-angle dynamic light scattering. Application Note.* Available at: https://particular.ie/wp-content/uploads/2018/09/AN180519LiposomesZetasizerNanosight-6_tcm50-56360.pdf (Accessed: 28 April 2021).

Mannaris, C., Yang, C., Carugo, D., Owen, J., Lee, J.Y., Nwokeoha, S., Seth, A. and Teo, B.M. (2020) 'Acoustically responsive polydopamine nanodroplets: A novel theranostic agent', *Ultrasonics Sonochemistry*, 60(August 2019), p. 104782. doi:10.1016/j.ultsonch.2019.104782.

Marcellini, S., Henriquez, J.P. and Bertin, A. (2012) 'Control of osteogenesis by the canonical Wnt and BMP pathways in vivo: Cooperation and antagonism between the canonical Wnt and BMP pathways as cells differentiate from osteochondroprogenitors to osteoblasts and osteocytes', *BioEssays*, 34(11), pp. 953–962. doi:10.1002/bies.201200061.

Massberg, S., Konrad, I., Schürzinger, K., Lorenz, M., Schneider, S., Zohlnhoefer, D., Hoppe, K., Schiemann, M., Kennerknecht, E., Sauer, S., Schulz, C., Kerstan, S., Rudelius, M., Seidl, S., Sorge, F., Langer, H., Peluso, M., Goyal, P., Vestweber, D., *et al.* (2006) 'Platelets secrete stromal cell–derived factor 1α and recruit bone marrow–derived progenitor cells to arterial thrombi in vivo', *The Journal of Experimental Medicine*, 203(5), pp. 1221–1233. doi:10.1084/jem.20051772.

Matoori, S. and Leroux, J.C. (2020) 'Twenty-five years of polymersomes: Lost in translation?', *Materials Horizons*, 7(5), pp. 1297–1309. doi:10.1039/c9mh01669d.

Matsumura, Y. and Maeda, H. (1986) 'A New Concept for Macromolecular Therapeutics in Cancer Chemotherapy: Mechanism of Tumoritropic Accumulation of Proteins and the Antitumor Agent Smancs', *Cancer Research*, 46, pp. 6387–6392.

Matsutani, T., Kang, S.-C., Miyashita, M., Sasajima, K., Choudhry, M.A., Bland, K.I. and Chaudry, I.H. (2007) 'Liver cytokine production and ICAM-1 expression following bone fracture, tissue trauma, and hemorrhage in middle-aged mice.', *American journal of physiology. Gastrointestinal and liver physiology*, 292(1), pp. G268-74. doi:10.1152/ajpgi.00313.2006.

Meijer, L., Flajolet, M. and Greengard, P. (2004) 'Pharmacological inhibitors of glycogen synthase kinase 3', *Trends in Pharmacological Sciences*, 25(9), pp. 471–480. doi:10.1016/j.tips.2004.07.006.

Meijer, L., Skaltsounis, A.-L., Magiatis, P., Polychronopoulos, P., Knockaert, M., Leost, M., Ryan, X.P., Vonica, C.A., Brivanlou, A.H., Dajani, R., Crovace, C., Tarricone, C., Musacchio, A., Roe, S.M., Pearl, L. and Greengard, P. (2003) 'GSK-3-Selective Inhibitors Derived from Tyrian Purple Indirubins', *Chemisty and Biology*, 10(2), pp. 1255–1266. doi:10.1016/j.

Michalski, M.N. and McCauley, L.K. (2017) 'Macrophages and skeletal health', *Pharmacology & Therapeutics*, 174, pp. 43–54. doi:10.1016/j.pharmthera.2017.02.017.

Miller, M.A. and Weissleder, R. (2017) 'Imaging the pharmacology of nanomaterials by intravital microscopy: Toward understanding their biological behavior', *Advanced Drug Delivery Reviews*, 113, pp. 61–86. doi:10.1016/j.addr.2016.05.023.

Miller, M.A., Zheng, Y.-R., Gadde, S., Pfirschke, C., Zope, H., Engblom, C., Kohler, R.H., Iwamoto, Y., Yang, K.S., Askevold, B., Kolishetti, N., Pittet, M., Lippard, S.J., Farokhzad, O.C. and Weissleder, R. (2015) 'Tumour-associated macrophages act as a slow-release reservoir of nano-therapeutic Pt(IV) pro-drug.', *Nature communications*, 6, p. 8692. doi:10.1038/ncomms9692.

Mills, L. and Simpson, A.H.R.W. (2012) 'The relative incidence of fracture non-union in a population of 5.17 million people; an epidemioloigcal study.', *BMJ Open*, 03, pp. 437–450.

Mills, L.A., Aitken, S.A. and Simpson, A.H.R.W. (2017) 'The risk of non-union per fracture: current myths and revised figures from a population of over 4 million adults', *Acta Orthopaedica*, 88(4), pp. 434–439. doi:10.1080/17453674.2017.1321351.

Minear, S., Leucht, P., Jiang, J., Liu, B., Zeng, A., Fuerer, C., Nusse, R. and Helms, J.A. (2010) 'Wnt Proteins Promote Bone Regeneration.', *Science translational medicine*, 2(29), p. 29ra30. doi:10.1126/scitranslmed.3000231.

Minear, S., Leucht, P., Miller, S. and Helms, J.A. (2010) 'rBMP represses Wnt signaling and influences skeletal progenitor cell fate specification during bone repair.', *Journal of bone and mineral research : the official journal of the American Society for Bone and Mineral Research*, 25(6), pp. 1196–207. doi:10.1002/jbmr.29.

Mitragotri, S., Anderson, D.G., Chen, X., Chow, E.K., Ho, D., Kabanov, A. V., Karp, J.M., Kataoka, K., Mirkin, C.A., Petrosko, S.H., Shi, J., Stevens, M.M., Sun, S., Teoh, S., Venkatraman, S.S., Xia, Y., Wang, S., Gu, Z. and Xu, C. (2015) 'Accelerating the Translation of Nanomaterials in Biomedicine', *ACS Nano*, 9(7), pp. 6644–6654. doi:10.1021/acsnano.5b03569.

Mizuno, K., Mineo, K., Tachibana, T., Sumi, M., Matsubara, T. and Hirohata, K. (1990) 'The osteogenetic potential of fracture haematoma. Subperiosteal and intramuscular transplantation of the haematoma.', *The Journal of bone and joint surgery. British volume*, 72(5), pp. 822–9.

Modi, S. and Anderson, B.D. (2013) 'Determination of drug release kinetics from nanoparticles: Overcoming pitfalls of the dynamic dialysis method', *Molecular Pharmaceutics*, 10(8), pp. 3076–3089. doi:10.1021/mp400154a.

Moghimi, S.M., Hunter, A.C. and Andresen, T.L. (2012) 'Factors Controlling Nanoparticle Pharmacokinetics: An Integrated Analysis and Perspective', *Annu. Rev. Pharmacol. Toxicol*, 52, pp. 481–503. doi:10.1146/annurev-pharmtox-010611-134623.

Monfoulet, L., Rabier, B., Chassande, O. and Fricain, J.C. (2010) 'Drilled hole defects in mouse femur as models of intramembranous cortical and cancellous bone regeneration', *Calcified Tissue International*, 86(1), pp. 72–81. doi:10.1007/s00223-009-9314-y.

Monroe, D.G., McGee-Lawrence, M.E., Oursler, M.J. and Westendorf, J.J. (2012) 'Update on Wnt signaling in bone cell biology and bone disease', *Gene*, 492(1), pp. 1–18. doi:10.1016/j.gene.2011.10.044.

Morgan, E.F., Giacomo, A. De and Gerstenfeld, L.C. (2014) 'Overview of fracture healing and its assesment', *Methods Mol Biol*, 1130(6), pp. 13–31. doi:10.1007/978-1-62703-989-5.

Narcisi, R., Arikan, O.H., Lehmann, J., ten Berge, D. and van Osch, G.J.V.M. (2016) 'Differential Effects of Small Molecule WNT Agonists on the Multilineage Differentiation Capacity of Human Mesenchymal Stem Cells', *Tissue Engineering Part A*, 22(21–22), pp. 1264–1273. doi:10.1089/ten.tea.2016.0081.

Narum, S.M., Le, T., Le, D.P., Lee, J.C., Donahue, N.D., Yang, W. and Wilhelm, S. (2019) *Passive targeting in nanomedicine: Fundamental concepts, body interactions, and clinical potential*, *Nanoparticles for Biomedical Applications: Fundamental Concepts, Biological Interactions and Clinical Applications*. Elsevier Inc. doi:10.1016/B978-0-12-816662-8.00004-7.

National Center for Biotechnical Information (2005) *6-Bromo-indirubin-3'oxime*, *PubChem Compound Database, CID=5287844*. Available at: https://pubchem.ncbi.nlm.nih.gov/compound/5287844 (Accessed: 7 April 2018).

National Center for Biotechnical Information (2006) *CHIR-99021*, *PubChem Compound Database, CID=9956119*. Available at: https://pubchem.ncbi.nlm.nih.gov/compound/9956119 (Accessed: 7 April 2018).

Naujok, O., Lentes, J., Diekmann, U., Davenport, C. and Lenzen, S. (2014) 'Cytotoxicity and activation of the Wnt/beta-catenin pathway in mouse embryonic stem cells treated with four GSK3 inhibitors.', *BMC research*

*notes*, 7(1), p. 273. doi:10.1186/1756-0500-7-273.

Neunaber, C., Oestern, S., Andruszkow, H., Zeckey, C., Mommsen, P., Kutter, D., Stöfen, M., Krettek, C. and Hildebrand, F. (2013) 'Cytokine productive capacity of alveolar macrophages and Kupffer cells after femoral fracture and blunt chest trauma in a murine trauma model', *Immunology Letters*, 152(2), pp. 159–166. doi:10.1016/j.imlet.2013.05.012.

Neves, V.C.M., Babb, R., Chandrasekaran, D. and Sharpe, P.T. (2017) 'Promotion of natural tooth repair by small molecule GSK3 antagonists', *Scientific Reports*, 7(39654), pp. 1–7. doi:10.1038/srep39654.

Nicolas, J., Mura, S., Brambilla, D., Mackiewicz, N. and Couvreur, P. (2013) 'Design, functionalization strategies and biomedical applications of targeted biodegradable/biocompatible polymer-based nanocarriers for drug delivery', *Chem. Soc. Rev.*, 42(3), pp. 1147–1235. doi:10.1039/C2CS35265F.

Niida, A., Hiroko, T., Kasai, M., Furukawa, Y., Nakamura, Y., Suzuki, Y., Sugano, S. and Akiyama, T. (2004) 'DKK1, a negative regulator of Wnt signaling, is a target of the β-catenin/TCF pathway', *Oncogene*, 23(52), pp. 8520–8526. doi:10.1038/sj.onc.1207892.

O'Brien, F.J. (2011) 'Biomaterials & scaffolds for tissue engineering', *Materials Today*, 14(3), pp. 88–95. doi:10.1016/S1369-7021(11)70058-X.

Oe, K., Miwa, M., Sakai, Y., Lee, S.Y., Kuroda, R. and Kurosaka, M. (2007) 'An in vitro study demonstrating that haematomas found at the site of human fractures contain progenitor cells with multilineage capacity', *Journal of Bone and Joint Surgery - Series B*, 89(1), pp. 133–138. doi:10.1302/0301-620X.89B1.18286.

Ogilvie, C., Thompson, Z., Miclau, T., Helms, J.A. and A. (2004) 'Non-Union Model', *Journal of Orthopaedic Research*, 22, pp. 1100–1107.

Ominsky, M.S., Li, C., Li, X., Tan, H.L., Lee, E., Barrero, M., Asuncion, F.J., Dwyer, D., Han, C.-Y., Vlasseros, F., Samadfam, R., Jolette, J., Smith, S.Y., Stolina, M., Lacey, D.L., Simonet, W.S., Paszty, C., Li, G. and Ke, H.Z. (2011) 'Inhibition of sclerostin by monoclonal antibody enhances bone healing and improves bone density and strength of nonfractured bones', *Journal of Bone and Mineral Research*, 26(5), pp. 1012–1021. doi:10.1002/jbmr.307.

Oreffo, R.O.C. and Triffitt, J.T. (1999) 'In vitro and in vivo methods to determine the interactions of osteogenic cells with biomaterials', *Journal of Materials Science: Materials in Medicine*, 10(10–11), pp. 607–611. doi:10.1023/a:1008931607002.

Owens, D.E. and Peppas, N.A. (2006) 'Opsonization, biodistribution, and pharmacokinetics of polymeric nanoparticles', *International Journal of Pharmaceutics*. Elsevier, pp. 93–102. doi:10.1016/j.ijpharm.2005.10.010.

Ozaki, A., Tsunoda, M., Kinoshita, S. and Saura, R. (2000) 'Role of fracture hematoma and periosteum during fracture healing in rats: Interaction of fracture hematoma and the periosteum in the initial step of the healing process', *Journal of Orthopaedic Science*, 5(1), pp. 64–70. doi:10.1007/s007760050010.

Ozaki, Y., Nishimura, M., Sekiya, K., Suehiro, F., Kanawa, M., Nikawa, H., Hamada, T. and Kato, Y. (2007) 'Comprehensive Analysis of Chemotactic Factors for Bone Marrow Mesenchymal Stem Cells', *Stem Cells and Development*, 16(1), pp. 119–130. doi:10.1089/scd.2006.0032.

Özcan, I., Bouchemal, K., Segura-Sánchez, F., Özer, Ö., Güneri, T. and Ponchel, G. (2011) 'Synthesis and Characterization of Surface-Modified PBLG Nanoparticles for Bone Targeting: In vitroand InVivoEvaluations', *Journal of pharmaceutical sciences*, 100(11), pp. 4877–4887. doi:10.1002/jps.

Pan, J.X., Xiong, L., Zhao, K., Zeng, P., Wang, B., Tang, F.L., Sun, D., Guo, H.H., Yang, X., Cui, S., Xia, W.F., Mei, L. and Xiong, W.C. (2018) 'YAP promotes osteogenesis and suppresses adipogenic differentiation by regulating β-catenin signaling', *Bone Research*, 6(1). doi:10.1038/s41413-018-0018-7.

Papini, E., Tavano, R. and Mancin, F. (2020) 'Opsonins and Dysopsonins of Nanoparticles: Facts, Concepts, and Methodological Guidelines', *Frontiers in Immunology*, 11(567365), pp. 1–19. doi:10.3389/fimmu.2020.567365.

Park, J.E. and Barbul, A. (2004) 'Understanding the role of immune regulation in wound healing', *American Journal of Surgery*, 187, pp. 11S-16S. doi:10.1016/S0002-9610(03)00296-4.

Park, S.-H., Silva, M., Bahk, W.-J., McKellop, H. and Lieberman, J.R. (2002) 'Effect of repeated irrigation and

debridement on fracture healing in an animal model', *Indian Journal of Animal Sciences*, 20, pp. 1197–1204.

Patil, S. and Montgomery, R. (2006) 'Management of complex tibial and femoral nonunion using the Ilizarov technique, and its cost implications', *The Journal of Bone and Joint Surgery. British volume*, 88-B(7), pp. 928–932. doi:10.1302/0301-620X.88B7.17639.

Peichl, P., Holzer, L., Maier, R. and Holzer, R. (2011) 'PTH accelerates pelvic fracture healing in elderly, osteoporotic women.', *J Bone Joint Surg Am*, 93, pp. 1583–1587. doi:10.1038/bonekey.2012.10.

Pfaffl, M.W. (2001) 'A new mathematical model for relative quantification in real-time RT-PCR', *Nucleic Acids Research*, 29(9), pp. 2002–2007. doi:10.1093/nar/29.9.e45.

Porges, E. (2021) *Nanoparticle-based antibiotic delivery for the treatment of intracellular bacterial infections*. University of Southampton.

Porter, C.J.H., Moghimi, S.M., Illum, L. and Davis, S.S. (1992) 'The polyoxyethylene/polyoxypropylene block co-polymer Poloxamer-407 selectively redirects intravenously injected microspheres to sinusoidal endothelial cells of rabbit bone marrow', *FEBS Letters*, 305(1), pp. 62–66. doi:10.1016/0014-5793(92)80655-Z.

Pountos, I., Walters, G., Panteli, M., Einhorn, T.A. and Giannoudis, P. V. (2019) 'Inflammatory Profile and Osteogenic Potential of Fracture Haematoma in Humans', *Journal of Clinical Medicine*, 9(1), p. 47. doi:10.3390/jcm9010047.

Prosser, I., Lawson, Z., Evans, A., Harrison, S., Morris, S., Maguire, S. and Kemp, A.M. (2012) 'A timetable for the radiologic features of fracture healing in young children', *American Journal of Roentgenology*, 198(5), pp. 1014–1020. doi:10.2214/AJR.11.6734.

Raggatt, L.J., Wullschleger, M.E., Alexander, K.A., Wu, A.C.K., Millard, S.M., Kaur, S., Maugham, M.L., Gregory, L.S., Steck, R. and Pettit, A.R. (2014) 'Fracture healing via periosteal callus formation requires macrophages for both initiation and progression of early endochondral ossification', *American Journal of Pathology*, 184(12), pp. 3192–3204. doi:10.1016/j.ajpath.2014.08.017.

Ralis, Z.A. and Watkins, G. (1992) 'Modified tetrachrome method for osteoid and defectively mineralized bone in paraffin sections', *Biotechnic and Histochemistry*, 67(6), pp. 339–345. doi:10.3109/10520299209110046.

Ramakrishnan, A.-B. and Cadigan, K.M. (2017) 'Wnt target genes and where to find them', *F1000Research*, 6(746), pp. 1–11. doi:10.12688/f1000research.11034.1.

Ransom, R.C., Hunter, D.J., Hyman, S., Singh, G., Ransom, S.C., Shen, E.Z., Perez, K.C., Gillette, M., Li, J., Liu, B., Brunski, J.B. and Helms, J.A. (2016) 'Axin2-expressing cells execute regeneration after skeletal injury', *Scientific Reports*, 6, pp. 1–11. doi:10.1038/srep36524.

Reddi, A.H. and Huggins, C. (1972) 'Biochemical Sequences in the Transformation of Normal Fibroblasts in Adolescent Rats', *Proceedings of the National Academy of Sciences*, 69(6), pp. 1601–1605.

Reismann, D., Stefanowski, J., Günther, R., Rakhymzhan, A., Matthys, R., Nützi, R., Zehentmeier, S., Schmidt-Bleek, K., Petkau, G., Chang, H.D., Naundorf, S., Winter, Y., Melchers, F., Duda, G.N., Hauser, A.E. and Niesner, R.A. (2017) 'Longitudinal intravital imaging of the femoral bone marrow reveals plasticity within marrow vasculature', *Nature Communications*, 8(1). doi:10.1038/s41467-017-01538-9.

Richards, J., Rivadeneira, F., Inouye, M., Pastinen, T., Soranzo, N., Wilson, S., Andrew, T., Falchi, M., Gwilliam, R., Ahmadi, K., Valdes, A., Arp, P., Whittaker, P., Verlaan, D., Jhamai, M., Kumanduri, V., Moorhouse, M., van Meurs, J., Hofman, A., *et al.* (2008) 'Bone mineral density, osteoporosis, and osteoporotic fractures: a genome-wide association study', *The Lancet*, 371(9623), pp. 1505–1512. doi:10.1016/S0140-6736(08)60599-1.

Ring, D.B., Johnson, K.W., Henriksen, E.J., Nuss, J.M., Goff, D., Kinnick, T.R., Ma, S.T., Reeder, J.W., Samuels, I., Slabiak, T., Wagman, A.S., Hammond, M.E.W. and Harrison, S.D. (2003) 'Selective glycogen synthase kinase 3 inhibitors potentiate insulin activation of glucose transport and utilization in vitro and in vivo', *Diabetes*, 52(3), pp. 588–595. doi:10.2337/diabetes.52.3.588.

Riss, T.L., Moravec, R.A., Niles, A.L., Duellman, S., Benink, H.A., Worzella, T.J. and Minor, L. (2013) 'Cell Viability Assays', *Assay Guidance Manual [Internet]*, 114(8), pp. 785–796. doi:10.1016/j.acthis.2012.01.006.

Rizzello, L., Robertson, J.D., Elks, P.M., Poma, A., Daneshpour, N., Prajsnar, T.K., Evangelopoulos, D., Canseco, J.O., Yona, S., Marriott, H.M., Dockrell, D.H., Foster, S., Geest, B. De, Koker, S. De, McHugh, T., Renshaw, S.A.

and Battaglia, G. (2017) 'Polymersomes Targeting Mononuclear Phagocytes', *bioRxiv*, p. 119297. doi:10.1101/119297.

Rodda, S.J. (2006) 'Distinct roles for Hedgehog and canonical Wnt signaling in specification, differentiation and maintenance of osteoblast progenitors', *Development*, 133(16), pp. 3231–3244. doi:10.1242/dev.02480.

van Rooijen, N. and Hendrikx, E. (2010) 'Liposomes for specific depletion of macrophages from organs and tissues.', *Methods in molecular biology (Clifton, N.J.)*, 605, pp. 189–203. doi:10.1007/978-1-60327-360-2_13.

Van Rooijen, N. and Van Kesteren-Hendrikx, E. (2002) 'Clodronate liposomes: Perspectives in research and therapeutics', *Journal of Liposome Research*, 12(1–2), pp. 81–94. doi:10.1081/LPR-120004780.

Rundle, C.H., Wang, H., Yu, H., Chadwick, R.B., Davis, E.I., Wergedal, J.E., Lau, K.H.W., Mohan, S., Ryaby, J.T. and Baylink, D.J. (2006) 'Microarray analysis of gene expression during the inflammation and endochondral bone formation stages of rat femur fracture repair', *Bone*, 38(4), pp. 521–529. doi:10.1016/j.bone.2005.09.015.

Saag, K.G., Petersen, J., Brandi, M.L., Karaplis, A.C., Lorentzon, M., Thomas, T., Maddox, J., Fan, M., Meisner, P.D., Grauer, A. and Abstract (2017) 'Romosozumab or Alendronate for Fracture Prevention in Women with Osteoporosis', *The New England Journal of Medicine*, 377(15), pp. 1417–1427. doi:10.1056/NEJMoa1708322.

Sarin, H. (2010) 'Physiologic upper limits of pore size of different blood capillary types and another perspective on the dual pore theory of microvascular permeability', *Journal of Angiogenesis Research*, 2(14), pp. 1–19.

Sato, N., Meijer, L., Skaltsounis, L., Greengard, P. and Brivanlou, A.H. (2004) 'Maintenance of pluripotency in human and mouse embryonic stem cells through activation of Wnt signaling by a pharmacological GSK-3-specific inhibitor', *Nature Medicine*, 10(1), pp. 55–63. doi:10.1038/nm979.

Scarpa, E. (2016) *Thesis - Polymeric nanoparticles loaded with a Wnt agonist for enhancing bone fracture healing.* University of Southampton. doi:10.1016/0041-2678(70)90288-5.

Scarpa, E., Bailey, J.L., Janeczek, A.A., Stumpf, P.S., Johnston, A.H., Oreffo, R.O.C., Woo, Y.L., Cheong, Y.C., Evans, N.D. and Newman, T.A. (2016) 'Quantification of intracellular payload release from polymersome nanoparticles', *Scientific Reports*, 6, pp. 1–13.

Scarpa, E., Janeczek, A.A., Hailes, A., de Andrés, M.C., De Grazia, A., Oreffo, R.O.C., Newman, T.A. and Evans, N.D. (2018) 'Polymersome nanoparticles for delivery of Wnt-activating small molecules', *Nanomedicine: Nanotechnology, Biology and Medicine*, 14(4), pp. 1267–1277. doi:10.1016/j.nano.2018.02.014.

Schädlich, A., Rose, C., Kuntsche, J., Caysa, H., Mueller, T., Göpferich, A. and Mäder, K. (2011) 'How stealthy are PEG-PLA nanoparticles? An NIR in vivo study combined with detailed size measurements', *Pharmaceutical Research*, 28(8), pp. 1995–2007. doi:10.1007/s11095-011-0426-5.

Schell, H., Duda, G.N., Peters, A., Tsitsilonis, S., Johnson, K.A., Schmidt-bleek, K. and Schmidt-bleek, K. (2017) 'The haematoma and its role in bone healing', *Journal of Experimental Orthopedics*, 4(4), pp. 1–11. doi:10.1186/s40634-017-0079-3.

Schemitsch, E.H., Miclau, T., Karachalios, T., Nowak, L.L., Sancheti, P., Poolman, R.W., Caminis, J., Daizadeh, N., Dent-Acosta, R.E., Egbuna, O., Chines, A., Maddox, J., Grauer, A. and Bhandari, M. (2020) 'Romosozumab for the Treatment of Hip Fractures', *The Journal of bone and joint surgery. British volume*, 102, pp. 693–702.

Schindeler, A., McDonald, M.M., Bokko, P. and Little, D.G. (2008) 'Bone remodeling during fracture repair: The cellular picture', *Seminars in Cell and Developmental Biology*, 19(5), pp. 459–466. doi:10.1016/j.semcdb.2008.07.004.

Schirmer, W.J., Schirmer, J.M., Townsend, M.C. and Fry, D.E. (1988) 'Femur Fracture With Associated Soft-Tissue Injury Produces Hepatic Ischemia Possible Cause of Hepatic', *Arch Surg*, 123, pp. 412–415.

Schlundt, C., El Khassawna, T., Serra, A., Dienelt, A., Wendler, S., Schell, H., van Rooijen, N., Radbruch, A., Lucius, R., Hartmann, S., Duda, G.N. and Schmidt-Bleek, K. (2018) 'Macrophages in bone fracture healing: Their essential role in endochondral ossification', *Bone*, 106, pp. 78–89. doi:10.1016/j.bone.2015.10.019.

Schmidt-Bleek, K., Schell, H., Kolar, P., Pfaff, M., Perka, C., Buttgereit, F., Duda, G.N. and Lienau, J. (2009) 'Cellular composition of the initial fracture hematoma compared to a muscle hematoma: A study in sheep', *Journal of Orthopaedic Research*, 27(9), pp. 1147–1151. doi:10.1002/jor.20901.

Schmidt-Bleek, K., Schell, H., Lienau, J., Schulz, N., Hoff, P., Pfaff, M., Schmidt, G., Martin, C., Perka, C.,

Buttgereit, F., Volk, H.-D. and Duda, G.N. (2014) 'Initial immune reaction and angiogenesis in bone healing', *Journal of Tissue Engineering and Regenerative Medicine*, 8(2), pp. 120–130. doi:10.1002/term.1505.

Schmidt-Bleek, K., Willie, B.M., Schwabe, P., Seemann, P. and Duda, G.N. (2016) 'BMPs in bone regeneration: Less is more effective, a paradigm-shift', *Cytokine and Growth Factor Reviews*, 27, pp. 141–148. doi:10.1016/j.cytogfr.2015.11.006.

Selye, H. (1932) 'On the stimulation of new bone-formation with parathyroid extract and irradiated ergosterol', *Endocrinology*, 16(5), pp. 547–558. doi:10.1210/endo-16-5-547.

Sfeir, C., Ho, L., Doll, B.A., Azari, K. and Hollinger, J.O. (2005) 'Fracture Repair', *Bone Regeneration and Repair: Biology and Clinical Applications*, (11), pp. 21–44. doi:10.1385/1-59259-863-3:021.

Shapiro, F. (2008) 'Bone development and its relation to fracture repair. The roleof mesenchymal osteoblasts and surface osteoblasts', *European Cells and Materials*, 15, pp. 53–76. doi:vol015a05 [pii].

Shi, C., Yuan, Z., Han, F., Zhu, C. and Li, B. (2016) 'Polymeric biomaterials for bone regeneration', *Annals of Joint*, 1(27), pp. 1–14. doi:10.21037/aoj.2016.11.02.

Shuai, X., Ai, H., Nasongkla, N., Kim, S. and Gao, J. (2004) 'Micellar carriers based on block copolymers of poly(ε-caprolactone) and poly(ethylene glycol) for doxorubicin delivery', *Journal of Controlled Release*, 98(3), pp. 415–426. doi:10.1016/j.jconrel.2004.06.003.

Shuai, X., Merdan, T., Schaper, A.K., Xi, F. and Kissel, T. (2004) 'Core-cross-linked polymeric micelles as paclitaxel carriers', *Bioconjugate Chemistry*, 15(3), pp. 441–448. doi:10.1021/bc034113u.

Siddiqui, M.R., Alothman, Z.A. and Rahman, N. (2017) 'Analytical techniques in pharmaceutical analysis: A review', *Arabian Journal of Chemisty*, 10, pp. S1409–S1421. doi:10.1016/j.arabjc.2013.04.016.

Sinha, V.R., Bansal, K., Kaushik, R., Kumria, R. and Trehan, A. (2004) 'Poly-ε-caprolactone microspheres and nanospheres: An overview', *International Journal of Pharmaceutics*, 278(1), pp. 1–23. doi:10.1016/j.ijpharm.2004.01.044.

Sisask, G., Marsell, R., Sundgren-Andersson, A., Larsson, S., Nilsson, O., Ljunggren, Ö. and Jonsson, K.B. (2013) 'Rats treated with AZD2858, a GSK3 inhibitor, heal fractures rapidly without endochondral bone formation', *Bone*, 54(1), pp. 126–132. doi:10.1016/j.bone.2013.01.019.

Street, J., Winter, D., Wang, J.H., Wakai, A., McGuinness, A. and Redmond, H.P. (2000) 'Is human fracture hematoma inherently angiogenic?', *Clinical Orthopaedics and Related Research*, (378), pp. 224–237. doi:10.1097/00003086-200009000-00033.

Stroncek, J.D. and Reichert, W.M. (2007) 'Overview of wound healing in different tissue types', in *Indwelling Neural Implants: Strategies for Contending with the in Vivo Environment*. CRC Press, pp. 3–38. doi:10.1201/9781420009309.pt1.

Suen, W.L.L. and Chau, Y. (2013) 'Specific uptake of folate-decorated triamcinolone-encapsulating nanoparticles by retinal pigment epithelium cells enhances and prolongs antiangiogenic activity', *Journal of Controlled Release*, 167(1), pp. 21–28. doi:10.1016/j.jconrel.2013.01.004.

Sun, X., Cheng, C., Zhang, J., Jin, X., Sun, S., Mei, L. and Huang, L. (2019) 'Intracellular Trafficking Network and Autophagy of PHBHHx Nanoparticles and their Implications for Drug Delivery', *Scientific Reports*, 9(1), pp. 1–10. doi:10.1038/s41598-019-45632-y.

Swami, A., Reagan, M.R., Basto, P., Mishima, Y., Kamaly, N., Glavey, S., Zhang, S., Moschetta, M., Seevaratnam, D., Zhang, Y., Liu, J., Memarzadeh, M., Wu, J., Manier, S., Shi, J., Bertrand, N., Lu, Z.N., Nagano, K., Baron, R., *et al.* (2014) 'Engineered nanomedicine for myeloma and bone microenvironment targeting.', *Proceedings of the National Academy of Sciences of the United States of America*, 111(28), pp. 10287–92. doi:10.1073/pnas.1401337111.

Takahashi, N., Udagawa, N. and Suda, T. (1999) 'A new member of tumor necrosis factor ligand family, ODF/OPGL/TRANCE/RANKL, regulates osteoclast differentiation and function', *Biochemical and Biophysical Research Communications*, 256(3), pp. 449–455. doi:10.1006/bbrc.1999.0252.

Tan, J.K., Mohamad Hazir, N.S. and Alias, E. (2021) 'Impacts of hypoxia on osteoclast formation and activity: Systematic review', *International Journal of Molecular Sciences*, 22(18). doi:10.3390/ijms221810146.

Tang, Q.Q. and Daniel Lane, M. (2012) 'Adipogenesis: From Stem Cell to Adipocyte Keywords'. doi:10.1146/annurev-biochem-052110-115718.

Taormina, D.P., Shulman, B.S., Karia, R., Spitzer, A.B., Konda, S.R. and Egol, K.A. (2014) 'Older Age Does Not Affect Healing Time and Functional Outcomes After Fracture Nonunion Surgery', *Geriatric Orthopaedic Surgery & Rehabilitation*, 5(5), pp. 116–121. doi:10.1177/2151458514532811.

Tare, R.S., Mitchell, P.D., Kanczler, J. and Oreffo, R.O.C. (2012) 'Isolation, differentiation, and characterisation of skeletal stem cells from human bone marrow in vitro and in vivo', *Methods in Molecular Biology*, 816, pp. 83–99. doi:10.1007/978-1-61779-415-5_7.

Tavares, A.J., Poon, W., Zhang, Y.-N., Dai, Q., Besla, R., Ding, D., Ouyang, B., Li, A., Chen, J., Zheng, G., Robbins, C. and Chan, W.C.W. (2017) 'Effect of removing Kupffer cells on nanoparticle tumor delivery', *Proceedings of the National Academy of Sciences*, pp. E10871–E10880. doi:10.1073/pnas.1713390114.

Thang, D.C., Wang, Z., Lu, X. and Xing, B. (2019) 'Precise cell behaviors manipulation through light-responsive nano-regulators: Recent advance and perspective', *Theranostics*. Ivyspring International Publisher, pp. 3308–3340. doi:10.7150/thno.33888.

Thurairajah, K., Broadhead, M. and Balogh, Z. (2017) 'Trauma and Stem Cells: Biology and Potential Therapeutic Implications', *International Journal of Molecular Sciences*, 18(3), p. 577. doi:10.3390/ijms18030577.

Tomlinson, R.E., Shoghi, K.I. and Silva, M.J. (2014) 'Nitric oxide-mediated vasodilation increases blood flow during the early stages of stress fracture healing', *J Appl Physiol*, 116, pp. 416–424. doi:10.1152/japplphysiol.00957.2013.-Despite.

Tomlinson, R.E. and Silva, M.J. (2013) 'Skeletal Blood Flow in Bone Repair and Maintenance', *Bone Research*. Sichuan University, pp. 311–322. doi:10.4248/BR201304002.

Torchilin, V.P. (2007) 'Micellar nanocarriers: Pharmaceutical perspectives', *Pharmaceutical Research*, 24(1), pp. 1–16. doi:10.1007/s11095-006-9132-0.

Tsuji, K., Bandyopadhyay, A., Harfe, B.D., Cox, K., Kakar, S., Gerstenfeld, L.C., Einhorn, T.A., Tabin, C.J. and Rosen, V.M. (2006) 'BMP2 activity, although dispensable for bone formation, is required for the initiation of fracture healing', *Nature Genetics*, 38(12), pp. 1424–1429. doi:10.1038/ng1916.

Tsunoda, M., Mizuno, K. and Matsubara, T. (1993) 'The osteogenic potential of fracture hematoma and its mechanism on bone formation--through fracture hematoma culture and transplantation of freeze-dried hematoma.', *The Kobe journal of medical sciences*, 39(1), pp. 35–50.

Urist, M.R., Huo, Y.K., Brownell, A.G., Hohl, W.M., Buyske, J., Lietze, A., Tempst, P., Hunkapiller, M. and DeLange, R.J. (1984) 'Purification of bovine bone morphogenetic protein by hydroxyapatite chromatography.', *Proceedings of the National Academy of Sciences of the United States of America*, 81(2), pp. 371–5. doi:10.1073/PNAS.81.2.371.

Urist, M.R. and Strates, B.S. (1971) 'Bone Morphogenetic Protein', *Journal of Dental Research*, 50(6), pp. 1392–1406. doi:10.1177/00220345710500060601.

De Vries, T.J., Schoenmaker, T., Aerts, D., Grevers, L.C., Souza, P.P.C., Nazmi, K., Van De Wiel, M.A., Ylstra, B., Van Lent, P.L., Leenen, P.J.M. and Everts, V. (2015) 'M-CSF priming of osteoclast precursors can cause osteoclastogenesis-insensitivity, which can be prevented and overcome on bone', *Journal of Cellular Physiology*, 230(1), pp. 210–225. doi:10.1002/jcp.24702.

Wagner, F.F., Bishop, J.A., Gale, J.P., Shi, X., Walk, M., Ketterman, J., Patnaik, D., Barker, D., Walpita, D., Campbell, A.J., Nguyen, S., Lewis, M., Ross, L., Weïwer, M., An, W.F., Germain, A.R., Nag, P.P., Metkar, S., Kaya, T., *et al.* (2016) 'Inhibitors of Glycogen Synthase Kinase 3 with Exquisite Kinome-Wide Selectivity and Their Functional Effects', *ACS Chemical Biology*, 11(7), pp. 1952–1963. doi:10.1021/acschembio.6b00306.

Wang, B., Zhao, L., Fish, M., Logan, C.Y. and Nusse, R. (2015) 'Self-renewing diploid Axin2 + cells fuel homeostatic renewal of the liver', *Nature*, 524(7564), pp. 180–185. doi:10.1038/nature14863.

Wang, Q., Jiang, J., Chen, W., Jiang, H., Zhang, Z. and Sun, X. (2016) 'Targeted delivery of low-dose dexamethasone using PCL-PEG micelles for effective treatment of rheumatoid arthritis', *Journal of Controlled Release*, 230, pp. 64–72. doi:10.1016/j.jconrel.2016.03.035.

Wang, X., Yu, Y.Y., Lieu, S., Yang, F., Lang, J., Lu, C., Werb, Z., Hu, D., Miclau, T., Marcucio, R. and Colnot, C. (2013) 'MMP9 regulates the cellular response to inflammation after skeletal injury', *Bone*, 52(1), pp. 111–119. doi:10.1016/j.bone.2012.09.018.

Wang, Y., Newman, M.R., Ackun-Farmmer, M., Baranello, M.P., Sheu, T.-J., Puzas, J.E. and Benoit, D.S.W. (2017) 'Fracture-Targeted Delivery of -Catenin Agonists via Peptide- β Functionalized Nanoparticles Augments Fracture Healing', *ACS Nano*, 11(9), pp. 9445–9458. doi:10.5588/ijtld.16.0716.Isoniazid.

Westgeest, J., Weber, D., Dulai, S., Bergman, J., Buckley, R. and Beaupre, L. (2016) 'Factors Associated With Development of Nonunion or Delayed Healing After an Open Long Bone Fracture: A Prospective Cohort Study of 736 Subjects.', *Journal of orthopaedic trauma*, 30(3), pp. 149–55. doi:10.1017/CBO9781107415324.004.

White, L.J., Kirby, G.T.S., Cox, H.C., Qodratnama, R., Qutachi, O., Rose, F.R.A.J. and Shakesheff, K.M. (2013) 'Accelerating protein release from microparticles for regenerative medicine applications', *Materials Science and Engineering C*, 33(5), pp. 2578–2583. doi:10.1016/j.msec.2013.02.020.

Williams, E.L., White, K. and Oreffo, R.O.C. (2013) 'Isolation and Enrichment of Stro-1 Immunoselected Mesenchymal Stem Cells from Adult Human Bone Marrow', *Stem Cell Niche*, 1035, pp. 67–73. doi:10.1007/978-1-62703-508-8.

*World Population Prospects - Population Division - United Nations* (no date). Available at: https://population.un.org/wpp/ (Accessed: 15 April 2020).

Wu, A.C., Kidd, L.J., Cowling, N.R., Kelly, W.L. and Forwood, M.R. (2014) 'Osteocyte expression of caspase-3, COX-2, IL-6 and sclerostin are spatially and temporally associated following stress fracture initiation', *BoneKEy Reports*, 3, p. 571. doi:10.1038/BONEKEY.2014.66.

Wu, A.C., Raggatt, L.J., Alexander, K.A. and Pettit, A.R. (2013) 'Unraveling macrophage contributions to bone repair', *BoneKEy Reports*, 2(March), pp. 1–7. doi:10.1038/bonekey.2013.107.

Wu, Y., Liu, F., Liu, Y., Liu, X., Ai, Z., Guo, Z. and Zhang, Y. (2015) 'GSK3 inhibitors CHIR99021 and 6-bromoindirubin-3'-oxime inhibit microRNA maturation in mouse embryonic stem cells.', *Scientific reports*, 5, p. 8666. doi:10.1038/srep08666.

Xin, H., Jiang, X., Gu, J., Sha, X., Chen, L., Law, K., Chen, Y., Wang, X., Jiang, Y. and Fang, X. (2011) 'Angiopep-conjugated poly(ethylene glycol)-co-poly(ε-caprolactone) nanoparticles as dual-targeting drug delivery system for brain glioma', *Biomaterials*, 32(18), pp. 4293–4305. doi:10.1016/j.biomaterials.2011.02.044.

Xing, Z., Lu, C., Hu, D., Yu, Y.Y., Wang, X., Colnot, C., Nakamura, M.C., Wu, Y., Miclau, T. and Marcucio, R.S. (2010) 'Multiple roles for CCR2 during fracture healing', *DMM Disease Models and Mechanisms*, 3(7–8), pp. 451–458. doi:10.1242/dmm.003186.

Yewle, J., Wattamwar, P., Tao, Z., Ostertag, E.M. and Ghoroghchian, P.P. (2016) 'Progressive Saturation Improves the Encapsulation of Functional Proteins in Nanoscale Polymer Vesicles', *Pharmaceutical Research*, 33(3), pp. 573–589. doi:10.1007/s11095-015-1809-9.

Yu, Y.Y., Lieu, S., Lu, C., Miclau, T., Marcucio, R.S. and Colnot, C. (2010) 'Immunolocalization of BMPs, BMP antagonists, receptors, and effectors during fracture repair', *Bone*, 46(3), pp. 841–851. doi:10.1016/J.BONE.2009.11.005.

Yuasa, M., Mignemi, N.A., Nyman, J.S., Duvall, C.L., Schwartz, H.S., Okawa, A., Yoshii, T., Bhattacharjee, G., Zhao, C., Bible, J.E., Obremskey, W.T., Flick, M.J., Degen, J.L., Barnett, J. V., Cates, J.M.M. and Schoenecker, J.G. (2015) 'Fibrinolysis is essential for fracture repair and prevention of heterotopic ossification', *The Journal of Clinical Investigation*, 125(8), pp. 3117–3131. doi:10.1172/JCI80313.

Zhai, Y., Iura, A., Yeasmin, S., Wiese, A., Wu, R., Feng, Y., Fearon, E. and Cho, K. (2011) 'MSX2 is an oncogenic downstream target of activated WNT signaling in ovarian endometrioid adenocarcinoma', *Oncogene*, 30, pp. 4152–4162. doi:10.1038/onc.2011.123.

Zhang, L., Gu, F.X., Chan, J.M., Wang, A.Z., Langer, R.S. and Farokhzad, O.C. (2008) 'Nanoparticles in Medicine: Therapeutic Applications and Developments', *Clinical Pharmacology & Therapeutics2*, 83(5), pp. 761–769. doi:10.1038/sj.clp.

Zhang, L., Radovic-Moreno, A.F., Alexis, F., Gu, F.X., Basto, P.A., Bagalkot, V., Jon, S., Langer, R.S. and Farokhzad, O.C. (2007) 'Co-delivery of hydrophobic and hydrophilic drugsfrom nanoparticle-aptamer bioconjugates',

*ChemMedChem*, 2(9), pp. 1268–1271. doi:10.1002/cmdc.200700121.

Zhang, Y.-N., Poon, W., Tavares, A.J., McGilvray, I.D. and Chan, W.C.W. (2016) 'Nanoparticle–liver interactions: Cellular uptake and hepatobiliary elimination', *Journal of Controlled Release*, 240, pp. 332–348. doi:10.1016/j.jconrel.2016.01.020.

Zhong, N., Gersch, R.P. and Hadjiargyrou, M. (2006) 'Wnt signaling activation during bone regeneration and the role of Dishevelled in chondrocyte proliferation and differentiation', *Bone*, 39(1), pp. 5–16. doi:10.1016/j.bone.2005.12.008.

Zou, L., Zou, X., Li, H., Mygind, T., Zeng, Y., Lü, N. and Bünger, C. (2006) 'Molecular mechanism of osteochondroprogenitor fate determination during bone formation', *Advances in Experimental Medicine and Biology*, 585, pp. 431–441. doi:10.1007/978-0-387-34133-0_28.

Zuckerman, J.E., Gritli, I., Tolcher, A., Heidel, J.D., Lim, D., Morgan, R., Chmielowski, B., Ribas, A., Davis, M.E. and Yen, Y. (2014) 'Correlating animal and human phase Ia/Ib clinical data with CALAA-01, a targeted, polymer-based nanoparticle containing siRNA', *Proceedings of the National Academy of Sciences*, 111(31), pp. 11449–11454. doi:10.1073/pnas.1411393111.

Zura, R., Xiong, Z., Einhorn, T.A., Watson, J.T., Ostrum, R.F., Prayson, M.J., Della Rocca, G.J., Mehta, S., McKinley, T., Wang, Z. and Steen, R.G. (2016) 'Epidemiology of Fracture Nonunion in 18 Human Bones', *JAMA surgery*, 151(11). doi:10.1001/JAMASURG.2016.2775.

# SUPPLEMENTARY MATERIAL

## S.1 MATERIALS USED IN METHODS

### S.1.1 REAGENTS

| Item | Supplier |
|---|---|
| alamarBlue™ | Invitrogen Thermo Fisher |
| ABC kit (Vectastain® Elite ABC kits peroxidase) | Vector Laboratories, USA |
| Agarose | Sigma Aldrich |
| α-MEM | Lonza |
| BIO | Sigma Aldrich |
| Biotinylated rabbit anti-rat IgG secondary antibody | Vector Laboratories, USA |
| Buprenorphine | Sigma Aldrich |
| CHIR-99021 | Sigma Aldrich |
| Clodronate & PBS Liposomes (CP-005-005) | Liposoma, Amsterdam |
| Collagenase II | Fisher Scientific |
| DAB (3,3'-Diaminobenzidine tetrahydrochloride hydrate 97%) | Acros Organics, USA |
| DAPI | Sigma Aldrich |
| DiR (XenoLight) | Perkin Elmer |
| DiI | Thermo Fisher |
| DMF (N,N-Dimethylformamide) | Sigma Aldrich |
| DMEM | Lonza |
| DPX | Sigma Aldrich |
| DNA ladder – exACTGene 50bp mini-DNA ladder 25bp-650bp | Fisher Scientific |
| EDTA | Sigma Aldrich |
| Ethanol | Fisher Chemicals |
| FBS (Fetal Bovine Serum) | Gibco |
| F4/80 Rat anti-mouse | Invitrogen eBiosciences. 14-4801-85 |
| GelRed nucleic acid stain | Biotium |
| GoTaq (SYBR Green) | Promega UK |
| 25 mM HEPES | Fisher Scientific |
| Histoclear | National Diagnostics |

| | |
|---|---|
| Hypnorm and Hypnovel | Janssen |
| Hydromount™ | National Diagnostics |
| ISOLATE II RNA mini kit | Bioline UK |
| Lamdba DNA Standard | Thermo Fisher |
| Loading dye blue/orange | Promega |
| LymphoprepTM Density Gradient Medium | Stem Cell Technologies UK |
| Lysis Buffer RLY | Bioline UK |
| Neolite | Perkin Elmer |
| OCT – Cellpath embedding matrix | Fisher Scientific |
| Paraffin | Sigma Aldrich |
| PBS Tablets | Oxoid |
| PBS 10x Stock | Fisher Bioreagents |
| PEG(5k)-b-PCL(18k) Polymer | Polymer Source Inc |
| Penicillin Streptomycin | PAA |
| PFA (Paraformaldehyde) | Thermofisher |
| Pico Green | Invitrogen Life Technologies |
| Primers | Sigma Aldrich |
| Propan-2-ol | Fisher Scientific |
| Sodium bicarbonate | Sigma Aldrich |
| Steady Glo | Promega |
| Sucrose | Sigma Aldrich |
| TaqMan Reverse Transcription | Applied biosystems |
| Triton™ X-100 (T9284) | Sigma Aldrich |
| Trypsin | Lonza |
| Trypan Blue | Sigma Aldrich |
| Virkon Tablets | DuPoint |
| Xylene | Thermofisher |

### S.1.2 EQUIPMENT

| Item | Supplier |
|---|---|
| Aladdin syringe pump | World precision instruments, Sarasota, Florida |
| Centrifuge Megafuge 1.0R | Heraeus |
| Centrifuge 5415R | Eppendorf |
| Coverslip (0.13-0.17 mm thickness) | Academy |
| Cryotome Microm H500 Cryostat | Thermo Fisher |
| Dialysis Tubing (10,000 MWCO) | Sigma Aldrich |
| Dremel Drill | Dremel |
| GloMax Discover | Promega |
| Incubator | Thermo Scientific |
| InGenius transilluminator | Syngene UK |
| IVIS Lumina Series III | Perkin Elmer USA |
| Microfilter 0.22 µm | Minisart |
| Microscope | Zeiss Axioplan 2 & Zeiss Axiovert |
| Microscope | Nikon E400 |
| Microtome HM355-S | Microm International GmbH, Germany |
| Nanodrop 200c | Thermo Fisher Scientific, UK |
| RT-PCR system 7500 | Applied Biosystems |
| Veriti PCR thermal cycle | Applied Biosystems |
| Zetasizer Nano ZS ZEN3600 | Malvern UK |
| Zetasizer Ultra | Malvern UK |

### S.1.3 DETAILED PROTOCOLS

**Hematoxylin and Eosin**

| Solution | Time (Minutes) | Solution Recipe |
|---|---|---|
| Histo-Clear | 7 | |
| Histo-Clear | 7 | |
| 100% Ethanol (EtOH) | 2 | |
| 100% EtOH | 2 | |
| 90% (v/v) EtOH in water | 2 | |
| 50% (v/v) EtOH in water | 2 | |
| $H_2O$ | 2 | |
| Hematoxylin Wiegerts Solution A+B (1:1) | 8 | Wiegert's hematoxylin A = 1% (w/v) hematoxylin in EtOH<br>Wiegert's hematoxylin B = 6 g Ferric Chloride and 5 mL hydrochloric acid (HCL) dissolved in 500 mL $H_2O$. |
| $H_20$ | 2 | |
| 1% (v/v) Acid Alcohol | 15 Seconds | 20 mL HCL in 2 L of 50% Methanol |
| $H_20$ | 3 | |
| Eosin Y | 12 | 3 g of eosin Y dissolved in 200 µL of acetic acid and 300 mL $H_2O$. Filtered. |
| $H_20$ | 3 | |
| 50 % EtOH | 1 | |
| 90% EtOH | 1 | |
| 100% EtOH | 1 | |
| 100% EtOH | 1 | |
| Histo-Clear | 1 | |
| Histo-Clear | 1 | |
| Mount in DPX | | |

## Goldner's Trichrome

| Solution | Time (Minutes) | Solution Recipe |
|---|---|---|
| Histo-Clear | 7 | |
| Histo-Clear | 7 | |
| 100% EtOH | 2 | |
| 100% EtOH | 2 | |
| 90% EtOH | 2 | |
| 50% EtOH | 2 | |
| $H_20$ | 2 | |
| Hematoxylin Wiegerts Solution A+B (1:1) | 8 | Wiegert's hematoxylin A = 1% (w/v) hematoxylin in EtOH<br>Wiegert's hematoxylin B = 6 g Ferric Chloride and 5 mL hydrochloric acid (HCL) dissolved in 500 mL $H_2O$. |
| $H_20$ | 5 | |
| 1% (v/v) Acid Alcohol | 15 Seconds | 20 mL HCL in 2 L of 50% Methanol |
| $H_20$ | 5 | |
| Final Ponceau-fuchsin-azophloxin Solution | 5 | Ponceau-fuchsin = 0.38 g Ponceau de xylidine and 0.13 g Acid fuchin, dissolved in 0.5 mL Acetic acid and 50 mL d.$H_2O$<br>Azophloxin = 0.25 g Azophloxin dissolved in 0.3 mL acetic acid and 50 mL d.$H_2O$<br>Final Solution = 2 mL Ponceau-fuchin solution and 0.4 mL Azophloxin in 17.6 mL of 0.2% (v/v) acetic acid. |
| 1% (v/v) acetic acid | 15 seconds | 3 mL Acetic acid in 297 mL d.$H_2O$ |
| Phosphomolybdic acid/orange G solution | 20 | 3 g Phosphomolybdic acid and 2 g Orange G, dissolved in 500 mL d.$H_2O$ with a crystal of thymol. |
| 1% (v/v) acetic acid | 15 seconds | |
| Light green | 5 | 1 g light green dissolved in 1 mL acetic acid and 500 mL d.$H_2O$. |
| 1% (v/v) acetic acid | 15 seconds | |
| 1% (v/v) acetic acid | 15 seconds | |
| 1% (v/v) acetic acid | 15 seconds | |
| d.$H_2O$ | 2 | |
| Mount DPX | | |

## Tetrachrome

| Solution | Time (Minutes) | Solution Recipe |
|---|---|---|
| Histo-Clear | 7 | |
| Histo-Clear | 7 | |
| 100% EtOH | 2 | |
| 100% EtOH | 2 | |
| 90% EtOH | 2 | |
| 50% EtOH | 2 | |
| $H_2O$ | 10 | |
| Hematoxylin Wiegerts Solution A+B (1:1) | 10 | Wiegert's hematoxylin A = 1% (w/v) hematoxylin in EtOH<br>Wiegert's hematoxylin B = 6 g Ferric Chloride and 5 mL hydrochloric acid (HCL) dissolved in 500 mL $H_2O$. |
| $H_20$ | 2 | |
| 1% (v/v) Acid Alcohol | 15 Seconds | 5 mL HCL in 495 mL of 100% Ethanol |
| $H_20$ | 1 | |
| 90% (v/v) EtOH in water | 2 | |
| 1% (w/v) Phosphotungstic acid solution | 5 | 0.5 g Phosphotungstic acid in 50 mL d. $H_20$. Buffered to pH 7 with sodium hydroxide. |
| d.$H_20$ | 15 seconds | |
| 0.1% (v/v) aniline blue solution | 8 | 0.0505 g of aniline blue dissolved in 1% (v/v) acetic acid. |
| d.$H_20$ | 5 seconds | |
| Picro-orange | 2 | 1% (w/v) Orange G solution – 0.502 g Orange G dissolved in 50 mL d.$H_20$. Then, 10 mL 1% Orange G solution in 90 mL saturated aqueous picric acid. |
| d.$H_20$ | 5 seconds | |
| Ponceau mixture | 5 | 4 mL of 2% Ponceau 2R in 1 % acetic acid = 1.0089 g of Ponceau Xylidine dissolved in 50 mL 1% acetic acid.<br>Added to 1 mL of 2% crystal ponceau in 1% acetic acid = 1.0076 g of crystal ponceau dissolved in 50 mL 1% acetic acid. |
| d.$H_20$ | 1 | |
| 50 % EtOH | 1 | |
| 90% EtOH | 1 | |
| 100% EtOH | 1 | |
| 100% EtOH | 1 | |
| Histo-Clear | 1 | |
| Histo-Clear | 1 | |
| Mount in DPX | | |

## F4/80 Immunohistochemistry

| Solution | Time (Minutes) | Solution Recipe |
|---|---|---|
| Incubate at 37°C | 30 | |
| Xylene | 10 | |
| Xylene | 10 | |
| 100% EtOH | 5 | |
| 100% EtOH | 5 | |
| 95% (v/v) EtOH in water | 5 | |
| 80% EtOH | 5 | |
| 70% EtOH | 5 | |
| PBS | 2 | |
| 1% (v/v) $H_2O_2$ in Methanol<br>200 µL per section | 15 | 100 µL 30% $H_2O_2$ in 2900 µL Methanol. |
| PBS Tween (0.05%) | 5 | 1 mL of 50% Tween in 1000 mL PBS. |
| PBS | 5 | |
| PBS | 5 | |
| Sodium Citrate Buffer<br>Heat in microwave then leave on bench | 3 & 5 | 1.92 g of 10 mM anhydrous Citric acid in 1000 mL d.$H_2O$. pH correct to 6.0. |
| Water | 5 | |
| PBS Tween (0.05%) | 5 | |
| PBS Tween (0.05%) | 5 | |
| 5% Normal Rabbit Serum<br>200 µL per section | 45 | |
| Primary Antibody<br>1/50 F4/80 Anti-mouse (Rat)<br>200 µL per section<br><br>Negative control – PBS only | Overnight (in fridge 4°C) | 1-part F4/80 antibody (Invitrogen) to 49 parts PBS. |
| PBS Tween (0.05%) | 5 | |
| PBS Tween (0.05%) | 5 | |
| Secondary Antibody<br>1/200 Anti-Rat (Rabbit) | 60 | 1 part a-rat antibody to 199 parts PBS. |
| PBS | 5 | |
| PBS | 5 | |
| ABC Solution | 30 | 1 drop A and 1 drop B to 5 mL PBS (Vectastain® ABC Kit, Vector laboratories) |
| PBS Tween (0.05%) | 5 | |
| PBS Tween (0.05%) | 5 | |
| DAB Solution | 40 seconds | 5 mL DAB and 125 µL $H_2O_2$ in 250 mL 0.1M phosphate buffer. |

| | | |
|---|---|---|
| | | Phosphate Buffer = 2.4 g $NaH_2PO_4$ and 11.36 g $Na_2HPO_4$ in 400 mL $H_2O$. pH correct to 7.4. |
| PBS | 5 | |
| PBS | 5 | |
| Hematoxylin | 10 seconds | |
| Water | 2 | |
| 1% (v/v) acid alcohol | 15 seconds | 4 mL HCL in 400 mL 70% (v/v) EtOH in water |
| Water | 2 | |
| 70% EtOH | 4 | |
| 80% EtOH | 4 | |
| 95% EtOH | 4 | |
| 100% EtOH | 4 | |
| 100% EtOH | 4 | |
| Xylene | 10 | |
| Xylene | 10 | |
| Mount DPX | | |

## S.2 SUPPLEMENTARY MATERIAL FOR CHAPTER 3

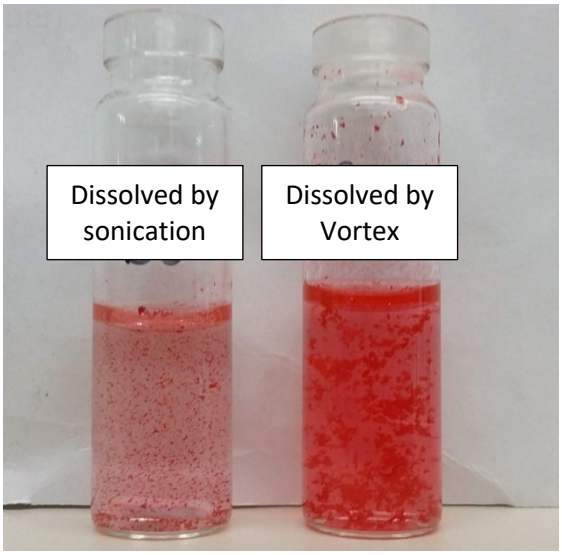


***Figure S 1: BIO precipitation in PBS***

*In the absence of polymersome encapsulation, 200 µM of free BIO precipitates (red) in aqueous solution. The photographed vials show 40 µl of 10 mM BIO dissolved in 2 mL of PBS either by sonication or vortex.*

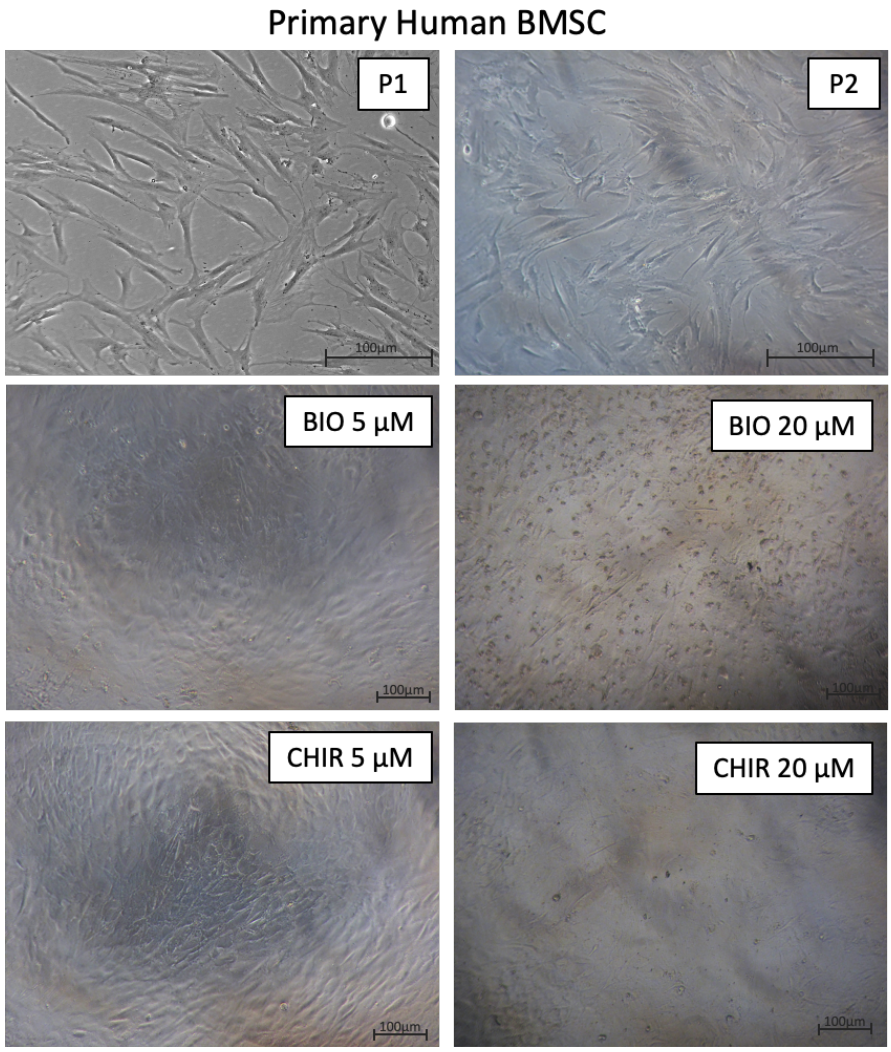


***Figure S 2: Cell culture images of primary human bone marrow stromal cells (hBMSCs)***

*Reference images of isolated primary hBMSC growth and morphology across cell culture passages (P) and following 24 hour incubation with labelled concentrations of BIO and CHIR.*

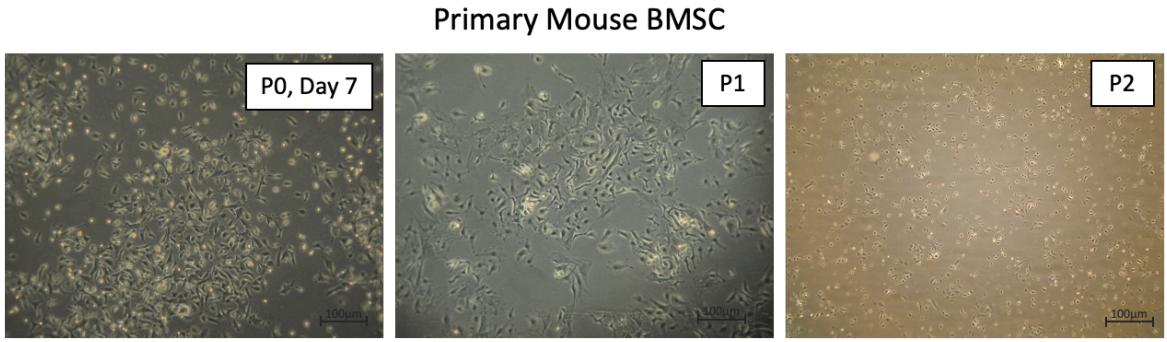


***Figure S 3: Cell culture images of primary mouse bone marrow stromal cells (mBMSCs)***

*Reference images of isolated primary mBMSC growth and morphology across cell culture passages (P).*

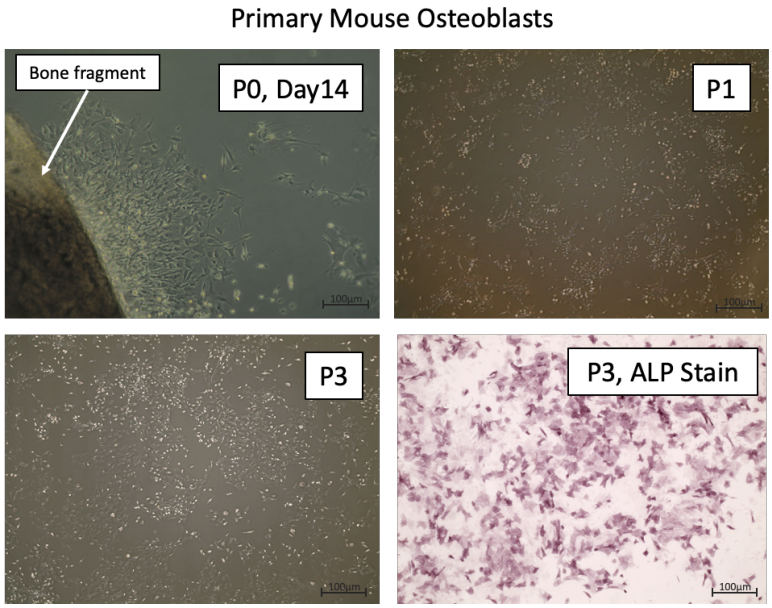


***Figure S 4: Cell culture images of primary mouse osteoblasts***

*Reference images of isolated primary mouse osteoblast growth and morphology across cell culture passages (P) and of a positive stain for alkaline phosphatase (ALP).*

## S.3 SUPPLEMENTARY MATERIAL FOR CHAPTER 4

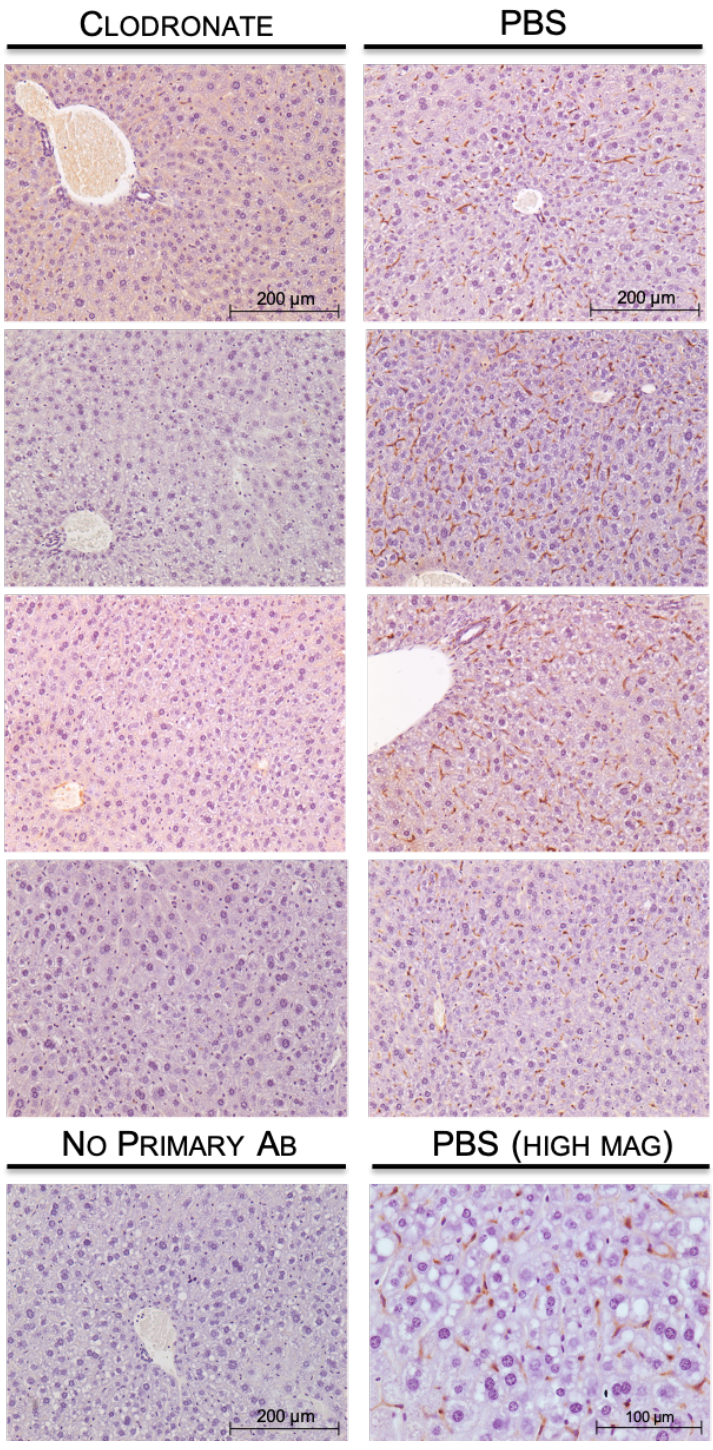


***Figure S 5: Histological sections of mouse liver tissue immunohistochemically stained with anti-F4/80 following treatment with clodronate or PBS liposomes***

*Each image from separate mice. 7 µm thick mouse liver sections extracted from MF1 mice (with a bone injury) 96 hours following IV injection of 250 µL of either clodronate (5 mg/mL) or vehicle control PBS liposomes. PBS images show positive F4/80 DAB stain, in brown, surrounding cells with small oblong nuclei, stained dark purple by hematoxylin, indicative of Kupffer cells. Clodronate images show no positive stain for Kupffer cells*

## S.4 SUPPLEMENTARY MATERIAL FOR CHAPTER 5

***Table S 1: UV-visible spectroscopy (NanoDrop) measurements of isolated RNA purity and yield extracted from cells, liver, and flushed bone marrow samples, following BIO, PM-BIO or PM-Empty treatment.***

*RNA A260/A230 colour coding represents samples with values below 1.8 and therefore likely to be contaminated with organic compounds. Samples in Red were discounted from use.*

| Samples | | | µg/µL | R260/280 | R60/230 |
|---|---|---|---|---|---|
| **Date** | **Details** | **No.** | | | |
| 17.10.17 | Mouse fibroblasts incubated with 5 µM BIO. | 6hr | 663.9 | 2.11 | 2.13 |
| | | 12hr | 541.6 | 2.11 | 2.16 |
| | | 24hr | 459.1 | 2.05 | 2.08 |
| | | Cont. | 751.3 | 2.11 | 2.16 |
| 20.12.17 | Non-injured Liver 48 hours | M1.C | 1176.6 | 2.10 | 2.10 |
| | | M2.C | 1108.4 | 2.06 | 1.78 |
| | | M3 | 714.0 | 2.12 | 2.23 |
| | | M4 | 2437.0 | 2.07 | 2.11 |
| | Non-injured Bone Marrow Left Leg 48 Hours | M1.C | 129.1 | 2.08 | 1.54 |
| | | M2.C | 105.2 | 2.07 | 1.95 |
| | | M3 | 117.7 | 2.09 | 1.49 |
| | | M4 | 205.0 | 2.06 | 1.38 |
| 19.01.18 | Non-injured Liver 48 hours | M1.C | 2734.0 | 2.06 | 2.05 |
| | | M2.C | 1035.0 | 2.13 | 2.19 |
| | | M3 | 3064.3 | 2.01 | 2.13 |
| | | M4 | 2827.4 | 2.04 | 2.10 |
| | Non-injured Bone Marrow Left Leg 48 hours | M1.C | 128.2 | 2.11 | 2.11 |
| | | M2.C | 88.8 | 2.10 | 2.16 |
| | | M3 | 95.6 | 2.18 | 1.80 |
| | | M4 | 95.3 | 2.07 | 2.22 |
| 15.12.17 | Injured Liver 48 hours | M1.C | 2016.8 | 2.10 | 2.16 |
| | | M2.C | 2859.4 | 2.03 | 2.06 |
| | | M3 | 2617.2 | 2.08 | 2.12 |
| | | M4 | 3013.2 | 2.02 | 2.10 |
| | Injured Bone Marrow | M1.C | 82.1 | 2.20 | 2.02 |
| | | M2.C | 58.1 | 2.11 | 0.49 |

| | | | | | |
|---|---|---|---|---|---|
| | Fractured Leg 48 hours | M3 | 115.9 | 2.03 | 2.07 |
| | | M4 | 42.5 | 2.25 | 1.65 |
| 31.1.18 | Injured Liver 48 hours | M1 | 1592.1 | 2.09 | 2.20 |
| | | M2 | 1490.0 | 2.12 | 2.11 |
| | Injured Bone Marrow Fractured leg 48 hours | M1 | 95.8 | 2.00 | 2.15 |
| | | M2 | 101.9 | 2.10 | 1.75 |
| 2.08.2018 | Non-Injured Liver 24 hours post control treatment PM-Empty | M1.C | 747.7 | 1.52 | 1.96 |
| | | M2.C | 654.5 | 0.92 | 1.78 |
| | | M3.C | 527.0 | 1.12 | 1.89 |
| | | M4.C | 427.6 | 1.25 | 1.87 |
| | Non-injured Liver 24 hours post-treatment PM-BIO | M1 | 370.8 | 1.02 | 1.80 |
| | | M2 | 383.5 | 1.13 | 1.85 |
| | | M3 | 409.5 | 1.19 | 1.86 |
| | | M4 | 445.9 | 1.23 | 1.82 |
| 3.8.2018 | Non-injured Left Bone Marrow 24 hours post control treatment PM-Empty | M1.C | 113.9 | 1.41 | 2.04 |
| | | M2.C | 155.4 | 1.01 | 2.01 |
| | | M3.C | 220.4 | 0.83 | 2.03 |
| | | M4.C | 104.3 | 1.30 | 1.90 |
| | Non-injured Left Bone Marrow 24 hours post treatment PM-BIO | M1 | 98.9 | 0.88 | 1.96 |
| | | M2 | 112.8 | 1.46 | 2.00 |
| | | M3 | 139.6 | 1.45 | 2.01 |
| | | M4 | 181.5 | 1.18 | 1.98 |
| 22.08.2018 | Right Bone Marrow Non-injured 24 hours post control treatment PM-Empty | M1.C | 149.2 | 0.98 | 1.99 |
| | | M2.C | 93.0 | 0.84 | 1.87 |
| | | M3.C | 85.1 | 0.97 | 1.95 |
| | | M4.C | 80.0 | 1.25 | 1.91 |
| | Right Bone Marrow Non-injured 24 hours post treatment PM-BIO | M1 | 91.0 | 1.35 | 1.92 |
| | | M2 | 102.3 | 0.64 | 2.01 |
| | | M3 | 62.1 | 0.66 | 1.96 |
| | | M4 | 76.0 | 0.44 | 1.92 |

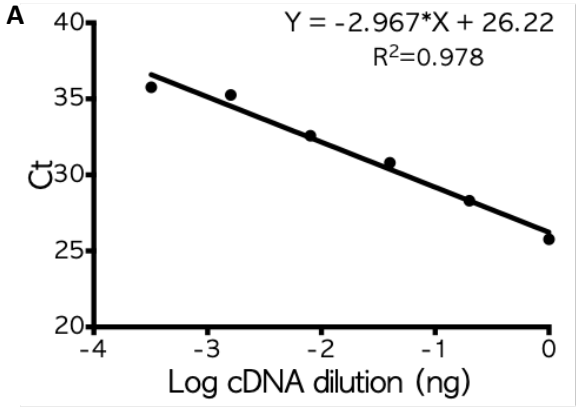


B

$$E\% = \left(10^{\left(\frac{-1}{-2.9672}\right)} - 1\right) \times 100$$

$$E\% = 117.2$$

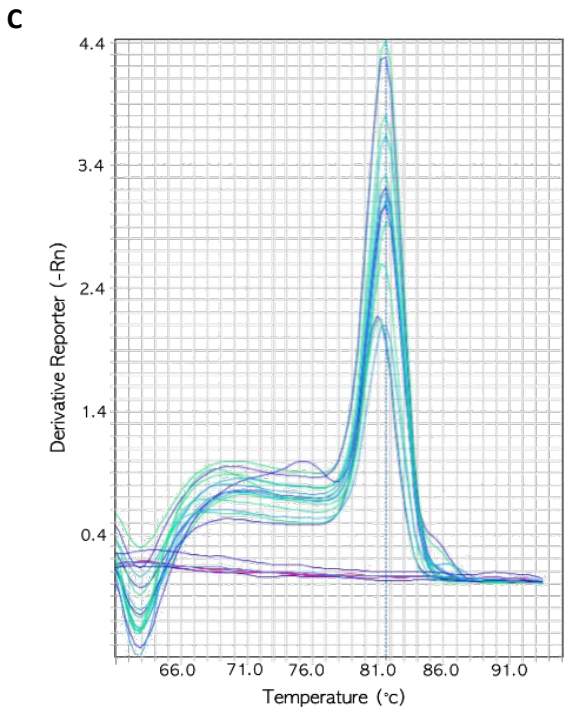


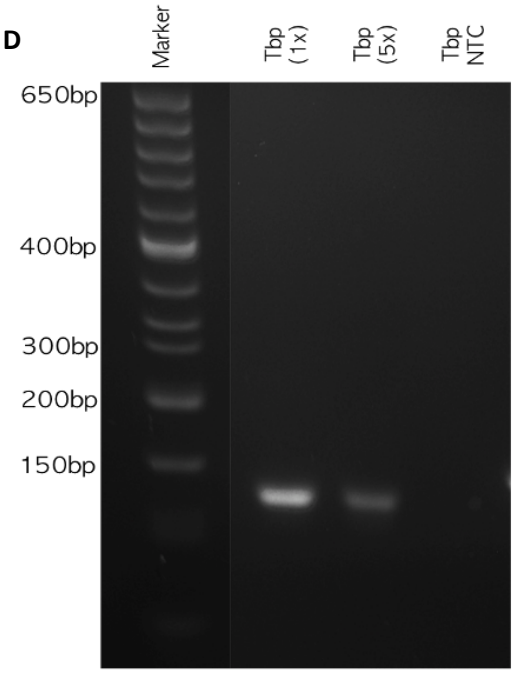


***Figure S 6: Tbp primer efficiency and validation***

*A) Standard Curve of the concentration of template cDNA diluted 5-fold against qPCR number ($C_T$) from 0.2 fluorescence threshold. Data presented is the mean and standard deviation of n=3 repeat diluted template samples. B) Percentage primer efficiency calculated using the standard curve slope value. C) qPCR amplification product derivative melt curve. D) Agarose gel of qPCR amplification product with DNA ladder, 25bp-650bp length markers. NTC = non-template (negative) control.*

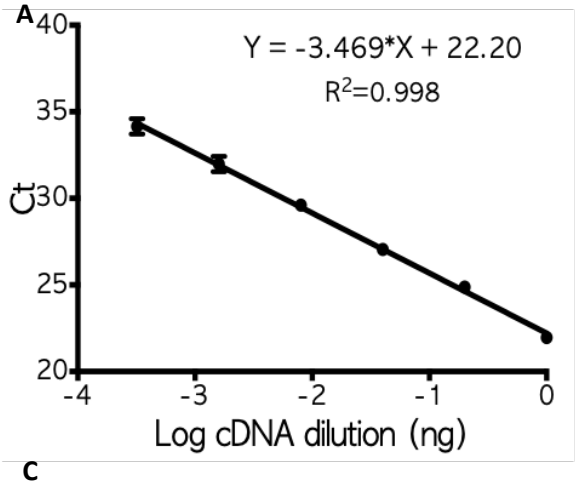


B

$$E\% = \left(10^{\left(\frac{-1}{-3.469}\right)} - 1\right) \times 100$$

$$E\% = 94.2$$

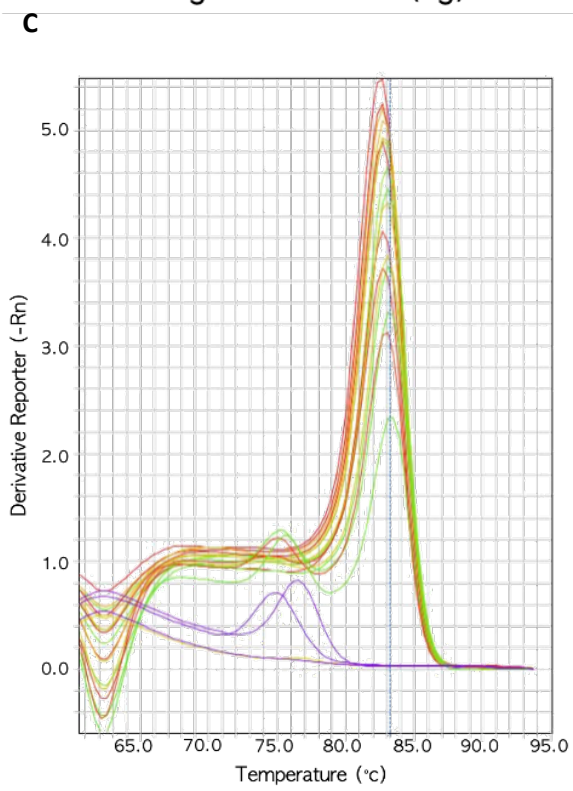


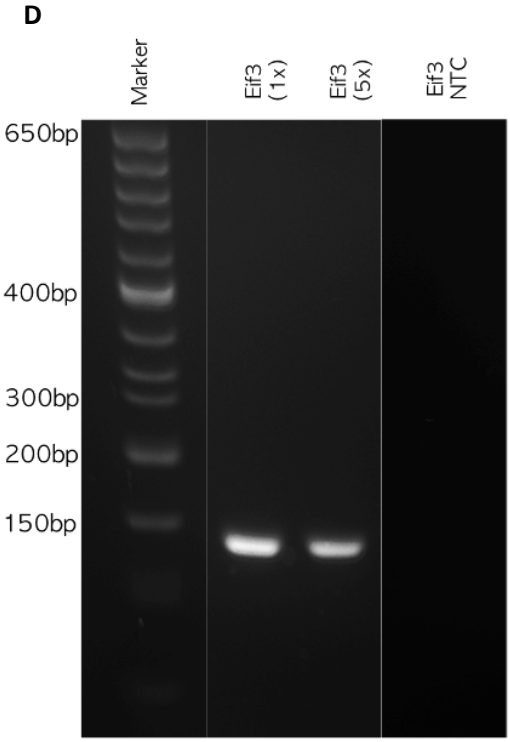


***Figure S 7: Eif3 primer efficiency and validation***

*A) Standard curve of the concentration of template cDNA diluted 5-fold against qPCR number ($C_T$) from 0.2 fluorescence threshold. Data presented is the mean and standard deviation of n=3 repeat diluted template samples. B) Percentage primer efficiency calculated using the standard curve slope value. C) qPCR amplification product derivative melt curve. D) Agarose gel of qPCR amplification product with DNA ladder, 25bp-650bp length markers. NTC = non-template (negative) control.*

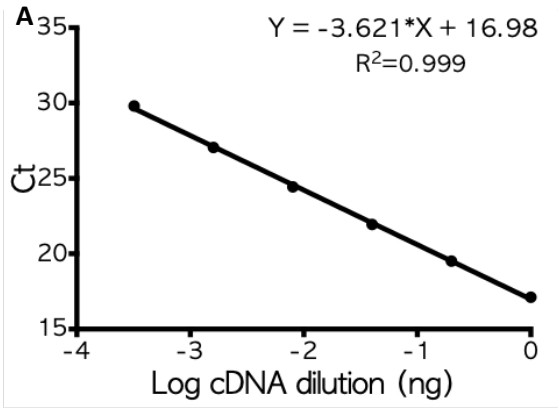


B

$$E\% = \left(10^{\left(\frac{-1}{-3.621}\right)} - 1\right) \times 100$$

$$E\% = 88.9$$

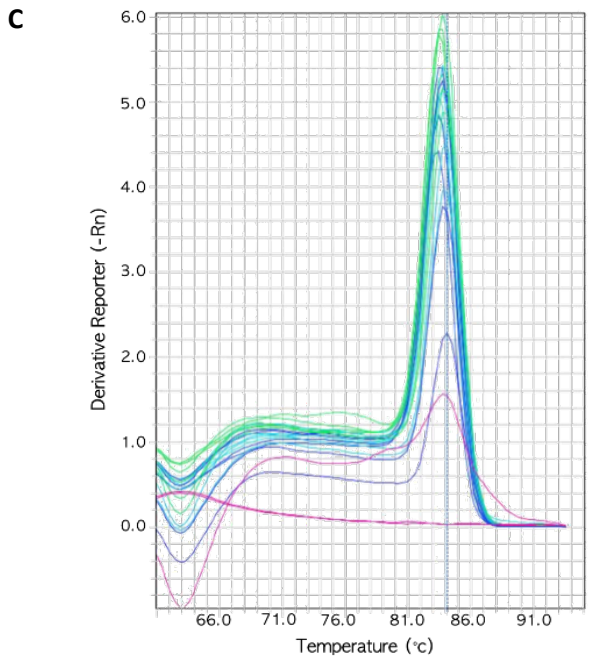


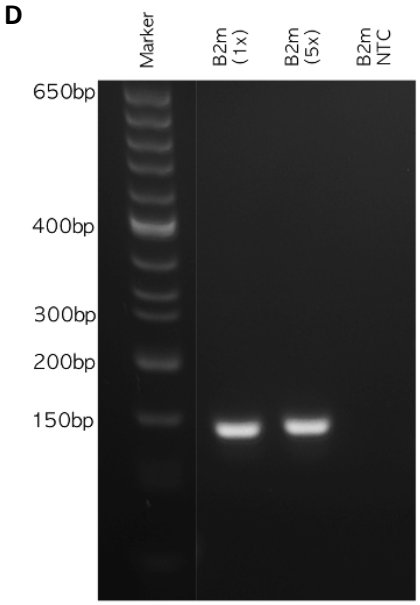


***Figure S 8: B2m primer efficiency and validation***

*A) Standard curve of the concentration of template cDNA diluted 5-fold against qPCR number ($C_T$) from 0.2 fluorescence threshold. Data presented is the mean and standard deviation of n=3 repeat diluted template samples. B) Percentage primer efficiency calculated using the standard curve slope value. C) qPCR amplification product derivative melt curve. D) Agarose gel of qPCR amplification product with DNA ladder, 25bp-650bp length markers. NTC = non-template (negative) control.*

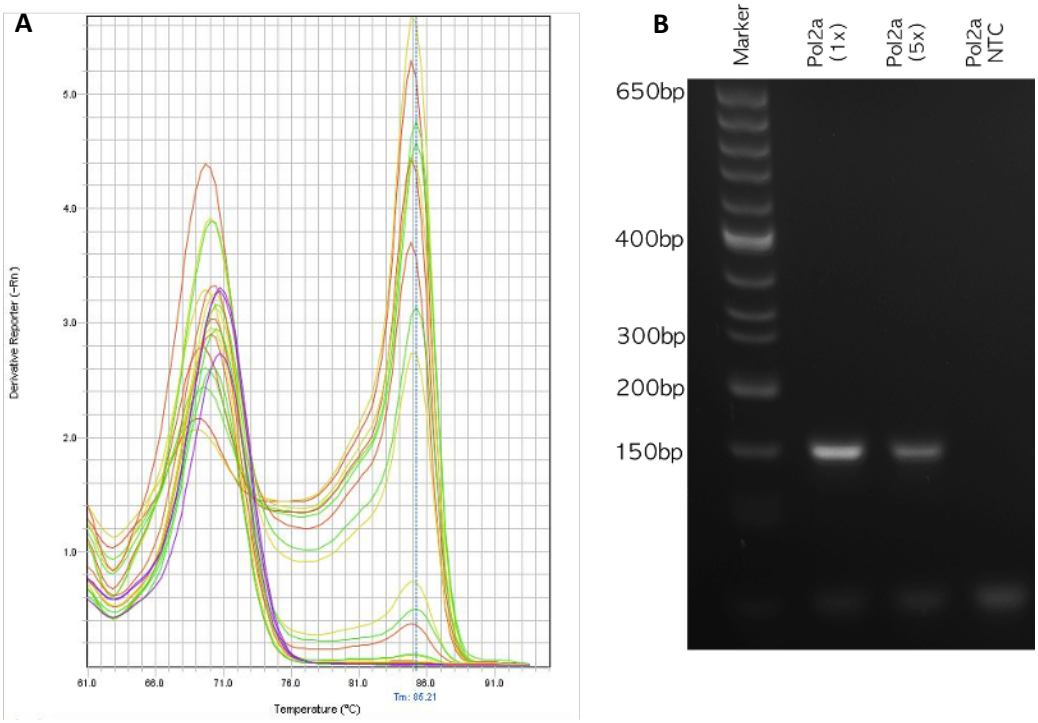


***Figure S 9: Pol2a primer efficiency and validation***

*A) qPCR amplification product derivative melt curve. B) Agarose gel of qPCR amplification product with DNA ladder, 25bp-650bp length markers. NTC = non-template (negative) control.*

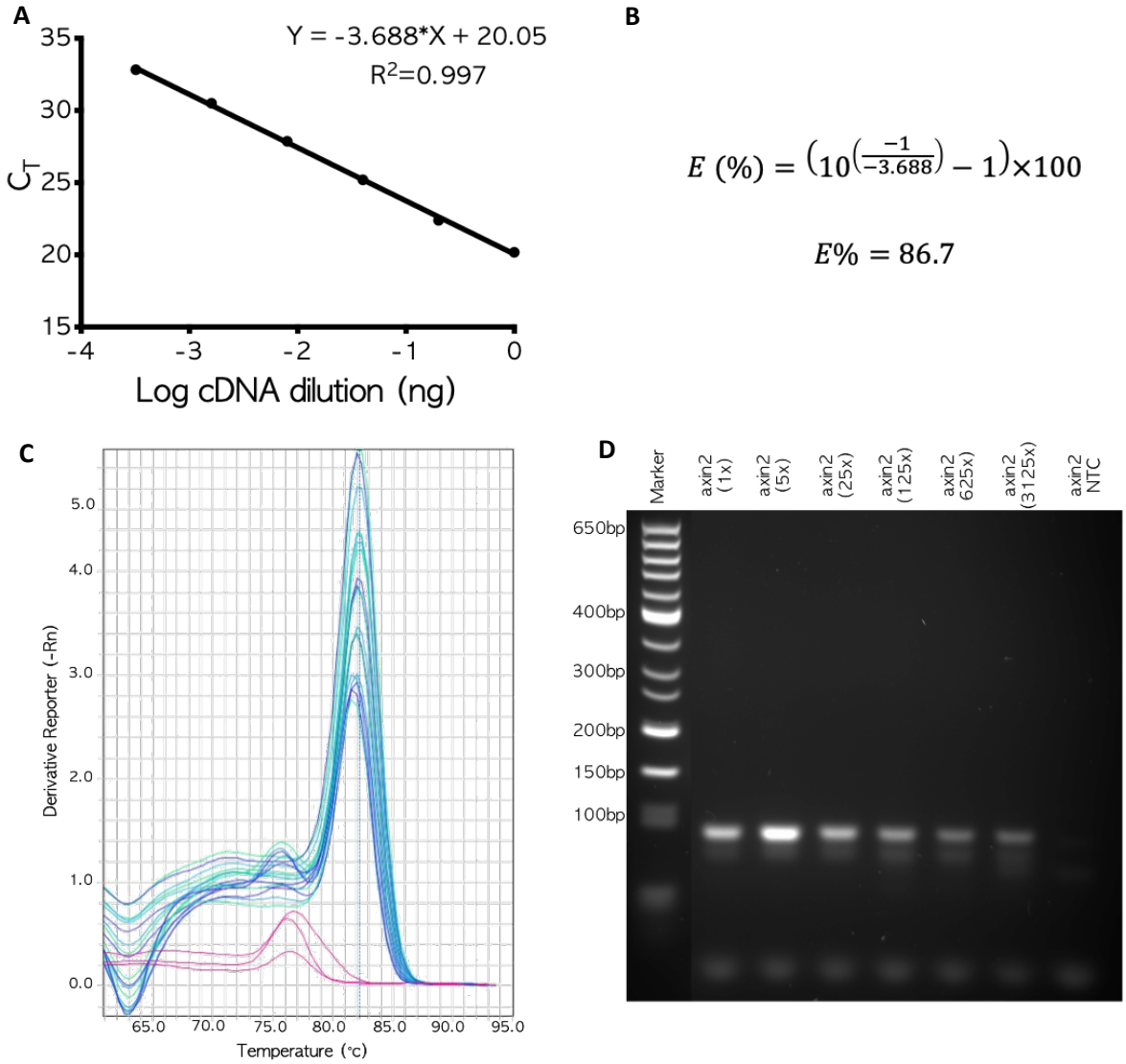


***Figure S 10: Axin2 Wnt target gene primer efficiency and validation***

*A) Standard curve of the concentration of template cDNA diluted 5-fold against qPCR number ($C_T$) from 0.2 fluorescence threshold. Data presented is the mean and standard deviation of n=3 repeat diluted template samples. B) Percentage primer efficiency calculated using the standard curve slope value. C) qPCR amplification product derivative melt curve. D) Agarose gel of qPCR amplification product with DNA ladder, 25bp-650bp length markers. NTC = non-template (negative) control.*

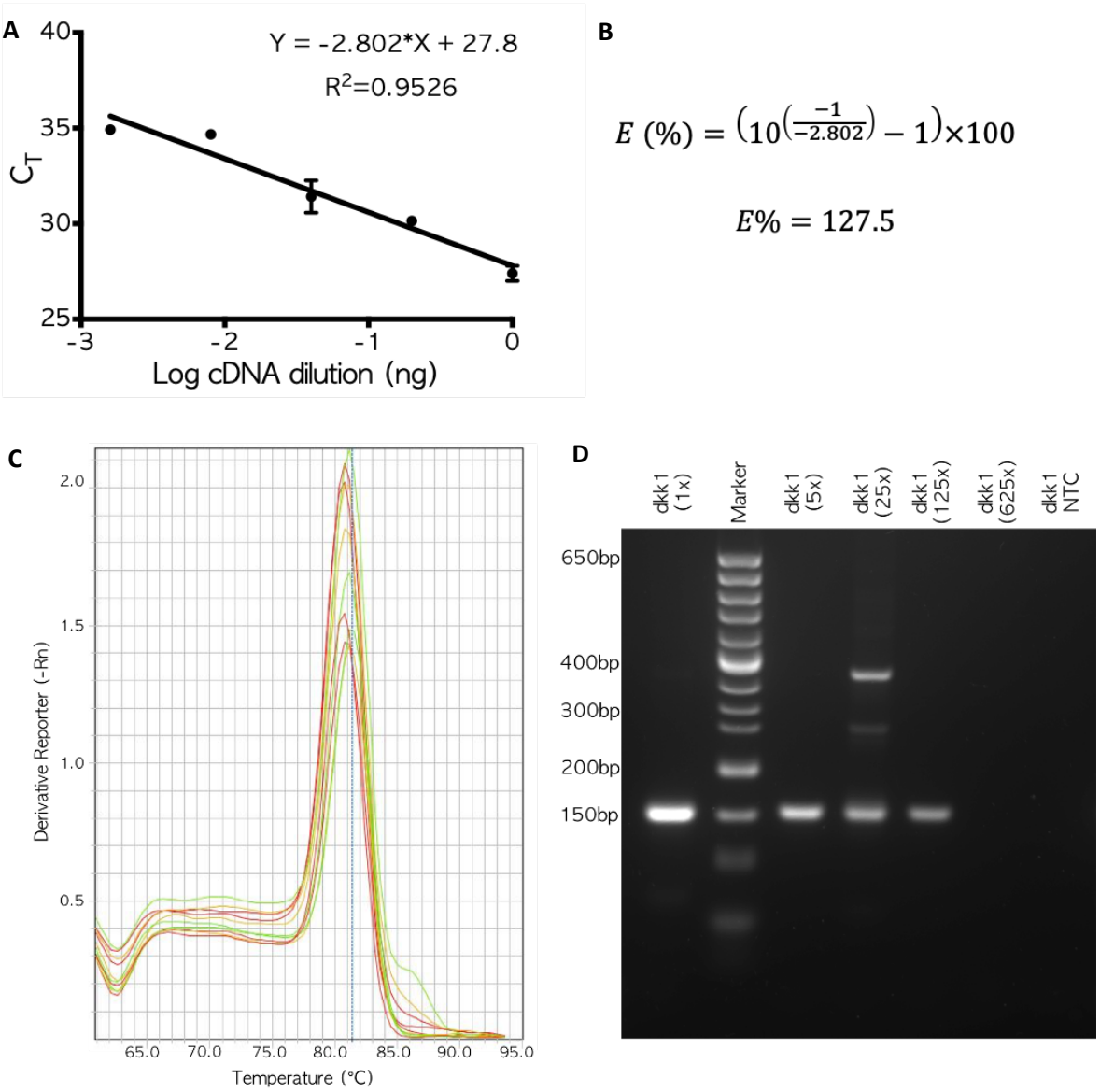


***Figure S 11: Dkk1 Wnt target gene primer efficiency and validation***

*A) Standard curve of the concentration of template cDNA diluted 5-fold against qPCR number ($C_T$) from 0.2 fluorescence threshold. Data presented is the mean and standard deviation of n=3 repeat diluted template samples. B) Percentage primer efficiency calculated using the standard curve slope value. C) qPCR amplification product derivative melt curve. D) Agarose gel of qPCR amplification product with DNA ladder, 25bp-650bp length markers. NTC = non-template (negative) control.*

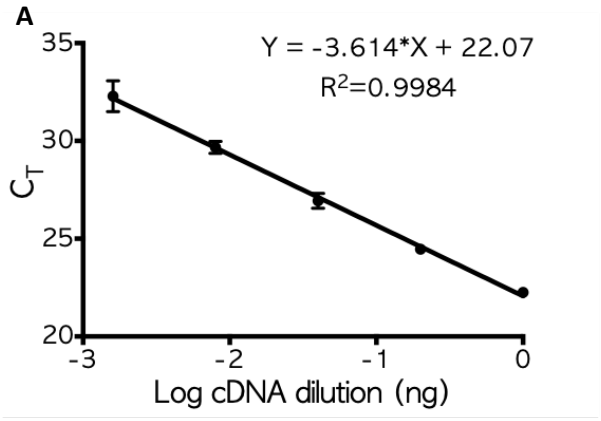


B

$$E\ (\%) = \left(10^{\left(\frac{-1}{-3.614}\right)} - 1\right) \times 100$$

$$E\% = 89.1$$

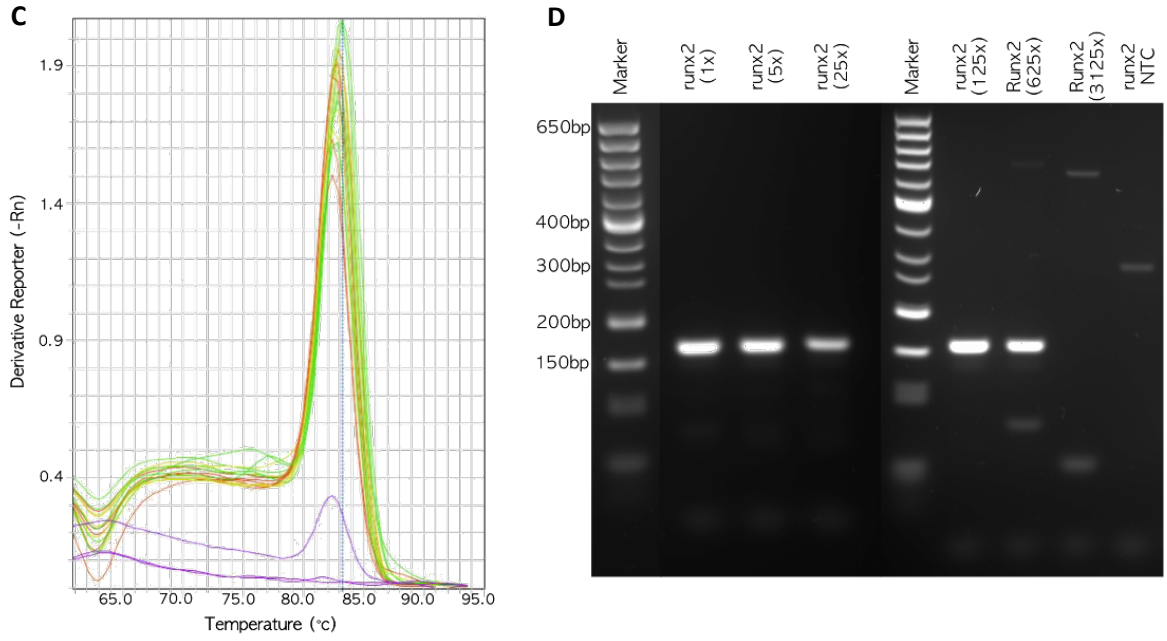


***Figure S 12: Runx2 osteogenic gene primer efficiency and validation***

*A) Standard curve of the concentration of template cDNA diluted 5-fold against qPCR number ($C_T$) from 0.2 fluorescence threshold. Data presented is the mean and standard deviation of n=3 repeat diluted template samples. B) Percentage primer efficiency calculated using the standard curve slope value. C) qPCR amplification product derivative melt curve. D) Agarose gel of qPCR amplification product with DNA ladder, 25bp-650bp length markers. NTC = non-template (negative) control.*

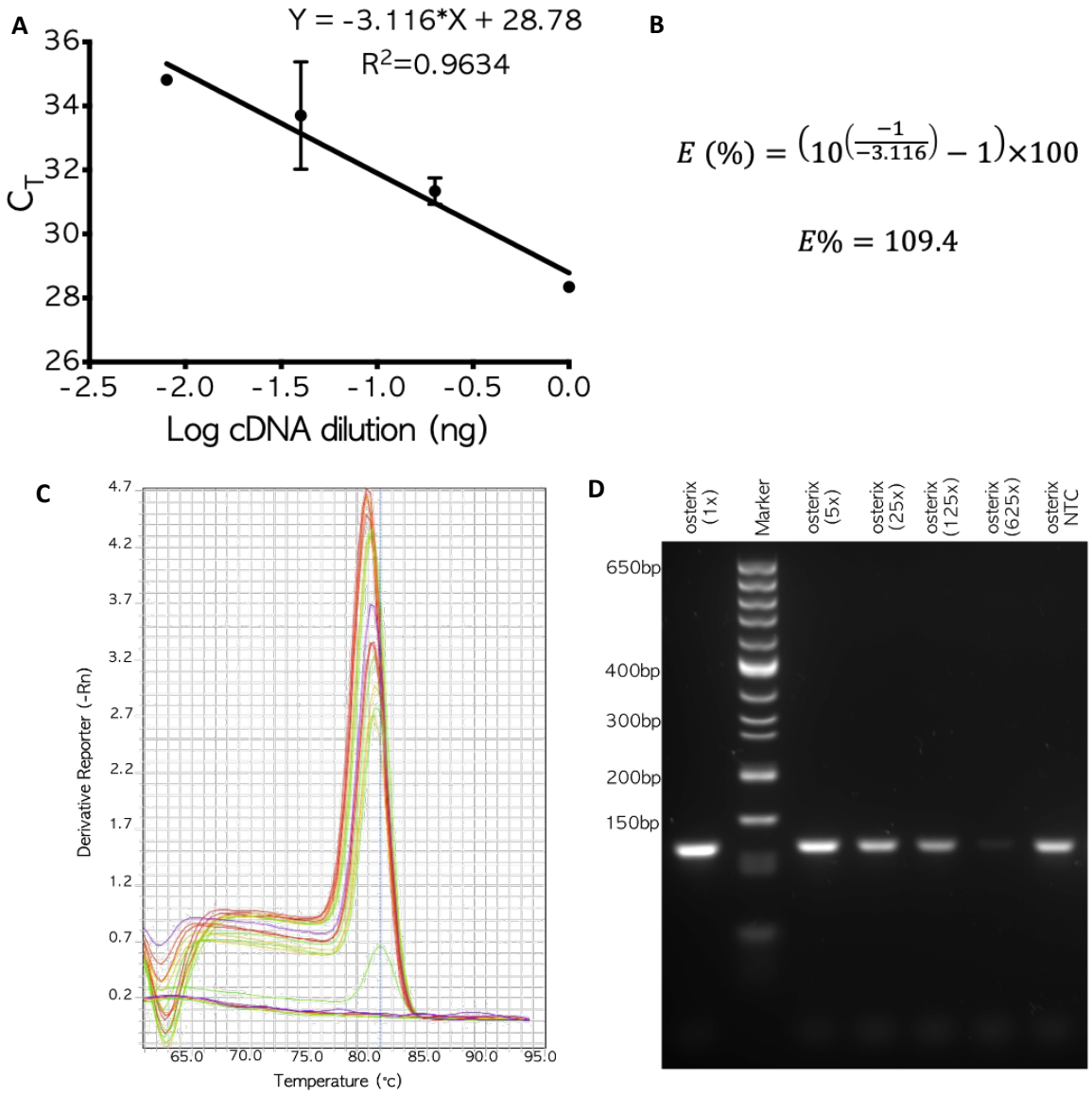


***Figure S 13: Osterix osteogenic gene primer efficiency and validation***

*A) Standard curve of the concentration of template cDNA diluted 5-fold against qPCR number ($C_T$) from 0.2 fluorescence threshold. Data presented is the mean and standard deviation of n=3 repeat diluted template samples. B) Percentage primer efficiency calculated using the standard curve slope value. C) qPCR amplification product derivative melt curve. D) Agarose gel of qPCR amplification product with DNA ladder, 25bp-650bp length markers. NTC = non-template (negative) control.*

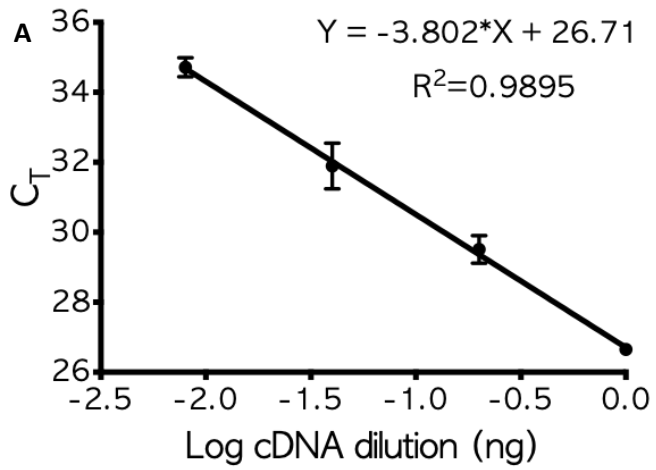


B

$$E\ (\%) = \left(10^{\left(\frac{-1}{-3.802}\right)} - 1\right) \times 100$$

$$E\% = 83.2$$

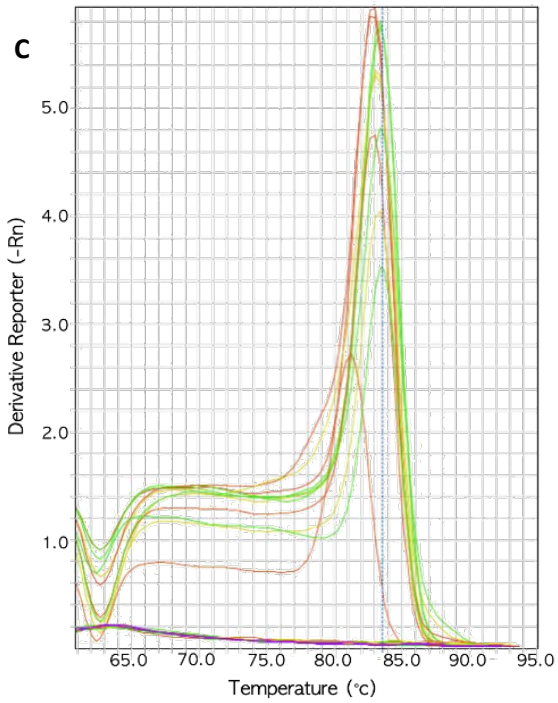


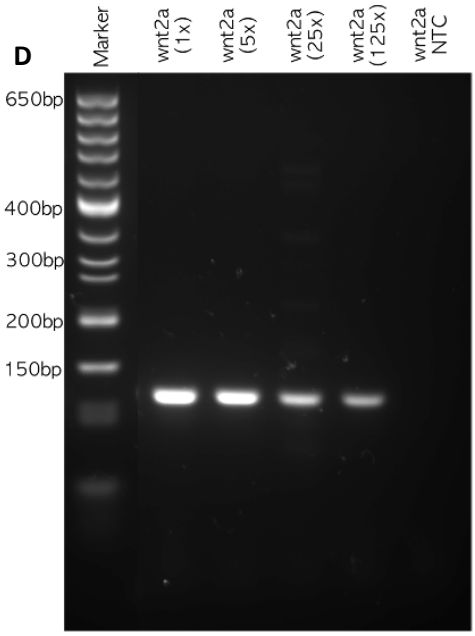


***Figure S 14: Wnt-2a primer efficiency and validation***

*A) Standard curve of the concentration of template cDNA diluted 5-fold against qPCR number ($C_T$) from 0.2 fluorescence threshold. Data presented is the mean and standard deviation of n=3 repeat diluted template samples. B) Percentage primer efficiency calculated using the standard curve slope value. C) qPCR amplification product derivative melt curve. D) Agarose gel of qPCR amplification product with DNA ladder, 25bp-650bp length markers. NTC = non-template (negative) control.*

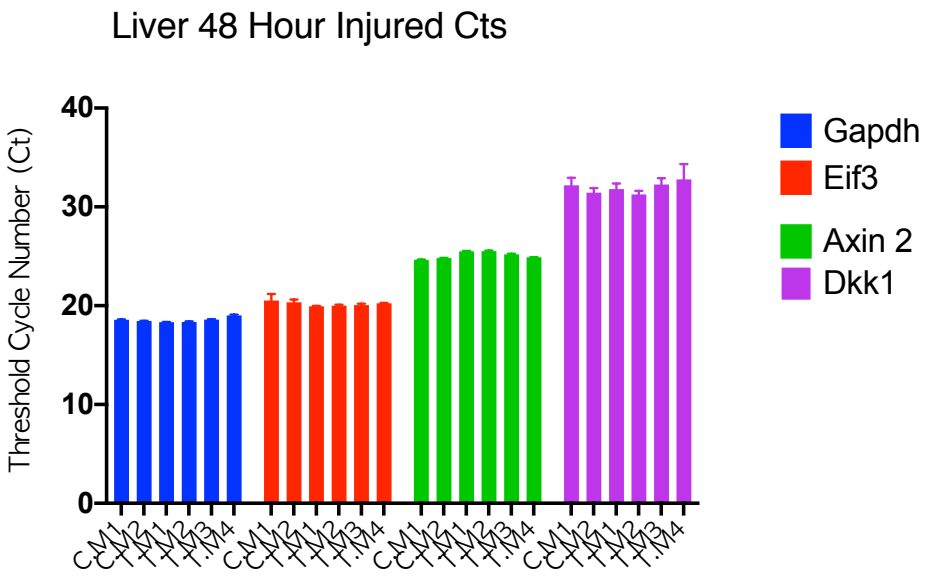


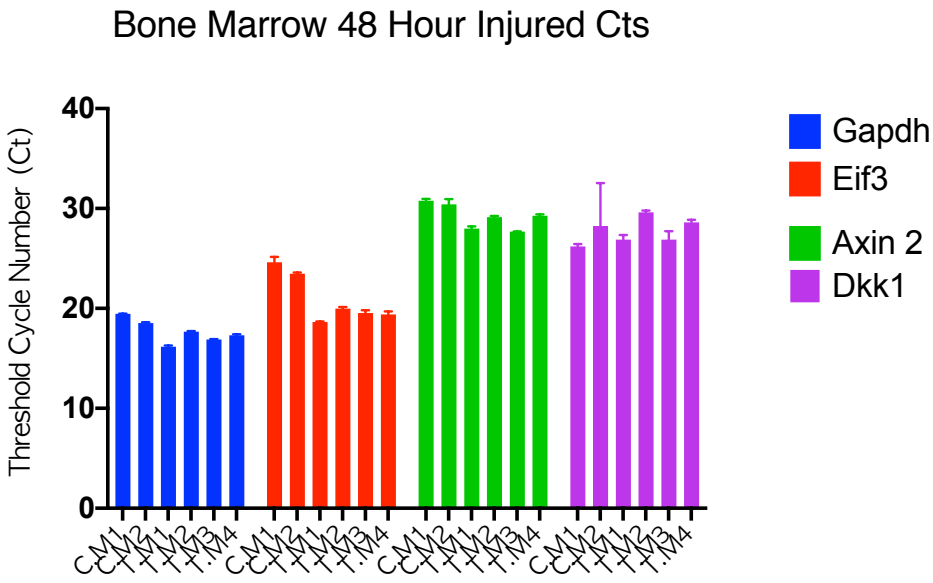


***Figure S 15: Reference of gene cycle expression at a set threshold in subjects (M) treated with PM-BIO (T) or PM-Empty Controls (C)***